

**CHIRAL EXPRESSION AT THE NANOSCALE,
ORIGIN AND RECOGNITION OF CHIRALITY**

By

Anna Ewa Walkiewicz



**UNIVERSITY OF
BIRMINGHAM**

A thesis submitted to
The University of Birmingham
For the degree of
DOCTOR OF PHILOSOPHY

School of Chemistry
The University of Birmingham

June 2010

UNIVERSITY OF
BIRMINGHAM

University of Birmingham Research Archive

e-theses repository

This unpublished thesis/dissertation is copyright of the author and/or third parties. The intellectual property rights of the author or third parties in respect of this work are as defined by The Copyright Designs and Patents Act 1988 or as modified by any successor legislation.

Any use made of information contained in this thesis/dissertation must be in accordance with that legislation and must be properly acknowledged. Further distribution or reproduction in any format is prohibited without the permission of the copyright holder.

Declaration

The work presented in this thesis is the original work of the author and contains no material which is result of collaboration except where otherwise stated.

This dissertation is not substantially the same as any other submitted by the author for a degree or diploma or any other qualification at any other university, and no part of this work has already been or is being concurrently submitted for any such degree, diploma or other qualification.

Anna E Walkiewicz

June 2010

Acknowledgments

Firstly, I must say words of 'thank you' to my supervisor- Professor Trevor Rayment, who gave me a lot of support and encouragement throughout my study. Also I would like to express my appreciation to the CHEXTAN- Marie Curie RTN for giving me an opportunity to work on a very interesting subject and for the financial support.

Secondly I'd like to thank Dr Yitzhak Mastai from Bar Ilan University for great scientific discussions, support and for NSOM measurements.

The collaborators from Chextan RTN cannot go without a mention. I'd like to say thank you to the group of Professor Alan Rowan, especially to Michal Juricek and Jan 'Johnny' Lauko for their amazing support in the organic synthesis.

Also I would like to express my gratitude to Dr Sarah Horswell for help in PM-IRRAS measurements.

Finally I would like to thank my colleagues from the Rayment group for their help and amazing support, especially to Joshua 'Reggie' Hammons for his help with programming and Richard Wiltshire for being my 'third hand' in the lab.

Also I need to thank the University of Birmingham Tango Society for lifting my life a few levels up.

Abstract

Chirality, familiar to all chemists, is usually applied to molecules or assemblies of molecules and plays an important role in both animate and inanimate systems. It is commonly the case that chirality of a system arises from a chiral building block yet chiral systems can also emerge from achiral units.

The objective of this research was to investigate the origin and recognition of chirality at the nanoscale level. To do this, self assembled monolayers made of chirally and achirally tailed molecules were used because such structures are known to form uniform surfaces, which can act as either a source of nucleation or the probing surfaces in chiral recognition.

The strategy adopted in the first part of this study was to use chirally modified self assembled monolayers as a source of nucleation for crystallization of achiral compounds that can form either left or right handed forms in chiral crystallization. Such compounds, widely reviewed by Matura, form chiral crystals even though their building blocks lack a chiral centre. This study presents experiments of induction of chirality in sodium chlorate, hippuric acid and 2,6-ditertbutyl-4-methylphenol crystals. Chiral crystallization of chosen compounds was conducted on D and L cysteine surfaces assembled on gold. The chirality of crystals grown on these surfaces was determined using polarised light microscopy, circular dichroism spectroscopy and NSOM. . The small enantiomeric excess achieved in experiments was explained by the limits of chirality determination methods. It was found that crystals formed in enantiomeric excess were of opposite chirality to the SAM they were grown on. This confirms previous results presented by Mastai on crystallization of histidine on cysteine surfaces.

The second part of this study presents studies of chiral recognition use of AFM technique-Force Distance Spectroscopy. Chirally and achirally modified SAMs were formed *via* the Cu-AAC reaction commonly called 'click chemistry'. This project investigated how the surface preparation influences chiral recognition and if the presence of the second chiral centre affects probing ability. For surface preparation, three types of linkers were used. To functionalize them two complementary compounds equipped with AlaAlaDL and AlaAlaLL dipeptide tail were used. Additional studies were carried out with hippuric acid and glutamic acid-modified SAMs. These studies showed that the way the surface is prepared plays an important role in chiral recognition. In the final recognition experiments it was found that use of molecules possessing either peptide groups or amino acid groups generates additional forces between interacting surfaces, which can be equilibrated by conducting measurements in pH close to their isoelectric point. An influence of the second chiral centre was found for the loosely packed surfaces where the molecules can freely coil.

Table of contents

List of Abbreviations	i
1 Introduction	1
1.1 Project 1- chiral crystallization on surfaces-studies on origin of chirality	1
1.2 Project 2-chiral recognition at the Nanoscale	2
1.3 Reference List.....	2
2 Chirality- from a molecule to a system.....	3
2.1 Definition of chirality	3
2.2 Formation of chiral systems	5
2.3 Chiral crystallization	8
2.4 Chiral crystals vs achiral crystals	9
2.4.1 Generation of chirality in chiral crystals made of achiral molecules	11
2.5 Reference List.....	14
3 Preparation and characterization of chiral Self Assembled Monolayers.....	17
3.1 Self assembly	17
3.2 Self assembled monolayers	17
3.2.1 Structure of self assembled monolayers.....	20
3.2.2 Reactions, reactivity and applications of SAMs	27
3.3 Reference List.....	37
4 Experimental methods.....	47
4.1 Preparation of substrates for gold deposition	47
4.1.1 Mica	47
4.1.2 Glass.....	47
4.1.3 Silicon	48
4.2 Evaporation of gold on mica/glass/silicon.....	48
4.3 Preparation of thiol solutions for self assembly	50
4.4 Preparation of SAMs	50
4.5 Characterization methods	51
4.5.1 Ellipsometry	51
4.5.2 Contact angle goniometry	57
4.5.3 PM-IRRAS.....	61
4.5.4 Electrochemical techniques.....	66
4.6 Methods for determination of crystals chirality.....	78
4.7 Methods used for chiral recognition at surfaces	87
4.7.1 Atomic force microscopy	87

4.7.2	Force- distance spectroscopy	89
4.7.3	Cantilevers and spring constant determination	93
4.8	Reference List.....	96
5	Characterization of self-assembled monolayers used in Project 01 and 02	100
5.1	Characterization of monolayers formed in one-step preparation.....	102
5.1.1	DDT (1).....	102
5.1.2	MDA (2).....	106
5.1.3	Cysteine L (3).....	110
5.1.4	Cysteine D (4)	114
5.2	Characterization of monolayers formed by two- step preparation	117
5.2.1	Characterization of linkers monolayers.....	117
5.2.2	Characterization of monolayers formed in 'click chemistry' reaction	129
5.2.3	Discussion and conclusions.....	159
5.3	Reference List.....	161
6	Project 01- chiral crystallization on surfaces-studies on the origin of chirality.....	163
6.1	Chiral crystals from achiral molecules	163
6.1.1	Crystallization on self assembled monolayers	170
6.2	Experimental details	172
6.2.1	Materials.....	172
6.2.2	Crystallization process –experimental details	174
6.2.3	Determination of chirality	178
6.3	Results	182
6.3.1	Crystallization of sodium chlorate on achiral SAMs	182
6.3.2	Crystallization of hippuric acid on achiral SAMs.....	190
6.3.3	Crystallization of sodium chlorate on chiral SAMs of cysteine L and cysteine D.....	193
6.3.4	Crystallization of hippuric acid on chiral surfaces- cysteine L and D	195
6.3.5	Crystallization of BHT on chiral SAMs- cysteine L and D	197
6.4	Discussion and conclusions	199
6.5	Reference List.....	201
7	Project 02-AFM study of chiral recognition on surfaces	204
7.1	Force distance spectroscopy as a tool for chiral recognition.....	204
7.1.1	Chemical Force Microscopy	205
7.2	Experimental details	208
7.2.1	Click chemistry as a tool for chiral SAMs formation	208
7.2.2	Cantilever modification.....	212
7.2.3	AFM experiment set-up	213
7.3	Chiral recognition studies of self assembly monolayers formed in 'click chemistry' reaction 216	
7.3.1	Determination of adhesion forces for unmodified systems.....	216
7.3.2	Determination of forces for fully modified systems	222
7.4	Discussion and conclusion.....	263
7.5	Reference List.....	266

8	Final conclusions.....	267
	Appendix 1.....	269
	Appendix 2.....	282

List of Abbreviations

Chapter 1

CHEXTAN- Chiral Expression and Transfer at the Nanoscale

AFM -Atomic Force Microscope

SAM-Self Assembled Monolayer

Chapter 2

NLO- Non Linear Optics

Chapter 3

HSR- organic thiols

RSSR- organic disulphides

RCOOH-organic acids

RSiOR₃ –organic siloxanes

Au(111)- substrate of gold crystal with (111) structure

STM- Scanning Tunneling Microscope

PM-IRRAS- Polarization Modulation Infrared Reflection-Absorption Spectroscopy

LEED- Low Energy Electron Diffraction

IR- Infra Red Specroscopy

SPM-Surface Probe Microscopy

Cu-AAC- copper mediated azide- alkyne 1,3-dipolar cycloaddition

RAIRS- Reflection Absorption Infra Red Spectroscopy

DCC-dicyclohexylcarbodiimide

HOBt- 1-hydroxybenzotriazole

UME-ultramicroelectrode

Chapter 4

HPLC- High Performance Liquid Chromatography

Si (100)- silicon crystal of (100) surface

MiliQ- ultrapure, laboratory grade water produced by purification system of Millipore Corporation

EtOH- ethyl alcohol

PTFE- Polytetrafluoroethylene

CCD-charge coupled device

EIS- Electrochemical Impedance Spectroscopy

CV-Cyclic Voltammetry

AC-alternating current

F- Faraday constant

DECON- decontamination washing liquid

SCE- Standard Counter Electrode

ORD- Optical Rotary Dispersion

NSOM- Near Field Scanning Optical Microscope

SNOM- Scanning Nearfield Optical Microscope

AAC- acoustic alternating current operating mode of atomic force microscope

F-D spectroscopy- force- distance spectroscopy

OLS- Optical Lever Sensitivity

Chapter 5

DDT- dodecanethiol

MDA-12-mercaptoundecanoic acid

Linker A- 4-ethynylbenzenethiol

Linker B- 11-azidoundecane-1-thiol

Linker C- 1,8-nonadiyne

Linker A-AlaAlaDL- surface produced in CuAAC reaction by clicking 4-ethynylbenzenethiol modified gold with N-formyl-D-alanyl-L-alanine azidopropyl amide

Linker A-AlaAlaLL- surface produced in CuAAC reaction by clicking 4-ethynylbenzenethiol modified gold with N-formyl-L-alanyl-L-alanine azidopropyl amide

Linker A-GluL- surface produced in CuAAC reaction by clicking 4-ethynylbenzenethiol modified gold with (2R)-2{[4-azidophenyl]carbonyl}amino}pantenedioic acid

Linker A-HA- surface produced in CuAAC reaction by clicking 4-ethynylbenzenethiol modified gold with 4-azido-benzyloaminoacetic acid

Linker B-AlaAlaDL- surface produced in CuAAC reaction by clicking 11-azidoundecane-1-thiol modified gold with N-formyl-D-alanyl-L-alanine-6-heptyn-1ol ester

Linker B-AlaAlaLL- surface produced in CuAAC reaction by clicking 11-azidoundecane-1-thiol modified gold with N-formyl-L-alanyl-L-alanine-6-heptyn-1ol ester

Linker C-AlaAlaDL- produced in CuAAC reaction by clicking 1,8-nonadiyne modified silicon with N-formyl-D-alanyl-L-alanine azidopropyl amide

Linker C-AlaAlaLL- produced in CuAAC reaction by clicking 1,8-nonadiyne modified silicon with N-formyl-L-alanyl-L-alanine azidopropyl amide

XPS-X-ray photoelectron spectroscopy

ODT- octadecanethiol

Chapter 6

HA- hippuric acid

BHT- 2,4-ditertbutyl-6-methyl-phenol

INBP- 4-iodo-4'-nitrobiphenyl

Chapter 7

CFM- Chemical Force Microscopy

CPS-2,2,2-trifluoro-1-(9-anthryl)ethanol

UVO cleaner- UV-ozone cleaner using photo-sensitized oxidation process for cleaning glassware and metal tools

MM2-molecular mechanics calculations program

1 Introduction

The projects presented in this work belong to a family of projects realised by CHEXTAN, a Marie Curie Research Training Network. The general goal of CHEXTAN is probing, understanding and using chiral molecular interactions at the nanoscale. The frames of CHEXTAN assume that knowledge of nanoscale chirality is gathered at a fundamental level of:

- i. effects of chirality on the organization of molecules at surfaces,
- ii. the way it which this chirality can be 'felt' by the surface,
- iii. templated by or transferred from it,
- iv. modulated by surface molecule interactions and used in over-layers and surface reconstruction.

1.1 Project 1- chiral crystallization on surfaces-studies on origin of chirality

The first part of this study is related to phenomena of crystallization. Our aim was to investigate the origin of an emerging crystal in terms of its chirality and whether it is possible to induce desired chirality in an early stage of its growth. As tools for this purpose achiral molecules, which undergo chiral crystallization, were chosen and self assembled monolayers were employed to induce specific chirality into growing crystals. An inspiration for this project was a review by Koshima and Matura¹ of chiral crystallization as well as recent studies on using self assembled monolayers as a nucleating agent and a template for crystallization.

1.2 Project 2-chiral recognition at the Nanoscale

In the second project of this work, AFM Force- Distance spectroscopy was used as a tool for investigation of interactions of chiral molecules on a molecular level. Purpose-designed SAMs were used to chirally feature AFM tip and gold surface and the adhesion force between them was measured during an approach- retract cycle. Specially designed dipeptides were used for tip and surface functionalization in order to investigate specifically the influence of hydrogen bonding on tip-surface chiral recognition. Also the influence of the presence of additional chiral centre was subjected to analysis. This study was inspired by recent developments in chemical force microscopy^{2,3} and chiral recognition^{4,5}.

1.3 Reference List

1. Matsuura, T.; Koshima, H. Introduction to chiral crystallization of achiral organic compounds spontaneous generation of chirality. *Journal of Photochemistry and Photobiology C-Photochemistry Reviews* **2005**, 6 (1), 7-24.
2. Frisbie, C. D.; Rozsnyai, L. F.; Noy, A.; Wrighton, M. S.; Lieber, C. M. Functional Group Imaging by Chemical Force Microscopy. *Science* **1994**, 265 (5181), 2071-2074.
3. Zlatanova, J.; Lindsay, S. M.; Leuba, S. H. Single molecule force spectroscopy in biology using the atomic force microscope. *Progress in Biophysics and Molecular Biology* **2007**, 74 (1-2), 37-61.
4. Mahapatro, M.; Gibson, C.; Abell, C.; Rayment, T. Chiral discrimination of basic and hydrophobic molecules by chemical force spectroscopy. *Ultramicroscopy* **2010**, 97 (1-4), 297-301.
5. McKendry, R.; Theoclitou, M. E.; Rayment, T.; Abell, C. Chiral discrimination by chemical force microscopy. *Nature* **1998**, 391 (6667), 566-568.

2 Chirality- from a molecule to a system

In 1848 Pasteur made his discovery of enantiomorphous crystals of sodium ammonium tartrate¹. After his discovery scientists started to explore the field of chirality and ask questions about the origin of life²⁻⁶. Pasteur's theory of 'chiral forces' as universal dissymmetric forces was questioned soon after it was presented; however, later studies showed that Pasteur was not totally wrong. Universal electroweak forces in nature are dissymmetric and it is proposed that producing a minute excess of one enantiomer could lead to chiral amplification². Chiral symmetry breaking is nowadays of an interest to scientists from many fields from mathematicians and cosmologists to chemists and nanotechnologists. The knowledge of origin of chirality and ways to create chiral systems offers engineers a doorway to invent new technologies, not only for drug synthesis but also for many technologies using non linear optic systems (NLO).

2.1 Definition of chirality

Chirality is a term familiar to all chemists, usually encountered as a molecular property. To be chiral a molecule must fulfil certain conditions, namely its symmetry must be devoid of an axis of improper rotation- an n- fold rotation: followed by reflection in the plane perpendicular to its axis, which brings the molecule onto congruence of itself. In simple words such a molecule is not superimposable on its mirror image. This could be easily observed in molecules which possess a centre of chirality- an atom with connection to four different substituents as shown in Figure 2-1⁷:

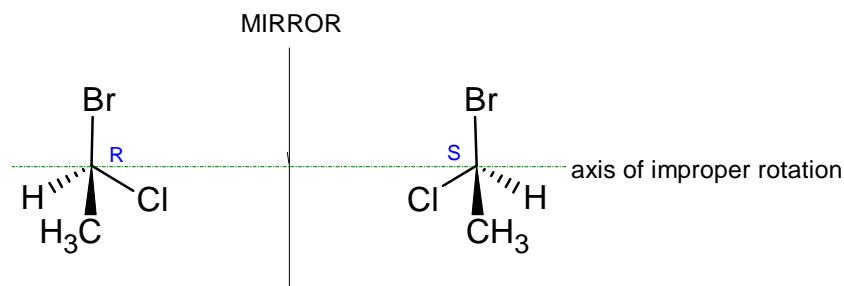


Figure 2-1 Mirror images of a chiral molecule: 1-bromo, 1-chloroethane⁷

In the case of chemical compounds, chirality is exhibited by optical activity. This allows the handedness of a chiral compound to be described by the d –dextrorotatory and l-levorotatory notation, related to the direction of a rotation of a polarized light plane (right and left, respectively). Such notation is usually used by biochemists and biologists. When a molecule has more than one chiral centre such notation is not adequate to describe this situation well. The Cahn, Ingold and Prelog convention determines handedness of a compound in a much better way. It denotes R for the right-handed (rectus) and S for the left-handed (sinister) way of substituents' arrangement at the chiral centre⁷. An asymmetric tetrahedral carbon is usually found at a centre of chirality; however, molecules such as trans- cycloalkanes do not have a tetrahedral carbon at the centre. Nevertheless they are chiral as shown in Figure 2-2 since the lack of appropriate symmetry elements. In trans-1, 2-dimethylcyclopropane the absence of reflective symmetry elements puts the molecule amongst dissymmetric compounds which are considered to be chiral. They are treated as rigid objects:

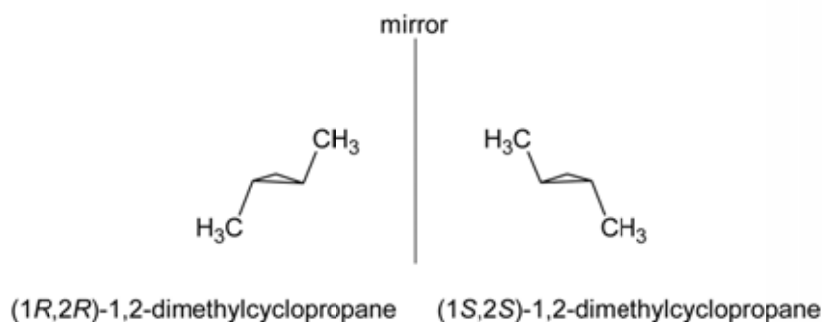
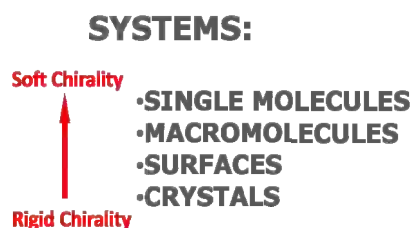


Figure 2-2 Chiral molecule: trans-1, 2-dimethylcyclopropane and its mirror image. Dissymmetry makes these molecules chiral

The non-superimposable mirror images of an object are called enantiomers, and a mixture of the equal amount of enantiomers is called a racemate. Racemates are usually included within the category of optically inactive compounds.

In 1991 the definition of chirality was revised by L.D. Barron and related not only to single molecules or rigid objects but to whole systems. His description implies that true chirality is shown by systems existing in two distinct enantiomeric states that are interconverted by space inversion, but not by time reversal combined with any proper spatial rotation⁸.

After this definition was presented, as shown below it has become normal to use the terms of soft chirality in regards to single molecules and rigid chirality for more complex systems.



2.2 Formation of chiral systems

The formation of chiral systems, which are enantiomerically pure, is not a trivial process. Chirality is a property of the living world, but even now there is no universally accepted unambiguous theory of how it happened that most of the natural aminoacids are L and sugars D. Knowing how to create chiral systems plays a significant role in drug synthesis because it is often the case that only one enantiomer (eutomer-the active enantiomer) has the desired properties whilst the other (distomer-less active enantiomer) has no influence or, worse, it is a strong toxin.

Soft chirality, pronounced in single molecules, was the first option for chemists to deal with but even now it is not easy for synthetic chemists to 'repeat Nature' and during a chemical reaction yield only one, pure enantiomer. Despite recent developments in organic synthesis that made production of pure enantiomers possible, there is still a large number of compounds for which

homochirality is unachievable. In such cases there is a need to employ analytical chemistry techniques to purify products. Those techniques, however, use other chiral systems in order to separate enantiomers. That made formation of chiral compounds a rapidly developing field.

The best examples of *systems* where chiral expression can be seen are surfaces and bulk materials such as crystals. Surfaces can be chiral in the sense that they are nonsuperimposable on their mirror images; the enantiospecificity is derived from the local structure of nanoscale features—molecular adsorbates or specific arrangements of atoms at a crystal surface.

The most obvious way of making a chiral surface is by cleaving a chiral crystal. It is sufficient to note the fact that any cut through a chiral crystal will produce two chiral (i.e. non-superimposable) surfaces. In nature there are comparatively few inorganic chiral solids that could be used in interfacial science, e.g. metal oxides such as $\text{La}_2\text{Ti}_2\text{O}_7$ or GaNbO_4 ^{9,10}

Chiral surfaces may be produced also in the ways that include chiral cuts through achiral solids, adsorption of chiral and achiral compounds on achiral metal surfaces and chiral electrodeposition. If an achiral metal with fcc (face centered cubic), bcc (body centered cubic), hcp (hexagonal close packed) cell type is cut along a high Miller index plane such as (641), (641), (643) it will produce two chiral surfaces¹¹. A model of such produced surfaces is shown in Figure 2-3.

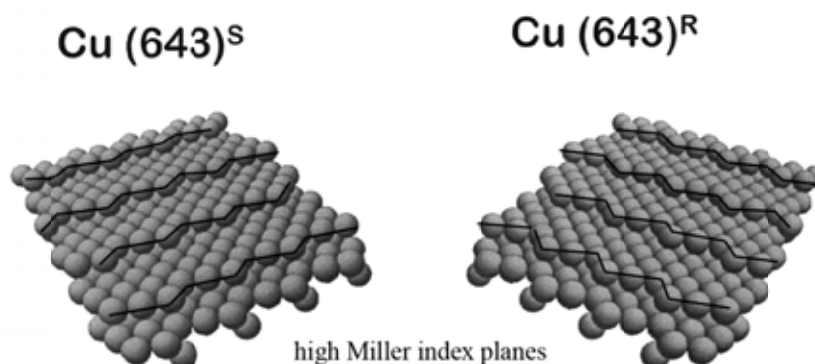


Figure 2-3 Models of the ideal Cu(643)-S and R surfaces made using LEED patterns obtained from such surfaces¹¹

A fresh approach to making chiral surfaces was presented a few years ago by Switzer- a stable surface was formed by electrodeposition of epitaxial films of low-symmetry material (CuO) onto high symmetry achiral surfaces (Au (001))¹². The chirality of solution precursors was found to control the handedness of the electrodeposited films. The handedness of the CuO films was determined by the chirality of the deposition solution because the Au (001) surface has high symmetry and does not impart the chirality. It was speculated that chiral electrodeposition was determined by free tartrate ion or Cu(II)(tartrate) complex on the Au surfaces. The R enantiomer of CuO was deposited in the presence of (R,R) tartaric acid and the S enantiomer in the presence of (S,S)-tartaric acid. Moreover, when the activity of obtained layers was tested, it transpired that S-CuO film is more active for the oxidation than R-CuO. A control film deposited from racemic mixture of (R,R) and (S,S)-tartrates has no selectivity for oxidation of the enantiomers.

It is commonly understood that we can build a chiral system out of chiral building blocks and an achiral system out of achiral components. This situation is best illustrated in crystals. A chiral compound, when it crystallizes, gives optically active crystals. This was first observed by Pasteur for tartaric acid¹ (Figure 2-4).

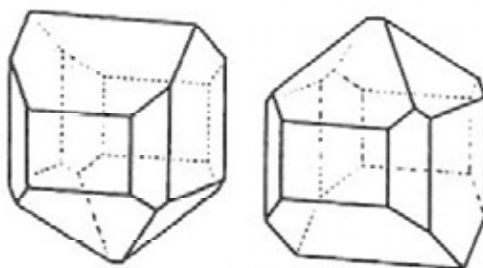


Figure 2-4 Enantiomers of tartaric acid crystals¹

For solids formed from achiral compounds the situation is more complicated. A large number of achiral compounds give optically inactive crystals; however, there is a group of achiral compounds which undergo a phenomenon of chiral crystallization.

2.3 Chiral crystallization

Louis Pasteur's study of crystals started a lengthy period of investigation of crystals and crystallization matter. He discovered that from optically inactive silicate ions of silicon oxide there is a way to obtain crystals of chiral morphologies, as shown in Figure 2-5:



Figure 2-5 Chiral crystallization and enantiomers of quartz crystals^{7,13}

From many experiments, the rule of crystallization has been concluded. The principle is shown in Figure 2-6.

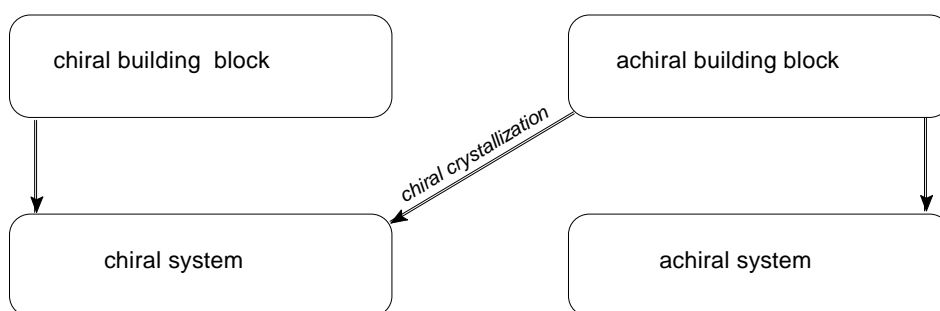
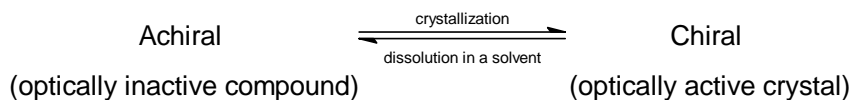


Figure 2-6 The principle of chiral and achiral systems formation

The rule presented above shows that we are not only able to form chiral system from chiral building blocks but also using achiral building blocks, whereas an achiral system can be built only from achiral building blocks.

Chiral crystallization is a process in which from an optically inactive compound an optically active crystal is formed according to the scheme:



The most studied example of this process has been reported by Kondepudi¹⁴ who found that sodium chlorate crystals in non stirred vessels are in ratio of L to D enantiomers equal to 50:50. However when the solution was stirred in the left or right direction the ratio of number of L to D crystals was shifted towards left and right handed crystals respectively¹⁵.

In practice, the realization of such symmetry breaking is hard to achieve since it requires two mechanisms- chiral autocatalysis and competition (direct or indirect) between enantiomers (growth of one enantiomer suppresses the growth of the other). Also in chiral symmetry breaking there is a need to distinguish between two types. In the first the symmetric state of equal L- and D- enantiomers becomes unstable and the system makes a transition to an asymmetric state. This is spontaneous symmetry breaking. The second type is one in which the symmetric state is stable, but due to the nature of the kinetics, the system evolves into an asymmetric state dominated by one enantiomer - kinetic symmetry breaking.

2.4 Chiral crystals vs achiral crystals

When considering the chirality of crystals¹⁶, it is very important to distinguish between the three different parts, which can be chiral or achiral:

- The molecular components of the crystal
- The crystal structure itself
- The symmetry group of the crystal structure

The symmetry group of a molecule is a point group and that of a crystal structure - a space group. Whether a crystal is chiral or not depends upon its symmetry group. The symmetry group of a chiral

object contains symmetry operations of a first kind- such as rotations and translations, but not of a second kind, *i.e.* roto- inversions. An achiral object contains symmetry operations of both kinds in equal amounts¹⁷. The term ‘chiral space group’ means the space group of a chiral structure although for example, the space group $P2_1$ itself is achiral since it does not form one member of an enantiomorphous pair; therefore, a crystal belonging to this group is chiral.

Using such criteria among the 230 space groups we can distinguish 65 that are chiral (containing only symmetry elements of the first kind) and within them we can find examples of chiral crystals¹³.

System	Class	Chiral space group
Triclinic	1	$P1$ (#1)
Monoclinic	2	$P2$ (#3) $P2_1$ (#4) $C2$ (#5)
Orthorhombic	222	$P222$ (#16) $P222_1$ (#17) $P2_12_12_1$ (#18) $P2_12_12_1$ (#19) $C222_1$ (#20) $C222$ (#21) $F222$ (#22) $I222$ (#23) $I2_12_12_1$ (#24)
Tetragonal	4	PA (#15) $P4_1$ (#76) $P4_2$ (#77) $P4_3$ (#78) $I4$ (#79) $I4_1$ (#80) 422 $P422$ (#89) $P42_12$ (#90) $P4_122$ (#91) $P4_12_12$ (#92) $P4_322$ (#93) $P4_22_12$ (#94) $P4_322$ (#95) $P4_32_12$ (#96) $I422$ (#97) $I4_122$ (#98)
Trigonal and rhombohedral	3	$P3$ (#143) $P3_1$ (#144) $P3_2$ (#145) $R3$ (#146) 32 $P312$ (#149) $P32_1$ (#150) $P3_112$ (#151) $P3_12_1$ (#152) $P3_212$ (#153) $P3_12_1$ (#154) $R32$ (#155)
Hexagonal	6	$P6$ (#168) $P6_1$ (#169) $P6_5$ (#170) $P6_2$ (#171) $P6_2$ (#172) $P6_1$ (#173) 622 $P622$ (#177) $P6_122$ (#178) $P6_522$ (#179) $P6_222$ (#180) $P6_422$ (#181) $P6_322$ (#182)
Cubic	23	$P23$ (#195) $F23$ (#196) $I23$ (#197) $P2_13$ (#198) $I2_13$ (#199) 432 $P432$ (#207) $P4_232$ (#208) $F432$ (#209) $F4_132$ (#210) $I432$ (#211) $F4_332$ (#212) $P4_132$ (#213) $I4_132$ (#214)

Figure 2-7 The 65 chiral space groups (contained within the 230 total space groups)¹³

Amongst these 65 chiral space groups there are crystals that are formed in a process of chiral crystallization, the compound which makes the crystal is achiral itself but the crystal it makes exhibits optical activity. Matura and Koshima¹³ compiled an extensive list of achiral organic compounds which can undergo chiral crystallization. Generation of chirality in such crystals could have several origins but they are all related to the structure of the compound.

2.4.1 Generation of chirality in chiral crystals made of achiral molecules

There are three requirements for the generation of chirality from achiral organic molecules. The first one, rotation of bonds, is related to the conformations of bonds of a molecule and is the most visible in n-butane. The molecule has two chiral conformations- both *gauche* (M-helicity and P-helicity) and they are enantiomeric to each other. The conditions such as temperature or influence of other compounds make the conformation stable and formation of chiral crystals possible. Such an example was reported by Fumio Toda, who presented a chiral host- guest complex, where 1,2-dichloroethane (guest) had a nearly eclipsed conformation (7) of the (M)-form in the host molecule¹⁸.

A helical arrangement of the molecules in a crystal lattice is the second way of generating chirality. This could be illustrated well by the example of hexahelicene¹⁹⁻²¹ and helical triskelion monophosphites²² as shown in the Figure2-7.

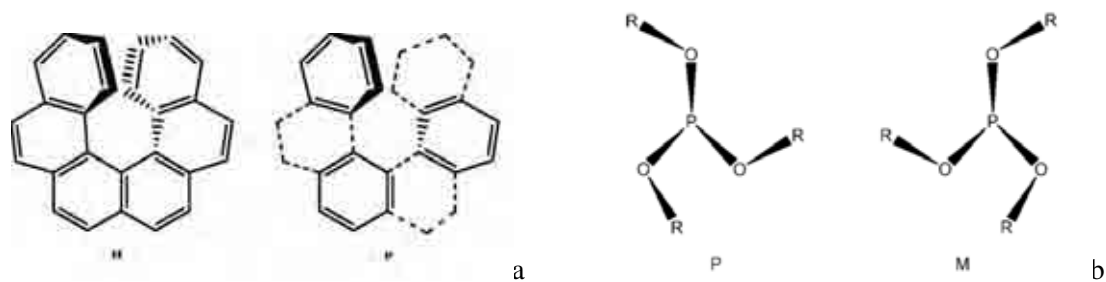


Figure 2-8 a) 10 M and P hexahelicene²¹ b) P and M enantiomers of triskelion monophosphites P(OR)₃²²

Both of these factors above are necessary for the generation of chirality; however, they are not sufficient for forming enantiomorphic crystals. It is also the case that right handed and left handed molecules can simultaneously exist in the unit cell, which may cancel the chirality of the crystal.

Formation of a head to head stacking columnar arrangement is a third factor for chirality generation and plays an essential role -either by rotation of bonds or helical arrangement. The best examples of these are benzophenone²³ and phenanthridine²⁴ (Figure 2-9).

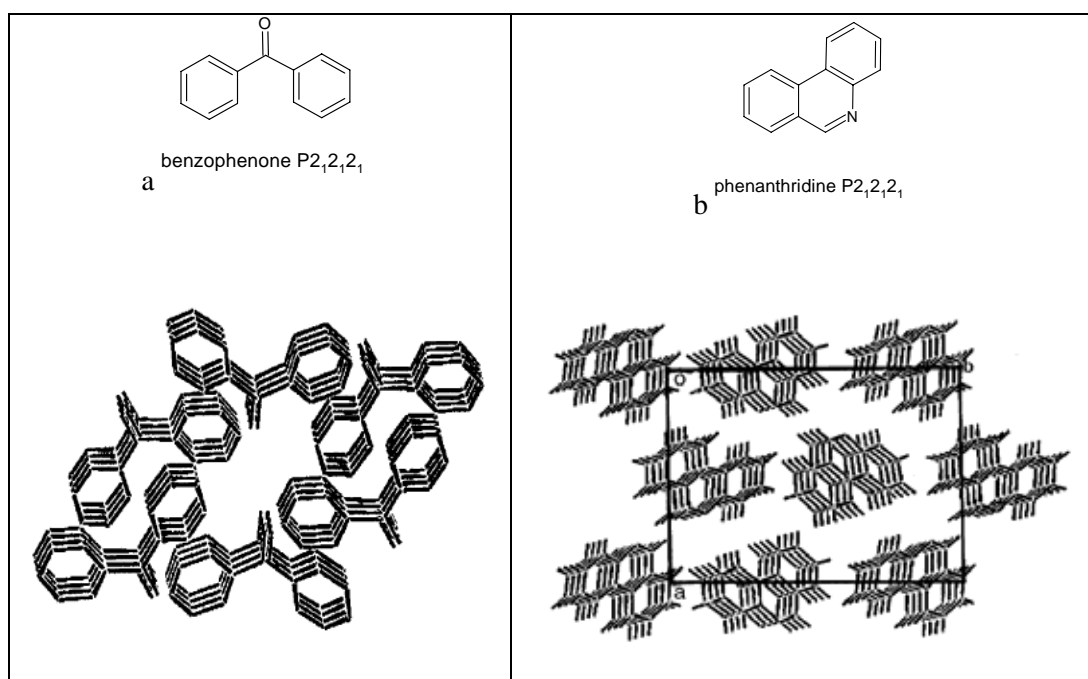


Figure 2-9 Stacking column structure along c-axis a) benzophenone²³ b) phenanthridine²⁴.

In 2005 Matura and Koshima presented several hypotheses on factors controlling chiral crystallization. The first one indicated that carboxylic acids and amides having a second hydrogen bonding function may form a spiral chain, facilitating the formation of chiral crystals. If the acid or amide has a second hydrogen bonding function such as $-OH$, NH , $S=O$, intermolecular interaction between the groups may occur to form a linear chain structure, which likely results in a helical arrangement²⁵. It was reported by Leiserovitz that phenylsulphonylacetic acid crystallizes in a chiral space group having a linear chain structure with a two-fold screw axis in the crystal lattice²⁶.

The next hypothesis, first presented by Collet, showed that molecules having a C_2 or C_3 axis tend to crystallize in chiral structures²⁷. It could be seen the best for benzophenone derivatives, which possess a C_2 axis, and tri-*o*-thymolide, which has a C_3 axis.

It has been also discovered that two-component molecular crystals may promote the generation of chirality²⁸. The working hypothesis was based on the fact that crystal chirality can be induced by freezing a flexible molecule into a chiral conformation when undergoing self-assembly with another molecule through hydrogen bonding and a salt bridge. This hypothesis was based on a comprehensive study of two-component molecular crystals. It was discovered that they form two types of crystals: a propeller type and a helical type. In propeller-type crystals (diphenylacid and phenanthridine, diphenylacetic acid and acridine) O-H \cdots N hydrogen bonding was formed between two molecules and the crystal chirality was generated from the existence of molecular pairs of single absolute configuration in the lattice^{28,29}.

In helical type of crystals (*i.e.* 3-indolepropionic acid and phenanthridine) O-H \cdots N hydrogen bonding acts as an auxiliary for the formation of a helical structure in two places- between the indole imino group and the carboxylic acid group within the same molecule (that forms two fold helix) and the second between constituent molecules of the crystal^{30,31} as shown in Figure 2-10:

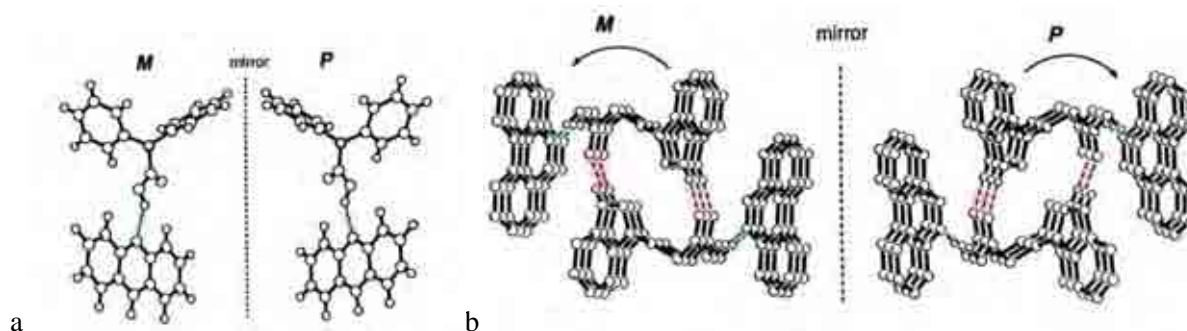


Figure 2-10 Molecular arrangements of a) propeller crystal of diphenylacetic acid and acridine b) helical crystal of 3- indolepropionic acid and phenanthridine³². Hydrogen bonding between two different constituent molecules is indicated with blue and between the same constituent molecules with red.

However, in many cases of two-component molecular crystals *i.e.* diphenylacetic acid and acridine- their molecular pairs stack in head-to-head fashion to form a chiral conformation. That brought a conclusion that a head to head stacking columnar arrangement of molecules is a necessary condition for the generation of chirality³².

2.5 Reference List

1. Pasteur, M. L. Sur les relations qui peuvent exister entre la forme cristalline, la composition chimique et le sens de la polarisation rotatoire. *Ann. Chim. Phys.* **1948**, *24*, 442-459.
2. Lee, T. D.; Yang, C. N. Question of Parity Conservation in Weak Interactions. *Phys. Rev.* **1956**, *104* (1), 254.
3. Kuhn, H. Origin of life -- Symmetry breaking in the universe: Emergence of homochirality. *Current Opinion in Colloid & Interface Science* **2008**, *13* (1-2), 3-11.
4. Lahav, M. Basic questions about the Origin of Life: On chirobiogenesis. *Origins of Life and Evolution of Biospheres* **2007**, *37* (4-5), 371-377.
5. Lahav, N.; Nir, S.; Elitzur, A. C. The emergence of life on Earth. *Progress in Biophysics & Molecular Biology* **2001**, *75* (1-2), 75-120.
6. Lahav, N. Minerals and the Origin of Life - Hypotheses and Experiments in Heterogeneous Chemistry. *Heterogeneous Chemistry Reviews* **1994**, *1* (2), 159-179.
7. McMurry, J. E. *Organic Chemistry, 7th Edition*; 7th ed.; Cengage Learning: 2008.
8. Barron, L. D. Fundamental symmetry aspects of optical activity. *Chemical Physics Letters* **1981**, *79* (2), 392-394.
9. Hazen, R. M.; Sholl, D. S. Chiral selection on inorganic crystalline surfaces. *Nature Materials* **2003**, *2*, 367-374.
10. Halasyamani, P. S.; Poeppelmeier, K. R. Noncentrosymmetric Oxides. *Chemistry of Materials* **1998**, *10* (10), 2753-2769.
11. Horvath, J. D.; Gellman, A. J. Naturally chiral surfaces. *Topics in Catalysis* **2003**, *25* (1-4), 9-15.

12. Bohannon, E. W.; Kothari, H. M.; Nacic, I. M.; Switzer, J. A. Enantiospecific Electrodeposition of Chiral CuO Films on Single-Crystal Cu(111). *Journal of the American Chemical Society* **2003**, *126* (2), 488-489.
13. Matsuura, T.; Koshima, H. Introduction to chiral crystallization of achiral organic compounds spontaneous generation of chirality. *Journal of Photochemistry and Photobiology C-Photochemistry Reviews* **2005**, *6* (1), 7-24.
14. Buhse, T.; Durand, D.; Kondepudi, D.; Laudadio, J.; Spilker, S. Chiral symmetry breaking in crystallization: The role of convection. *Physical Review Letters* **2000**, *84* (19), 4405-4408.
15. Durand, D. J.; Kondepudi, D. K.; Moreira, P. F.; Quina, F. H. Generation of molecular chiral asymmetry through stirred crystallization. *Chirality* **2002**, *14* (4), 284-287.
16. Flack, H. D. Chiral and achiral crystal structures. *Helvetica Chimica Acta* **2003**, *86* (4), 905-921.
17. Koch, E.; Fisher, W.; Muller, U. International Tables for Crystallography, Volume A: Space Group Symmetry Revised. 5th ed.; Hahn, Th., Ed.; Springer: 2002; pp 887-905.
18. Toda, F.; Tanaka, K.; Kuroda, R. Isolation of a nearly eclipsed chiral rotamer of 1,2-dichloroethane as an inclusion crystal with a chiral host compound. *Chemical Communications* **1997**, (13), 1227-1228.
19. Eliel, E. L.; Wilen, S. H. *Stereochemistry of Organic Compounds*; Wiley: 1994.
20. Morino, K.; Watase, N.; Maeda, K.; Yashima, E. Chiral amplification in macromolecular helicity assisted by noncovalent interaction with achiral amines and memory of the helical chirality. *Chemistry-A European Journal* **2004**, *10* (19), 4703-4707.
21. Lightner, D. A.; Hefelfinger, D. T.; Powers, T. W.; Frank, G. W.; Trueblood, K. N. Hexahelicene. Absolute configuration. *Journal of the American Chemical Society* **1972**, *94* (10), 3492-3497.
22. Reetz, M. T.; Guo, H.; Ma, J. A.; Goddard, R.; Mynott, R. J. Helical Triskelion Monophosphites as Ligands in Asymmetric Catalysis. *Journal of the American Chemical Society* **2009**, *131* (11), 4136-4142.
23. Matsuura, T.; Koshima, H. Photochemistry of Two-Component Molecular Crystals. *Photochemistry (Kokagaku)-in Japanese* **1995**, *19*, 10-20.
24. Roychowdhury, P. Crystal and molecular structure of phenanthridine. *Acta Crystallographica Section B* **1973**, *29* (6), 1362-1364.
25. Green, B. S.; Lahav, M.; Rabinovich, D. Asymmetric Synthesis Via Reactions in Chiral Crystals. *Accounts of Chemical Research* **1979**, *12* (6), 191-197.
26. Leiserowitz, L.; Weinstein, M. Studies in crystal chirality. I. Chiral hydrogen-bonded structures. *Acta Crystallographica Section B* **1975**, *31* (5), 1463-1466.
27. Collet, A.; Brienne, M. J.; Jacques, J. Spontaneous Double Decomposition and Enantiomeric Conglomerates. *Bulletin de la Societe Chimique de France* **1972**, (1), 127-&.

28. Koshima, H.; Hayashi, E.; Matsuura, T. Preparation and Structure of Chiral Two-component Molecular Crystals from 3-(3-Indolyl)propanoic Acid and Aza Aromatic Compounds. *Supramolecular Chemistry* **1999**, *11* (1), 57-66.
29. Koshima, H.; Hayashi, E.; Matsuura, T.; Tanaka, K.; Toda, F.; Kato, M.; Kiguchi, M. Preparation, structure and discrimination of a chiral bimolecular crystal by the self-assembly of 3-indolepropionic acid and phenanthridine. *Tetrahedron Letters* **1997**, *38* (28), 5009-5012.
30. Koshima, H.; Nakagawa, T.; Matsuura, T.; Miyamoto, H.; Toda, F. Synthesis, Structure, and Discrimination of Chiral Bimolecular Crystals by Using Diphenylacetic Acid and Aza Aromatic Compounds. *The Journal of Organic Chemistry* **1997**, *62* (18), 6322-6325.
31. Koshima, H.; Ding, K. L.; Chisaka, Y.; Matsuura, T. Generation of chirality in a two-component molecular crystal of acridine and diphenylacetic acid and its absolute asymmetric photodecarboxylating condensation. *Journal of the American Chemical Society* **1996**, *118* (48), 12059-12065.
32. Koshima, H. Generation of chirality in two-component molecular crystals from achiral molecules. *Journal of Molecular Structure* **2000**, *552*, 111-116.

3 Preparation and characterization of chiral Self Assembled Monolayers

3.1 Self assembly

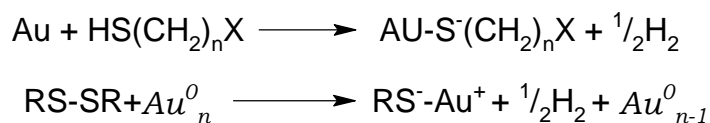
When a disordered system of the same components starts to organize itself under local interactions of its components and exhibits structure or pattern without external direction, such a process is called self assembly. Scientists are interested in this process for many reasons¹ that range from self assembly of living cells to making nanostructures. Its beauty lies in its spontaneity and reversibility. Forces which act as a drive for self assembly are non- covalent and act at a local level.

3.2 Self assembled monolayers

Nanoscience could not function without self assembly. The most commonly used example is found in the self assembled monolayers. An organization of molecular units into ordered structures is readily achieved by immersion of an appropriate substrate in an adsorbate solution. Self assembled monolayers (SAMs) and multilayers can be prepared on various metallic and inorganic substrates that include: Ag, Au, Cu, Ge, Pt, Si, GaAs, SiO₂. The materials chosen for formation of SAM include thiols (HSR), sulphides (RSR), disulphides (RSSR), acids (RCOOH) or siloxanes (RSiOR₃)². Molecules of these compounds consist of two regions, a head and a tail group^{3,4}.

The most representative and subsequently the most commonly used are SAMs formed by ω -terminated alkenethiols on surfaces of gold (111)⁵. Understanding the process of the assembly, its parameters and structures formed upon the process, is the key to using SAMs in an effective way in nanotechnology. The main advantage of this technique lies in its simplicity. Intensive studies carried out by Whitesides^{6,7} group showed that either thiols' or disulphides' reaction with gold yield the same product - a gold thiolate. Despite the fact that the reaction mechanism is not yet completely understood, the reaction is considered as an oxidative addition.

Adsorption chemistry for the thiols and dialkylsulphides on gold is given below:



Reaction 3-1

The wide use of gold in this technique is caused by the fact that it does not form stable oxides. Gold surfaces are stable under ambient conditions. Preparation of a SAM is carried out by immersion of a freshly clean or freshly prepared gold surface into a dilute solution of an organosulphur compound in an organic solvent. The concentration of such solutions is not high and usually of 1×10^{-3} mM.

Alkanethiols form on gold structures of the anatomy shown in Figure 3-1.

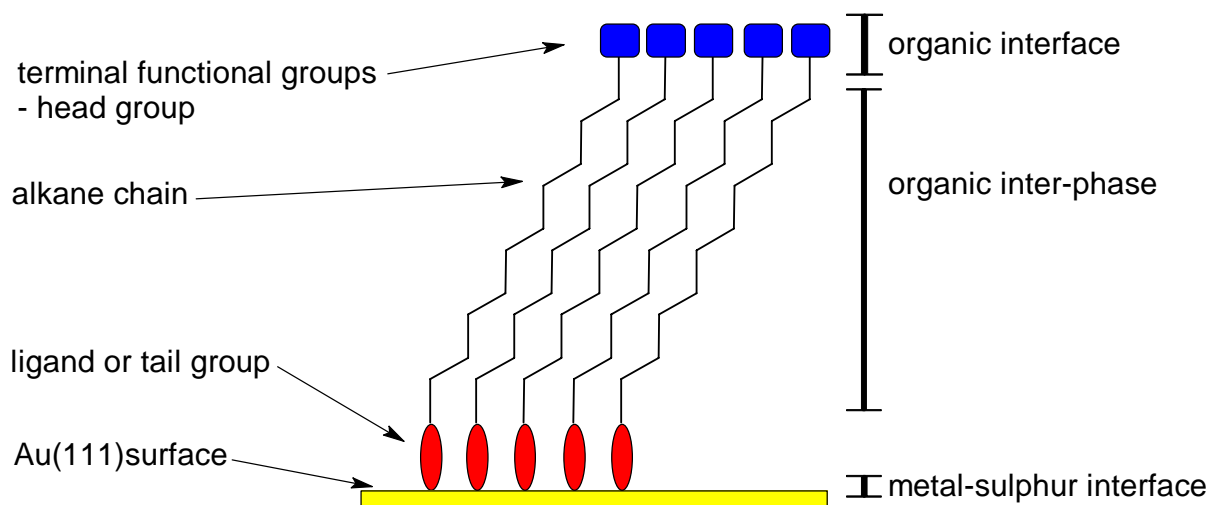


Figure 3-1 Cartoon projection of an ideal single crystalline SAM of alkanethiol prepared on gold surface of (111) structure

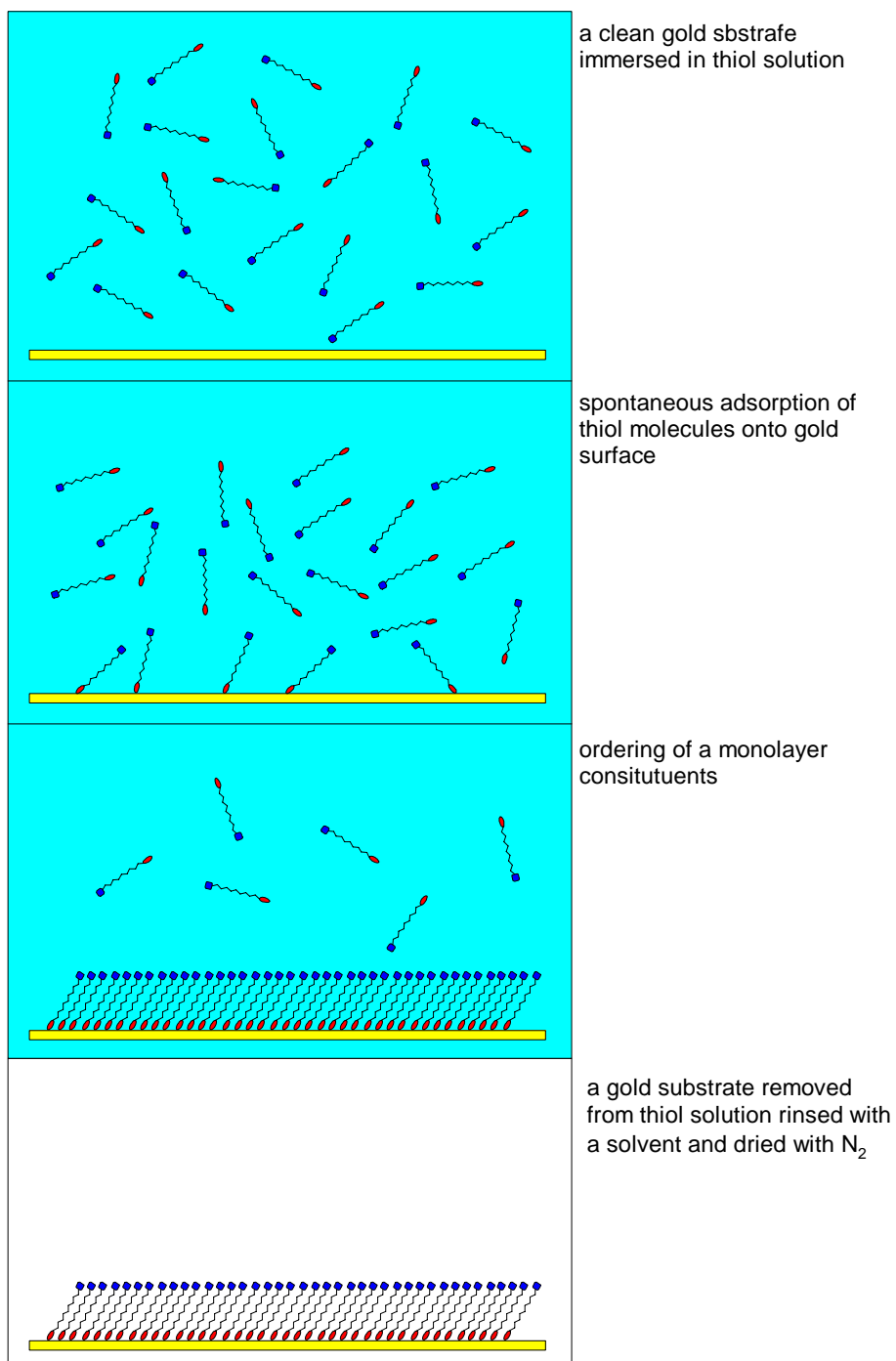


Figure 3-2 Schematic for SAMs formation

The organic interface presented in Figure 3-1 and 3-2 determines surface properties and presents functional groups. A head group could be designed in the way to further react with other compounds after the monolayer is formed. The middle part of a SAM –the organic inter-phase- is

formed by an alkane chain and provides a well defined thickness. This part of a SAM acts as a physical barrier and alters electronic conductivity and optical properties. The metal –sulphur interface acts as the link to surface atoms and modifies electronic states.

3.2.1 Structure of self assembled monolayers

Extensive research into the structural properties of SAMs has been carried out for over the past 20 years. At the beginning, the majority of studies were conducted on samples of alkanethiols deposited from a solution on a gold substrate- Au (111)⁸⁻¹¹. A wide range of different techniques has been employed to describe their structural properties. Information about film thickness and the coverage was obtained from optical ellipsometry measurements⁵. Infra-red spectroscopy and Raman Spectroscopy¹²⁻¹⁴ were used to characterize the packing, contributions of chain conformation, orientation and coverage of self assembled monolayer films. Electron diffraction techniques as well as STM measurements¹⁵⁻¹⁷ allowed determination of the structure and lattice spacing of the molecules on gold. To examine the effect of a chemical structure of an interface on wettability, the contact angle measurements were performed^{18,19}.

3.2.1.1 Structure of the alkanethiol monolayer

Porter and co-workers examined a large number of alkanethiols, finding that there is a correlation between film thickness and the chain length. Ellipsometry studies showed the existence of two regions: between 1-5 carbon atoms and between 9-21 carbon atoms⁵. Only for the latter a linear correlation between film thickness and the number of carbon atoms in an alkanethiol chain was found. Thiols with a short chain were found to form more disordered, liquid-like structures, whereas thiols with chains longer than 9 carbon atoms produced densely packed assemblies with alkyl chains tilted at 20-30° to the surface normal. The tilt of the alkanethiol chains was also studied by Nuzzo and co-workers^{11,14}, who estimated it to be of *ca.* 40° from the surface normal. Finally, from electron

diffraction and Raman spectroscopy studies the tilt was confirmed to be ca. 30° ^{11,11,17}. Raman spectroscopy, PMIRRAS and contact angle studies revealed also a parity (even- odd) effect which is illustrated in Figure 3-3.

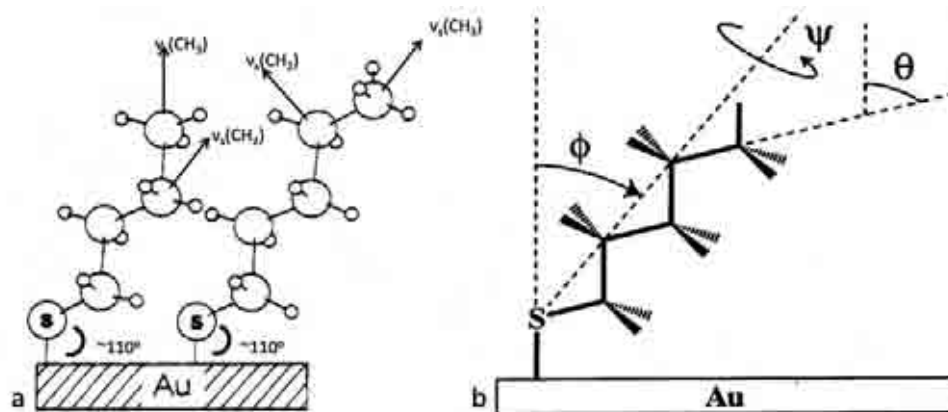


Figure 3-3 a) A cartoon representation of parity effect for tilted alkanethiols on gold and their symmetric stretching modes b) a schematic view of all-trans model where ϕ , ψ and θ are the tilt angle of the alkyl chain with respect to the surface normal, the rotation angle around the main axis of the alkyl chain and the methyl angle respectively¹¹.

The parity effect is the most observed in contact angle measurements as this technique is sensitive to the local order at the interface. For CH_3 -terminated SAMs having an odd number of total carbon atoms, values of contact angles are lower than for even numbers. The phenomenon is proposed to arise from the change in orientation of the terminal methyl group as the number of carbon atoms in the alkyl chains alternates between odd and even²⁰. The parity effect was also observed in infrared spectroscopy measurements^{13,21,22}. An analysis of the vibrational intensities with respect to the angle between the main axis of the methyl group and the surface normal revealed that the structure of the alkanethiol SAMs gradually changes with n . The analysis of the orientation of the methyl groups showed the structure changes toward more-tilted and less-rotated orientation with the decrease in n . It was proposed to arise from the weaker van der Waals interaction in alkanethiol SAMs with the short chain²².

Low energy atomic diffraction was a first technique used to determine the structure of saturated monolayers on gold. Studies of Strong and Whitesides revealed that the symmetry of chains in a monolayer on Au (111) is pseudo-hexagonal and the spacing is of 4.97 \AA ¹⁷. Low-energy helium

diffraction studies^{23,24} as well as surface X-ray diffraction and measurements of surface coverage using reductive desorption also confirmed $(\sqrt{3} \times \sqrt{3})R 30^\circ$ structure. The $(\sqrt{3} \times \sqrt{3})R 30^\circ$ structure corresponds to a molecule- molecule spacing of $\sim 5 \text{ \AA}$ and area per molecule of 21.6 \AA^2 . LEAD measurements suggested also that the terminating methyl groups have different heights and orientations. This was resolved by IR studies which suggested that there are two different types of molecules in the unit cell with different orientations of the molecular backbone²⁵⁻²⁷. Nuzzo and co-workers also found that there are odd-even chain length –dependent orientations of the terminating methyl groups, which was a proof for a conserved bonding configuration of the head group²⁸.

Fast developing SPM techniques allowed direct imaging of SAM structures on Au(111) at the molecular level. Poirier and co-workers studied the self-assembly mechanism of alkanethiols on Au(111) using ultrahigh vacuum scanning tunnelling microscopy^{29,30}. They presented the formation of a $c(4 \times 2)$ superlattice of the alkyl chains.

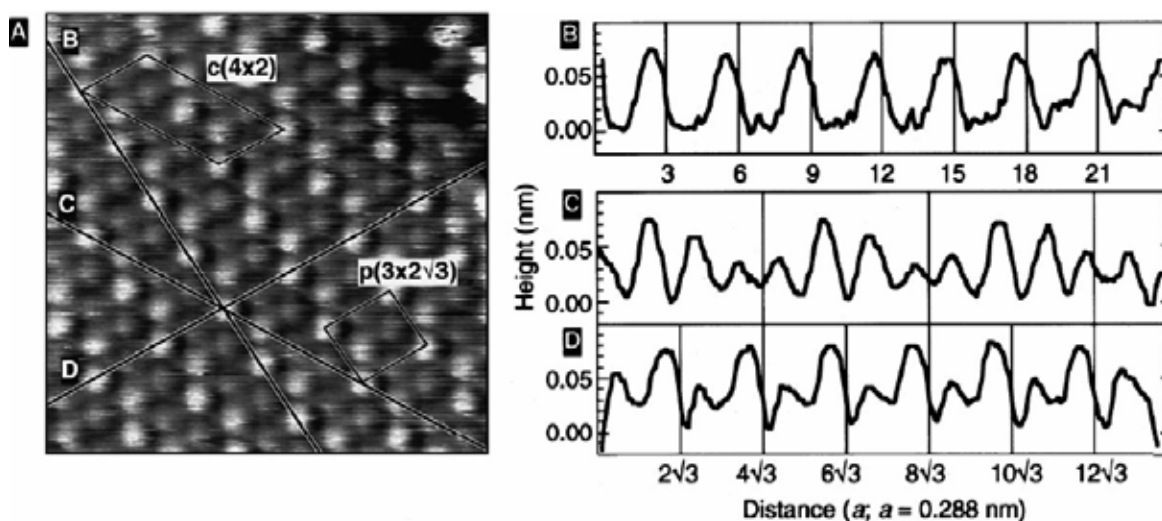


Figure 3-4 STM image of octanethiol on Au(111) $6.0 \times 6.0 \text{ nm}$ in standing up phase. The $2\sqrt{3} \times 3$ unit mesh and $c(4 \times 2)$ superlattice unit cell are outlined. (B) plot of cross-section B in (A) running in the Au- neighbour direction. (C and D) cross-sectional plots running in two next nearest neighbour (NNN) directions of gold⁴.

STM images showed that SAMs pack in a $(\sqrt{3} \times \sqrt{3})R30^\circ$ structure with $c(4 \times 3)$ superlattice. There are four thiolate molecules in the unit cell. The images presented also pit-like defects. These pits are 2.5 \AA in depth, consistent with the single atom step height, confirming that they are defects of

the Au surface layer and not defects of the alkanethiol layer. The authors made a suggestion that these pits are due to the etching of gold in the alkanethiol solution, on the basis of atomic absorption spectroscopy measurements of the incubated liquid.

These studies also explained how sulphur binds to the gold surface. In the Figure 3-5 yellow balls represent the underlying Au(111) lattice, green circles indicate the arrangement of sulphur from alkanethiol molecules. The unitcell of $(\sqrt{3} \times \sqrt{3}) R30^\circ$ structure is marked in blue and the simplest representation of C (4x2) superlattice in red¹⁷.

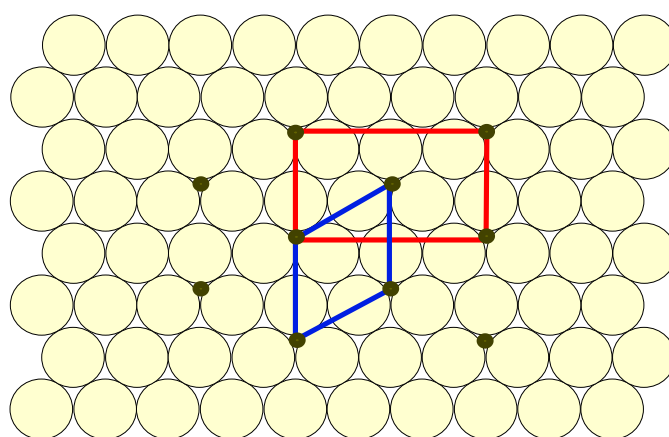


Figure 3-5 Schematic projection of the structures of *n*- alkanethiols on gold¹⁷.

Other highly-ordered structures have been also observed with use of the techniques of STM and low-energy helium diffraction, which have slight deviation from the $(\sqrt{3} \times \sqrt{3}) R30^\circ$ on Au³¹.

An influence of different head groups on the SAM structure has been also studied. Infra red spectroscopy showed that long chain alkanethiols functionalized by small groups as -OH form well organized structures similar to *n*-alkanethiols^{32,33}. In the contrary, large groups or backbones are incommensurate with the $(\sqrt{3} \times \sqrt{3}) R30^\circ$ structure. However studies of fluorinated thiols resulted in a $(\sqrt{3} \times \sqrt{3}) R30^\circ$ arrangement, despite the fact that the CF₃ group is about 40% larger than CH₃.

3.2.1.2 SAM formation kinetics

Shreiber review on SAMs⁴ presents a comprehensive description of SAM formation. The process is divided into two steps: first, initial adsorption and second, adsorption and reorganization. Whilst the first step takes usually a few minutes and gives up to 90% coverage the second step can take even a few days. More detailed studies on the SAMs formation kinetics were made by Godin³⁴. He showed that formation of an alkanethiol SAM involves a sequence of several structural phase transitions illustrated in Figure 3-6.

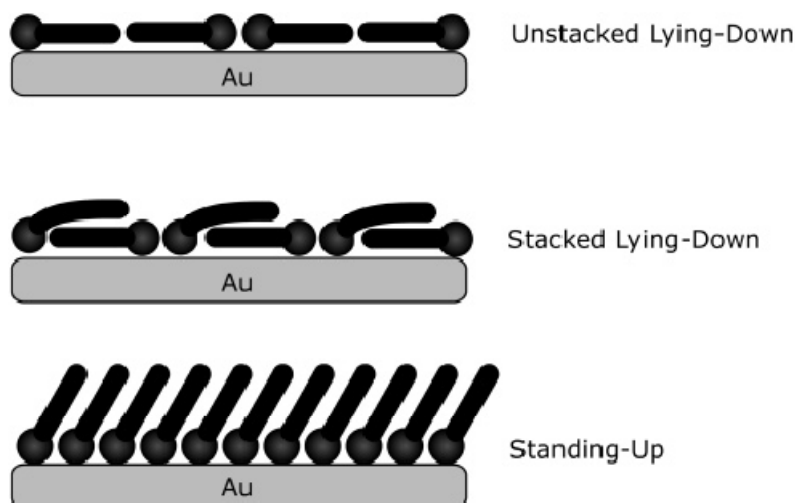


Figure 3-4 SAMs formation, the transition phases³⁴

In the lower coverage regimes, the structure of SAMs is the best described by a unstacking-lying down phase. Transition into the standing-up phase occurs at greater coverage.

Investigation of the influence of a time scale, substrate and concentration on the SAMs characteristics resulted with observation of different phases prior to the formation of $(\sqrt{3} \times \sqrt{3}) R30^\circ$; faster convergence was observed for smoother gold surfaces and higher thiol concentrations³⁵.

From all of the factors that influence SAM formation³⁶, a solvent used for preparation plays the most important role^{9,10}. Ethanol, a polar and protic solvent, was found to be the best for SAM formation

although for longer chain thiols poor solubility was observed. For a polar but non-protic solvent as well as for nonpolar, the resulting monolayers were found to be less dense and, consequently, less well oriented.

3.2.1.3 SAMs resulting properties

Chemical and mechanical properties of SAMs are directly related to their microscopic structure and can be determined by several methods. The wettability of a surface gives a great deal of information about film interfacial properties. A quantitative way of obtaining information of interfacial properties is contact angle goniometry. Many different self assembled monolayers have been studied by this technique: from single component films with different tail groups to mixed monolayers^{9,10,37-39}. Different liquids have been used to probe specific molecular interactions. Water and hexadecane were used by Laibinis⁶ to investigate wetting properties of different chain length thiols adsorbed on SAMs. For both liquids it was clear that the length of the thiol chain has influence on the contact angle value up to carbon number $n=11$ beyond the contact angle constant, *c.a.* 120° and 45° for water and hexadecane, respectively. Measurements for different tail groups presented by Bain and Whitesides showed that the structure of a tail has a great influence on the monolayer properties³⁷ and that a film of desired properties can be created by use of mixed SAMs. The same authors gave proof of the high sensitivity of this method by comparison of a monolayer made of a thiol with ether tail group and the corresponding thiol with oxygen four carbon units below the interface. The identical results showed that the interaction of the closed packed structures is determined only by the outermost few angstroms of the monolayer. The technique of contact angle measurements is widely used for monolayer characterisation although it is very sensitive to contaminations and gives complications due to surface heterogeneity and roughness.

Porter and co-workers studied the nature and extent of structural defects in SAMs by electrochemical techniques: heterogeneous electron transfer and differential capacitance⁵. The extent of electron transfer between a compound in solution and the electrode substrate gives an idea of the

SAM integrity; impedance analysis provides information on the density of holes and on the presence and distribution of regions seldom occupied by the SAM. The authors showed that SAMs provide an effective pinhole-free barrier between solution and gold surface, especially for long chain thiols, where the van der Waals interactions of the chains appear to sustain a stable ordered structure. Shorter chain lengths promote a loss of film organization. Electron transfer and ion penetration through the monolayer is greatly reduced in comparison with a clean gold surface.

3.2.2 Reactions, reactivity and applications of SAMs

The ability to control the chemical and structural properties of surfaces is very important for advancements in fields like selective catalysis, chemical sensing and electronics. Self assembled monolayers provide a way to produce surfaces with desired properties not only by their own tail groups but also by their ability for further reaction. SAMs equipped with special tail groups can be used for introducing different functionality onto surfaces⁴⁰. It is highly desirable that the modification of surfaces proceeds smoothly at room temperature to high yield and without the production of insoluble surface contamination. The surface reaction should have all of the benefits of the solid phase reactions: the separation of desired product should be straightforward; *e.g.* removing the gold substrate from the reaction and rinsing with a solvent. However, when monolayers are subjected to a number of successive reactions, a problem with purity can arise since the formation of a surface attached by products at each step leads to accumulation of defects.

The main advantages of modifying SAMs after their formation are that they:

- permit use of common synthetic procedures and thus simplify the preparation of functionalized surfaces
- enable the incorporation of ligands into SAMs that are not compatible with thiols or the synthetic methods for preparing them
- can generate multiple samples with different types of ligands in a short period of time (because the SAMs are easy to prepare)
- preserve the ordered underlying structure of the SAM
- are economical processes. Modifying the SAM after formation means that the amount of ligand required for immobilization is very small (nanomoles); this characteristic is especially important for linking to surfaces biological ligands that may be in short supply

Despite these benefits it is essential to remember that after SAMs have been modified the extent of surface coverage is often unknown. Reactions can produce a mixture of functional groups on the surface and, consequently, the structure of the resulting surface is unknown.

There are several methods for direct reaction or non-covalent coupling of SAMs with molecules from solution. The majority of the strategies derive from procedures established in the 1970s⁴¹ for functionalizing organic films supported on electrodes used for electrochemistry and on solid-phase materials used for chromatography.

Reactions such as nucleophilic substitution, free radical halogenation, oxidation/reduction can be performed on a surface of SAMs. Examples of direct interfacial reactions of exposed functional groups of SAMs are presented in Figure 3-7.

The majority of these reactions come from immobilization techniques used for DNA, peptides and proteins *e.g.* SAMs with maleimide functional groups react with active ligands - peptides and carbohydrates - of thiols⁴². Figure 3-7b presents the reaction of disulphide- thiol exchange used to immobilize DNA, peptides and carbohydrates⁴³⁻⁴⁶. A cross - metathesis reaction for linking acrylamide, acrylic acid and methyl acrylate to vinyl - terminated SAMs was presented by Choi⁴⁷. The reaction of olefin cross-metathesis is catalysed by ruthenium and, from that, formation of carbon-carbon bonds can occur under mild conditions. A beautiful approach to forming a stable linkage between molecules by cycloadditions of acetyl groups to azides was presented by Collman⁴⁸. The so-called 'click chemistry' reaction is not only thermally stable but also extremely specific and high yielding. It is the main reason for using click chemistry in both of the projects presented in this dissertation. The reaction was studied extensively in 'both' ways, having azides attached to undecanethiolates and reacting them with molecules modified with acetylenes and the opposite, where SAMs were functionalized with acetylenyl groups (Figure 3-8 e and f)⁴⁹. The 'click chemistry' in both cases requires a time interval of 3 h for completion as well as the presence of catalyst: copper (I) ions.

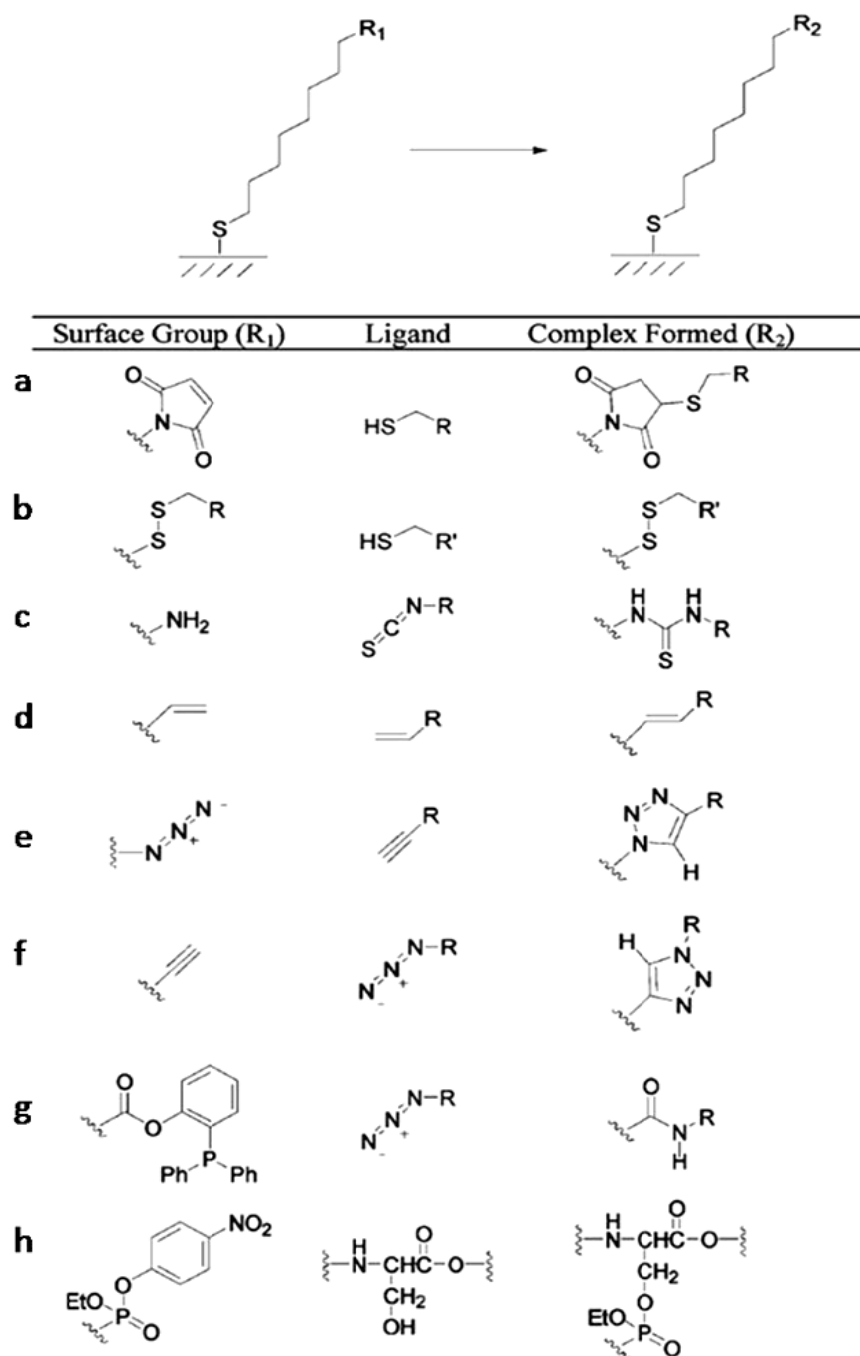
Figure 3-5 Direct interfacial reactions of exposed functional groups of SAMs a⁴², b⁴⁴⁻⁴⁶, c⁴³, d⁴⁷, e⁴⁸, f⁴⁹, g^{50,51}, h^{52,53}.

Figure 3-7g presents a reaction of substituted phosphanes with azides, called the Staudinger reaction (Staudinger ligation), where the amide bond is formed. This reaction was used for cell surface modification⁵⁰ and immobilization of small molecules on glass slides⁵¹.

Another direct interfacial reaction conducted on SAMs was presented by the group of Mrksich^{52,53}. SAMs presenting phosphonates form covalent adducts with an engineered fusion protein enzyme- cutinase and a protein of interest (calmodulin). This approach (figure 3-7h) enabled researchers to leave the enzyme bound to the surface but the attached protein extends into the ambient solution with a defined orientation.

Another group of reactions that allows further reacting the surfaces of SAMs involves use of intermediate functional groups which are then coupled to a ligand. Such common intermediates can react with variety of ligands and allow spatial discrimination of active and inactive regions. Some examples of this approach are given in Figure 3-8.

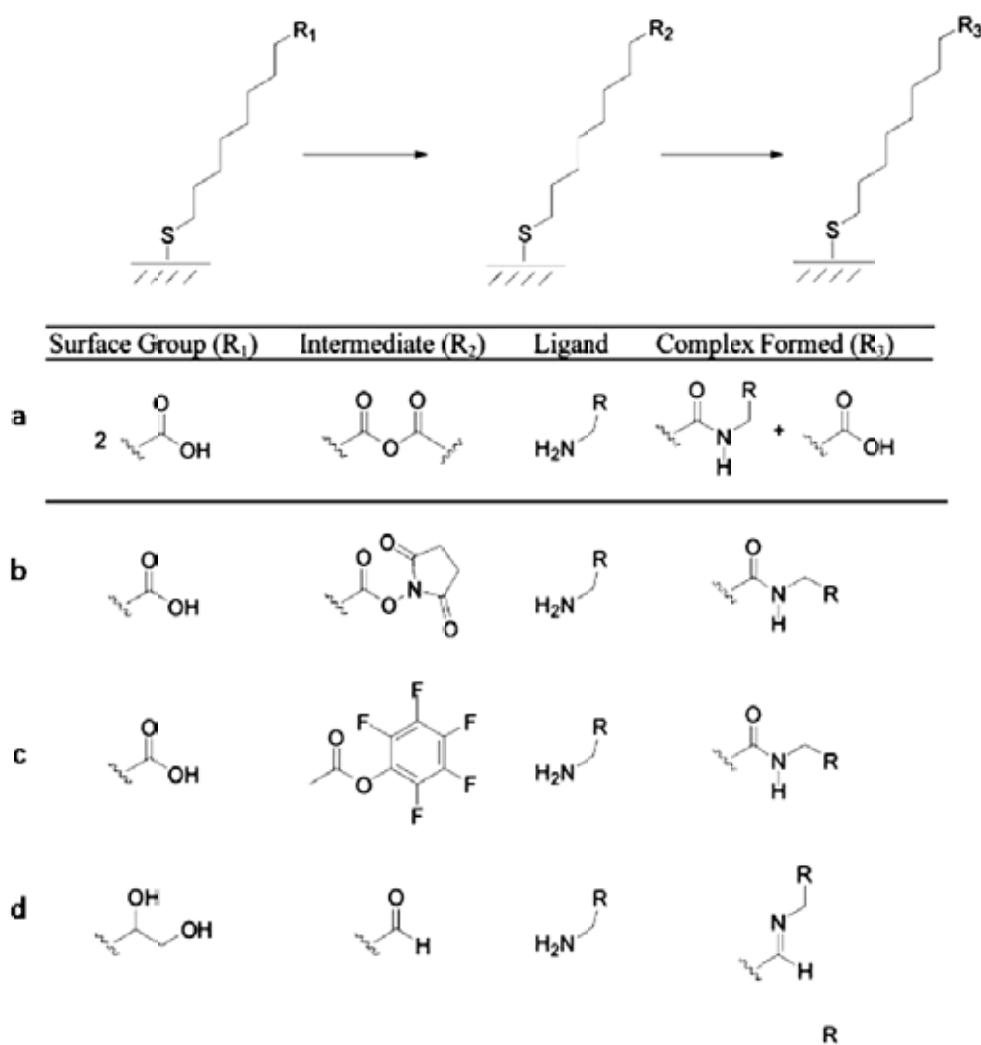


Figure 3-6 Interfacial reactions that involve intermediate functional groups a⁵⁴, b³⁹, d⁵⁵

The leading reaction in this group is the formation of amide linkages *via* an interchain anhydride intermediate⁵⁴. A SAM terminated with COOH groups is dehydrated with trifluoroacetic anhydride to form interchain anhydrides. Exposure of such activated surfaces to amines generates amide bonds. This method is called an ‘anhydride method’ and produces a SAM with a 1:1 mixture of functional groups on the surface.

An amide bond can be generated in a SAM by activation of a free carboxylic acid by NHS- N-hydroxysuccinimidyl, which is illustrated in Figure 3-8 b, c. Amendment of NHS for pentafluorophenol causes an increase in reactivity for an order of magnitude³⁹. This method is used for immobilization of ligands and proteins on mixed SAMs (derivatives of tri(ethylene glycol)- and hexa(ethylene glycol glycol)-carboxylic-acid- terminated thiols).

Functional surfaces of SAMs can be also activated with use of electrochemical potential and photoradiation⁵⁶. These techniques allow transforming unreactive functional groups into reactive centres for the subsequent attachment of ligands. For example electrochemical oxidation of SAMs terminated with hydroquinone results with quinone, which can subsequently react with a diene, undergoing a Diels-Alder reaction⁵⁵, and a tert-butyl azobenzene group terminated SAM undergoes de-estryfication photochemically in the presence of a photoacid generator⁵⁷.

Another strategy for modifying the interfacial composition of SAMs is the cleavage of covalent bonds of a terminal surface group. This can result with a release of a bound molecule into solution and generation of a new organic surface for subsequent reactions⁵⁸. Mrksich *et al* presented reactions of quinines modified with propionic esters that undergo intermolecular cyclization upon electrochemical reduction – ligands bound to the propionic ester moiety are released with the formation of a lactone⁵⁹.

The SAMs structure influences reactivity on surfaces in many ways. First of all, on a surface there are geometric constraints arising from the presence of surface that may limit the accessibility of interfacial functional groups. The parameters of the solution used for reaction can differ at the interface from the bulk solutions, *e.g.* solvent density, viscosity, pH, ion concentration⁶⁰⁻⁶².

The kinetics of the reaction on SAMs can be influenced by the following factors:

- the organization of the chains in the monolayer
- the density and orientation of functional groups on the surface

The crystallinity of a SAM can influence the kinetics of the reactions on its functional groups. The effect of chain organization on the rate constants of the base-catalysed hydrolysis of NHS esters has been studied with use of *ex-situ* RAIRS. For SAMs composed of undecanethiolates the termini of NHS esters reacted more rapidly compared with those of hexadecanethiolates SAMs, although both reactions were two orders of magnitude slower than the hydrolysis reaction of the precursor molecules in solution⁶³. Similar results were obtained by Vaidya *et al*⁶⁴, who showed that the rate of hydrolysis for terminal ester groups on SAMs formed from structural isomers depends on density and orientation of the organic components. The conclusion of both of these studies is that the functional groups attached to highly oriented organic interfaces can have poor reactivities and also conformational and steric effects are important in determining the reactivity of a surface.

- lateral steric effects

Studies of Mrksich and Housemann⁶⁵ as well as Huck⁶⁶ confirmed that lateral steric crowding affects an reaction and that the rates of interfacial reactions change with increasing concentrations of reactive sites in SAM, depending strongly on the type of reaction.

- position of reactive sites
- the distance of the functional group from the interface between the SAM and the solution

Reactive sites situated below the surface of the SAM may be less accessible to reactants in the surrounding medium than those positioned at the termini of the SAMs⁶⁷. Steric effects are also reduced when the reactive centre is tethered to a molecular component of a mixed SAM that is longer than those comprising the surrounding organic background³⁹.

- the partitioning of the free reactants

The rate of the reaction at the interface can be affected by solvation of reactants from solution as well as by partitioning of reagents in the monolayer or adsorption of reagents.

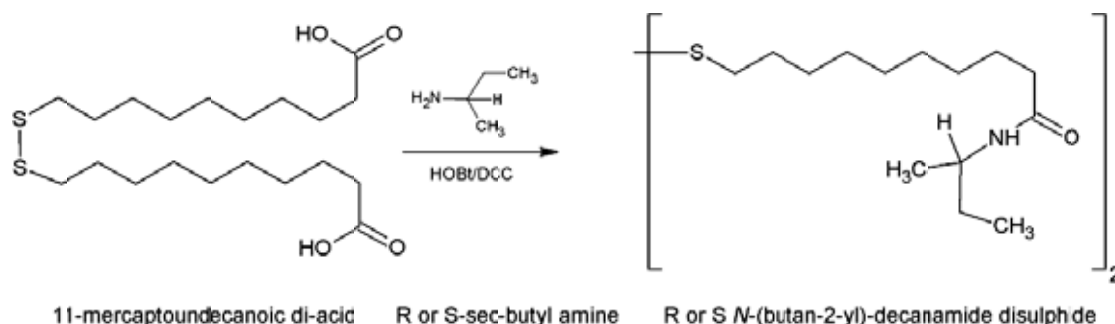
3.2.2.1 *Chirally functionalized SAMs*

For realization of both projects chirally functionalized SAMs were required. There are only few naturally existing compounds which can form chiral self assembled monolayers on gold and usually these are short amino acids. For more complex systems, special synthesis of thiols or reaction on existing monolayers is required.

The most simple, and subsequently the most elegant, naturally existing chiral thiol is cysteine. It is a small and highly polar molecule in which a variety of intermolecular forces (hydrogen and electrostatic bonding) can govern its packing on a gold structure. Recent studies on its deposition on gold have shown that it could be deposited by several methods: from evaporation in high vacuum conditions to deposition from liquid⁶⁸⁻⁷³. Evaporation in high vacuum and room temperature on Au (111) surfaces revealed that cysteine forms disordered islands growing from the step edges. When the coverage increases, the disordered islands grow in size, but still no order is achieved. A distinct change in the molecular structure is achieved upon annealing the substrate at 380 K. A local order is observed in both low and high coverage. Cysteine deposited from aqueous solutions forms an ordered film on gold (111) and the coverage of bound molecules is about 1/3 of monolayer while the coverage of unbound molecules is in a range of 1/6 to 1/3 of the bound molecular coverage. Cysteine deposited on gold was found to be in zwitterionic form and electrostatic interactions can facilitate the coupling of unbound molecules. Studies conducted by Dodero⁶⁹ unambiguously indicate that cysteine chemisorption has strong similarities with alkanethiol chemisorption. The cysteine adlayers adopt a $(\sqrt{3}\times\sqrt{3})R30^\circ$ hexagonal structure.

A cysteine monolayer could be used as a source of chirality on a surface but it is a short molecule. When there is a need to use a thicker monolayer (longer carbon chain), synthesis of a chirally tailed thiol must be performed. Usually synthesis of thiols is not easy and consists of many steps. The easiest way of coupling a chiral component to a thiol molecule is by using a disulphide

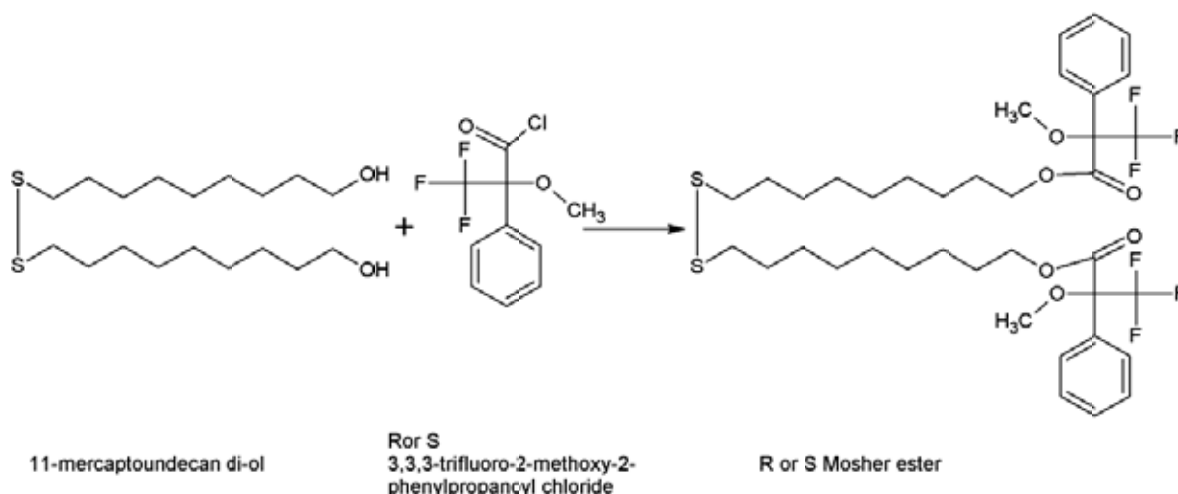
equipped with acid groups and an amine facilitated by DCC (dicyclohexylcarbodiimide) in the presence of HOBT (1-hydroxybenzotriazole). This results with formation of an amide as presented below:



Reaction 3-2

The main advantage of this method is that it has the least amount of racemisation during the reaction. The R form of the amide resulted in an optical rotation of -11.6° and S of $+12.2^\circ$. SAMs formed from these thiols were comparable in thickness: 1.67 and 1.69 nm, respectively⁷⁴.

Another example of formation, of a chirally tailed thiol is coupling disulphides fitted with terminal alcohol group with chiral derivatives of Mosher acid, as it is presented below:



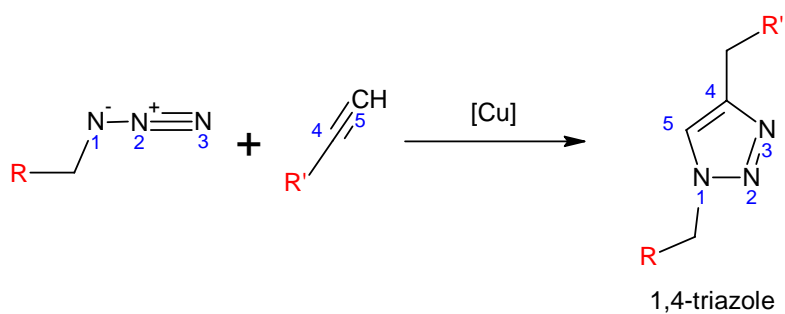
Reaction 3-3

Optical rotation for R and S enantiomers are 14.6° and -16.3° respectively⁷⁴.

3.2.2.2 Click chemistry as a tool for chiral SAMs formation.

For the needs of both projects, click chemistry on existing SAMs was performed. As mentioned before, reactions performed on existing monolayers have opened a way to further functionalization of monolayers. Click chemistry refers to a set of covalent reactions with high reaction yields that can be performed under extremely mild conditions⁷⁵. From this pool, a classic Huisgen, copper mediated azide –alkyne 1,3-dipolar cycloaddition (CuAAC) was chosen as a reaction proceeding in high yield under mild conditions with a tolerance for a wide range of functional groups, that is not exhibited by traditional coupling reactions, all of which give the possibility to conduct it on a surface. The reaction was adapted to functionalize either azide⁴⁸ or alkyne⁴⁹ terminated surfaces. A catalyst, Cu(I), could be used in a form of its relatively stable compounds or the *in situ* chemical or electrochemical reduction of Cu(II) to Cu(I). Chemical reduction could be achieved by use of copper (II) sulphate or copper (II) chloride with sodium ascorbate or by electrochemical reduction. As the first is more than intuitive, the second, described by Collman⁷⁶, was conducted with use of $0.5 \mu\text{M}$ copper(II) bis(bathophenanthroline)disulfonic acid solution with application of a bias potential around -300 mV of the Cu(II/I) standard potential. That caused Cu(I) formed at the electrode surface and reaction catalysis. Another example of electrochemical reduction near the reaction surface was presented by Bard⁷⁷, whose group used an ultramicroelectrode (UME) to synthesize Cu(I) locally in a gap between the tip of the electrode and the surface. The use of UME provided not only a immobilization of acetylene derivatives onto a small area but also maintained a stability of Cu(I). An idea similar in scale was recently presented by Stoddart⁷⁸. His group reported an alternative approach toward direct- write coupling of molecules to surfaces via CuAAC by using a movable heterogenous copper surface, in the form of a thin copper layer deposited onto an AFM tip. It has been shown that this method is capable to catalyze CuAAC on a suitable surface locally without a need of auxiliary reagents.

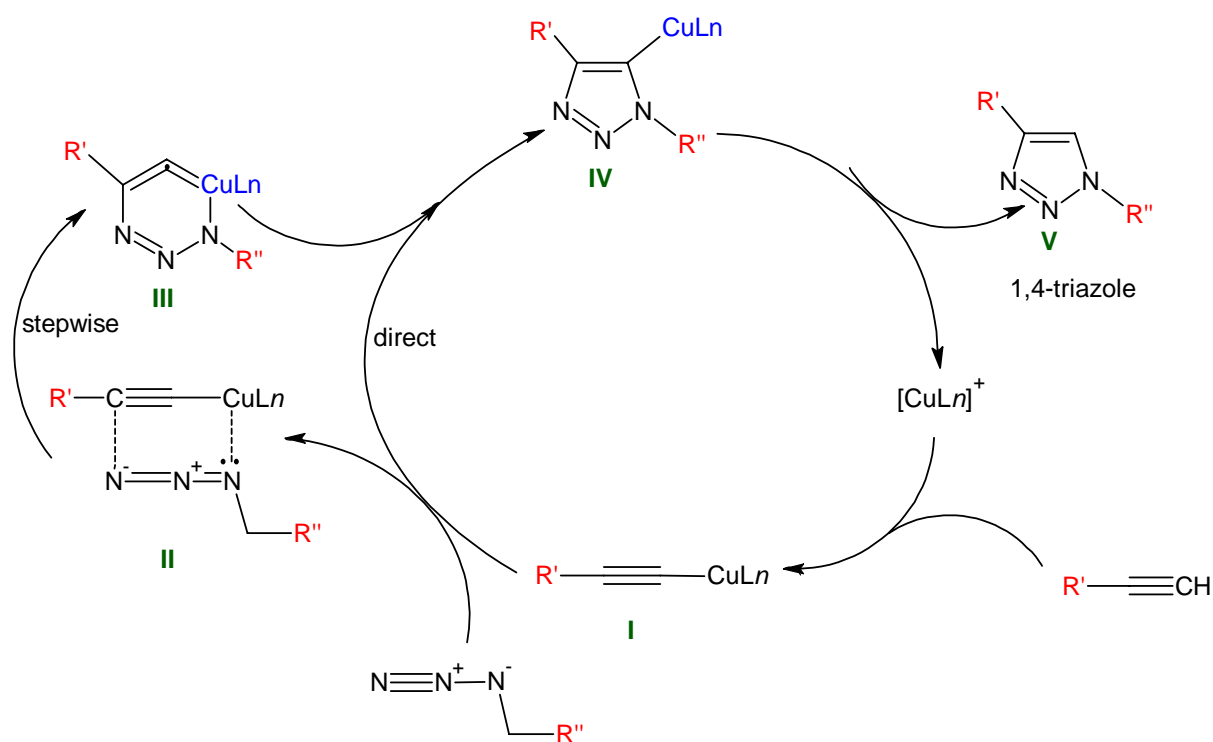
The CuAAC reaction can be presented schematically:



Reaction 3-4

The mechanism of this reaction is still under investigation. Several possible explanations have been proposed^{79,80}.

The catalytic cycle by Sharpless⁷⁹, presented below, describes the most probable mechanism for CuAAC reaction.



Reaction 3-5

The reaction of CuAAC has been discovered to be highly regioselective. Data provided by Sharpless⁷⁹ indicate that the 1,4-triazole (or its derivatives) yield is higher than 90% whilst the same cycloaddition conducted without copper, but in high temperature, products of 1,4 and 1,5- triazole in the ratio 1.6:1.

3.3 Reference List

1. Philp, D.; Stoddart, J. F. Self-assembly in natural and unnatural systems. *Angewandte Chemie-International Edition* **1996**, *35* (11), 1155-1196.
2. Ulman, A. *An Introduction to Ultrathin Organic Films*; Academic Press: 1991.
3. Schreiber, F. Thiol-based Self-assembled Monolayers: Structure of. In *Encyclopedia of Materials: Science and Technology*, Jorgen Buschow, K. H., Robert, W. C., Merton, C. F., Bernard Ilshner, Eds.; Elsevier: Oxford, 2001; pp 9323-9331.
4. Schreiber, F. Structure and growth of self-assembling monolayers. *Progress in Surface Science* **2011**, *65* (5-8), 151-257.
5. Porter, M. D.; Bright, T. B.; Allara, D. L.; Chidsey, C. E. D. Spontaneously organized molecular assemblies. 4. Structural characterization of n-alkyl thiol monolayers on gold by optical ellipsometry, infrared spectroscopy, and electrochemistry. *Journal of the American Chemical Society* **2002**, *109* (12), 3559-3568.
6. Laibinis, P. E.; Whitesides, G. M.; Allara, D. L.; Tao, Y. T.; Parikh, A. N.; Nuzzo, R. G. Comparison of the structures and wetting properties of self-assembled monolayers of n-alkanethiols on the coinage metal surfaces, copper, silver, and gold. *Journal of the American Chemical Society* **2002**, *113* (19), 7152-7167.
7. Bain, C. D.; Biebuyck, H. A.; Whitesides, G. M. Comparison of self-assembled monolayers on gold: coadsorption of thiols and disulfides. *Langmuir* **2002**, *5* (3), 723-727.
8. Bain, C. D.; Whitesides, G. M. Correlations between wettability and structure in monolayers of alkanethiols adsorbed on gold. *Journal of the American Chemical Society* **2002**, *110* (11), 3665-3666.
9. Bain, C. D.; Evall, J.; Whitesides, G. M. Formation of monolayers by the coadsorption of thiols on gold: variation in the head group, tail group, and solvent. *Journal of the American Chemical Society* **2002**, *111* (18), 7155-7164.
10. Bain, C. D.; Troughton, E. B.; Tao, Y. T.; Evall, J.; Whitesides, G. M.; Nuzzo, R. G. Formation of monolayer films by the spontaneous assembly of organic thiols from solution onto gold. *Journal of the American Chemical Society* **2002**, *111* (1), 321-335.
11. Nuzzo, R. G.; Allara, D. L. Adsorption of bifunctional organic disulfides on gold surfaces. *Journal of the American Chemical Society* **2002**, *105* (13), 4481-4483.

12. Bryant, M. A.; Pemberton, J. E. Surface Raman scattering of self-assembled monolayers formed from 1-alkanethiols: behavior of films at gold and comparison to films at silver. *Journal of the American Chemical Society* **2002**, *113* (22), 8284-8293.
13. Nuzzo, R. G.; Dubois, L. H.; Allara, D. L. Fundamental studies of microscopic wetting on organic surfaces. 1. Formation and structural characterization of a self-consistent series of polyfunctional organic monolayers. *Journal of the American Chemical Society* **2002**, *112* (2), 558-569.
14. Nuzzo, R. G.; Fusco, F. A.; Allara, D. L. Spontaneously organized molecular assemblies. 3. Preparation and properties of solution adsorbed monolayers of organic disulfides on gold surfaces. *Journal of the American Chemical Society* **2002**, *109* (8), 2358-2368.
15. Camillone III, N.; Chidsey, C. E. D.; Liu, G.; Scoles, G. Superlattice structure at the surface of a monolayer of octadecanethiol self-assembled on Au(111). *The Journal of Chemical Physics* **1993**, *98* (4), 3503-3511.
16. Samant, M. G.; Brown, C. A.; Gordon, J. G. Structure of an ordered self-assembled monolayer of docosyl mercaptan on gold(111) by surface x-ray diffraction. *Langmuir* **2002**, *7* (3), 437-439.
17. Strong, L.; Whitesides, G. M. Structures of self-assembled monolayer films of organosulfur compounds adsorbed on gold single crystals: electron diffraction studies. *Langmuir* **2002**, *4* (3), 546-558.
18. Bain, D.; Whitesides, G. M. Depth sensitivity of wetting: monolayers of .omega.-mercapto ethers on gold. *Journal of the American Chemical Society* **2002**, *110* (17), 5897-5898.
19. Laibinis, P. E.; Nuzzo, R. G.; Whitesides, G. M. Structure of monolayers formed by coadsorption of two n-alkanethiols of different chain lengths on gold and its relation to wetting. *The Journal of Physical Chemistry* **2002**, *96* (12), 5097-5105.
20. Sellers, H.; Ulman, A.; Shnidman, Y.; Eilers, J. E. Structure and binding of alkanethiolates on gold and silver surfaces: implications for self-assembled monolayers. *Journal of the American Chemical Society* **2002**, *115* (21), 9389-9401.
21. Colorado, R. Jr.; Graupe, M.; Takenaga, M.; Koini, T. R. Surface Dipoles Influence the Wettability of Terminally Fluorinated Organic Films. *Materials Research Society Symposia Proceedings* **1999**, *546*.
22. Nishi, N.; Hobara, D.; Yamamoto, M.; Kakiuchi, T. Chain-length-dependent change in the structure of self-assembled monolayers of n-alkanethiols on Au(111) probed by broad-bandwidth sum frequency generation. *The Journal of Chemical Physics* **2003**, *118* (4), 1904-1911.
23. Anderson, M. R.; Evaniak, M. N.; Zhang, M. Influence of Solvent on the Interfacial Structure of Self-Assembled Alkanethiol Monolayers. *Langmuir* **1996**, *12* (10), 2327-2331.
24. Bracco, G.; Pedemonte, L. Spectrum of the interaction potential between He and as-deposited self-assembled monolayers of decanethiol chemisorbed on Au(111). *Surface Science* **2004**, *562* (1-3), 269-274.
25. Allara, D. L.; Parikh, A. N. Quantitative determination of molecular structure in multilayered thin films of biaxial and lower symmetry from photon spectroscopies. I. Reflection

- infrared vibrational spectroscopy. *The Journal of Chemical Physics* **1992**, *96* (2), 927-945.
26. Camillone III, N.; Chidsey, C. E. D.; Liu, G.; Putvinski, T. M.; Scoles, G. Surface structure and thermal motion of n-alkane thiols self-assembled on Au(111) studied by low energy helium diffraction. *The Journal of Chemical Physics* **1991**, *94* (12), 8493-8502.
 27. Nuzzo, R. G.; Korenic, E. M.; Dubois, L. H. Studies of the temperature-dependent phase behavior of long chain n-alkyl thiol monolayers on gold. *The Journal of Chemical Physics* **1992**, *93* (1), 767-773.
 28. Dubois, L. H.; Nuzzo, R. G. Synthesis, Structure, and Properties of Model Organic Surfaces. *Annual Review of Physical Chemistry* **1992**, *43* (1), 437-463.
 29. Poirier, G. E.; Pylant, E. D. The Self-Assembly Mechanism of Alkanethiols on Au(111). *Science* **1996**, *272* (5265), 1145-1148.
 30. Poirier, G. E.; Tarlov, M. J. The c(4X2) Superlattice of n-Alkanethiol Monolayers Self-Assembled on Au(111). *Langmuir* **2002**, *10* (9), 2853-2856.
 31. Camillone III, N.; Chidsey, C. E. D.; Liu, G.; Scoles, G. Substrate dependence of the surface structure and chain packing of docosyl mercaptan self-assembled on the (111), (110), and (100) faces of single crystal gold. *The Journal of Chemical Physics* **1993**, *98* (5), 4234-4245.
 32. Alves, C. A.; Porter, M. D. Atomic force microscopic characterization of a fluorinated alkanethiolate monolayer at gold and correlations to electrochemical and infrared reflection spectroscopic structural descriptions. *Langmuir* **2002**, *9* (12), 3507-3512.
 33. Liu, G.; Fenter, P.; Chidsey, C. E. D.; Ogletree, D. F.; Eisenberger, P.; Salmeron, M. An unexpected packing of fluorinated n-alkane thiols on Au(111): A combined atomic force microscopy and x-ray diffraction study. *The Journal of Chemical Physics* **2009**, *101* (5), 4301-4306.
 34. Godin, M.; Williams, P. J.; Tabard-Cossa, V.; Laroche, O.; Beaulieu, L. Y.; Lennox, R. B.; Grutter, P. Surface Stress, Kinetics, and Structure of Alkanethiol Self-Assembled Monolayers. *Langmuir* **2004**, *20* (17), 7090-7096.
 35. Terrill, R. H.; Tanzer, T. A.; Bohn, P. W. Structural Evolution of Hexadecanethiol Monolayers on Gold during Assembly: Substrate and Concentration Dependence of Monolayer Structure and Crystallinity. *Langmuir* **1998**, *14* (4), 845-854.
 36. Schwartz, D. K. Mechanisms and kinetics of self-assembled monolayer formation. *Annual Review of Physical Chemistry* **2001**, *52*, 107-137.
 37. Bain, C. D.; Whitesides, G. M. Modeling organic surfaces with self-assembled monolayers. *Angewandte Chemie* **1989**, *101* (4), 522-528.
 38. Dubois, L. H.; Zegarski, B. R.; Nuzzo, R. G. Fundamental studies of microscopic wetting on organic surfaces. 2. Interaction of secondary adsorbates with chemically textured organic monolayers. *Journal of the American Chemical Society* **2002**, *112* (2), 570-579.

39. Lahiri, J.; Isaacs, L.; Tien, J.; Whitesides, G. M. A Strategy for the Generation of Surfaces Presenting Ligands for Studies of Binding Based on an Active Ester as a Common Reactive Intermediate: A Surface Plasmon Resonance Study. *Analytical Chemistry* **1999**, *71* (4), 777-790.
40. Chechik, V.; Crooks, R. M.; Stirling, C. J. M. Reactions and reactivity in self-assembled monolayers. *Advanced Materials* **2000**, *12* (16), 1161-1171.
41. Love, J. C.; Estroff, L. A.; Kriebel, J. K.; Nuzzo, R. G.; Whitesides, G. M. Self-assembled monolayers of thiolates on metals as a form of nanotechnology. *Chemical Reviews* **2005**, *105*, 1103-1169.
42. Houseman, B. T.; Gawalt, E. S.; Mrksich, M. Maleimide-Functionalized Self-Assembled Monolayers for the Preparation of Peptide and Carbohydrate Biochips. *Langmuir* **2002**, *19* (5), 1522-1531.
43. Delamarche, E.; Sundarababu, G.; Biebuyck, H.; Michel, B.; Gerber, C.; Sigrist, H.; Wolf, H.; Ringsdorf, H.; Xanthopoulos, N.; Mathieu, H. J. Immobilization of Antibodies on a Photoactive Self-Assembled Monolayer on Gold. *Langmuir* **1996**, *12* (8), 1997-2006.
44. Smith, E. A.; Wanat, M. J.; Cheng, Y.; Barreira, S. V. P.; Frutos, A. G.; Corn, R. M. Formation, Spectroscopic Characterization, and Application of Sulfhydryl-Terminated Alkanethiol Monolayers for the Chemical Attachment of DNA onto Gold Surfaces. *Langmuir* **2001**, *17* (8), 2502-2507.
45. Smith, E. A.; Thomas, W. D.; Kiessling, L. L.; Corn, R. M. Surface Plasmon Resonance Imaging Studies of Protein-Carbohydrate Interactions. *Journal of the American Chemical Society* **2003**, *125* (20), 6140-6148.
46. Wegner, G. J.; Lee, H. J.; Corn, R. M. Characterization and Optimization of Peptide Arrays for the Study of Epitope-Antibody Interactions Using Surface Plasmon Resonance Imaging. *Analytical Chemistry* **2002**, *74* (20), 5161-5168.
47. Lee, J. K.; Lee, K. B.; Kim, D. J.; Choi, I. S. Reactivity of Vinyl-Terminated Self-Assembled Monolayers on Gold: Olefin Cross-Metathesis Reactions. *Langmuir* **2003**, *19* (20), 8141-8143.
48. Collman, J. P.; Devaraj, N. K.; Chidsey, C. E. D. Clicking Functionality onto Electrode Surfaces. *Langmuir* **2004**, *20* (4), 1051-1053.
49. Lee, J. K.; Chi, Y. S.; Choi, I. S. Reactivity of Acetylenyl-Terminated Self-Assembled Monolayers on Gold: Triazole Formation. *Langmuir* **2004**, *20* (10), 3844-3847.
50. Saxon, E.; Luchansky, S. J.; Hang, H. C.; Yu, Ch.; Lee, S. C.; Bertozzi, C. R. Investigating Cellular Metabolism of Synthetic Azidosugars with the Staudinger Ligation. *Journal of the American Chemical Society* **2002**, *124* (50), 14893-14902.
51. Köhn, M.; Wacker, R.; Peters, C.; Schröder, H.; Soulère, L.; Breinbauer, R.; Niemeyer, Ch. M.; Waldmann, H. Staudinger Ligation: A New Immobilization Strategy for the Preparation of Small-Molecule Arrays. *Angewandte Chemie International Edition* **2003**, *42* (47), 5830-5834.
52. Hodneland C.D; Lee Y.S; Min D.H; Mrksich, M. Selective Immobilization of Protein to Self-Assembled Monolayers Presenting Active Site Directed Capture Ligands. *Proceedings of the National Academy of Sciences USA* **2002**, *99* (8), 5048-5052.

53. Murphy, W. L.; Mercurius, K. O.; Koide, S.; Mrksich, M. Substrates for cell adhesion prepared via active site-directed immobilization of a protein domain. *Langmuir* **2004**, *20* (4), 1026-1030.
54. Yan, L.; Marzolin, C.; Terfort, A.; Whitesides, G. M. Formation and reaction of interchain carboxylic anhydride groups on self-assembled monolayers on gold. *Langmuir* **1997**, *13* (25), 6704-6712.
55. Yousaf, M. N.; Mrksich, M. Diels-Alder Reaction for the Selective Immobilization of Protein to Electroactive Self-Assembled Monolayers. *Journal of the American Chemical Society* **1999**, *121* (17), 4286-4287.
56. Dillmore, W. S.; Yousaf, M. N.; Mrksich, M. A Photochemical Method for Patterning the Immobilization of Ligands and Cells to Self-Assembled Monolayers. *Langmuir* **2004**, *20* (17), 7223-7231.
57. Lee, K.; Pan, F.; Carroll, G. T.; Turro, N. J.; Koberstein, J. T. Photolithographic Technique for Direct Photochemical Modification and Chemical Micropatterning of Surfaces. *Langmuir* **2004**, *20* (5), 1812-1818.
58. Niklewski, A.; Azzam, W.; Strunskus, T.; Fischer, R. A.; Woll, C. Fabrication of Self-Assembled Monolayers Exhibiting a Thiol-Terminated Surface. *Langmuir* **2004**, *20* (20), 8620-8624.
59. Hodneland, Ch. D.; Mrksich, M. Design of Self-Assembled Monolayers That Release Attached Groups Using Applied Electrical Potentials. *Langmuir* **1997**, *13* (23), 6001-6003.
60. Creager, S. E.; Clarke, J. Contact-Angle Titrations of Mixed .omega.-Mercaptoalkanoic Acid/Alkanethiol Monolayers on Gold. Reactive vs Nonreactive Spreading, and Chain Length Effects on Surface pKa Values. *Langmuir* **2002**, *10* (10), 3675-3683.
61. Kim, H. I.; Kushmerick, J. G.; Houston, J. E.; Bunker, B. C. Viscous Interphase Water Adjacent to Oligo(ethylene glycol)-Terminated Monolayers. *Langmuir* **2003**, *19* (22), 9271-9275.
62. Gurau, M. C.; Kim, G.; Lim, S.-L.; Albertorio, F.; Fleisher, H. C.; Cremer, P. S. Organization of Water Layers at Hydrophilic Interfaces. *ChemPhysChem* **2003**, *4* (11), 1231-1233.
63. Schonherr, H.; Feng, Ch.; Shovsky, A. Interfacial Reactions in Confinement: Kinetics and Temperature Dependence of Reactions in Self-Assembled Monolayers Compared to Ultrathin Polymer Films. *Langmuir* **2003**, *19* (26), 10843-10851.
64. Vaidya, B.; Chen, J.; Porter, M. D.; Angelici, R. J. Effects of Packing and Orientation on the Hydrolysis of Ester Monolayers on Gold. *Langmuir* **2001**, *17* (21), 6569-6576.
65. Houseman, B. T.; Mrksich, M. The Role of Ligand Density in the Enzymatic Glycosylation of Carbohydrates Presented on Self-Assembled Monolayers of Alkanethiolates on Gold. *Angewandte Chemie International Edition* **1999**, *38* (6), 782-785.
66. Darren, J. M.; Brown, A. A.; Huck, W. T. S. Surface-Initiated Polymerizations in Aqueous Media: Effect of Initiator Density. *Langmuir* **2002**, *18* (4), 1265-1269.

67. Kwon, Y.; Mrksich, M. Dependence of the Rate of an Interfacial Diels-Alder Reaction on the Steric Environment of the Immobilized Dienophile: An Example of Enthalpy-Entropy Compensation. *Journal of the American Chemical Society* **2002**, *124* (5), 806-812.
68. Dakkouri, A. S.; Kolb, D. M.; Edelstein-Shima, R.; Mandler, D. Scanning Tunneling Microscopy Study of L-Cysteine on Au(111). *Langmuir* **1996**, *12* (11), 2849-2852.
69. Dodero, G.; De Michieli, L.; Cavalleri, O.; Rolandi, R.; Oliveri, L.; Dacca, A.; Parodi, R. L-cysteine chemisorption on gold: an XPS and STM study. *Colloids and Surfaces A-Physicochemical and Engineering Aspects* **2000**, *175* (1-2), 121-128.
70. De Renzi, V.; Lavagnino, L.; Corradini, V.; Biagi, R.; Canepa, M.; del Pennino, U. Very low energy vibrational modes as a fingerprint of H-bond network formation: L-cysteine on Au(111). *Journal of Physical Chemistry C* **2008**, *112* (37), 14439-14445.
71. Honda, M.; Matsui, F.; Daimon, H. Chemisorption of L-cysteine on Au(111)/Si(111) and Si(111)root 3x root 3-Au surfaces. *Surface Review and Letters* **2006**, *13* (2-3), 197-200.
72. Kuhnle, A.; Linderoth, T. R.; Schunack, M.; Besenbacher, F. L-cysteine adsorption structures on Au(111) investigated by scanning tunneling microscopy under ultrahigh vacuum conditions. *Langmuir* **2006**, *22* (5), 2156-2160.
73. Wang, D.; Lei, S. B.; Wan, L. J.; Wang, C.; Bai, C. L. Effect of chemical structure on the adsorption of amino acids with aliphatic and aromatic substitution groups: In situ STM study. *Journal of Physical Chemistry B* **2003**, *107* (33), 8474-8478.
74. Seneviratne, V. PhD thesis Frictional Force Microscopy Studies on Mixed Self Assembled Monolayers. 2006.
75. Colb, H. C.; Finn, M. G.; Sharpless, K. B. Click Chemistry: Diverse Chemical Function from a Few Good Reactions. *Angewandte Chemie International Edition* **2001**, *40* (11), 2004-2021.
76. Devaraj, N. K.; Dinolfo, P. H.; Chidsey, Ch. E. D.; Collman, J. P. Selective Functionalization of Independently Addressed Microelectrodes by Electrochemical Activation and Deactivation of a Coupling Catalyst. *Journal of the American Chemical Society* **2006**, *128* (6), 1794-1795.
77. Ku, S. Y.; Wong, K. T.; Bard, A. J. Surface Patterning with Fluorescent Molecules Using Click Chemistry Directed by Scanning Electrochemical Microscopy. *Journal of the American Chemical Society* **2008**, *130* (8), 2392-2393.
78. Paxton, W. F.; Spruell, J. M.; Stoddart, J. F. Heterogeneous Catalysis of a Copper-Coated Atomic Force Microscopy Tip for Direct-Write Click Chemistry. *Journal of the American Chemical Society* **2009**, *131* (19), 6692-6694.
79. Rostovtsev, V. V.; Green, L. G.; Fokin, V. V.; Sharpless, K. B. A Stepwise Huisgen Cycloaddition Process: Copper(I)-Catalyzed Regioselective Ligation of Azides and Terminal Alkynes. *ChemInform* **2002**, *33* (43), 45.
80. Tornoe, Ch. W.; Christensen, C.; Meldal, M. Peptidotriazoles on Solid Phase: [1,2,3]-Triazoles by Regiospecific Copper(I)-Catalyzed 1,3-Dipolar Cycloadditions of Terminal Alkynes to Azides. *The Journal of Organic Chemistry* **2002**, *67* (9), 3057-3064.

4 Experimental methods

4.1 Preparation of substrates for gold deposition

All experiments were carried out on gold surfaces prepared by thermal evaporation onto mica, glass and silicon wafers. These surfaces were selected for their high flatness with the indication that, whilst gold on mica has the best parameters; in some experiments it is hard to use.

4.1.1 Mica

Mica (Ruby Grade V) was obtained from Agar Scientific UK. Preparation of mica substrates was carried out in a laminar flow clean hood. Before evaporation of gold, mica sheets were cut into the desired dimensions using clean tools. Following this, each piece was cleaved into two, revealing very clean and flat surfaces. The cleavage was done with use of a needle, handling a piece of mica with clean tweezers. The pieces of mica were then placed and fixed into a specially designed holder, with clean surface facing upwards. After mounting all of the mica pieces, the holder was transferred into the evaporator. During the transportation an aluminium foil cover was used to prevent touching the mica sheets and dust contamination.

4.1.2 Glass

Microscope glass slides (made from borosilicate glass) were purchased from Fisher Scientific. Glass substrate preparation consisted of pre-cutting with a diamond pen for easier cleaving after deposition, cleaning the glass slides with washing liquid, rinsing with water and then immersing for two hours in freshly made piranha solution (1:3 ratio of hydrogen peroxide 100 vol and sulphuric acid H_2SO_4 98%). The glass slides were then removed from solution, rinsed with ultrapure water (MilliQ),

and sonicated in ultra pure water three times. Glass slides were handled with special, clean tweezers, rinsed with isopropanol (HPLC grade) and dried in a stream of a clean N₂. After drying they were placed into sample holders lined with aluminium foil to prevent contamination. Clean glass samples were transferred immediately to the sample holder of the evaporator and after making sure all were fixed well, they were placed in the evaporation chamber for gold coating.

4.1.3 Silicon

Si (100) wafers of 76.20 mm in diameter and thickness *ca* 380 µm were purchased from Compart Technology Ltd. UK. Before cleaning they were placed on aluminium foil, cut with use of a diamond pen and a ruler into smaller pieces and incised for easier cleaving (similar to procedure for the glass substrate). During the cutting, the polished side of wafers was facing towards aluminium foil to prevent unwanted contaminations and damage to the polished surface. The small pieces with incisions were then cleaned in piranha solution following the procedure used for cleaning glass substrates.

4.2 Evaporation of gold on mica/glass/silicon

For gold evaporation on all of the substrates gold beads *ca* 3 mm diameter, 99.999% and chromium pieces purchased from Birmingham Metal Ltd were used. Thermal evaporation of gold was carried out using a *MINILAB deposition system HST 60M* (Moorfield.Ltd).

After mounting the sample holder, the chamber was closed and pumped down to the base pressure of 5×10^{-7} mbar. When the pressure reached a value of around 10^{-6} mbar, sufficient current was passed through the filaments to pre-melt first the chromium, and then the gold in order to remove any adsorbed gases or contamination. When the pressure stopped rising, pre-melting was stopped and the

system was evacuated to the base pressure. When the target pressure was reached again 3nm of chromium was deposited. The deposition rate for the chromium layer was maintained below 0.5 \AA s^{-1} and the pressure during the process was no higher than 5.5×10^{-6} mbar. After coating the substrate with the Cr adhesive layer, the pressure was brought back to the base value of 10^{-7} mbar. Different layer thicknesses were deposited, according to need. The deposition rate of gold was maintained less than 0.5 \AA s^{-1} with the pressure in the chamber less than 10^{-6} mbar. The deposition chamber was kept under a high vacuum during cooling down. When the temperature dropped to ambient the chamber was vented with clean nitrogen and samples were removed.

Typical deposition substrates, coating material and thickness are presented in table 4-1.

Table 4-1 Substrates, coating materials and their thicknesses used in the study

Substrate	Glass	Mica	Silicon
Coating and thickness	30 nm Au	300 nm Au	
	2 nm Cr, 100 nm Au	3 nm Cr, 100nm Au	3 nm Cr, 100 nm Au

For achieving specially flat gold on mica (mica coated with 300 nm Au), a thermal deposition was performed on heated substrates¹⁻⁸. No chromium adhesive layer was deposited. After the system reached the base pressure of 10^{-7} mbar the sample was heated to 574 K. When the substrate reached the target value of the temperature the pre-melting procedure was carried out. After removing adsorbed gasses and contamination the chamber was evacuated back to the base pressure and then the gold deposition started. After the deposition has finished the temperature of 574 K was held in the chamber for the following 3 h in order to anneal the gold. After that time the temperature was reduced slowly and, when it reached room temperature, the chamber was vented and the substrates were removed from the evaporator.

4.3 Preparation of thiol solutions for self assembly

Self assembled monolayers were formed by soaking gold surfaces in appropriate thiol solutions. Solutions were prepared in very clean glassware (glassware cleaned according to the procedure 4.1.2) with use of HPLC grade ethanol or MilliQ water, diluted to the concentration of 1 mM. Only thiols for further reacting in CuAAC reaction were used at the concentration of 2 mM. Solutions of thiols were made as stock solutions at a concentration of 10 mM by dissolving an appropriate mass of a thiol in a small volume of EtOH, sonicated, topped up to reach desired volume in a volumetric flask. Solutions were stored in a freezer.

Preparation of mixtures of final concentration was carried out by keeping stock solutions at room temperature for about two hours. Then thiols were filtered with PTFE filters (13 mm, pore size 0.22 μm - Fisher Scientific, UK). Solutions were made in freshly cleaned vials. Desired volumes were measured with a micropipette, 200 μL (Gilson).

4.4 Preparation of SAMs

All self assembled monolayers were prepared using gold surfaces freshly prepared, as described in section 4.2. The immersion time of gold substrates in thiol solutions was 24 ± 1 h, after which, gold samples were removed from thiol solutions, rinsed with HPLC grade EtOH, dried in a stream of clean N_2 and used for experiments immediately after drying⁹.

4.5 Characterization methods

The most common and subsequently efficient methods for characterization of SAMs' properties are: ellipsometry, electrochemical impedance spectroscopy, cyclic voltamperometry, contact angle microscopy, atomic force microscopy and PM-IRRAS. Information gained from measurements give an insight in to the quantitative and qualitative properties of self assembled monolayers.

4.5.1 Ellipsometry

Ellipsometry is an optical method based upon the measurement of changes in the polarization of light after its reflection from a sample¹⁰⁻¹². It offers a non-destructive, accurate way to determine film thickness and optical constants that does not require specialised sample preparation or ultra high vacuum. It is not a direct readout technique but is model-based. With use of ellipsometry we are able to measure thickness down to the submonolayer level; for example, following partial SAM formation¹¹.

4.5.1.1 Theory

Light is an electromagnetic wave, which consists of an electric field \vec{E} and a magnetic field \vec{B} . The field vectors are mutually perpendicular and also perpendicular to the propagation direction as given by the wave vector \vec{k} . All states of polarization are classified according to the trace of the electrical field vector during one period. Linearly polarized light means that the electrical field vector oscillates within a plane; elliptically polarized light means that the trace of the electric field vector during one period is an ellipse. A convenient mathematical representation of a given state of polarization is based on a superposition of two linearly polarized light waves within an arbitrarily chosen orthogonal coordinate system¹⁰.

$$\vec{E}(\vec{r}, t) = \begin{pmatrix} |E_p| \cos(2\pi vt) - \vec{k} \cdot \vec{r} + \delta_p \\ |E_s| \cos(2\pi vt) - \vec{k} \cdot \vec{r} + \delta_s \end{pmatrix}$$

Equation 4-1

Where $|E_p|$ and $|E_s|$ are the amplitudes, δ_p and δ_s are the phases, $|\vec{k}| = 2\pi/\lambda$ is the magnitude of wave vector and ν is the frequency.

$$\vec{E} = \begin{pmatrix} E_p \\ E_s \end{pmatrix}$$

Equation 4-2

A surface modification, for example in SAMs, causes modification in polarization state of reflected light, which is used to calculate the thickness or refractive index of the film.

When light hits a surface at an angle ϕ_1 a part of it will be transmitted at an angle ϕ_2 , and the remainder will be reflected back at an angle ϕ_1 . This is described by Snell's Law, as shown in Figure 4-1.

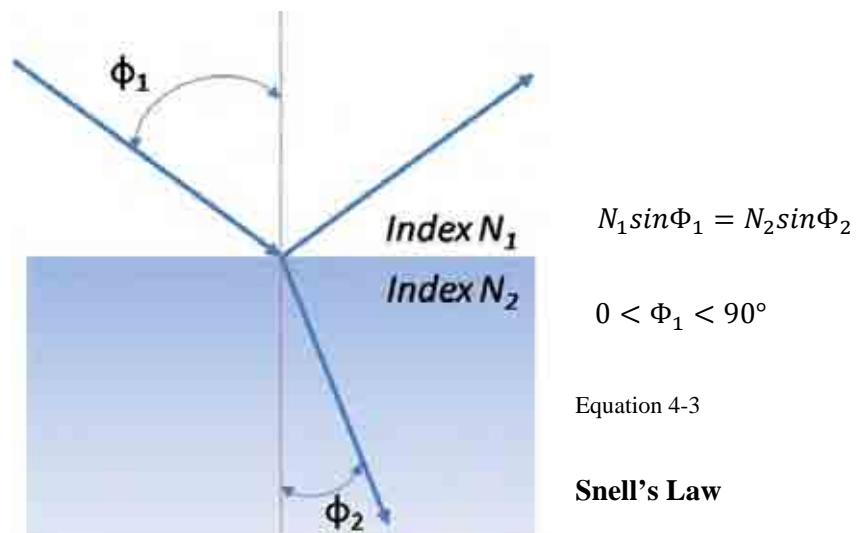


Figure 4-1 The incident, transmitted and reflected light at the interface of two media with different refractive indices

The basic principles for an ellipsometry experiment are shown in Figure 4-2.

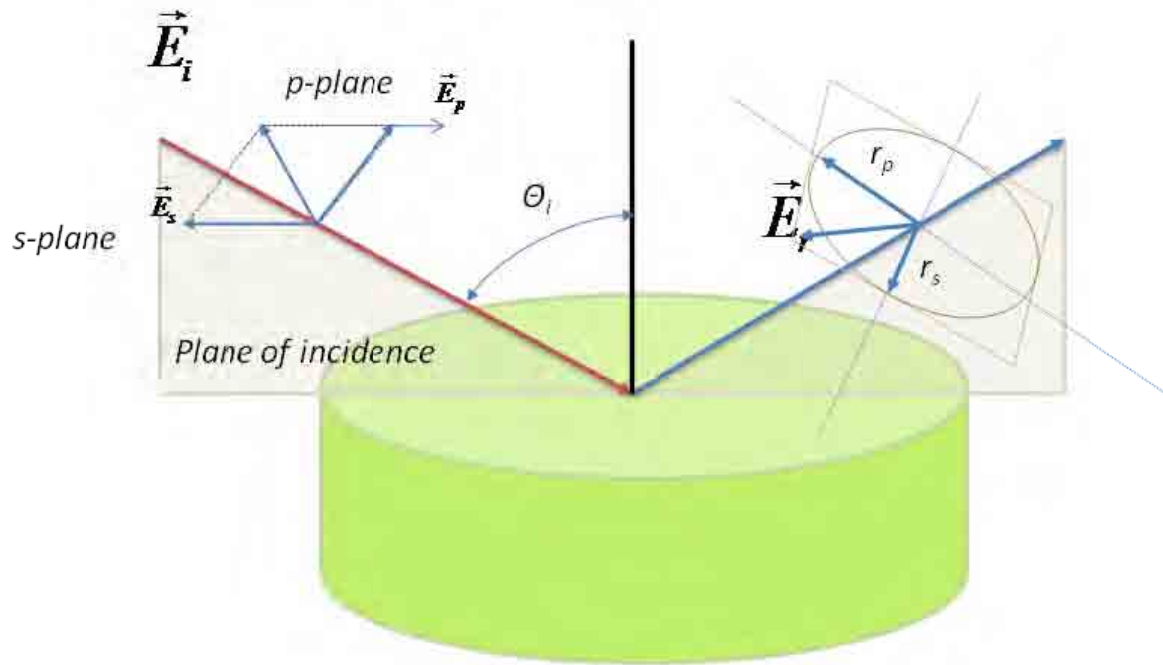


Figure 4-2 Ellipsometric experiment in reflection mode¹¹, for the incident and reflected light the plane of incidence can be decomposed into an s and p component, where s -component oscillates parallel to the sample surface and p -component oscillates perpendicular to the sample surface.

The reflected light usually differs in its state of polarization and these changes are measured and quantified in an ellipsometric experiment^{12,13}. The intensity of the s and p component, after reflection, are denoted by R_s and R_p . Two quantities Ψ and Δ are introduced in order to describe the changes in the state of polarization. Complex reflectance ratio ρ could be then expressed by the equation:

$$\rho = \tan(\psi) e^{i\Delta} = \frac{R_p}{R_s}$$

Equation 4-4

Spectroscopic ellipsometry measures this complex ratio ρ as a function of wavelength.

The reflection coefficient gives the ratio of the amplitude of the reflected wave to that of the incident wave. Reflection affects the component of the incident light polarised within a plane of incidence (p) in a different manner to the light polarised perpendicular to the plane of incidence (s). This is exhibited by the Fresnel reflection coefficients. This difference in the reflection of the two components leads to the overall change in polarisation.

$$r_{12}^p = \frac{N_2 \cos \phi_1 - N_1 \cos \phi_2}{N_2 \cos \phi_1 + N_1 \cos \phi_2} \quad r_{12}^s = \frac{N_1 \cos \phi_1 - N_2 \cos \phi_2}{N_1 \cos \phi_1 + N_2 \cos \phi_2}$$

Equation 4-5

N_1 and N_2 are refractive indices of each medium.

The situation of self assembled monolayers requires a consideration of additional factors because there are now three phases: air, the film and substrate, as it is illustrated in Figure 4-3.

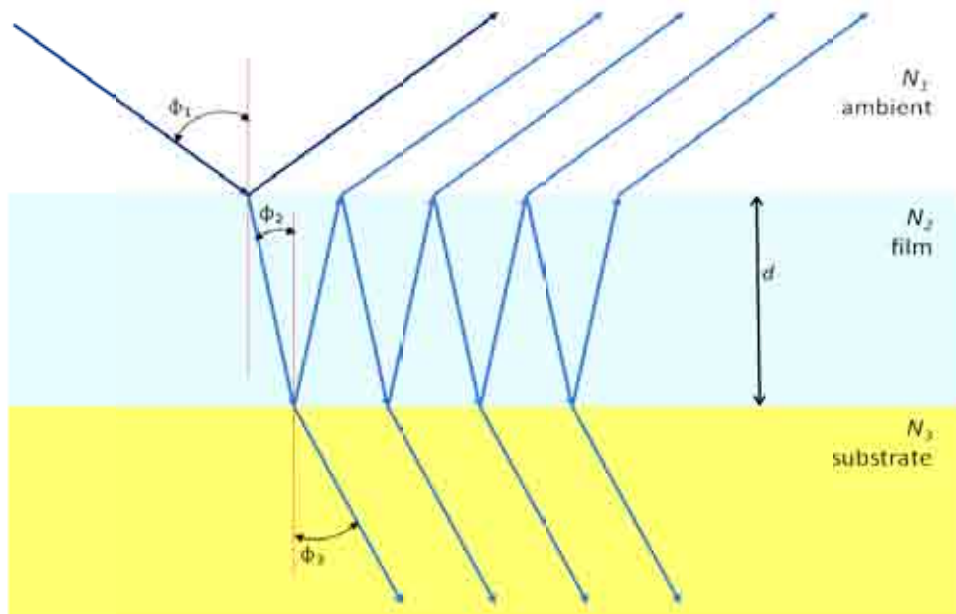


Figure 4-3 The reflection and transmission of light through two interfaces

The reflection coefficients for both components of incident light are:

$$R^p = \frac{r_{12}^p + r_{23}^p e^{-j2\beta}}{1 + r_{12}^p \cdot r_{23}^p e^{-j2\beta}} \quad R^s = \frac{r_{12}^s + r_{23}^s e^{-j2\beta}}{1 + r_{12}^s \cdot r_{23}^s e^{-j2\beta}}$$

Equation 4-6

where

$$\beta = 2\pi \left(\frac{2}{\lambda} \right) N_2 \cos \phi_2$$

Equation 4-7

Knowing ρ and β , we are able to calculate the thickness of a SAM.

In the case of very thin films it is common that a refractive index needs to be assumed, due to limitations of the resolution of measured angles. Within the model, this is shown by a strong correlation between the layers and derived optical constants. That situation happens when the refractive index is straightforward highly correlated to the thickness; for all other cases the thickness measurements are always model-dependent^{13,14}.

The majority of spectroscopic ellipsometers are built as presented in the Figure 4-4.

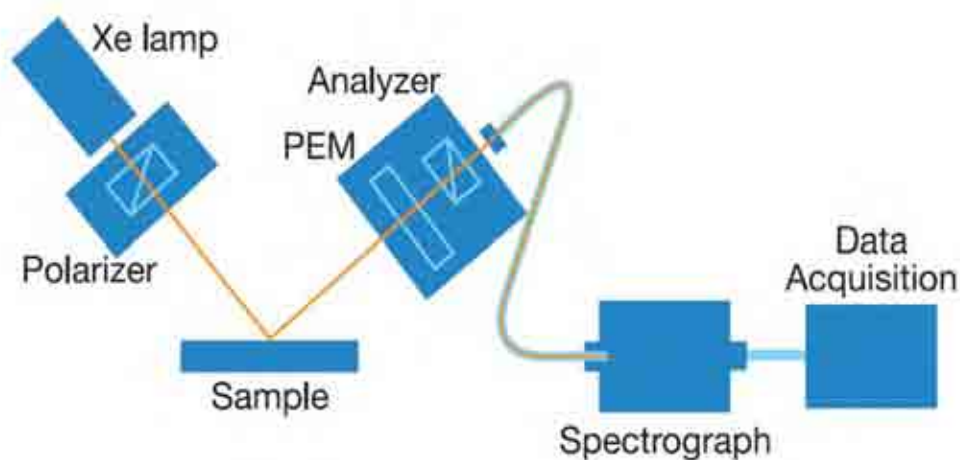


Figure 4-4 Schematic representation of spectroscopic ellipsometer

4.5.1.2 Procedure for ellipsometry measurements for film thickness determination

Since ellipsometry is a model based technique, special procedures are needed in order to obtain the data required for calculation.

Firstly, measurements on the bare substrate should be conducted. This gives values of Ψ and Δ which are then converted to refractive indices *via* use of a two- layer model. It is due to the fact that there is always a very thin film of organic layer (contamination from the air) on a substrate, even when the substrate is cleaned beforehand. These refractive indices are then used for creating a 3-layer model. After these calculations measurements on target samples (substrate with examined monolayer) could be performed. The values of Ψ and Δ are then used in a 3-layer model to fit experimental data and calculate the thickness of the deposited monolayers.

In this study, all measurements were made with an angle of incidence of 70° . For determination of film thickness, two models were used: the classical, and the Cauchy model. χ^2 values for fitting were taken into consideration during modelling the thickness. A smaller χ^2 value indicates better fitting. At least five measurements in different places of each sample were taken, then after modelling the thickness was averaged.

All measurements were conducted with a UNIVESSEL 640 spectroscopic ellipsometer HORIBA-YOVIN. Data modelling was performed with DELTA PSI2 software¹⁵.

4.5.2 Contact angle goniometry

The technique of contact angle goniometry uses the phenomenon of the interface/surface tension between liquid and solid surrounded by vapour^{13,16-19}. The simplicity and sensitivity of the technique to the interfacial chemical structure of an interface causes its popularity in materials testing; however, contact angle measurements are only complementary to the other techniques. They give qualitative insight into the properties and quality of self assembled monolayers.

4.5.2.1 Theory

The contact angle is a quantitative measure of the wetting of a solid by a liquid. Unless it is very volatile, any liquid (including liquid metals such as mercury) having a low viscosity can be used. Figure 4-5 illustrates the technique. When a droplet of a liquid is added to a solid surface it will spread until it reaches equilibrium. If the liquid does not entirely wet the surface it forms a droplet of a finite contact angle θ . Low values of θ indicate a strong liquid–solid interaction such that the liquid tends to spread on the solid, or wets well, while high θ values indicate weak interaction and poor wetting. If θ is less than 90° , then the liquid is said to wet (or sometimes partially wet) the solid. A zero contact angle represents complete wetting. If θ is greater than 90° , then it is said to be non-wetting.

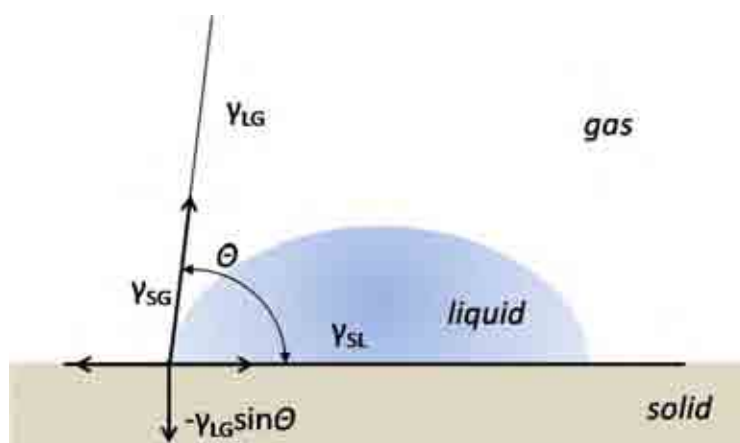


Figure 4-5 Cartoon representation of the vectorial equilibrium for a drop of a liquid on a solid surface, γ_{SG} , γ_{LG} , γ_{SL} are the surface tensions of the solid-gas, liquid-gas and solid-liquid interface respectively and θ is the equilibrium contact angle¹⁸.

Equilibrium is described by the Young equation:

$$\gamma_{SG} = \gamma_{LG} \cos\theta + \gamma_{SL}$$

Equation 4-8

γ_{SG} , γ_{LG} , γ_{SL} are surface tensions of the solid-gas, liquid-gas and solid-liquid interface respectively and θ is the equilibrium contact angle. The Young equation requires the system to be in equilibrium. However, from experiments, it is known that the contact angles of a droplet being added or removed from the surface are different. This hysteresis between advancing and receding contact angles means that droplets of liquid on a real surface are not in equilibrium. This observation caused the development of different methods for measurements of contact angles:

- static sessile droplet method,
- dynamic sessile droplet method,
- dynamic Wilhelmy method,
- single fibre Wilhelmy method
- powder contact angle method

In this study the dynamic sessile droplet method was used. A typical setup for this type of measurements consists of a goniometer-microscope equipped with a video camera connected to a computer with image-analysis software for contact angle determination. For video recording, a suitable cold light source shining on a sample stage is required. A typical contact- angle instrumentation set up is presented in Figure 4-6.



Figure 4-6 Contact angle experimental set up used for measurements of this study

This method is similar to the static sessile drop but during measurement the drop is modified. A typical experiment of dynamic sessile drop study determines the largest contact angle possible without increasing its solid/liquid interfacial area, by adding volume dynamically. This maximum angle is the advancing angle θ_a . Liquid is removed to produce the smallest possible angle, the receding angle θ_r . The difference between the advancing and receding angle is the contact angle hysteresis. Both θ_a and θ_r depend on the surface roughness (detailed shapes and configurations often patches or strips) and also on the surface chemical heterogeneity¹⁸.

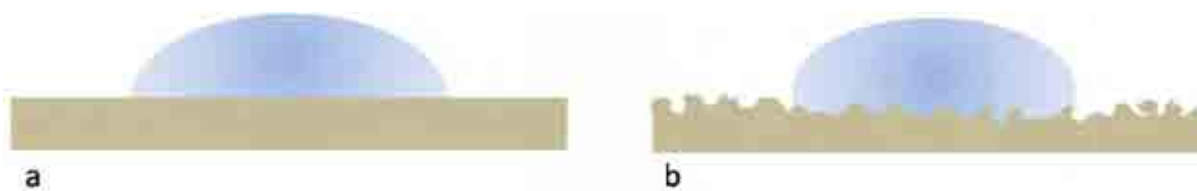


Figure 4-7 A cartoon projection of a droplet on a smooth (a) and a rough (b) sample. In the latter case, a rough surface forces a greater contact angle than a droplet would have on a flat surface of the same material¹⁸.

Determination of θ_a within $\pm 2^\circ$ is easy, but it is difficult to reduce the relative error to $\pm 0.5^\circ$. This is because the direction of a liquid profile rapidly changes with the distance from the three phase contact

point. The difference between θ_a and θ_r gives the contact angle hysteresis, H , ($H \equiv \theta_a - \theta_r$), which can be quite large, around $5\text{--}20^\circ$ in conventional measurements (or $20\text{--}50^\circ$ in some exceptional cases)^{18,19}.

All measurements were performed on a system built in the surface lab (home-made stage apparatus with a Charge-Coupled Device (CCD) KP-M1E/K camera (Hitachi)) with use of FRA32 Video Analysis Software for contact angle images analysis. All data were collected at room temperature and pressure under ambient humidity conditions.

4.5.3 PM-IRRAS

PM-IRRAS -Polarization Modulation-Infrared Reflection-Absorption Spectroscopy is a powerful method for IR-spectroscopic analysis of floating and solid monolayers. Because modulated reflectivity is independent on isotropic absorption from water (either in gaseous or bulk state) the method has been widely used for characterization of SAMs. It is a non-invasive technique which gives a spectrum of the differential IR absorption between the s - and p -linearly polarized light for the molecules adsorbed on a metal surface^{20,21}.

4.5.3.1 Theory

The method bases on the fact that absorption in isotropic media is independent of polarization, so that any difference between the s - and p -polarized signals can be assigned to surface specific absorption. "Polarization Modulation" (PM) – an advance in component design- removes interference of water vapour and CO₂ and also reduces instrumental noise.

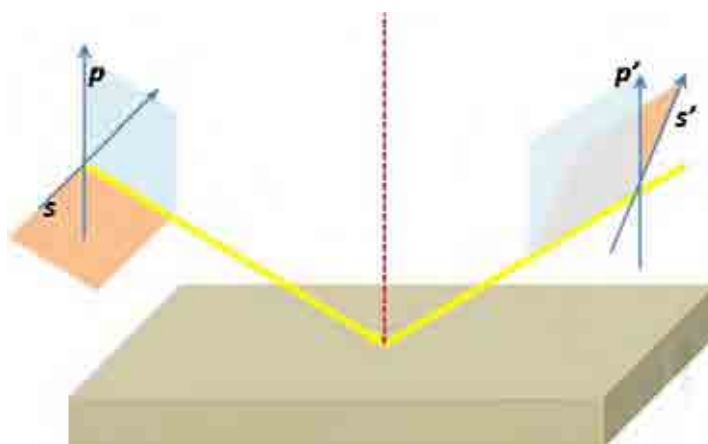


Figure 4-8 Schematic representation of p and s polarised light

In polarization modulation, incoming light is modulated between s - and p - polarization (shown in Figure 4-8) at high frequency, which allows simultaneous measurement of spectra for the two

polarizations, the difference providing surface-specific information, and the sum providing the reference spectrum. As the spectra are measured simultaneously, the effect of water vapour is largely removed.

Polarization modulation is provided by a photoelastic modulator (PEM). The PEM consists of two components: the modulator head and the control unit. The modulator head (made from an IR-transparent crystal) is placed in the beam line. The control unit generates high frequency oscillations that drive a stress transducer attached to the polarization modulator crystal. The stress applied along one axis of the PEM crystal induces anisotropy in the refractive index of the crystal. This results in a rotation of the polarization of the transmitted light and causes the polarization state of the IR beam to alternate. Desired polarization (*s* or *p*) is provided by a fixed polarizer placed in the optical path before the PEM. The sample is placed directly after the PEM.

Since the PEM is not achromatic, complete modulation of the polarization can only be achieved at one wavelength (this is determined by the stress voltage applied to the PEM).

A schematic projection of PM-IRRAS set up is presented in Figure 4-9.

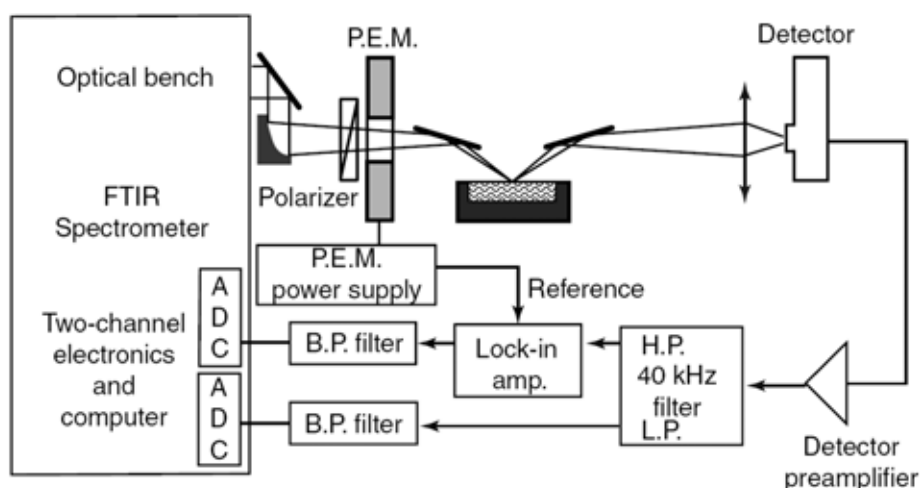


Figure 4-9 A typical PM-IRRAS set up²² PEM- photoelastic modulator, BP-bandpass, LP-low pass HP-high pass.

The PM-IRRAS signal from an ultrathin film on a metallic surface is given by:

$$I_D(\varphi) = \frac{I_s + I_p}{2} + \frac{I_s - I_p}{2} \cos\varphi$$

Equation 4-9

Where $I_D(\varphi)$ is for the intensity of the radiation at the detector, I_p and I_s are the components of the beam in front of the detector (oriented perpendicular or parallel to the optical bench), and φ is the phase shift, which depends on the frequency of PEM and time.

The polarization of the incident beam is periodically changed between p and s and every 90° of a period either I_s or I_p is incident at the detector. If the wavelength of the incident beam departs from the selected wavelength, the polarization of the incident beam becomes circular. Consequently, we can only fully optimize an experiment for a single wavelength.

Therefore, in polarization modulation it is necessary to distinguish between the theoretical and experimental spectrum. A demodulation technique needs to be applied to measure the signal arriving at the detector. The experimental signal is given by²¹:

$$\frac{I_D^{Diff}(2\omega)}{I_D^{Ave}} = \frac{\Delta I \cdot J_2(\varphi)}{\langle I \rangle + \frac{1}{2} \Delta I \cdot J_0(\varphi_0)}$$

Equation 4-10

Demodulation may be carried out by synchronous sampling demodulator where J_2 and J_0 are described by²¹:

$$J_2(\varphi_0) = \frac{1 - \cos\varphi_0}{2}$$

Equation 4-11

$$J_0(\varphi_0) = \frac{1 + \cos\varphi_0}{2}$$

Equation 4-12

Then the reflection absorption spectrum may be described by:

$$\frac{I_D^{Diff}(2\omega)}{I_D^{Ave}} = \frac{\Delta I \left[\frac{1 - \cos\varphi_0}{2} \right]}{\langle I \rangle + \frac{1}{2} \Delta I \left[\frac{1 + \cos\varphi_0}{2} \right]}$$

Equation 4-13

In order to achieve a correct spectrum, the corrections for PEM response functions need to be introduced:

$$I_D^{Ave}(cal) = \frac{I_p(cal)}{2} + \frac{I_p(cal)}{2} J_0(\varphi_0)$$

Equation 4-14

$$I_D^{Diff}(cal) = I_p(cal) J_2(\varphi_0)$$

Equation 4-15

From here we have:

$$\langle I \rangle = \frac{I_s + I_p}{2} = I_D^{Ave} - \frac{I_D^{Diff}(2\omega)}{2} \frac{I_p(cal)}{I_D^{Diff}(cal)} \left(2 \frac{I_D^{Ave}(cal)}{I_p(cal)} - 1 \right)$$

Equation 4-16

$$\Delta I = I_p - I_s = I_D^{Diff}(2\omega) \frac{I_p(cal)}{I_D^{Diff}(cal)}$$

Equation 4-17

Finally, a correction for must be made the fact that the ratio of the optical throughputs of the experimental set-up for p- and s- polarized light γ is not equal to 1²¹:

$$\frac{\Delta I}{\langle I \rangle} = 2 \frac{(\gamma + 1)\Delta I(\omega) + 2(\gamma - 1)\Delta I(\omega)}{(\gamma - 1)\Delta I(\omega) + 2(\gamma + 1)\Delta I(\omega)}$$

Equation 4-18

Where $\gamma = 1.01$ for the experimental set up was used for this study.

All the PM IRRAS spectra were measured using a Bruker Vertex 80 spectrometer with the polarization modulation set (PMA 50) equipped with a photoelastic modulator and synchronous sampling demodulator (in place of L/A in Figure 4-9) (Bruker, Germany and Hinds Instruments, US). Infrared radiation was incident on the sample at a set angle of 80° and the light reflected from the sample was focused by aspheric lens (ZnSe) onto the detector (liquid nitrogen-cooled MCT infrared detector with a BaF₂ window). Usually a thousand scans were acquired for a single sample to ensure good spectra quality. Samples were studied by performing measurements at characteristic regions of : 1200, 1600, 2100, 2900 and 3500 cm⁻¹. The PM-IRRAS spectra were processed using the OPUS program.

4.5.4 Electrochemical techniques

Electrochemical techniques, such as electrochemical impedance spectroscopy (EIS) and cyclic voltammetry (CV), are techniques suitable for the monitoring of self-assembled monolayers' (SAMs) properties. They give useful information on the distribution of defects/holes, the properties of the linked redox probes, the kinetics and mechanism of the monolayer formation process and the surface coverage^{23,24}.

4.5.4.1 Electrochemical Impedance

Electrochemical impedance is commonly used to determine the capacitance of a film adsorbed on the electrode surface²⁴⁻²⁶. The methodology used with this technique is based on the comparison of the results obtained with the unmodified and monolayer-modified electrode substrate.

4.5.4.1.1 Theory

The electrochemical properties of an electrode can be described in terms of a circuit composed of resistors and capacitors. The primary parameter is the impedance²⁴.

When an AC potential is applied to an electrochemical cell the impedance is measured by recording the AC current going through the cell. If the potential applied has sinusoidal characteristics, the response wave for this potential is a sinusoidal wave as well. For impedance measurements a small excitation sinusoidal signal is used.

$$E_t = E_0 \sin(\omega t)$$

Equation 4-19

$$\omega = 2\pi f$$

Equation 4-20

E_t -potential at time t , E_0 -amplitude of the signal, ω -angular frequency

For a linear system the response for applied potential is described by the equation:

$$I_t = I \sin(\omega t + \varphi)$$

Equation 4-21

where φ is a shift in phase.

Using Ohm's equation the electrochemical impedance can be described as:

$$Z = \frac{E_t}{I_t} = \frac{E_0 \sin(\omega t)}{I \sin(\omega t + \varphi)} = Z_0 \frac{\sin(\omega t)}{\sin(\omega t + \varphi)}$$

Equation 4-22

Where Z_0 is the magnitude.

Usually impedance is presented as a complex number:

$$Z(\omega) = Z_0 e^{j\varphi} = Z_0 (\cos \varphi + j \sin \varphi)$$

Equation 4-23

There are two graphical projections of this equation- the Nyquist plot and the Bode plot. The Nyquist plot presents a relation between the imaginary and real parts of Z . Both parts are frequency dependent. The Bode plot presents magnitude (gain) and phase as a function of frequency, usually in a logarithmic scale.

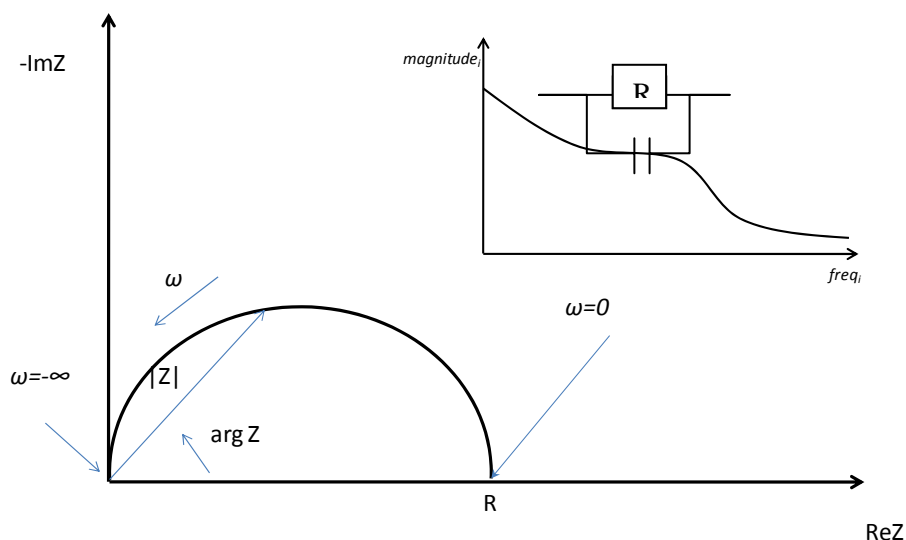


Figure 4-10 Nyquist and Bode plot for a circuit consisting of parallel elements- R and C

Electrochemical impedance data are usually analysed by fitting them to an equivalent circuit. This should be the simplest circuit which describes the electrochemical properties and it is usually build up from linear, passive elements.

The case of self assembled monolayers adsorbed on gold electrodes is more complicated and cannot be described by the equivalent circuit presented above. Wide studies carried out on self assembled monolayers revealed that more complex equivalent circuits need to be used in order to include all processes undergoing in SAMs on gold electrode^{27,28}. Usually a mixed kinetic and charge transfer control model is used. The processes which need to be considered when designing an equivalent circuit are presented in Figure 4-11²⁹.

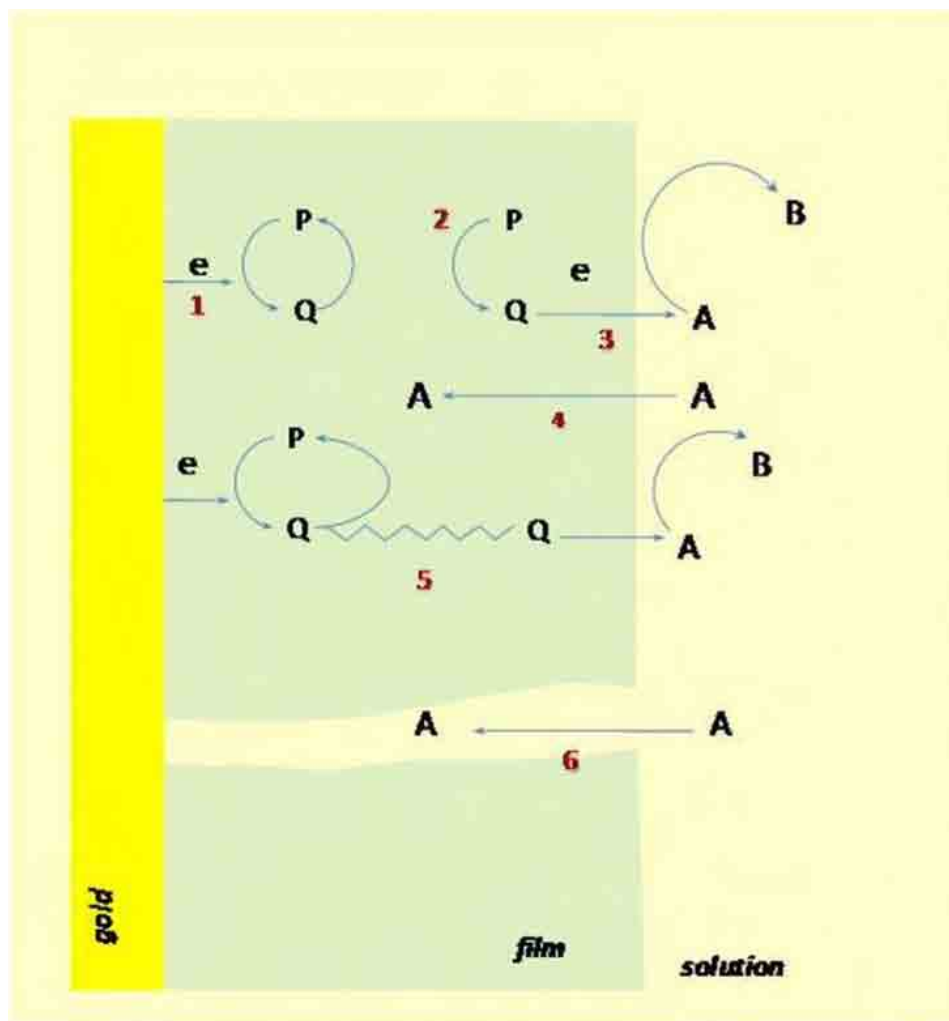


Figure 4-11 A cartoon representation of processes occurring on modified gold electrode²⁹

P and A are reducible substances in the film and the solution. Processes numbered in the figure are follows:

1. Electron transfer undergoing on P to produce Q
2. Electron transfer from P to another species of Q in the film (electron diffusion in the film)
3. Electron transfer from Q to A in the film/solution interface
4. Penetration of A into the film where it can further react with Q at the film/solution interface
5. Movement of Q within the film (mass transfer).
6. Movement of A through a pinhole or channel in the film.

Processes which can occur on a gold electrode modified with SAMs depend on the type of SAM involved. Processes involving electron transfer, mass transfer and electron diffusion need to be taken into consideration when SAM used for modification consist of a redox active species. A SAM formed on the gold surface electrode can be treated as a sol. For that sol- based redox reactions should be taken into consideration when modelling equivalent circuit.

For modelling of experimental data recorded for SAMs used within this study the equivalent circuit presented below has been used:

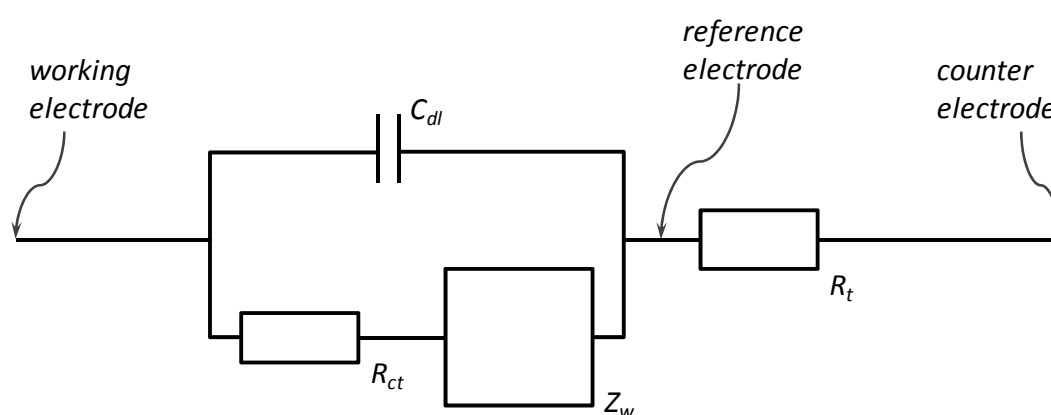


Figure 4-12 The equivalent circuit used for modelling data recorded during SAMs measurements, C_{dl} - double layer capacitance, R_{ct} - charge transfer resistance, Z_w - mass transfer impedance, R_t -solution resistance.

This circuit takes into consideration processes that occur in the whole system- in the electrolyte and on the electrode. In the model C_{dl} stands for double layer capacitance, R_{ct} - charge transfer resistance, Z_w -mass transfer impedance and R_t - solution resistance

4.5.4.2 Cyclic voltammetry

Cyclic voltammetry is a technique in which current response to a swept applied potential is measured, providing information about the mechanism of the cell reaction of interest. The utility of cyclic voltammetry is highly dependent on the analyte being studied. For SAM properties it is complementary technique to EIS^{23,25,26,30}.

4.5.4.2.1 Theory

In cyclic voltammetry the potential of the working electrode is swept from a value E_1 at which A cannot undergo reduction or oxidation to a value E_2 where the electron transfer is driven rapidly. When the potential E_2 is reached the direction of sweep is reversed and the electrode potential is scanned back to the original value E_1 (at which the oxidation of the SAM is complete and the current returns to the charging current, near zero). The electrode potential ramps linearly as shown in Figure 4-13:

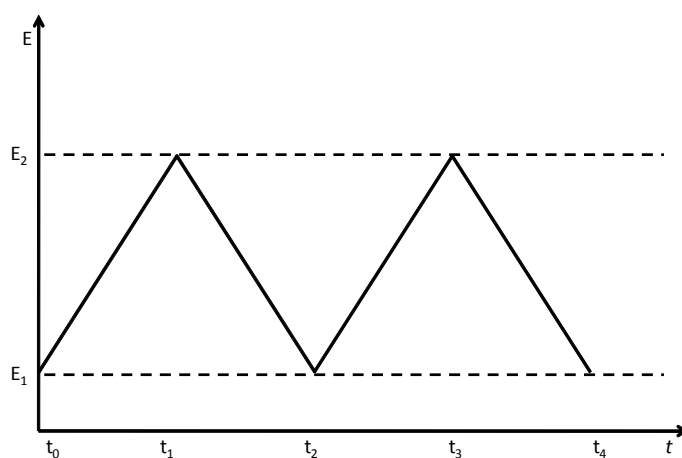


Figure 4-13 Cyclic voltammetry waveform E_1 –initial potential, E_2 - final potential²⁵

A three electrode arrangement is used in which the potential of a working electrode (WE) relative to a reference electrode (RE) is controlled by means of a feedback circuit and a counter electrode (CE). Current flows between the WE and CE so that the current passing through the RE is practically zero. This arrangements ensures that (i) the composition of RE is unaltered and (ii) voltage drop arising from the resistance of the electrolyte solution is minimized.

The shape of cyclic voltammogram depends directly on the scanned analyte (A/B redox couple). An example of a reversible redox process (fast e^- transfer kinetics) is given in the Figure 4-14.

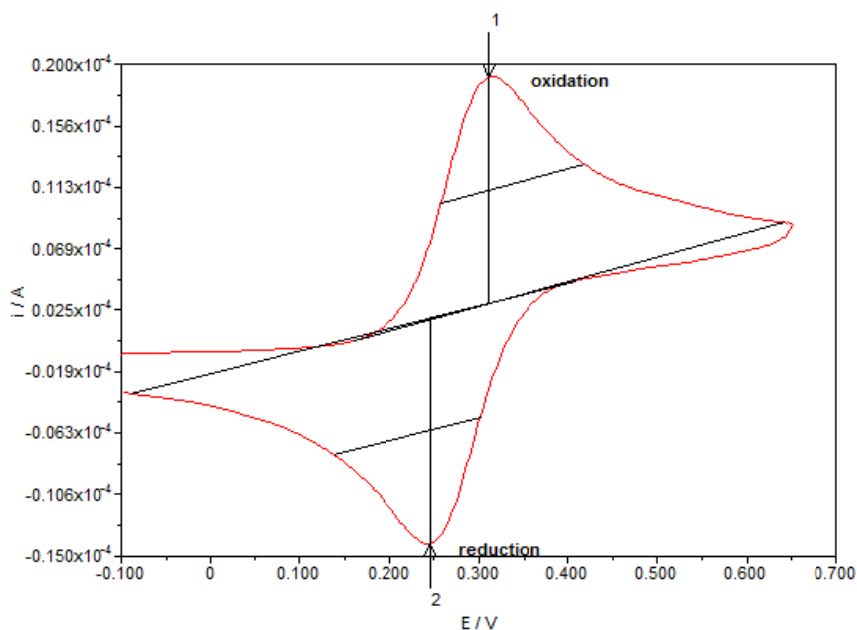


Figure 4-14 Cyclic voltammogram for bare gold electrode in 1 M KCl / 1 mM $K_3Fe(CN)_6$ / 1mM $K_4Fe(CN)_6$ solution.

For study of defects in SAMs the analyte has to be redox active and display fast (reversible) electrode kinetics.

When a process is reversible it means that the concentrations of oxidized and reduced forms at the electrode are maintained at the values required by the Nernst equation and could be characterized by:

- Peak potential separation at all scan rates and a temperature of 25°C:

$$|E_{pox} - E_{pred}| = 2.218 \frac{RT}{nF}$$

Equation 4-24

$$\Delta E E_p = E_{pox} - E_{pred} = 59/n \text{ mV}$$

Equation 4-25

Where ΔE_p is the voltage separation between the current peaks, n is the number of electrons transferred/molecule and F is the Faraday constant.

The position of the peaks is related to the formal potential of the redox process. The formal potential is positioned in between E_{pox} and E_{pred} :

$$E^\circ = \frac{E_{pox} + E_{pred}}{2}$$

Equation 4-26

- Peak current ratio:

$$r = \frac{i_{ox}}{i_{pred}} = 1$$

Equation 4-27

Reversibility depends on kinetics of electron transfer; hence it also depends on the relative values of standard heterogeneous electron transfer rate constant (k_s) and the rate of potential change (the scan rate- n).

When the ratio k_s/n is sufficiently small that the Nernstian concentration cannot be maintained the process is quasi-reversible and $\Delta E_p > 59/n$ mV. A reverse peak on the voltammogram is of similar magnitude to the forward peak but the separation of the two peaks is dependent on the scan rate.

For irreversible processes the individual peaks are reduced in size and widely separated. Irreversible systems are characterized by a shift of the peak potential with the scan rate:

$$E_p = E^\circ - (RT/\alpha nF) \left[0.78 - \ln \left(k_s/D \right)^{1/2} + \ln(\alpha nFv/RT)^{1/2} \right]$$

Equation 4-28

Where: α - is transfer coefficient, n - number of electrons, E° - formal potential, k_s - formal electron transfer rate constant. The overpotential is related to standard rate constant and transfer coefficient. This peak displacement can be compensated by a change of the scan rate. Quasi-reversible and irreversible processes are illustrated in Figure 4-15.

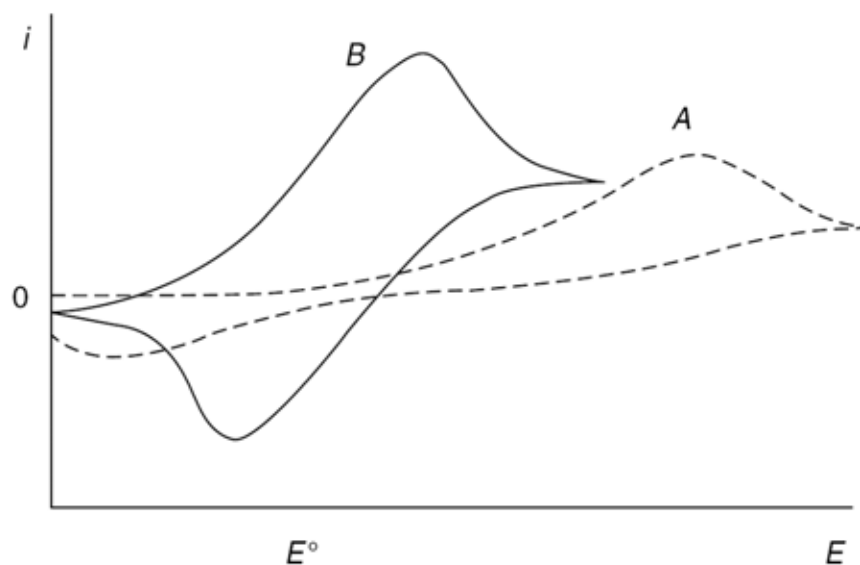


Figure 4-15 Cyclic voltammograms for irreversible (A) and quasi-reversible (B) process

Both methods, electrochemical impedance and cyclic voltammetry, have been employed for investigation of SAM parameters such as surface coverage, pinhole size and distance between pinholes.

4.5.4.3 Electrochemical methods experimental setup

4.5.4.3.1 Instrumentation

The same system was used for both electrochemical impedance and cyclic voltammetry measurements. Experiments were carried out with an AUTOLAB PGSTAT-12 (EcoChemie, Netherlands) and the data processed with FRA 4.9 and GPES 4.9 Autolab software (EcoChemie, Netherlands).

4.5.4.3.2 The electrochemical cell

The cell used for electrochemical measurements is shown in Figure 4-16. The cell body was made of Teflon and the sample placed along a side of the cell was connected to a gold wire using a pressure contact. The reference electrode (standard calomel electrode (Radiometer Analytical)) was placed in a Luggin capillary tube. The counter electrode was a platinum foil (Advent research materials Ltd).

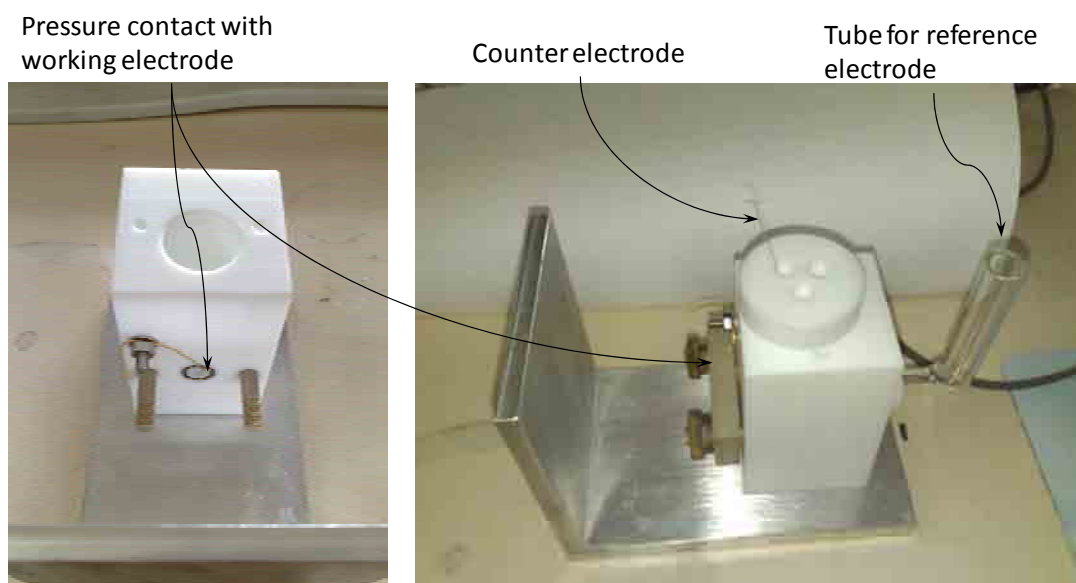


Figure 4-16 The electrochemical cell used for measurements

4.5.4.3.3 Materials

During experiments the following compounds were used:

- potassium chloride KCl- analytical grade,
- $K_3Fe(CN)_6$ Potassium ferricyanide - analytical grade,
- $K_4Fe(CN)_6$ Potassium ferrocyanide - analytical grade .

All electrolytes were purchased from Sigma Aldrich and used with no further purification. For electrolyte solution preparation MQ water (Milli Q) of 18 M Ω cm resistivity was used. Ethyl alcohol for platinum foil and gold connecting wire cleaning was of HPLC grade (Aldrich).

The working electrode was a sample of SAM on gold on glass (substrate for SAM formation prepared as described in 4.1-4.4) connected with a gold wire by a pressure contact. The exposed surface area was 0.2828 cm².

The counter electrode was a platinum foil of the following dimensions: 15 x 20 x 0.05 mm (Advent research materials LTD).

Reference electrode was a standard calomel electrode. All potentials quoted are with respect to this electrode.

The electrochemical cell was cleaned by sonication for 30 min using a 5% solution of DECON. Then the cell was rinsed with ultrapure water (MQ) several times to remove remaining DECON solution, followed by rinsing with HPLC grade ethyl alcohol. The cell was then dried in the oven set at 30°C.

All glassware used for electrochemistry measurements were cleaned following the procedure 4.1

4.5.4.3.4 Electrochemical measurements

Electrochemical impedance studies were performed in a solution of concentrations:

1 mM K₄Fe(CN)₆, 1 mM K₃Fe(CN)₆, 1 M KCL

Before connecting the cell to the potentiostat, N₂ was purged through the cell for at least 30 min. After connecting the cells a cyclic voltammetry sweep was performed in order to determine redox potential. Electrochemical impedance measurements were performed at the redox potential. The impedance data were collected in the frequency range 10⁵-10⁻² Hz (sine wave of 10 mV amplitude was generated to the electrode over the formal potential, which was 0.25 V vs SCE). The steady state of the system was achieved by stabilization for 60 s. Data were processed as described

above using fitting to the equivalent circuit by FRA 4.9 Autolab software. Electrochemistry measurements were carried out at room temperature.

Cyclic voltammetry measurements were performed in solution of concentrations of:

5mM $K_4Fe(CN)_6$, 1 M KCL

As before, the cell was purged with N_2 before connecting the electrodes to the potentiostat. Data were collected at a scan rate of 100 mV s^{-1} and the potential limits were -0.2 V and 0.65 V. Collected data were processed with use of GPES 4.9 Autolab software.

4.6 Methods for determination of crystals chirality

Crystals can have different optical properties, which are related to their structure, number of optical axis and refractive indices³¹. Optically active crystals possessing one refractive index can rotate linearly polarized light, resulting in change of their colour. This phenomenon is used to determine their chirality. Unfortunately, for crystals possessing two or more refractive indices such measurement is impossible. Birefringency obscures the effect of rotation of linearly polarized light, making the measurement difficult and multirefringency of a crystal renders such measurement impossible to conduct. For determination of chirality for birefringent and multirefringent crystals, techniques such as circular dichroism spectrometry must be employed.

4.6.1.1 *Optical microscopy with polarized light*

Polarization of light is widely used in many aspects of optical microscopy. The polarized light microscope is designed to observe and photograph specimens that are visible primarily due to their optically anisotropic character. Anisotropic materials have optical properties that vary with the propagation direction of light passing through them. In this study polarizing light microscopy is used for determination of chiral properties of crystals. To use polarized light as a basis for the method a microscope must be equipped with both a polarizer, positioned in the light path before the specimen, and an analyser (a second polarizer), and placed in the optical pathway between the objective rear aperture and the observation tubes or camera port, as shown in Figure 4-17.

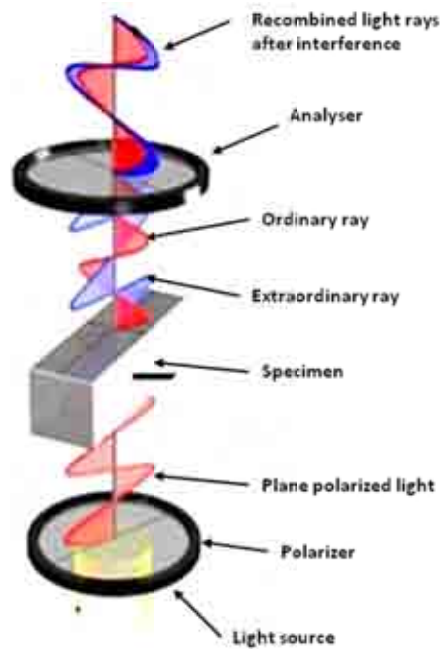


Figure 4-17 The optical layout of polarizer and analyser in optical microscope at transmission³¹

Polarizing light microscopy relies upon crossed polarizers to examine materials possessing birefringent properties or doubly refracting specimens. When two polarizers are crossed, their transmission axes are oriented perpendicular to each other and light passing through the first polarizer is completely extinguished, or absorbed, by the second polarizer, which is typically termed an analyser as it is shown in the Figure 4-18.

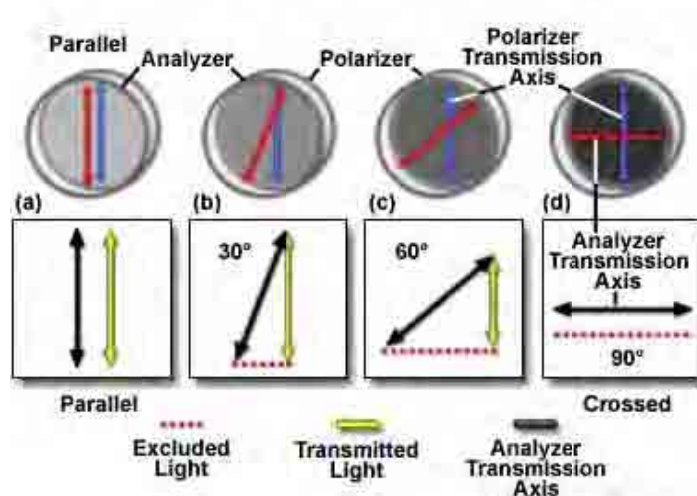


Figure 4-18 Transmission of light through a polarizer and analyzer³¹

The light-absorbing quality of a dichroic polarizing filter determines exactly how much random light is extinguished when the polarizer is utilized in a crossed pair, and is referred to as the extinction factor of the polarizer. Quantitatively, the extinction factor is determined by the ratio of light that is passed by a pair of polarizers when their transmission axes are oriented parallel versus the amount passed when they are positioned perpendicular to each other. In general, extinction factors between 10,000 and 100,000 are required to produce jet-black backgrounds and maximum observable specimen birefringence (and contrast) in polarized optical microscopy.

Image contrast arises from the interaction of plane-polarized light with a birefringent (or doubly-refracting) specimen to produce two individual wave components that are polarized in mutually perpendicular planes. The velocities of these components are different and vary with the propagation direction through the specimen. After exiting the specimen, the light components are out of phase and sweep an elliptical geometry that is perpendicular to the direction of propagation, but are recombined through constructive and destructive interference when they pass through the analyser³². Polarized light microscopy is a contrast-enhancing technique that improves the quality of the image obtained with birefringent materials when compared with other techniques such as dark field and bright field illumination, differential interference contrast, phase contrast, Hoffman modulation contrast, and fluorescence. In addition, use of polarized light allows the measurement of optical properties of minerals and similar materials and can aid in the classification and identification of unknown substances.

Linearly polarized light measurements were conducted with a polarizing light microscope AxioImager1 Zeiss, equipped with camera.

4.6.1.2 Circular dichroism for solid samples

Circular dichroism spectrometry is usually used for determination of chirality of liquid samples such as proteins, peptides and DNA³³⁻³⁵. However, if a sample is introduced to the beam light in a suitable way, it is possible to investigate chirality of solid samples, namely crystals^{36,37}. This fact plays a significant role in this study. Circular dichroism measurements were performed using auxiliary techniques of Nujol Mull and KBr pellet.

4.6.1.2.1 Theory

As introduced in section 4.5.1, light is an electromagnetic wave which can be linearly, elliptically or circularly polarized. This property of light wave gives an opportunity to use it as a basis for spectroscopic techniques.

Optically active samples possess different refractive indices for left and right circularly polarized light, thus the beams travel at a different speeds and are absorbed to different extents at each energy. Circularly polarized light can be produced by superposition of two linearly polarised light beams oscillating perpendicular to each other and propagating with a phase difference $\frac{\pi}{2}$ rad.

When a light ray passes through a sample with a different absorbance A for the two components, the amplitude of the stronger absorbed component will be smaller than that of the less absorbed component. As a consequence, a projection of the resulting amplitude yields an ellipse instead of the usual line (for linearly polarized light) and the polarization direction is not changed. The occurrence of ellipticity is called Circular Dichroism. This is not the same as optical rotation. Rotation of the polarization plane (or the axes of the dichroic ellipse) by a small angle α occurs when the phases for the 2 circular components become different, which requires a difference in the refractive index n . This effect is called circular birefringence. It can be shown that when a CD exists, optical rotation must exist as well, and that they are related by a Kronig- Kramers transformation. The change of optical rotation with wavelength is called optical rotary dispersion (ORD).

When a molecule exhibits a combination of ORD and CD in the region of absorbance, then the transmitted light is said to be elliptically polarized.

The differential extinction for CD effect $\Delta\varepsilon$ is described by the equation³⁵:

$$\Delta\varepsilon = \varepsilon_L - \varepsilon_R$$

Equation 4-29

and is related to the absorbance value by:

$$A = \log_{10} \frac{I_0}{I} = \varepsilon cl$$

$$A_L = \log_{10} \frac{I_0}{I_L}$$

$$A_R = \log_{10} \frac{I_0}{I_R}$$

$$\Delta A = A_L - A_R = \log_{10} \frac{I_R}{I_L}$$

$$\Delta\varepsilon = \frac{1}{cl} \Delta A$$

Equation 4-30

Where ε_L and ε_R is the extinction for left and right circularly polarized light and A_L and A_R is the absorbance.

The final equation does not include the intensity of the incoming light I_0 , which means that the measurement does not require a reference beam. However because the instruments are single-beam type, care is needed to normalise the spectra from the left and right polarized form.

A CD spectrum is a plot of ΔA against wavelength.

Solid samples can be examined with a cd spectrometer by applying two auxiliary techniques: Nujol Mull and KBr pellet. Both of these are widely known as techniques for IR spectroscopy³⁸.

Nujol Mull technique

This technique is based upon suspending a ground sample in small amount of mineral oil. The amount of sample can be very small, even 1.5 mg is sufficient to perform the test. As a holder two plates of NaCl crystal are used.

Nujol Mull procedure:

A solid sample for CD should be a single crystal of a mass not less than 1.5 mg. Too small a ratio of sample to mulling agent will cause no spectra to be observed. Too large a ratio causes scattering and insufficient transmission of light.

Crystals subjected to CD analysis were weighed before performing measurements and ground with an agate mortar and pestle (one at a time) to a powder.

After grinding a sample two drops of mineral oil (Nujol Mull) were added to the powder and mixed with it until a homogenous paste was formed.

The paste was then transferred with a spatula onto the cleaned NaCl plate, spread evenly and covered with the second NaCl plate.

KBr pellet technique

The KBr pellet technique is based on making pellets of a mixture of sample and alkali metal halide. The pellets are not big, usually of 1 cm diameter. The amount of samples needed to conduct analysis is not much: 5 mg of a sample and 200 mg of alkali metal halide.

KBr pellet procedure:

A solid sample of a single crystal was weighed, ground with an agate mortar and pestle and mixed with the clean, dry alkali metal halide (KBr).

After the halide and sample were mixed, the whole powder was pressed in order to form a pellet in a hydraulic press ($\sim 1.5 \times 10^5 \text{ kg m}^{-2}$). The discs must be not too thin and not too thick. Unfortunately, they were fragile and difficult to handle.

Circular dichroism spectrometry measurements were conducted with a Jasco-J810 spectrometer.

4.6.1.3 NSOM with polarized light

A novel approach to investigating the optical properties of crystals was recently presented by the group of Mastai (Bar Ilan, Israel). They constructed a sub-micrometre polarimeter using a near-field scanning optical microscope to control the polarization properties in the near field³⁹. The system is equipped with three detectors to allow concurrent measurements of the surface topography and surface optical properties by gathering signals from reflected and transmitted light.

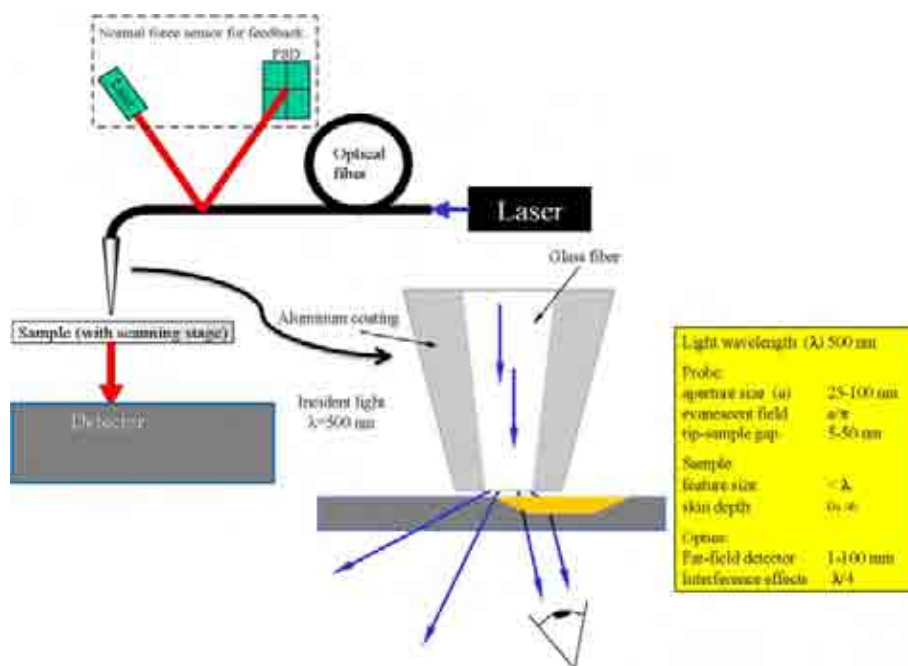


Figure 4-19 NSOM/AFM schematic⁴⁰

A laser source is used as the light source, the light passes through a half-wave plate to the NSOM tip in a polarized state. The resulting linearly polarized light is coupled into a bent single-mode optical fibre. The light emitted from the tip aperture and reflected from the sample is collected by a microscope objective lens through a microscope column equipped with circular (dichroism mode) analyser and a photomultiplier tube.

There are four possible modes of operation with NSOM/SNOM:

- Transmission mode imaging. The sample is illuminated through the probe, and the light passing through the sample is collected and detected.
- Reflection mode imaging. The sample is illuminated through the probe, and the light reflected from the sample surface is collected and detected.
- Collection mode imaging. The sample is illuminated with a macroscopic light source from the top or bottom, and the probe is used to collect the light from the sample surface.
- Illumination/collection mode imaging. The probe is used for both the illumination of the sample and for the collection of the reflected signal.

The instrument used in reflected light mode operates in the way that linearly polarized light comes from the probe aperture vertically to the surface and serves as a light source. After the near-field light interacts with a chiral surface the light scattered and reflected from the surface is collected in the far field. After the light collection, a polarization analyser is used to measure selectively the transverse polarization of collected light. The minimum polarized light emerging from the optical fibre is set as the zero point of polarization of the system. This set up is illustrated in figure 4-20.

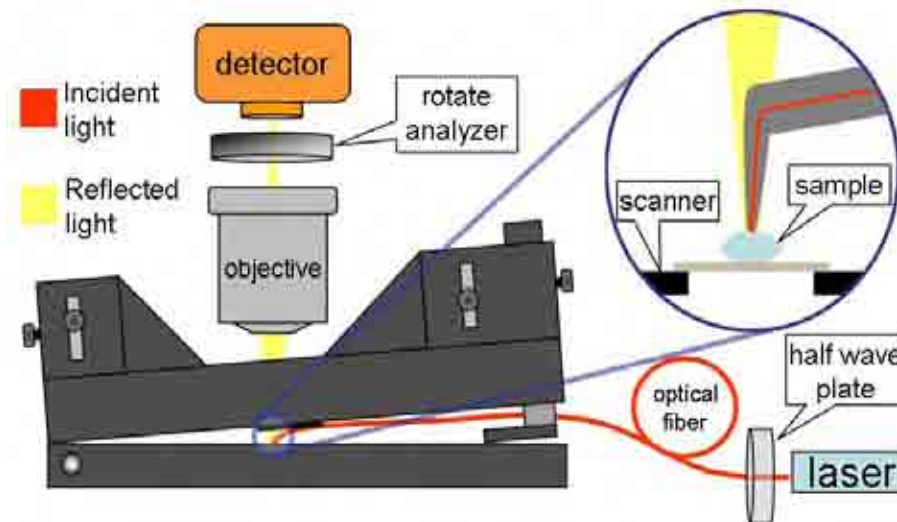


Figure 4-20 NSOM/ AFM in reflected mode⁴⁰.

A laser source (488 nm) was used as the light source. In experiments of determination of chirality NSOM tips of extinction ratios of 1:20 were used. Polarization analyzer is of extinction ratio 6000:1.

4.7 Methods used for chiral recognition at surfaces

4.7.1 Atomic force microscopy

AFM- Atomic Force Microscopy belongs to the SPM (Scanning Probe Microscopy) family of techniques and it provides high resolution surface images. Despite the fact that its development started just in early 1980s, now it is one of the most common techniques used for surface analysis. The invention of STM and AFM gave Binnig and Rohrer a Nobel Prize for Physics in 1986⁴¹.

Atomic force microscopy is based on the existence of separation-dependent forces between two bodies: in this case a sharp tip and a substrate⁴². Typically silicon nitride probes are used. The detection of force is achieved by measuring a deflection of a cantilever upon which the tip is mounted. The deflection is measured using light reflected from the back of the cantilever onto a quadrant photodiode, as shown in Figure4-31. The voltage differences recorded are proportional to the cantilever deflection which is related to the force according to Hooke's law:

$$F = -k\Delta z$$

Equation 4-31

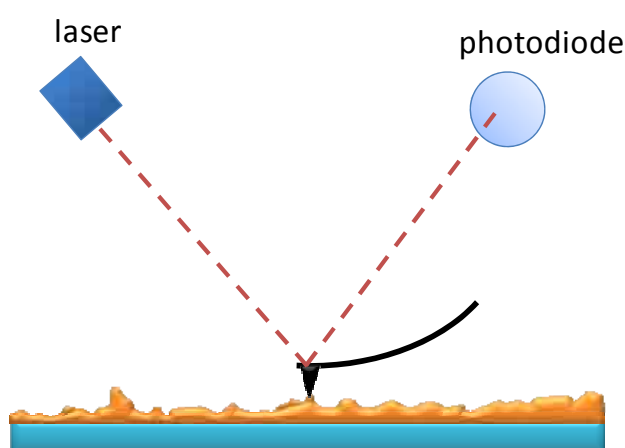


Figure 4-21 Basics of AFM

A feedback mechanism is employed in order to adjust the tip-sample distance so that a constant force between the tip and the sample is maintained. This prevents the tip colliding with the sample. Fine positioning is usually achieved by use of a piezoelectric actuator due to its quick response.

To produce a topography image of the sample the tip is scanned across the sample surface and the vertical displacement s necessary to maintain a constant force on the tip is recorded. The resulting map of $s(x, y)$ represents the topography of the sample.

Atomic force microscopes may be operated in a number of different ways. The most important of them are the contact and non-contact modes.

Contact mode

There are two types of AFM contact modes- constant force and constant height.

Constant force

The feedback loop pre-determines the force between the tip and surface. This mode is usually used for imaging rough samples.

Constant height

This mode operates with the feedback loop switched off. It is used to image very flat surfaces at high resolution for which a very little feedback is needed to compensate thermal drift and unexpected roughness.

Non-contact modes

Non-contact modes are also known as acoustic modes in which the cantilever is externally oscillated close to its resonant frequency. There are two types of non-contact mode: frequency modulation and amplitude modulation and the latter is known as tapping mode or AAC mode.

Frequency modulation

The detection scheme is based on measuring changes to the resonant frequency. The forces between the tip and sample are low, on the order of pN (10^{-12} N).

Amplitude modulation (tapping mode)

In this mode a stiff cantilever is oscillated closer to the sample than in contact mode. Part of the oscillation extends into the repulsive regime, so the tip intermittently touches or “taps” the surface. (Very stiff cantilevers are typically used, as tips can get “stuck” in the water contamination layer.)

Changes in the oscillation amplitude yield information about the sample and phase which can be used to discriminate between different types of materials on the surface. AFM has the advantage of imaging almost any type of surface.

4.7.2 Force- distance spectroscopy

The main application of the atomic force microscope is surface imaging; however the AFM may be used for many other measurements. Force-distance spectroscopy is an AFM mode used to study the interactions between the cantilever and the surface⁴²⁻⁴⁴. In this mode a measurement is performed by approaching and retracting a tip from a surface. During the approach-retract cycle the cantilever deflection is recorded, from which the force between the tip and surface may be measured. A typical approach-retract cycle is depicted in Figure 4-22:

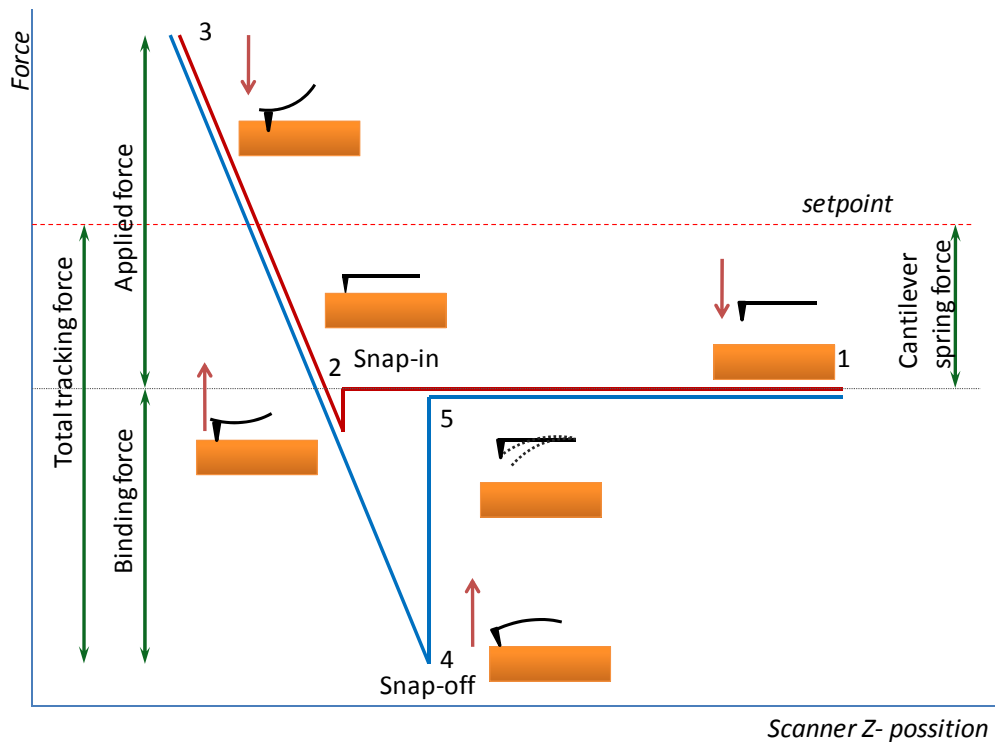


Figure 4-22 Force- distance curve constituents- approaching (red) and retracting (blue) and referring tip positions

At the resting position, the tip is separated from the surface enough not to 'feel' any forces. As the tip approaches the surface it undergoes the attractive forces caused by long- range electrostatic or van der Waals forces. At the point 2 shown in Figure 4-22, the tip jumps into contact with the sample when the surface force exceeds the spring constant of the cantilever. After the snap- in point the force becomes repulsive in nature. The force can be calculated from the Hooke's law (the linear compliance regime). After the direction shift at the max loading force point the cantilever is dragged away from the surface. The deflection at the contact part in approach and retract cycle usually overlays. (Hysteresis in this case may be observed due to the conditions of the measurement.) At the point 5, contact with the sample is broken and the tip jumps back to the resting position. The difference between the snap off and the resting position, the force necessary to separate the tip and the sample is called the adhesive force.

The name – Force-Distance (F-D) Spectroscopy can be slightly misleading since the AFM measures the change in deflection during performing the force-distance cycle hence an additional calculation is needed to determine the binding force. The force can be calculated using the equation:

$$F = InvOLS \cdot k \cdot \Delta z$$

$$InvOLS = \frac{1}{OLS}$$

Equation 4-32

In the above equations *OLS* stands for optical lever sensitivity and it is the slope of the contact part of the force- distance curve, *k*- spring constant and Δz voltage difference.

The features of the F-D curve could be well explained by employing a simple model system in which a parabolic tip is put above a flat sample and both the tip and the sample consist of fixed Lennard-Jones atoms with density ρ .

The interaction between an atom of the tip and an atom from the sample is described by the equation:

$$V(r) = 4\varepsilon \left[\left(\frac{\sigma}{r} \right)^{12} - \left(\frac{\sigma}{r} \right)^6 \right]$$

Equation 4-33

Where ε stands for the depth of the potential well, σ is the distance at which the inter-atoms potential is zero and r is the distance between the atoms. The slope of the curve described by this equation is illustrated in Figure 4-23.

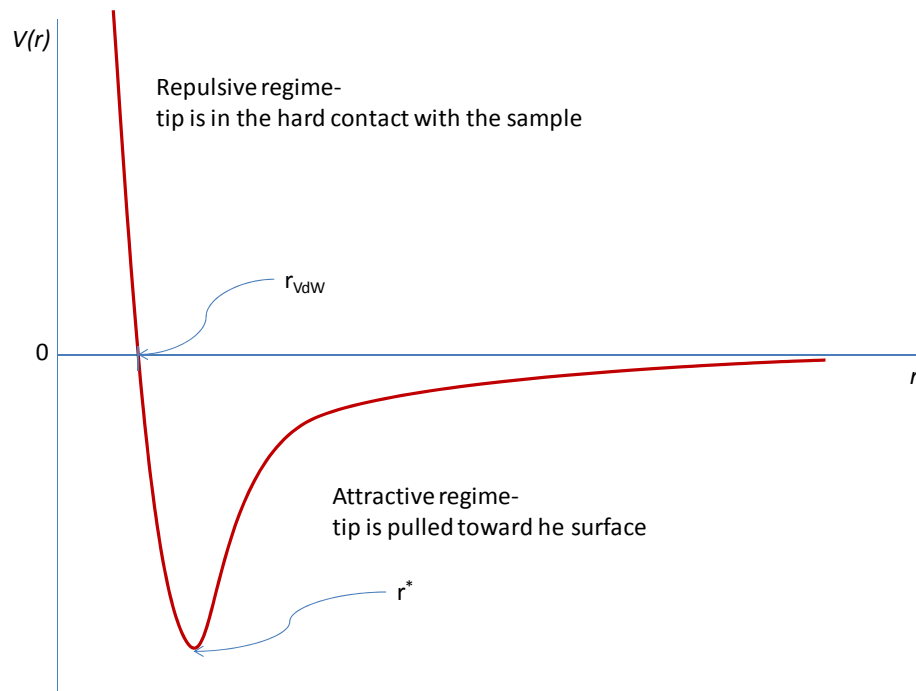


Figure 4-23 The Lennard-Jones interaction potential

The conditions under which the force-distance experiment is conducted, the tip and the sample properties have significant impact on the shape of the F-D curve. Butt and Cappella⁴³ have proposed a comprehensive guide on interpreting force-distance plots with the dependence on the conditions, in which they were recorded. For single molecules interaction studies they suggest conducting experiments in liquid, in order to eliminate the capillary condensation between tip and the sample that leads to large adhesion forces when performing such experiments in the air.

4.7.3 Cantilevers and spring constant determination

There are a large number of different types of AFM cantilevers because each AFM application requires specific cantilever parameters. The spring constant, resonant frequency, length, sharpness and material have an impact on the image quality. For the force-distance spectroscopy the desired properties are: low spring constant, high resonant frequency and a short lever ended with an ultra sharp tip.

Typically, rectangular and V-shaped cantilevers are used and the tips are of conical or pyramidal shape. Some examples are shown in Figures 4-24 and 4-25:

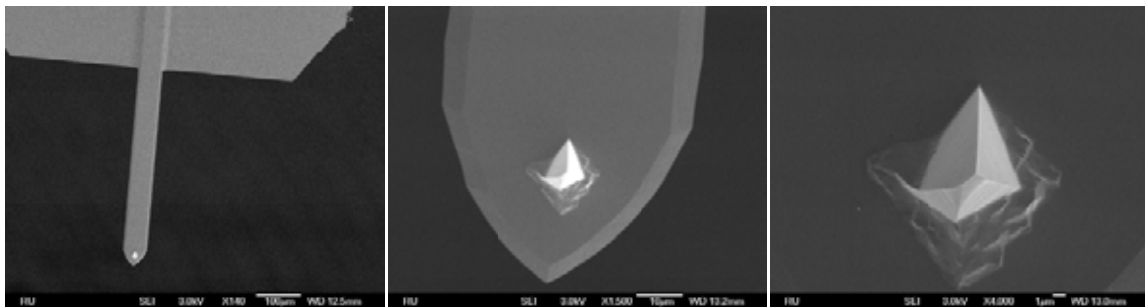


Figure 4-24 SEM images of rectangular cantilever, conical tip

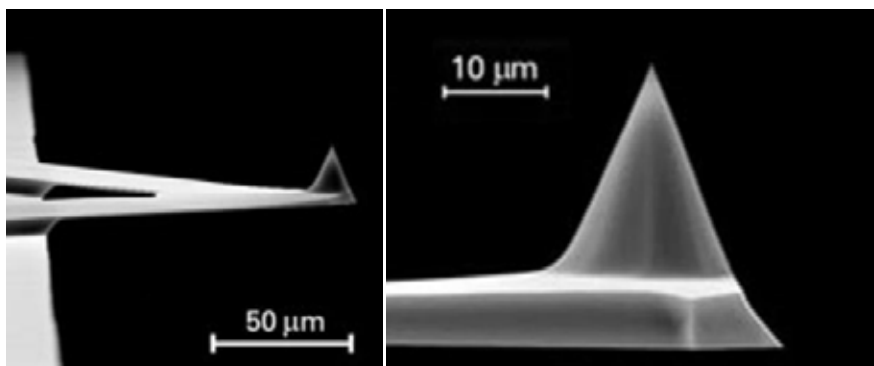


Figure 4-25 SEM images of v- shaped cantilever, conical tip

Force distance spectroscopy can be used to determine single molecule interactions but without knowledge of the cantilever spring constant no quantitative force measurement is possible. AFM cantilevers are produced with a certain tolerance and manufacturers can only give a range of their spring constants, the determination of the accurate values is needed. For this purpose several calibration methods have been proposed⁴⁵⁻⁵¹. The most popular of calibration methods are:

- Dimensional method (Euler's formula)
- Sadler method
- Thermal noise method
- Nanoforce calibrator
- Cantilever on cantilever (COC) method

Since the AFM instrumentation used for this study was equipped with a THERMAL K module (National Instruments), this technique was used for spring constant determination.

Thermal noise method is a non destructive technique in which a cantilever is modelled as a simple harmonic oscillator. Pioneers in use of this technique, Hutter and Bechhoefer⁵², employed the equipartition theorem and related the Brownian motion of the first oscillation mode to its thermal energy by the equation:

$$k = \frac{k_B T}{\langle z_c^2 \rangle}$$

Equation 4-34

Where k_B represents the Boltzman constant, T is the absolute temperature and $\langle z_c^2 \rangle$ is the mean square displacement of the cantilever. In this study the $\langle z_c^2 \rangle$ parameter is obtained by performing a power spectral density analysis of cantilever oscillations and integrating the area under the peak of the first oscillating mode. An example of a power spectra density plot is given in Figure 4-26.

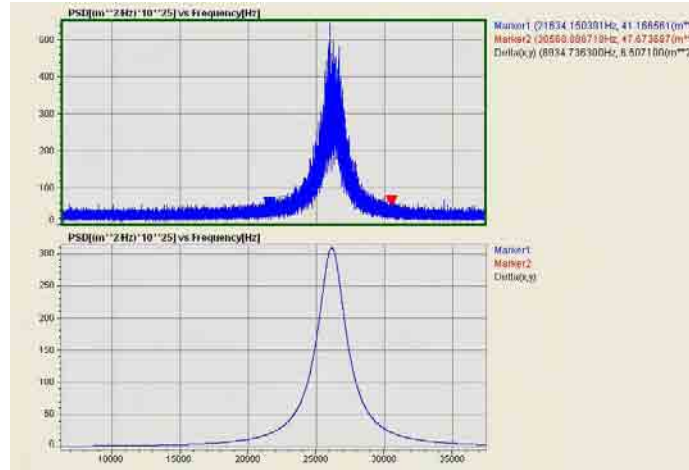


Figure 4-26 Power Spectral Density plot and its Gaussian fitting

The equation above needs to be corrected according to the shape of the cantilever. For rectangular cantilevers Hutter⁵³ proposes the equation:

$$k = 0.817 \frac{k_B T}{\langle z_c^{*2} \rangle} \cos^2 \theta$$

Equation 4-35

Where $\langle z_c^{*2} \rangle$ is the 'virtual' cantilever displacement (the displacement as measured by the optical lever scheme) contributed to by only the first mode of oscillation and θ is the angle that a cantilever is mounted at.

For V-shaped cantilevers Stark and co workers⁵⁴ propose to treat the cantilever by modelling it as a multiple-degree-of freedom system. $\langle S^2 \rangle_j$ – the photodiode signal of the N - oscillator cantilever at node j may be calculated from the equation:

$$\langle S^2 \rangle_j = \sum_{n=1}^N \langle u_n^2 \rangle_j$$

Equation 4-36

Where $\langle u_n^2 \rangle_j$ is the mean square of the cantilever deflection. The results obtained with use of this method indicate that there is a systematic deviation in the thermomechanical noise of V-shaped

cantilevers as compared to rectangular cantilevers. The authors concluded that if a fast and non-destructive calibration for V-shaped cantilever is needed, a numerical finite element analysis of the cantilever geometry to be calibrated is required.

All force-distance experiments were performed on Pico Plus 5500 Atomic Force Microscope, Agilent Technologies, equipped with Thermal K module, National Instruments.

4.8 Reference List

1. Lassef, B.; Karthzuser, S.; Haselier, H.; Waser, R. The origin of faceting of ultraflat gold films epitaxially grown on mica. *Applied Surface Science* **2005**, *249* (1-4), 197-202.
2. Nogues, C.; Wanunu, M. A rapid approach to reproducible, atomically flat gold films on mica. *Surface Science* **2004**, *573* (3), L383-L389.
3. Sobotok, P.; Ostfdal, I. Temperature induced change of surface roughness of Au(111) epitaxial films on mica. *Journal of Crystal Growth* **1999**, *197* (4), 955-962.
4. Liu, Z. H.; Brown, N. M. D. Studies using AFM and STM of the correlated effects of the deposition parameters on the topography of gold on mica. *Thin Solid Films* **1997**, *300* (1-2), 84-94.
5. DeRose, J. A.; Thundat, T.; Nagahara, L. A.; Lindsay, S. M. Gold grown epitaxially on mica: conditions for large area flat faces. *Surface Science* **1991**, *256* (1-2), 102-108.
6. Putnam, A.; Blackford, B. L.; Jericho, M. H.; Watanabe, M. O. Surface topography study of gold deposited on mica using scanning tunneling microscopy: Effect of mica temperature. *Surface Science Letters* **1989**, *217* (1-2), A366.
7. Chidsey, C. E. D.; Loiacono, D. N.; Sleanor, T.; Nakahara, S. STM study of the surface morphology of gold on mica. *Surface Science* **1988**, *200* (1), 45-66.
8. Allpress, J. G.; Sanders, J. V. The structure and orientation of crystals in deposits of metals on mica. *Surface Science* **1967**, *7* (1), 1-25.
9. Hayashi, T.; Wakamatsu, K.; Ito, E.; Hara, M. Effect of Steric Hindrance on Desorption Processes of Alkanethiols on Au(111). *The Journal of Physical Chemistry C* **2009**, *113* (43), 18795-18799.
10. Azzam, R. M.; Bashara, N. M. *Ellipsometry and polarised light*; North-Holland Pub. Co.: 1977.
11. Neal, W. E.; Fane, R. W. Ellipsometry and its applications to surface examination. *Journal of Physics E. Scientific instruments*. **2010**, *6*, 409-416.

12. Tompkins, H. G. *A user guide to ellipsometry*; Academic Press: 1993.
13. Rossow, W.; Richter, W. Optical characterization of epitaxial semiconductor layers. Buer, G., Richter, W., Eds.; Springer: 1996.
14. Keddie, J. L. Structural analysis of organic interfacial layers by ellipsometry. *Current opinion in Colloid and Interface Science* **2001**, *6*, 102-110.
15. Horiba Scientific Internet Communication 2008.
16. Adamson, A. W. *Physical chemistry of surfaces*; Wiley: 1990.
17. Istaelachvili, J. *Intermolecular and surface forces.*; Academic Press, London: 1992.
18. Mittal, K. L. *Contact Angle, Wettability and Adhesion*; VSP, Utrecht: 2006; Vol. 4.
19. Whitesides, G. M.; Laibinis, P. E. Wet chemical approaches to the characterization of organic surfaces: self-assembled monolayers, wetting, and the physical-organic chemistry of the solid-liquid interface. *Langmuir* **1990**, *6* (1), 87-96.
20. Leitch, J.; Kunze, J.; Goddard, J. D.; Schwan, A. L.; Faragher, R. J.; Naumann, R.; Knoll, W.; Dutcher, J. R.; Lipkowski, J. In Situ PM-IRRAS Studies of an Archaea Analogue Thiolipid Assembled on a Au(111) Electrode Surface. *Langmuir* **2009**, *25* (17), 10354-10363.
21. Zamlynny, V.; Lipkowski, J. Quantitative SNIFTIRS and PM IRRAS of Organic Molecules at Electrode Surfaces. In *Advances in Electrochemical Science and Engineering. Diffraction and spectroscopic methods in electrochemistry.*, Alkirie, R. C., Kolb, D. M., Lipkowski, J., Ross, Ph. N., Eds.; Wiley-VCH: Weinheim, 2006; pp 315-374.
22. Tolstoy, V. P.; Chernyshova, I. V.; Skryshevsky, V. A. Absorption and Reflection of Infrared Radiation by Ultrathin Films. In *Handbook of Infrared Spectroscopy of Ultrathin Films*, Wiley: 2003.
23. Donovan-Merkert, B. T. *Electroanalytical Chemistry.*; Marcel Dekker Inc.: New York, 1966; Vol. 19.
24. Orazem, M. E.; Tribollet, B. *Electrochemical Impedance Spectroscopy*; Wiley: 2008.
25. Balzani, V. *Electron Transfer in Chemistry*; Wiley: 2008.
26. Saveant, J. M. Single Electron Transfer at an Electrode. In *Elements of Molecular and Biomolecular Electrochemistry*, Wiley: 6006.
27. Porter, M. D.; Bright, T. B.; Allara, D. L.; Chidsey, C. E. D. Spontaneously organized molecular assemblies. 4. Structural characterization of n-alkyl thiol monolayers on gold by optical ellipsometry, infrared spectroscopy, and electrochemistry. *Journal of the American Chemical Society* **1987**, *109* (12), 3559-3568.
28. Xing, Y. F.; O'Shea, S. J.; Li, S. F. Y. Electron transfer kinetics across a dodecanethiol monolayer self assembled on gold. *Journal of Electroanalytical Chemistry* **2003**, *542*, 7-11.
29. Seneviratne, V. PhD thesis Frictional Force Microscopy Studies on Mixed Self Assembled Monolayers. 2006.

30. Fisher, A. C. *Electrode Dynamics*; Oxford University Press: 8996.
31. <http://www.microscopyu.com/articles/polarized/polarizedintro.html>. Internet Communication 2010.
32. Wahlstrom, E. E. *Optical crystallography*; 5 ed.; Wiley: 1979.
33. Purdie, N.; Swallows, K. A.; Murphy, L. H.; Purdie, R. B. Circular dichroism -- II. Analytical applications. *TrAC Trends in Analytical Chemistry* **1990**, *9* (4), 136-142.
34. Purdie, N.; Swallows, K. A.; Murphy, L. H.; Purdie, R. B. Analytical applications of circular dichroism. *Journal of Pharmaceutical and Biomedical Analysis* **1989**, *7* (12), 1519-1526.
35. Purdie, N.; Swallows, K. A. Circular dichroism -- I. Theory and practice. *TrAC Trends in Analytical Chemistry* **1990**, *9* (3), 94-97.
36. Matsuura, T.; Koshima, H. Introduction to chiral crystallization of achiral organic compounds spontaneous generation of chirality. *Journal of Photochemistry and Photobiology C-Photochemistry Reviews* **2005**, *6* (1), 7-24.
37. Koshima, H.; Ding, K. L.; Chisaka, Y.; Matsuura, T. Generation of chirality in a two-component molecular crystal of acridine and diphenylacetic acid and its absolute asymmetric photodecarboxylating condensation. *Journal of the American Chemical Society* **1996**, *118* (48), 12059-12065.
38. Stuart, B. H. Experimental methods. Solids. In *Infrared Spectroscopy: Fundamentals and Applications*, Wiley Inter Science: 2004.
39. Mastai, Y. Enantioselective crystallization on nanochiral surfaces. *Chemical Society Reviews* **2009**, *38* (3), 772-780.
40. Mastai, Yitzhak 2008, personal communication.
41. Binnig, G.; Quate, C. F.; Gerber, C. Atomic Force Microscope. *Physical Review Letters* **1986**, *56* (9), 930-933.
42. Johnson, D.; Hilal, N.; Bowen, W. R. Basic Principles of Atomic Force Microscopy. In *Atomic Force Microscopy in Process Engineering*, Butterworth-Heinemann: Oxford, 2009; pp 1-30.
43. Butt, H. J.; Cappella, B.; Kappl, M. Force measurements with the atomic force microscope: Technique, interpretation and applications. *Surface Science Reports* **2005**, *59* (1-6), 1-152.
44. Capella, B.; Baschieri, P.; Frediani, C.; Miccoli, P.; Ascoli, C. Force-distance curves by AFM - A powerful technique for studying surface interactions. *Ieee Engineering in Medicine and Biology Magazine* **1997**, *16* (2), 58-65.
45. Hahner, G. Normal spring constants of cantilever plates for different load distributions and static deflection with applications to atomic force microscopy. *Journal of Applied Physics* **2008**, *104* (8).

46. Choi, D.; Hwang, W.; Yoon, E. Improved lateral force calibration based on the angle conversion factor in atomic force microscopy. *Journal of Microscopy-Oxford* **2007**, *228*, 190-199.
47. Mendels, D. A.; Lowe, M.; Cuenat, A.; Cain, M. G.; Vallejo, E.; Ellis, D.; Mendels, F. Dynamic properties of AFM cantilevers and the calibration of their spring constants. *Journal of Micromechanics and Microengineering* **2006**, *16* (8), 1720-1733.
48. Clifford, C. A.; Seah, M. P. The determination of atomic force microscope cantilever spring constants via dimensional methods for nanomechanical analysis. *Nanotechnology* **2005**, *16* (9), 1666-1680.
49. Bogdanovic, G.; Meurk, A.; Rutland, M. W. Tip friction - torsional spring constant determination. *Colloids and Surfaces B-Biointerfaces* **2000**, *19* (4), 397-405.
50. Sader, J. E.; Larson, I.; Mulvaney, P.; White, L. R. Method for the Calibration of Atomic-Force Microscope Cantilevers. *Review of Scientific Instruments* **1995**, *66* (7), 3789-3798.
51. Senden, T. J.; Ducker, W. A. Experimental-Determination of Spring Constants in Atomic-Force Microscopy. *Langmuir* **1994**, *10* (4), 1003-1004.
52. Hutter, J. L.; Bechhoefer, J. Calibration of Atomic-Force Microscope Tips. *Review of Scientific Instruments* **1993**, *64* (7), 1868-1873.
53. Hutter, J. L. Comment on Tilt of Atomic Force Microscope Cantilevers: Effect on Spring Constant and Adhesion Measurements. *Langmuir* **2005**, *21* (6), 2630-2632.
54. Stark, R. W.; Drobek, T.; Heckl, W. M. Thermomechanical noise of a free v-shaped cantilever for atomic-force microscopy. *Ultramicroscopy* **2001**, *86* (1-2), 207-215.

5 Characterization of self-assembled monolayers used in Project 01 and 02

All surfaces used in the study were prepared and characterized according to Table 5-1. The abbreviations are described when first used in the text below.

Table 5-1 Self Assembled Monolayers used in the projects

Project 1	Project 2		
<i>One-step preparation</i>	<i>One-step preparation</i>	<i>One step preparation-linkers</i>	<i>Two-steps preparation linkers modified via click chemistry</i>
DDT(1)	DDT(1)	Linker A(5)	linkerA-AlaAlaDL(5A)
			linkerA-AlaAlaLL(5B)
MDA(2)	MDA(2)		linkerA-GluL(5C)
			linkerA-HA(5D)
Cysteine D	Cysteine D	Linker B(6)	linkerC-AlaAlaDL(6A)
			linkerB-AlaAlaLL(6B)
Cysteine L	Cysteine L	Linker C(7)	linkerC-AlaAlaDL(7A)
			linkerC-AlaAlaLL(7B)

All prepared monolayers were characterized by using ellipsometry, PM-IRRAS, EIS, cyclic voltammetry and the contact the angle technique. Because of the fact that surfaces subjected to adhesion measurements had to be very clean, all of the characterization was done after measurement of adhesion forces.

Due to the limitations of ellipsometry, measurements could be affected by several factors leading to inaccurate values of the thickness. First, the optical parameters for the gold substrate and adsorbed monolayer are difficult to determine. In this study a refractive index of 1.45 was used. In

previous studies¹, however, it was shown that a change from 1.45 to 1.47 in refractive index value results in drop of observed thicknesses of *ca.* 2.5%. Moreover, in almost all cases it is not possible to obtain the true optical response of a bare, not modified with SAM, gold surface, unless the measurement is conducted in ultra high vacuum. Soon after the gold substrate is taken out from the evaporation chamber it is exposed to contaminations from air (CO₂, H₂O, O₂). These contaminations affect the kinetics of SAM formation and are displaced during SAM adsorption. It is the case that when the thickness is measured –a monolayer of some sort is already adsorbed onto 'a bare gold'. That means the optical constants of it are not properly determined and the measured thickness is lower than the calculated².

The main aim of this part of the study is to determine the SAMs' composition and to detect their change during modification. All ellipsometry measurements are affected by the same error, which means that it does not prevent the observation of a change of the functionality 'click' in the monolayer thickness.

Electrochemical methods have been widely used to determine SAMs' composition since Porter's¹ and Chidsey's³ pioneering studies. In this study EIS and cyclic voltammetry were used to study stability and composition of formed SAMs as well as stability of their modification. EIS measurements give an opportunity to determine specific capacitance of monolayers, although as described in Chapter 4.5.4, this technique is model-dependent. Models used for specific capacitance calculations are described in detail in section 4.5.4.1.

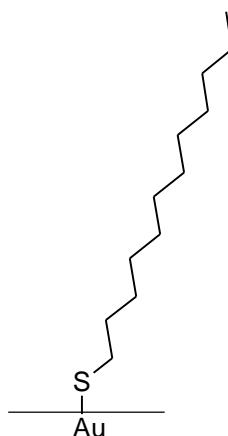
Infrared reflection absorption spectroscopy gives comprehensive knowledge on SAM structure. This technique allows qualitative and quantitative analysis. Since we were focused on observation of 'clicking functionalities' on linkers, this technique gave unambiguous proof of surface modification and its structure. PM-IRRAS measurements were done by setting the PEM to a specific wavenumber; the tests were performed for all characteristic regions: 1200, 1600, 2100, 2900, and 3500 cm⁻¹.

Contact angle microscopy was used to determine wetting properties of the produced monolayers. By performing contact angle measurements it is possible to detect changes in SAM properties, thus this technique was used in studies of SAMs' modification⁴⁻⁶.

5.1 Characterization of monolayers formed in one-step preparation

5.1.1 DDT (1)

A schematic representation of the DDT monolayer formed by dodecanethiol adsorbed on gold is presented below:



Gold surfaces modified with DDT were prepared according to the procedure presented in section 4.4.

PM-IRRAS measurements revealed the most characteristic peaks at 2900 cm^{-1} as the molecules do not possess any other functional groups. Figure 5-1 presents all characteristic bands of a monolayer of crystalline and all-*trans* chain structure⁷.

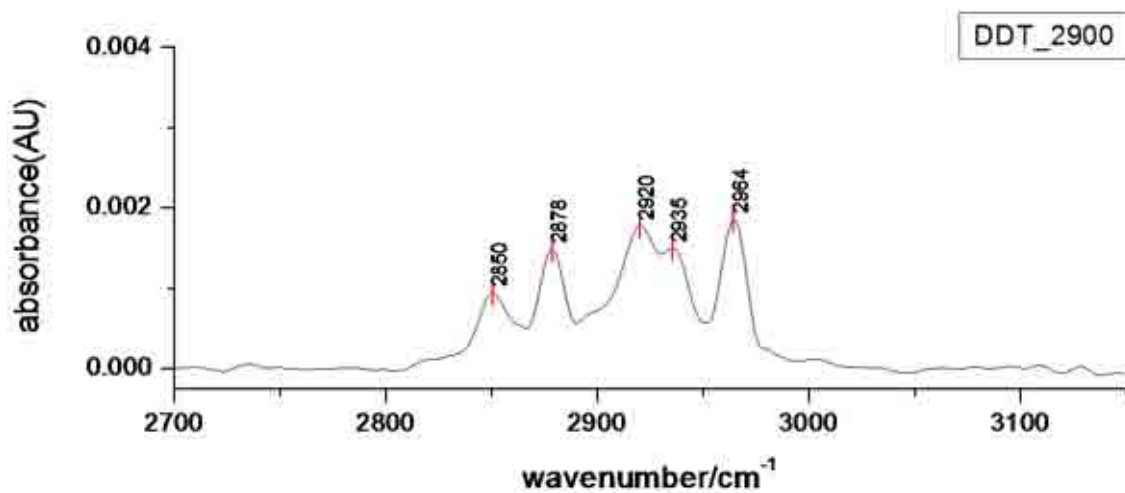


Figure 5-1 PM IRRAS spectra of the DDT monolayer adsorbed on gold – 2900 cm^{-1} region

Characteristic vibration bands for the DDT monolayer visible in the spectra and consistent with data published previously by Finot⁸ and Porter¹ are presented in Table 5-2:

Table 5-2 Characteristic vibration bands for the DDT monolayer on gold

Vibration type	Wavenumber/ cm^{-1}
$\nu_a(\text{CH}_3)$	2964
Γ_{FR}^+ (Fermi resonance)	2935
$\nu_a(\text{CH}_2)$	2920
$\nu_s(\text{CH}_3)$	2878
$\nu_s(\text{CH}_2)$	2850

Ellipsometry measurements of the monolayer thickness, displayed in Figure 5-2, gave the result of 2.2 ± 0.2 nm which is consistent with experimental data published by Porter¹ and Chidsey³.

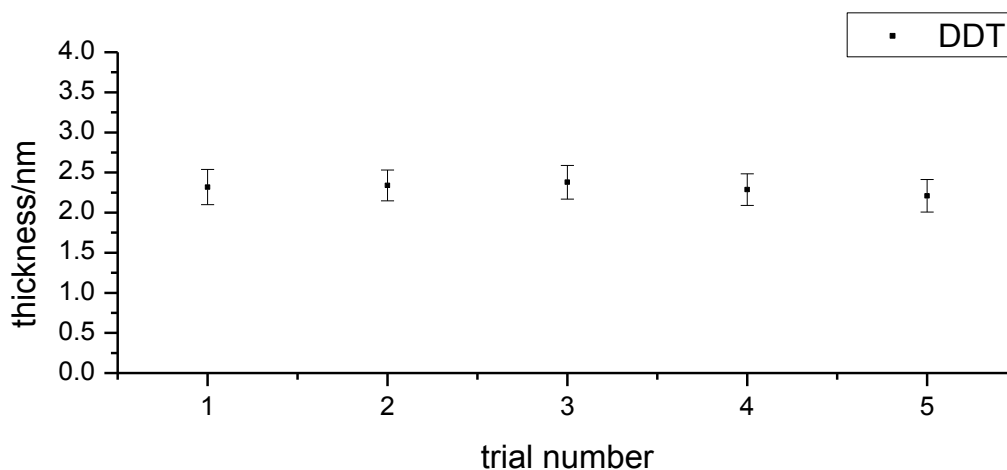


Figure 5-2 Ellipsometry measurements for DDT monolayer

Cyclic voltammetry showed the typical shape for a dense monolayer adsorbed on the gold electrode. In Figure 5-3, a typical shape of cyclic voltammogram for a DDT monolayer assembled over 24 h is presented. It shows clearly that a DDT monolayer adsorbed on gold blocks the diffusion of ferricyanide to the electrode surface. For bare gold there are characteristic peaks (corresponding to the diffusion-controlled reaction) observed. The DDT monolayer insulates the electrode surface from the electrolyte, thus blocks the diffusion and slows electron transfer (reducing the peaks). The more densely packed the monolayer, the more the peaks disappeared.

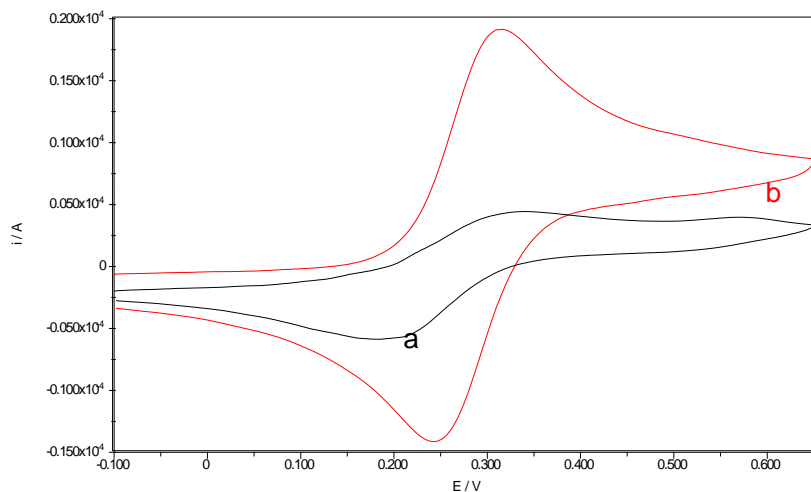


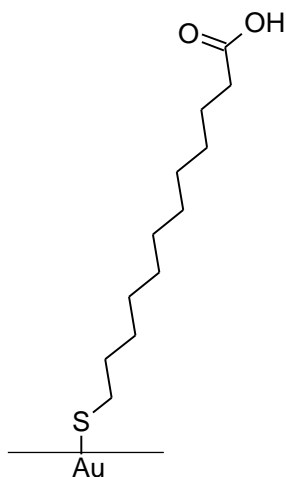
Figure 5-3 Cyclic voltammogram of (a) DDT monolayer adsorbed on gold surface, assembly time 24h, electrode area $A=2.828 \text{ cm}^2$, electrolyte : 1 mM $\text{K}_4\text{Fe}(\text{CN})_6$, 1 mM $\text{K}_3\text{Fe}(\text{CN})_6$, 1 M KCl, scan rate 100 mV s^{-1} , (b) bare gold surface.

EIS data resulted with the average value of specific capacitance $C_{spec}=1.06 \pm 0.06 \text{ } \mu\text{F cm}^{-2}$ (calculated for specific area $A=2.828 \text{ cm}^2$), similar to the values obtained by Porter¹ and Seneviratne⁹. Values of specific capacitance depend in majority on the roughness of gold surfaces used for measurements, thus it is not possible to obtain the same values for two different batches of gold.

Contact angle measurements confirmed the hydrophobic properties of the monolayer and the contact angle was found to be $108 \pm 2^\circ$.

5.1.2 MDA (2)

A schematic projection of the MDA monolayer formed by 12-mercaptoundecanoic acid adsorbed on gold is presented below:



PM-IRRAS prominent peaks of a MDA monolayer adsorbed on gold are presented in Figure 5-4.

The spectra showed the presence of characteristic bands corresponding to the presence of the COOH group and the hydrocarbon chain. In the case of carboxylic acid it is usually the case to observe a broad peak in 1600 cm^{-1} region as the peaks coming from different vibrations are overlapping^{10,11}. In the spectra presented in Figure 5-4 there is a peak of a methyl vibration present, which comes from the residual solvent in the MDA stock.

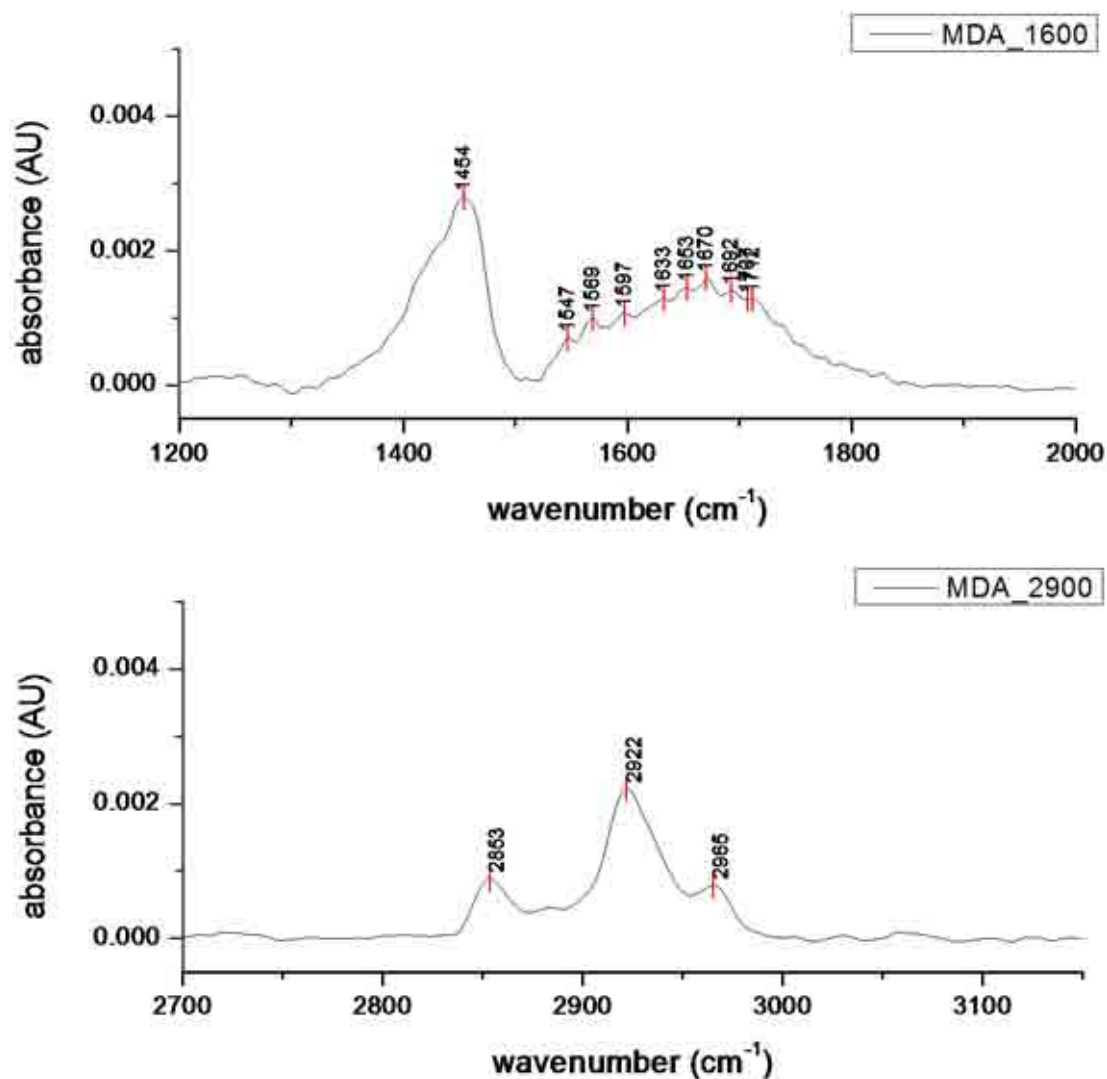


Figure 5-4 PM IRRAS spectra of MDA adsorbed on gold

Characteristic vibration bands are presented in Table 5-3¹²:

Table 5-3 Characteristic vibration bands for MDA monolayer on gold

Vibration type	Wavenumber/cm ⁻¹
$\nu_a(\text{COO}^-)$, $\nu_{\text{def}}(\text{CH}_2)$	1454
$\nu_s(\text{C=O})$	1670
$\nu_s(\text{C=O})$	1740
$\nu_a(\text{CH}_3)$	2965
$\nu_a(\text{CH}_2)$	2922
$\nu_s(\text{CH}_2)$	2853

Ellipsometry measurements carried out on the MDA modified surface showed that the thickness of the monolayer is *ca.* 1.4 ± 0.2 nm. Those results are presented in Figure 5-5.

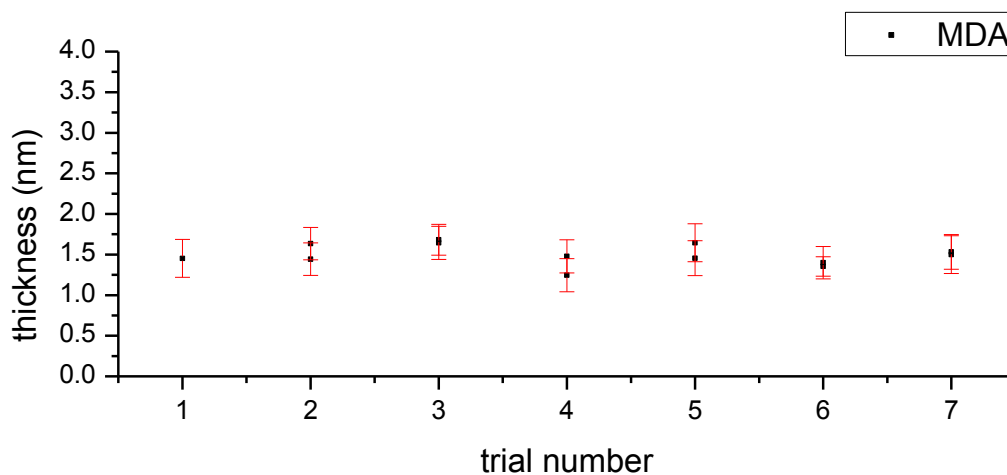


Figure 5-5 Ellipsometry measurements of MDA adsorbed on a gold surface

Electrochemistry measurements confirmed formation of the MDA monolayers on the gold surface. A typical cyclic voltammogram is presented in Figure 5.6.

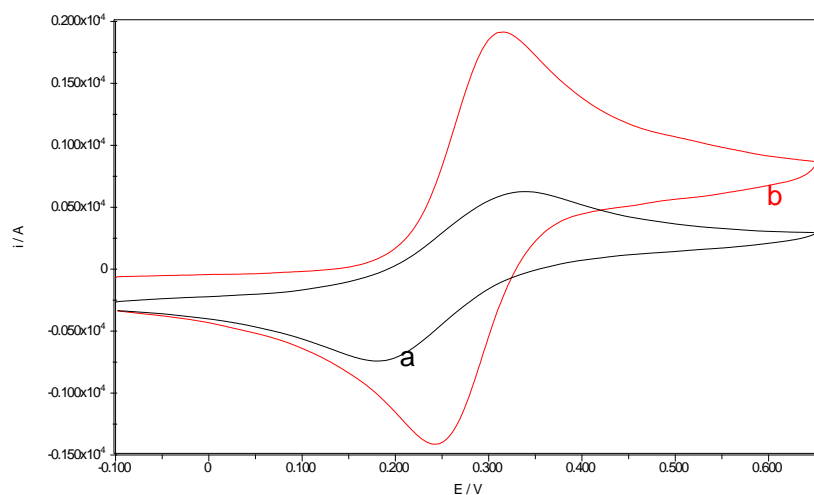


Figure 5-6 Cyclic voltammetry of (a) MDA monolayer adsorbed on gold, assembly time 24 h (b) bare gold electrode, scan rate 100 mV s^{-1}

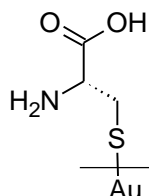
Carboxyl- terminated SAMs are known to behave differently in electrolytes of different pH according to the charge of the COOH groups. They could be present in protonated (carboxylic acid) form or deprotonated (carboxylate)¹³. It has tremendous influence on the order of the formed monolayer. In the case of MDA, the length of carbon chain makes the molecule to be more 'packed' on the surface and, as was found by Molinero¹⁴, the influence of the electrolyte pH vanishes. In comparison to the DDT monolayer, the COOH terminated surface has slightly higher peaks on CV which is a result of a functional group presence, less monolayer density thus slightly less blocking properties.

EIS measurements revealed that the average specific capacitance of MDA monolayers on gold is $1.2 \pm 0.4 \mu\text{F cm}^{-2}$. The obtained average value is more than for the corresponding SAM without the functional group and was expected as introduction of any surface functionality reduces monolayer order and makes the monolayer less dense¹⁵.

The contact angle measurements confirmed hydrophilic properties. The contact angle was found to be $44 \pm 1^\circ$.

5.1.3 Cysteine L (3)

A schematic projection of a monolayer formed by cysteine L adsorbed on gold is presented below:



PM-IRRAS

Figure 5-7 presents PM-IRRAS spectra of L-cysteine on gold. It was observed that cysteines adsorbed on gold showed peaks in the region of 1600 cm^{-1} , which indicates that the monolayer might formed in the zwitterionic form. A similar situation was also observed by Shin¹⁶. The spectra obtained for the rest of the characteristic bands are consistent with the data published by Ihs¹⁷. It has also been found that the form of gold has an impact of the cysteine's ability to adsorb on its surface. Gold (110) exhibits higher adsorption efficiency than gold (111) because its structure is more 'open'¹⁸.

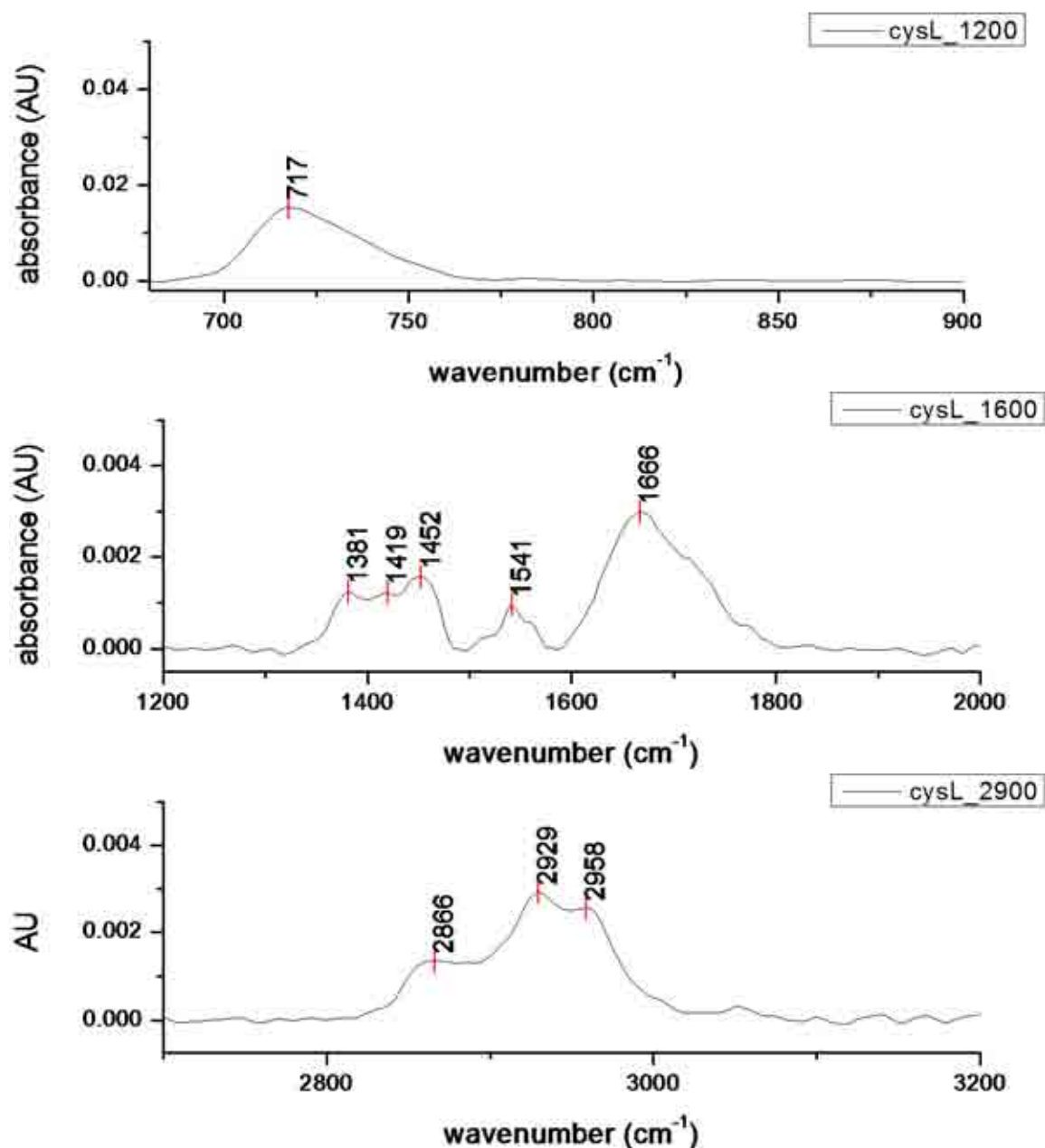


Figure 5-7 PM IRRAS spectra of cysteine L adsorbed on gold

The characteristic bands are assigned in Table 5-4^{7,12,19-21}:

Table 5-4 characteristic vibrational bands for L-cysteine adsorbed on gold

Vibration type	Wavenumber/cm ⁻¹	Vibration type	Wavenumber/cm ⁻¹
$\nu_s(\text{C-S})$	717	$\nu_{\text{def asym}}(\text{NH}_3^+)$	1666
$\nu_s(\text{C=O})$	1381	$\nu_s(\text{C=O})$	~1700
$\nu_{\text{def}}(\text{CH})$	1381	$\nu_s(\text{CH}_2)$	2866
$\nu_s(\text{COO}^-)$	1419	$\nu_a(\text{CH}_2)$	2929
$\nu_{\text{def sym}}(\text{NH}_3^+)$	1541	$\nu_a(\text{CH}_3)$	2958

In the spectra there are 5 characteristic regions for the molecule of cysteine adsorbed on gold, first in region of 717 cm^{-1} , characteristic for carbon- sulphur bond, second between 1300 and 1500 cm^{-1} , where in the broad peak we can distinguish signals from C=O stretch and C-H deformation vibrations plus stretching vibrations of COO^- group. The third band between 1500 and 1580 cm^{-1} consists of several vibrations, the most visible- symmetric deformation of NH_3^+ group and less visible, overlapped by the first one, related to the vibrations of the free amino acid. The fourth band between 1600 and 1800 cm^{-1} consist of overlapping vibrations from asymmetric deformation of NH_3^+ and stretching vibrations from C=O group. The last band shows vibrations from the short carbon chain. The vibrations are in similar positions to those of DDT and MDA monolayer, although, they are more broad and overlapping, as there is only one CH_2 group in the cysteine molecule.

Ellipsometry measurements conducted in order to determine thickness of the monolayer revealed that the measured thickness was of the same range as the error. The roughness of the gold surface and small thickness of the monolayer made the measurement impossible to conduct. Even if atomically flat gold (111) deposited on mica were used, the substrate properties (the air trapped between mica layers) made the measurement not possible to conduct.

Electrochemistry studies revealed that adsorption of cysteine L molecules on gold prepared by thermal evaporation described in section 4.1 is enough to use it in both projects. A typical cyclic voltammetry plot is presented in Figure 5-8. For the cysteine monolayer the peaks are more visible than in the example for DDT monolayer. There are two reasons for this result: first, the monolayers were prepared in water solutions and were not annealed (a distinct change in the molecular structure of cysteine monolayers is achieved upon annealing the substrate to $380\text{ K}^{22,22,23,23}$); second, cysteine has two functional groups, both possessing a charge, which makes it behave differently in electrolytes of different pH¹⁴. The electrolyte used in this study was of the same pH for all the tested monolayers, and the pH was greater than 7. Those two factors influence the shape of the cyclic voltammogram. In the pH higher than the isoelectric point (5.02) the cysteine molecule is ionized and the negative charge of the COO^- group establishes a coulombic barrier for the approach of $\text{Fe}(\text{CN})_6^{3-}$ to the electrode surface^{14,14,24,24}. This causes the appearance of two peaks in the volammogram of cysteine monolayer.

EIS measurements showed an average specific capacitance of adsorbed monolayer of $10.41 \pm 0.5 \mu\text{F cm}^{-2}$, slightly less than presented by Zhang¹⁸. However, it was shown before that the type of gold used for experiments as well as the way of sample preparation has tremendous influence on the resulting monolayer. In the work of Zhang, the cysteine monolayer was prepared from solutions of higher concentrations and assembled directly in the electrochemistry cell. That might be the reason why our values of specific capacitance are lower.

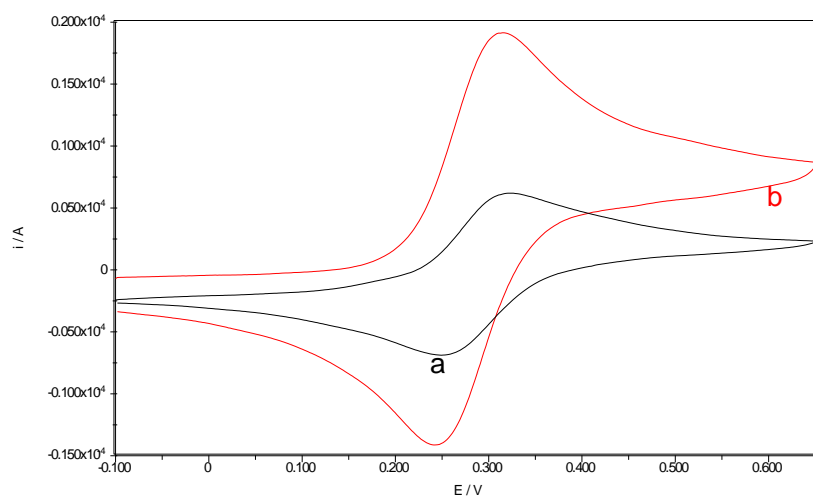
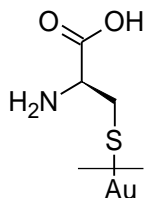


Figure 5-8 Cyclic voltammetry of (a) cysteine L adsorbed on gold surface, assembly time 6 h, (b) bare gold electrode, scan rate 100 mV s^{-1}

Contact angle measurements confirmed that the resulting surface has hydrophilic properties; the contact angle was found to be $23 \pm 2^\circ$.

5.1.4 Cysteine D (4)

A schematic projection of a cysteine D monolayer on gold is presented below:



PM-IRRAS measurements revealed are presented in Figure 5-9 and the characteristic bands are tabulated in Table 5-5. Peaks observed for cysteine D adsorbed on gold are the same bands as those observed for cysteine L layers achieved under the same conditions. Slight differences in the molecules' packing on gold surfaces due to the enantiomers' conformation were observed. For cysteine L, peaks of NH_3^+ deformation vibrations are more visible. It could be explained by poor peak separation in the 1600 cm^{-1} region, where strong signals from COO^- asymmetric stretch, symmetric stretch and NH_3^+ degenerate (deg) deformation are usually overlapping (amide band I and II^{20,21}).

The spectra recorded for cysteine D are slightly different than achieved for cysteine L. The differences are visible in two regions 1400 and $\sim 1700\text{cm}^{-1}$. For cysteine D the peak at 1381 cm^{-1} , related to $\text{C}=\text{O}$ stretching is less apparent than for cysteine L, instead there is a peak at 1516 cm^{-1} related to COO^- stretch deformations. Additionally, in the region between 1600 and 1800 cm^{-1} there are two broad peaks visible, whilst for cysteine L in this region only one broad peak can be seen. This is caused by the arrangements of molecules in the monolayer related to their conformations.

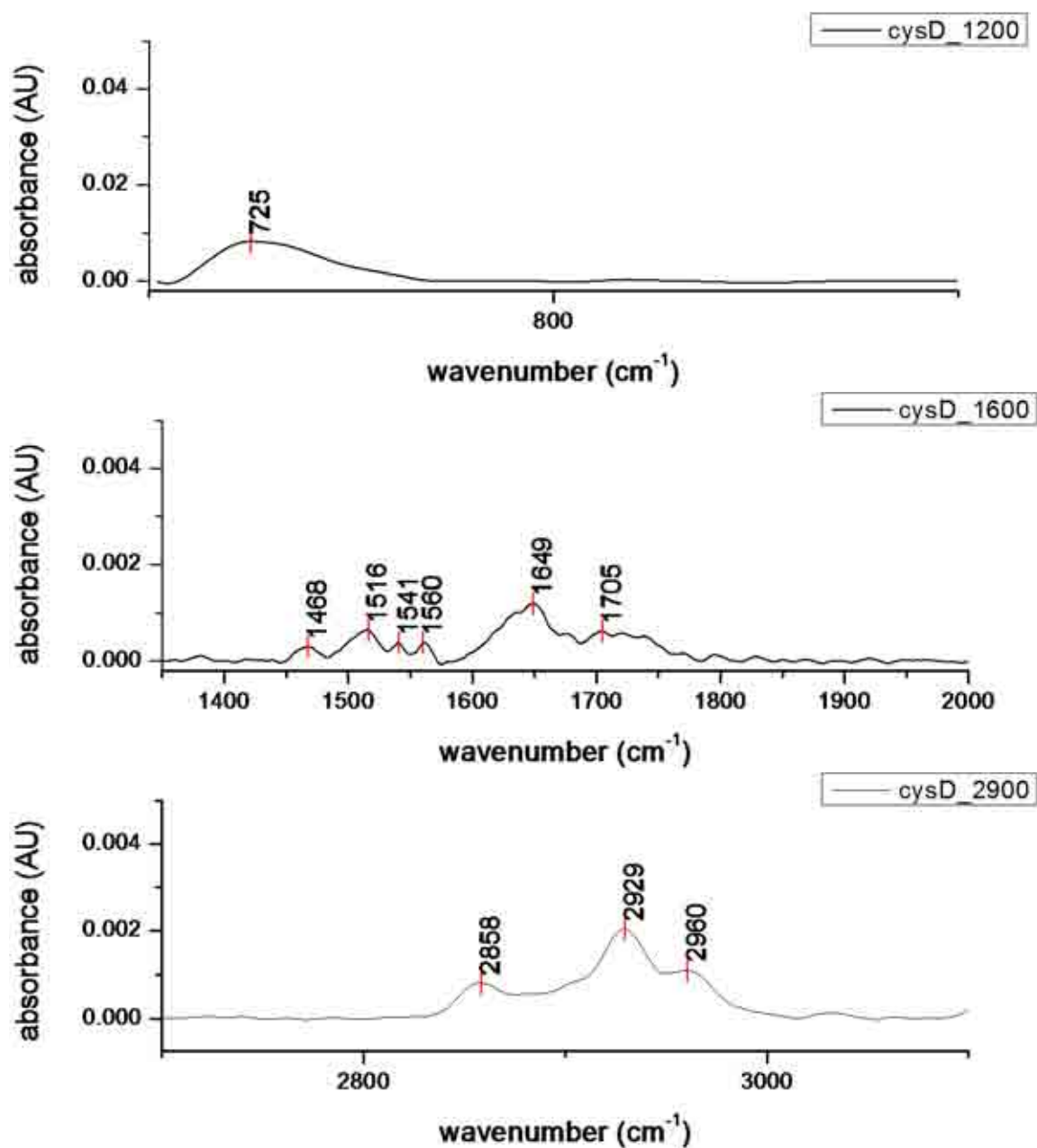


Figure 5-9 PM IRRAS spectra of cysteine D adsorbed on gold

Characteristic vibration bands:

Table 5-5 characteristic vibration bands for cysteine D monolayer adsorbed on gold

Vibration type	Wavenumber/cm ⁻¹	Vibration type	Wavenumber/cm ⁻¹
$\nu_s(\text{C-S})$	725	$\nu_{\text{def}}(\text{NH}_3^+)$	1649
$\nu_{\text{def}}(\text{CH}_2)$	1468	$\nu_s(\text{C=O})$	1700
$\nu_s(\text{COO}^-)$	1516	$\nu_s(\text{CH}_2)$	2858
$\nu_{\text{def}}(\text{NH}_3^+)$	1541	$\nu_a(\text{CH}_2)$	2929
$\nu_s(\text{COO}^-)$	1560	$\nu_a(\text{CH}_3)$	2958

Electrochemistry measurements conducted on cysteine D adsorbed on gold showed similar results to cysteine L. A typical cyclic voltammetry spectrum is presented in Figure 5-10.

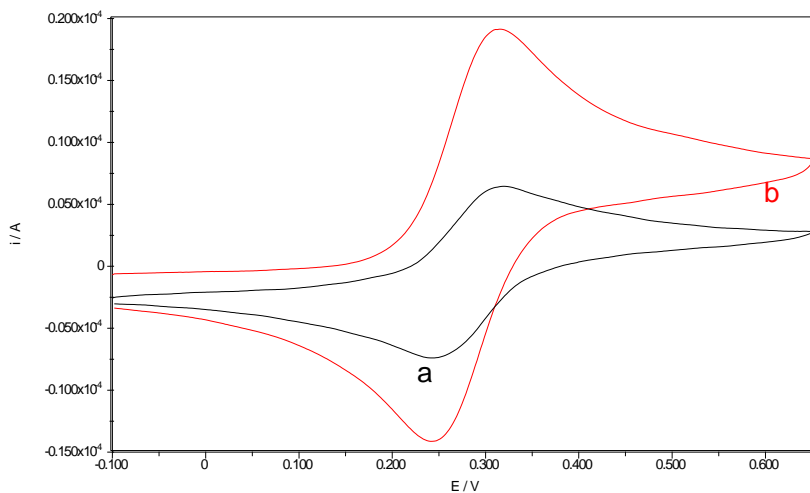


Figure 5-10 Cyclic voltammetry for (a) bare gold electrode (b) cysteine D monolayer adsorbed on gold, assembly time 6h, scan rate 100 mV s^{-1}

EIS studies revealed, however, that the specific capacitance of cysteine D assembled on gold is slightly less than that of cysteine L. The average specific capacitance was found to be $8.74 \pm 0.28 \mu\text{F cm}^{-2}$. This difference might be explained by the fact that cysteine D assembly on gold has its steric constraints and its monolayer is less dense than that made of cysteine L. The presence of current peaks indicates that there are some regions of uncovered gold electrode. This was observed for both D and L cysteines and is related to the fact that cysteine molecules tend to form domains on gold surfaces^{16,25}.

Contact angle measurements confirmed that the surface has hydrophilic properties; the contact angle was found to be $23 \pm 2^\circ$.

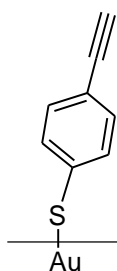
5.2 Characterization of monolayers formed by two- step preparation

For preparation of chiral self assembled monolayers the 'click chemistry' reaction has been employed, which is a two- step process. In the first step the gold surface is modified with a linker, which in the second step is functionalized by subjecting it to the AAC reaction. Surfaces produced in both steps of preparation were characterized to monitor changes in the surface structure.

5.2.1 Characterization of linkers monolayers

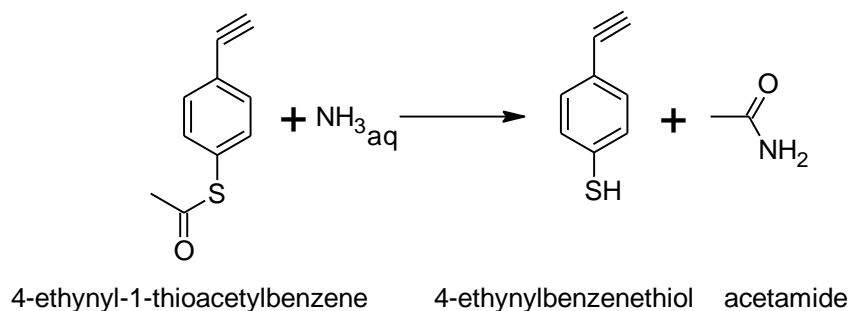
5.2.1.1 *Linker A (5)*

A schematic projection of a linker A monolayer formed by 4-ethynylbenzenethiol adsorbed on gold is presented below:



4-ethynylbenzenethiol was synthesized in the collaborating group of Prof. A. Rowan, Radboud University Nijmegen, Netherlands²⁶.

Since thiols are not very stable, linker A was synthesized as a thioacetyl to protect the thiol group from acid. To modify the gold surface with Linker A, the following reaction was performed to activate the thiol group:

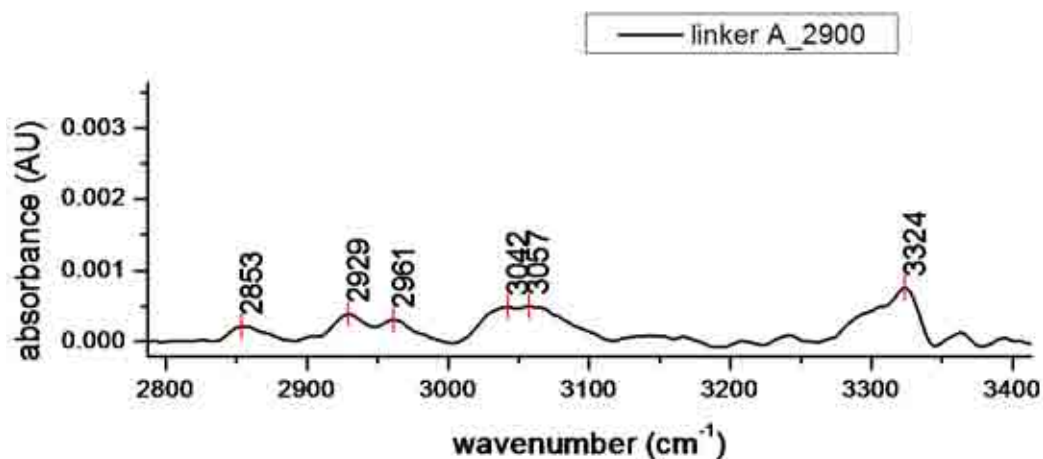


A 100 μ L droplet of 3% ammonia solution was added to 2 mL 4-ethynyl-1-thioacetylbenzene ethanol solution of a concentration 2 mM. The reaction occurs rapidly so the solution was filtered with use of syringe filters (22 μ m Waltham) and used for gold modification. Modification was carried out at room temperature over 24 hours.

Characterization conducted by PM IRRAS was also supported by XPS to confirm that all ammonia used for that process was removed. No peaks were found in the regions of 397 and 530 keV, corresponding to nitrogen and oxygen, respectively.

PM-IRRAS bands are presented in Figure 5-11 and the corresponding bands tabulated in Table 5-6.

Linker A is a very short molecule, with a characteristic triple bond at the end. The peak corresponding to the vibrations of the C-H bond within the acetylene group is a fingerprint for this compound.

Figure 5-11 PM IRRAS spectra of 2900 cm^{-1} region of linker A

Characteristic vibration bands¹²:

Table 5-6 Vibration bands of linker A monolayer deposited on gold

Vibration type	Wavenumber/ cm^{-1}
$\nu_s(\text{CH}_2)$	2853
$\nu_a(\text{CH}_2)$	2929
$\nu_a(\text{CH}_3)$	2961
$\nu_s(\text{CH})$ in benzene ring	3042
$\nu_s(\text{CH})$ in benzene ring	3056
$\nu_s(\text{C-H})$ in acetylene group	3318

In the spectra of linker A frequencies there are two characteristic bands: first between 3000 and 3100 cm^{-1} , where signals from the C-H stretches in the benzene ring are present and second in 3300 cm^{-1} of C-H vibrations in acetylene group. Additionally in 2900 cm^{-1} region there are visible three peaks, which are not linker A bond vibrations. The peaks of 2853, 2929 and 2961 cm^{-1} arise from remaining solvent (ethanol) used for monolayer formation.

Ellipsometry studies conducted on linker A monolayer on gold were difficult to conduct due to the shortness of the linker A molecule. The measurements, displayed in Figure 5-12, showed that there is a large uncertainty – ten subsequent measurements gave results in a range of 0.4-0.6 nm. However, these values were decided to be good enough to use in comparison with the thickness of modified linker A monolayers, which are described in sections 5.2.2.1 and 5.2.2.3.

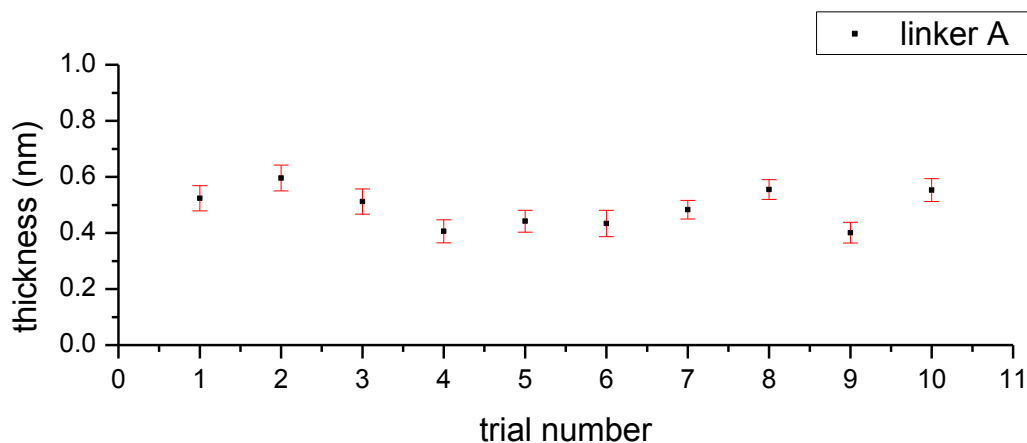


Figure 5-12 Ellipsometry measurements of linker A monolayer thickness

Electrochemistry studies were used to investigate the adsorption ability on the gold surface. A set of cyclic voltammograms is presented in Figure 5-13. It can be seen that in 4 hours of deposition the monolayer is already formed; however, only just after 24 h it is densely packed-with the current peaks broad, low and more separated.

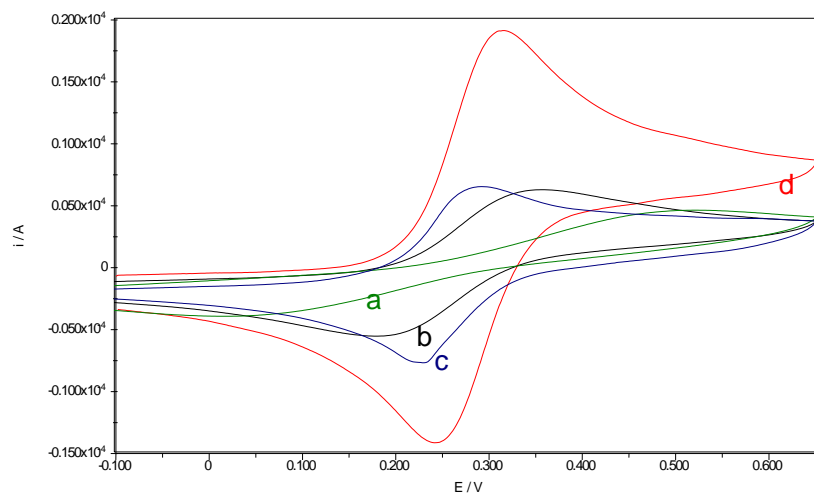


Figure 5-13 Cyclic voltammetry for linker A, (a) assembly time 24 h, (b) 12 h, (c) 4 h, (d) bare gold electrode, scan rate 100 mV s^{-1}

EIS measurements presented in Figure 5-14 revealed that the average specific capacitance of linker A monolayer on gold is $16 \pm 1 \mu\text{F cm}^{-2}$ and R_{ct} is $1.5 \pm 0.1 \text{ k}\Omega \text{ cm}^2$. Its high value of specific

capacitance is due to the molecule shortness and lack of chargeable and bulky functional groups but the high value of R_{ct} shows that some blocking still occurs, which ties in well with the CV data in Figure 5-13. This specific capacitance was calculated for the first measurement as it was found that next measurements values of specific capacitance around 15% lower. This can be seen in Figure 5-14b. This behaviour indicates that the monolayer is not as stable as those formed from ODT (oktadecanethiol) or DDT (dodecanethiol) and it is sensitive to applied potential.

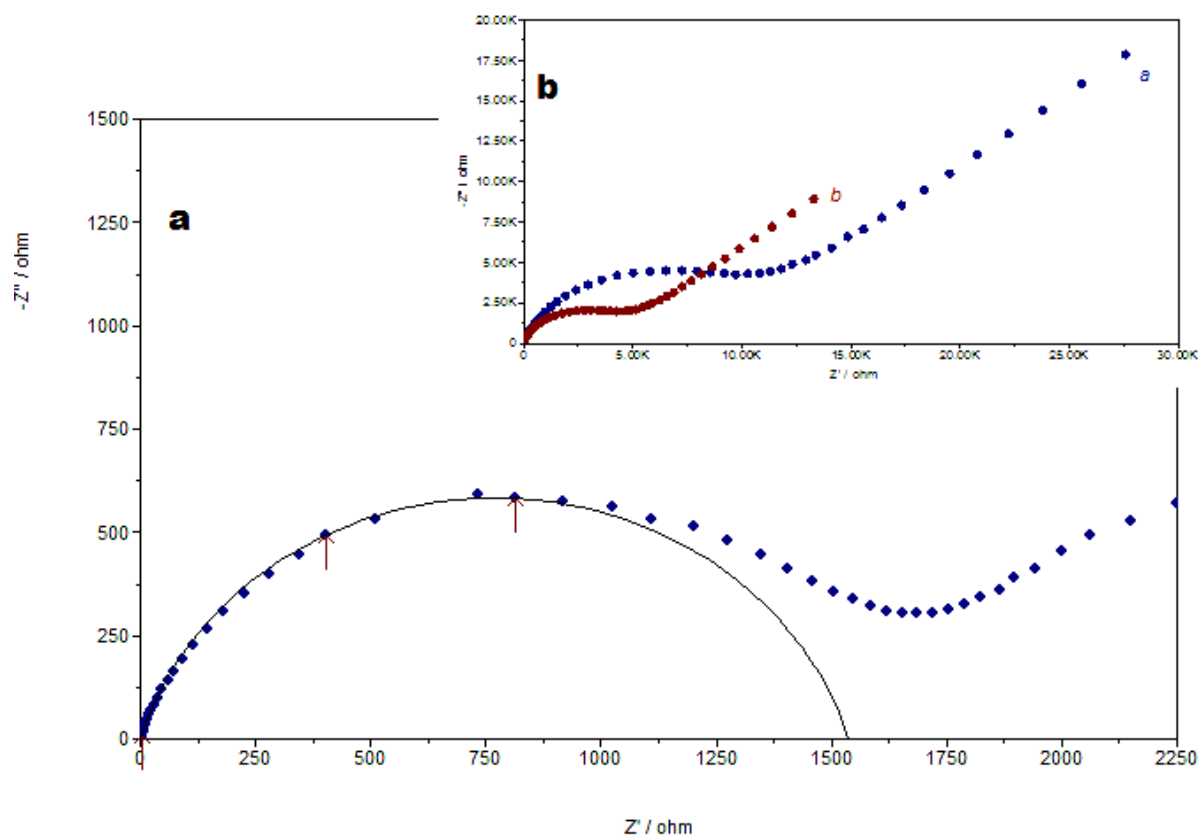
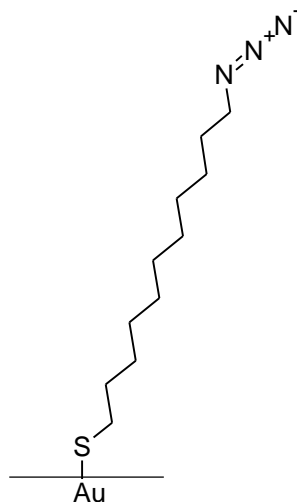


Figure 5-14 Electrochemical impedance spectra of a) linker A monolayer on gold b) two subsequent measurements of linker A monolayer adsorbed on gold (blue dots) first trial, (red dots) second trial, frequency range 10000-0.1 Hz.

Contact angle microscopy confirmed hydrophobic properties of the monolayer formed by linker A. The contact angle was found to be $85 \pm 2^\circ$.

5.2.1.2 Linker B (6)

A schematic projection of a linker B monolayer formed by 11-azidoundecane-1-thiol assembled on gold is presented below:



11-azidoundecane-1-thiol²⁷ of analytical grade was obtained from Prochimia, Poland and was used without further purification. A 1 mM ethanol solution was used for gold surface modification. The time allowed for surface modification was 24 h and it was carried out at room temperature.

PM-IRRAS spectra of a linker B monolayer on gold are presented in Figure 5-15 and the characteristic bands tabulated in Table 5-7.

Linker B is functionalized with a triazide group (N_3^-), which has its strongest characteristic band in the 2100 cm^{-1} region^{27,28}. This band is a fingerprint for this compound and is used to follow click chemistry reactions. As will be shown in section 5.2.2.3, its vanishing from the spectra with concomitant increasing in monolayer thickness could be taken as proof for surface modification.

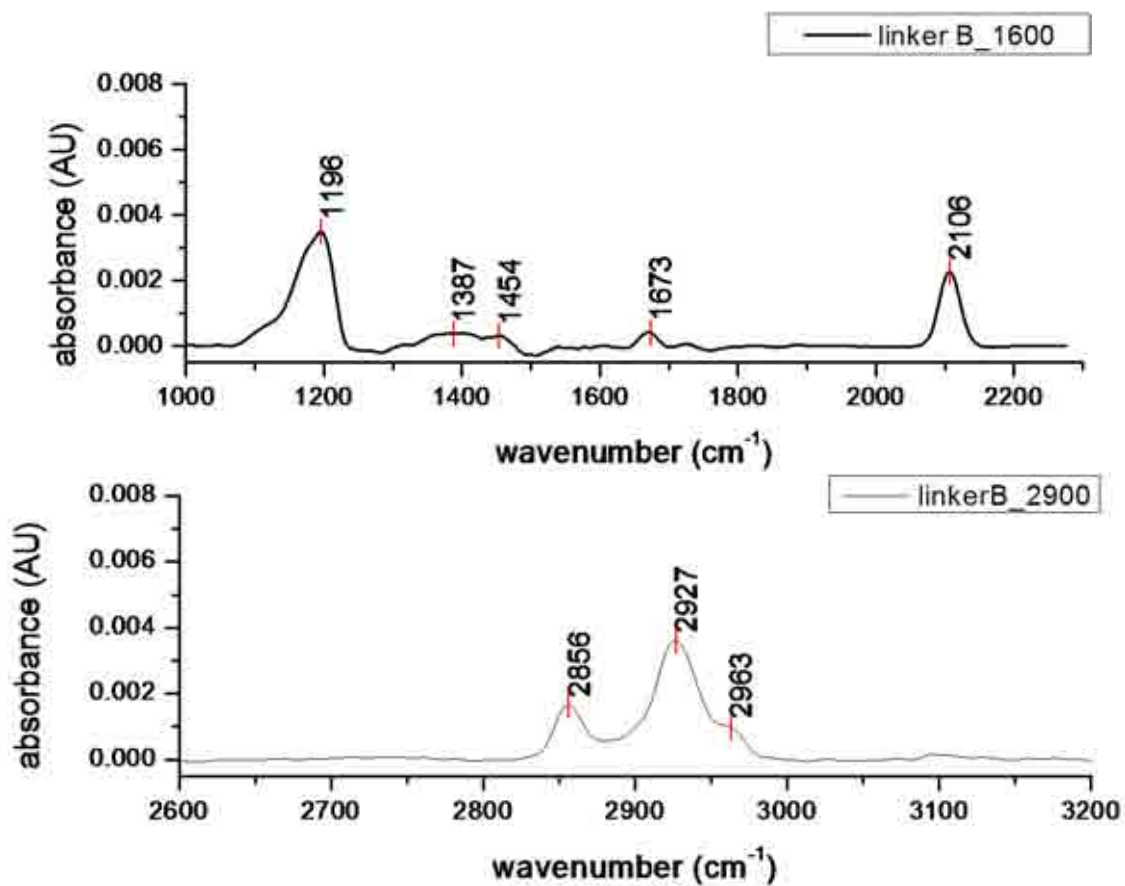


Figure 5-15 PM IRRAS spectra of linker B on gold monolayer

Characteristic vibration bands¹²:

Table 5-7 Vibration bands of linker B monolayer on gold

Vibration type	Wavenumber/cm ⁻¹
$\nu_s(\text{CN})$	1196
$\nu_s(\text{CH}_2)$	1387
$\nu_s(\text{CH}_2)$	1454
$\nu_{\text{def}}(\text{CH})$	1673
$\nu_s(\text{N}_3^-)$	2106
$\nu_s(\text{CH}_2)$	2856
$\nu_a(\text{CH}_2)$	2927
$\nu_a(\text{CH}_3)$	2963

Ellipsometry measurements showed that the thickness of the monolayer is 1.1 ± 0.2 nm as presented in Figure 5-16.

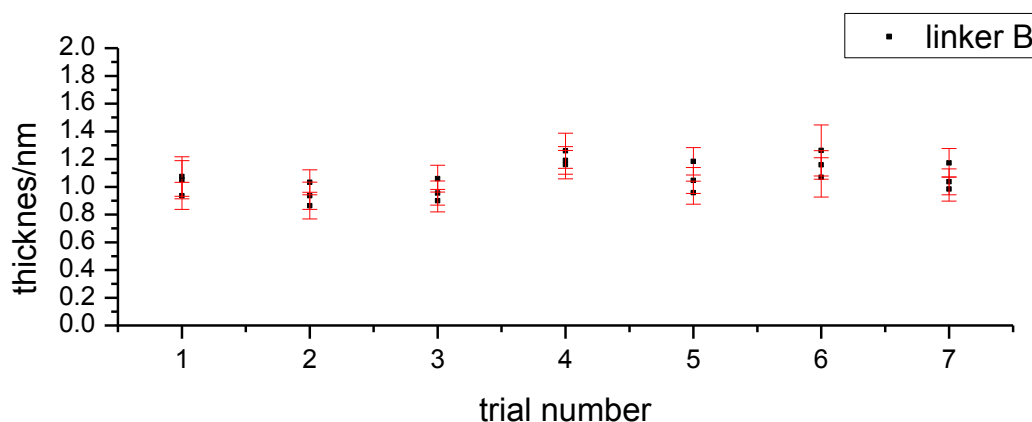


Figure 5-16 Linker B monolayer thickness measurement

Electrochemistry measurements performed on linker B monolayers showed excellent adsorption of the molecule on gold electrodes to form dense films. Figure 5-17 shows cyclic voltammetry measurements done after different adsorption time intervals. After 24 h the monolayer was closely packed and could be used for further functionalization.

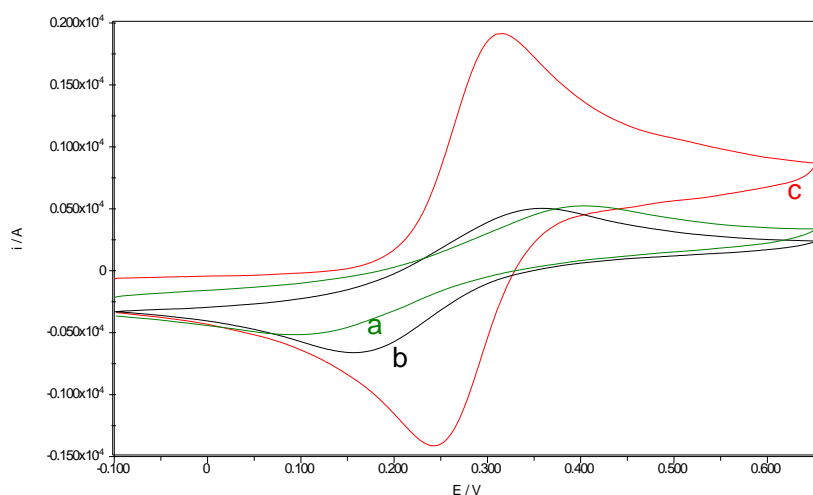


Figure 5-17 Cyclic voltammetry of (a) linker B monolayer, assembly time 24 h, (b) linker B monolayer, assembly time 12 h, (c) bare gold electrode, scan rate 100 mV cm^{-1}

EIS measurements revealed the average specific capacitance of linker B monolayers to be $1.25 \pm 0.01 \mu\text{F cm}^{-2}$ with R_{ct} of $18.75 \pm 0.2 \text{ k}\Omega \text{ cm}^{-2}$, which indicates that the formed monolayer is very compact and almost defect free. A typical EIS spectrum is presented in Figure 5-18.

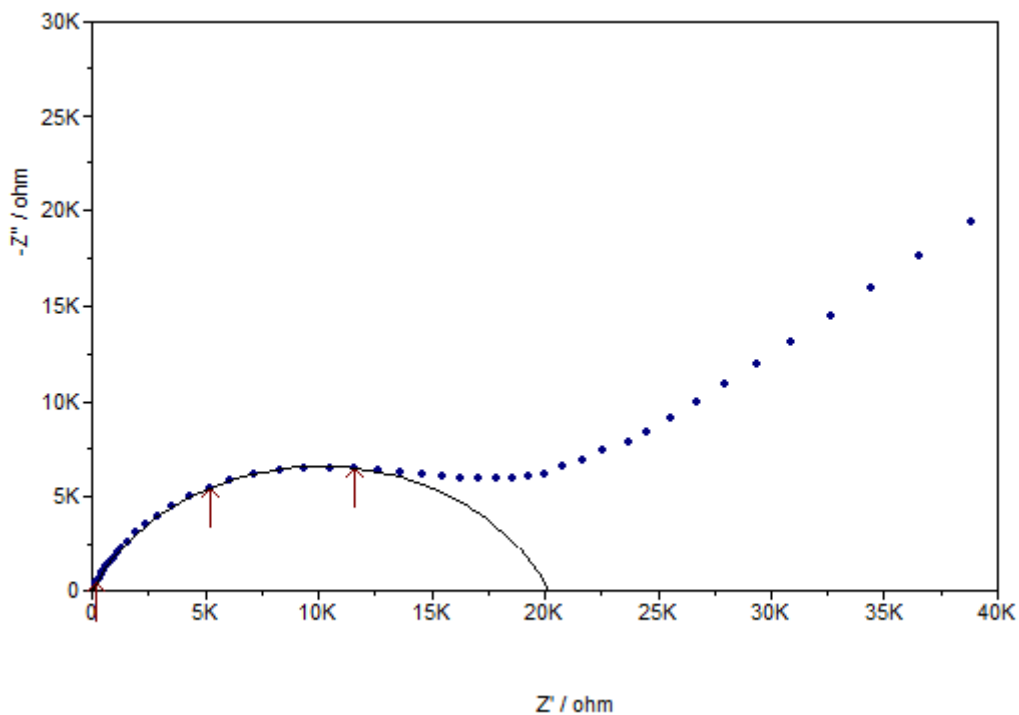
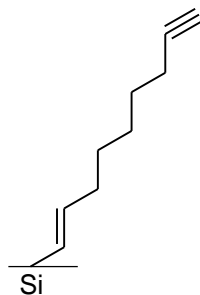


Figure 5-18 Electrochemical impedance spectra of linker B monolayer (blue dots) and semi circle fitted (black line), frequency range 10000 - 0.1 Hz

Contact angle measurements confirmed hydrophobic properties of the linker B surface. The contact angle was found to be of $78 \pm 2^\circ$, which perfectly matches with the published data²⁸.

5.2.1.3 Linker C (7)

A schematic representation of a linker C monolayer formed by adsorption of 1,8-nonadiyne on silicon is presented below:



Linker C of analytical grade was obtained from Sigma. Before using it to derivatise the Si surface, prior purification and drying was necessary in order to remove any water excess from the diyne solution²⁹.

1,8-nonadiyne was distilled from sodium borohydride under reduced pressure at 79°C (7-8 Torr). Before the distillation the solution was stirred over NaBH₄ (sodium borohydride) for 12 h under argon. After the distillation, freshly dried molecular sieves were added and the solution was degassed in the vacuum line by performing 6-8 freezing- thaw cycles.

Silicon wafers preparation:

Silicon wafers were cut to the desired dimension incised for easier cleaving and cleaned according to the procedure in section 4.1.3. After that an incised silicon wafer was etched with HF to produce Si-H bonds.

HF etching procedure:

5 mL of 2.5% HF solution was used for the etching experiment. Etching was performed in PTFE vessels in the fume cupboard, taking extra care as HF is highly toxic. A silicon wafer was immersed into HF solution for 90 seconds and removed with PTFE tweezers. Removing the remaining acid was performed by contacting the edges of the wafer with a piece of clean paper. Then the wafer was held in a stream of argon at the entrance of the reaction flask. After that time the wafer was placed carefully into the specially designed reaction flask shown in Figure 5-19.



Figure 5-19 Flat compartment flask for modification of silicon wafers with 1,8-nonadiyne

Silicon surface modification with 1,8-nonadiyne:

A grease- free Schlenk line connected to argon was used to perform silicon surface modification. The distilled 1,8-nonadiyne was poured into the reaction flask under argon *via* the Schlenk technique. Next a freshly etched silicon wafer was placed in the flat compartment under argon flow. The modification reaction was started by immersing the flat part of the reaction flask into an oil bath at 170 °C for 3 h. After that time the flask was removed from the oil bath, cooled and opened to the atmosphere. The silicon wafer was carefully removed and rinsed with chloroform, ethyl acetate and ethanol, then dried with argon and placed in a desiccator to store before further reacting.

Due to difficulty with conducting PM-IRRAS measurements on silicon surfaces only ellipsometry and contact angle characterization of the linker C surface were conducted.

Ellipsometry measurements, presented in Figure 5-20, showed that the thickness of the monolayer formed by linker C on silicon surface is 1.8 ± 0.2 nm.

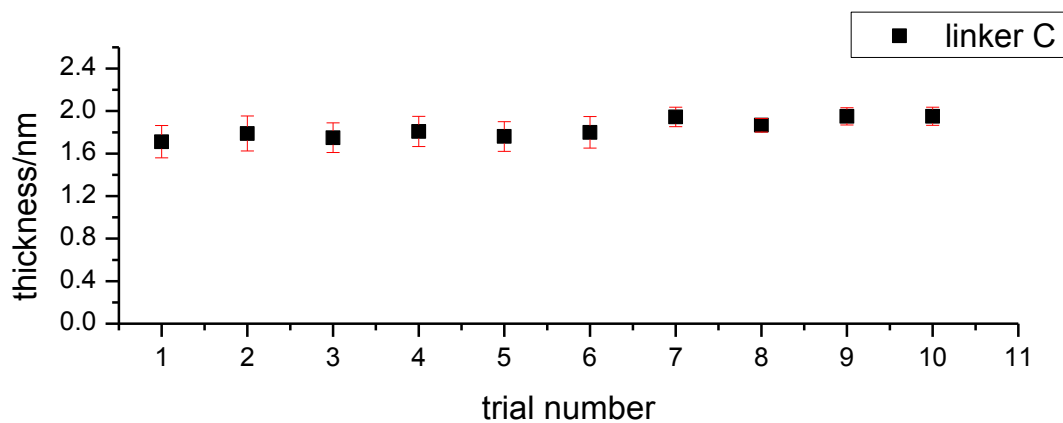


Figure 5-20 Ellipsometry measurements for linker C monolayer

Contact angle measurements confirmed the hydrophobic properties of the linker C monolayer. The contact angle was found to be of $86.5 \pm 2^\circ$, which is consistent with data published by Campi²⁹.

5.2.2 Characterization of monolayers formed in 'click chemistry' reaction

To perform the click chemistry reaction on the surfaces modified with linkers, a solution of a catalyst was prepared beforehand.

Sodium ascorbate and copper acetate, both of analytical grade, were obtained from Aldrich and used without further purification. For a batch of 12 surfaces a 10 mL aqueous solution of the catalyst was made of concentration of 1 mM of copper acetate and 5 mM sodium ascorbate). When the solution changed colour to orange, the catalyst was ready to use.

Reacting solutions for linkers functionalization were made up of 4 mL of Ethanol and 2 mL of catalyst water solution to give final concentration of functionalizing substance of 1 mM. This amount of reaction solution was used for 3 surface specimens.

Functionalization reactions were performed in shell vials with copper holders for the specimens. Samples were placed in the vials perpendicular to the bottom to prevent crystallization on the surface. After placing the specimens in the holders the reacting solution was added and the vials were closed tightly with clean septa. A barbotage technique was used to stir the solution. Needles connected to the nitrogen flow were pierced through the septa. Additional needles were put through the septa to allow evacuation of the excess gas. The reaction was performed with gentle bubbling for 24 h in the dark. A typical set up is presented in Figure 5-21.

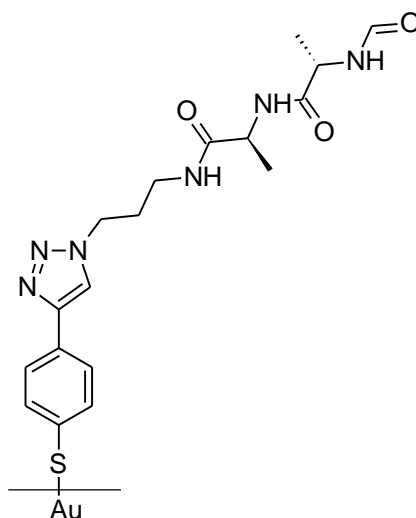


Figure 5-21 Reaction set up for clicking functionalities onto linkers surfaces

5.2.2.1 LinkerA-AlaAlaDL (5A)

For linker A modification two enantiomeric dipeptides equipped with a triazide group were chosen.

A schematic representation of the surface generated by clicking functionality of AlaAlaDL on linker A is presented below:



PM-IRRAS measurements were conducted in order to confirm the modification of the linker A surface. The most prominent bands for linker A-AlaAlaDL are presented in Figure 5-22 and the characteristic bands are tabulated in Table 5-8. In the region of 1600 cm^{-1} there are bands corresponding to the vibrations of amide bonds (I band), which are not present in the spectra of only linker A. Also, at 3300 cm^{-1} there is no peak corresponding to the acetylene group, which demonstrates linker A surface modification. In the spectra there is a peak at 2961 cm^{-1} , which corresponds to remaining of a solvent.

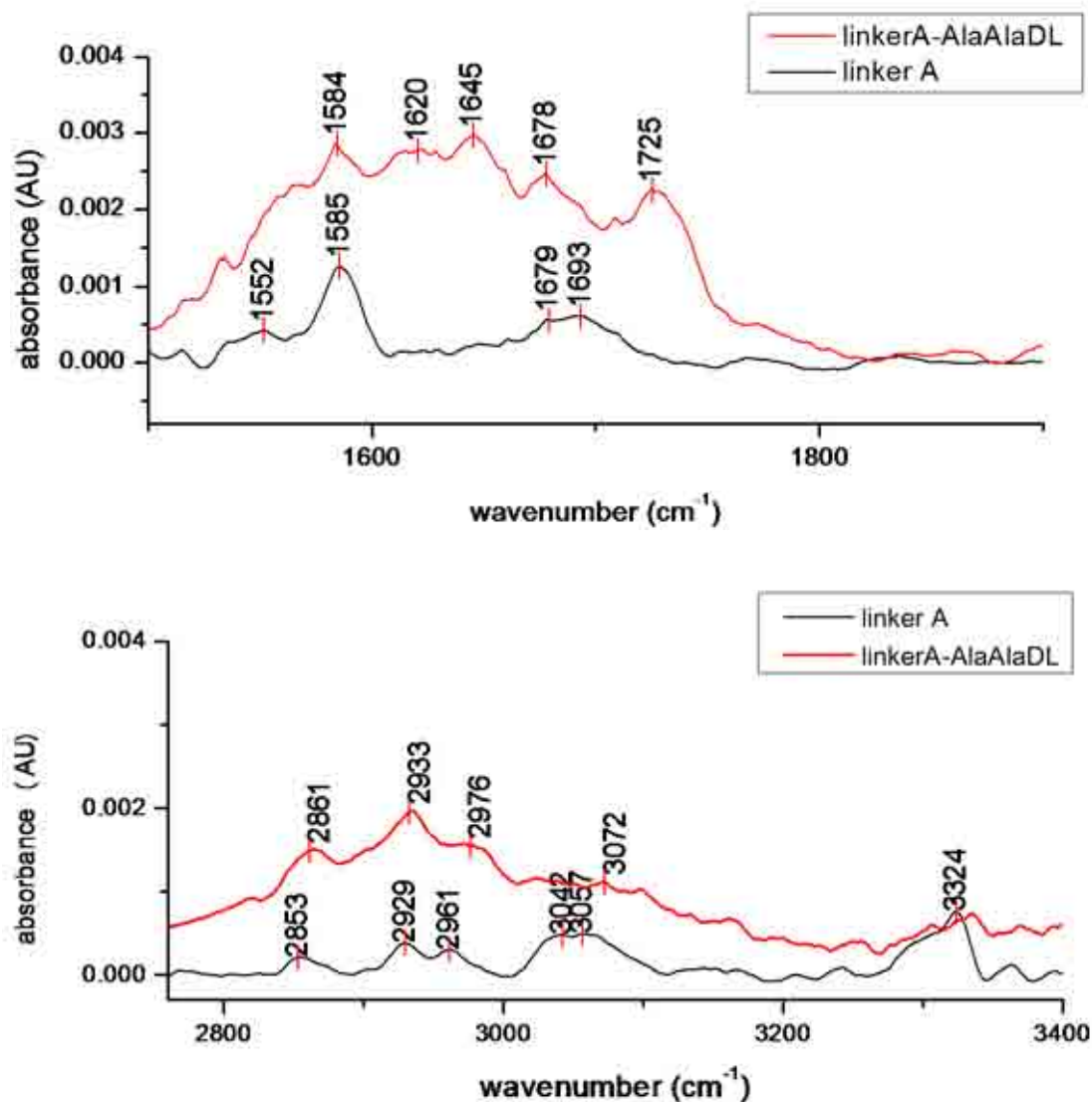


Figure 5-22 PM-IRRAS spectra of linker A-AlaAlaDL (red) and linker A (black) monolayer

Characteristic vibration bands¹²:

Table 5-8 Characteristic vibration bands for linker A-AlaAlaDL monolayer

Vibration type	Wavenumber/cm ⁻¹
$\nu_{\text{bend}}(\text{N-H})$ amide (I)	1584
$\nu_{\text{bend}}(\text{N-H})$ amide (II)	1620
$\nu_{\text{s}}((\text{C=O})\text{N})$ amide (I)	1645
$\nu_{\text{s}}(\text{C=O})$ amide (I)	1678
$\nu_{\text{s}}(\text{N=N-C})$	1725
$\nu_{\text{s}}(\text{CH}_2)$	2857
$\nu_{\text{a}}(\text{CH}_2)$	2929
$\nu_{\text{as}}(\text{CH}_3)$	2960
$\nu_{\text{s}}(\text{C=CH})$	3072
$\nu_{\text{s}}(\text{C-H})$ in acetylene group	3323

Ellipsometry measurements were carried out in 2 steps to observe monolayer building up. Despite the fact that we encountered problems in linker A monolayer thickness determination it was possible to investigate the thickness of the monolayer after modification. The results are shown in Figure 5-23. The final monolayer was found to be 1.25 ± 0.2 nm thick and so it is possible to demonstrate that the resulting monolayer was thicker than a layer of linker A alone.

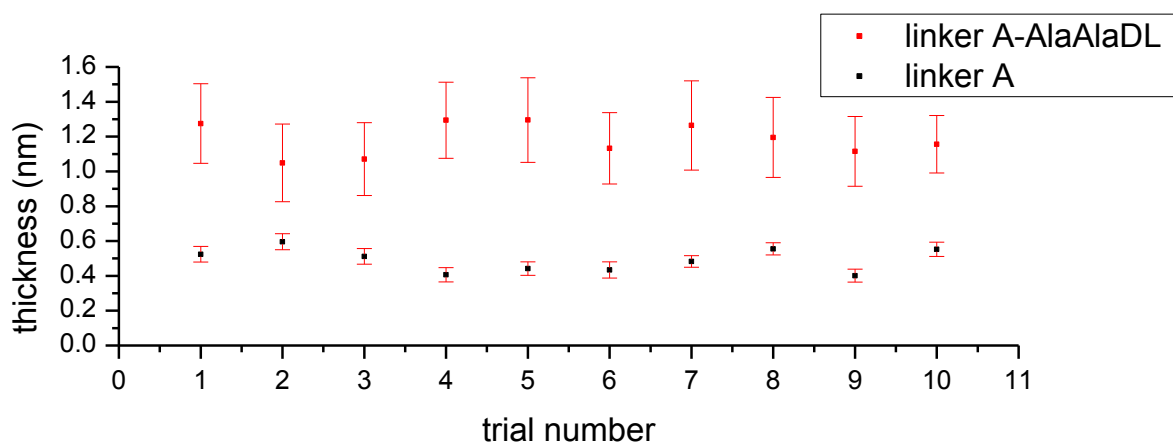


Figure 5-23 Ellipsometry measurements of linkerA-AlaAlaLL monolayers

Electrochemistry measurements showed differences between only linker A and linker A-AlaAlaDL monolayers. Cyclic voltammograms of linker A-AlaAlaDL and linker A are presented in Figure 5-24.

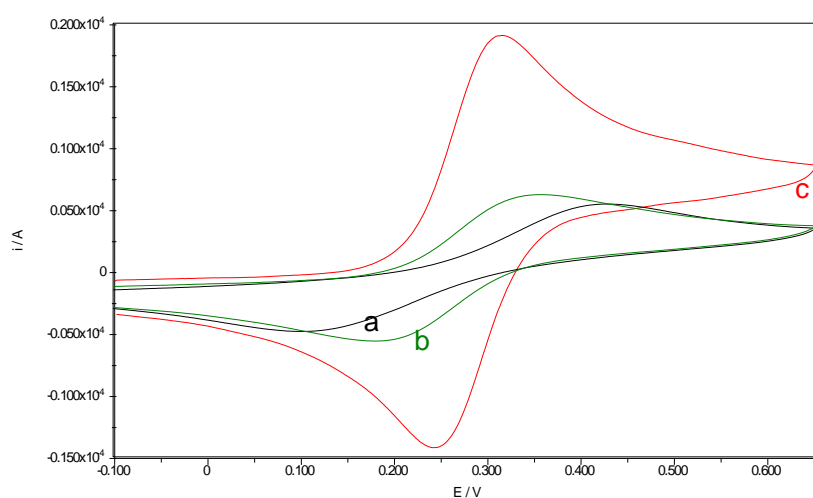


Figure 5-24 Cyclic voltammogram of (a) gold modified with linkerA (b) gold modified with linkerA-AlaAlaDL (c) bare gold electrode, scan rate 100 mV s^{-1}

Cyclic voltammograms of only linker A and linker A AlaAlaDL are different in peak height and width. A linker A monolayer effectively blocks an access of $\text{Fe}(\text{CN}_6)^{+3}$ ions to the gold electrode. In the case of linker A-AlaAlaDL monolayers the peaks are higher; however, their appearance is not related to less ability for charge transfer blocking but to the fact that the clicked functionality is not charged free. As it was shown before^{14,24} monolayers possessing chargeable parts behave different in electrolytes of different pH, thus the observed effect is understandable and expected.

EIS measurements shown in Figure 5-25 revealed the specific capacitance of the monolayer to be $18 \pm 0.5 \mu\text{F cm}^{-2}$. R_{ct} was $0.12 \pm 0.01 \text{ k}\Omega \text{ cm}^2$. This value is affected by two factors: first- how well the surface was modified with linker A and the second what percent of linker molecules reacted with linker A. The specific capacitance of linker A monolayer was found to be *ca.* $16 \mu\text{F cm}^{-2}$, the charge transfer resistance $1.5 \text{ k}\Omega \text{ cm}^2$. Taking into consideration that the linker A-AlaAlaDL monolayer consists of chargeable parts, such rise of specific capacitance and drop of charge transfer resistance is understandable. However, to determine fully the change in specific capacitance during click chemistry reactions *in situ* studies of the system should be done.

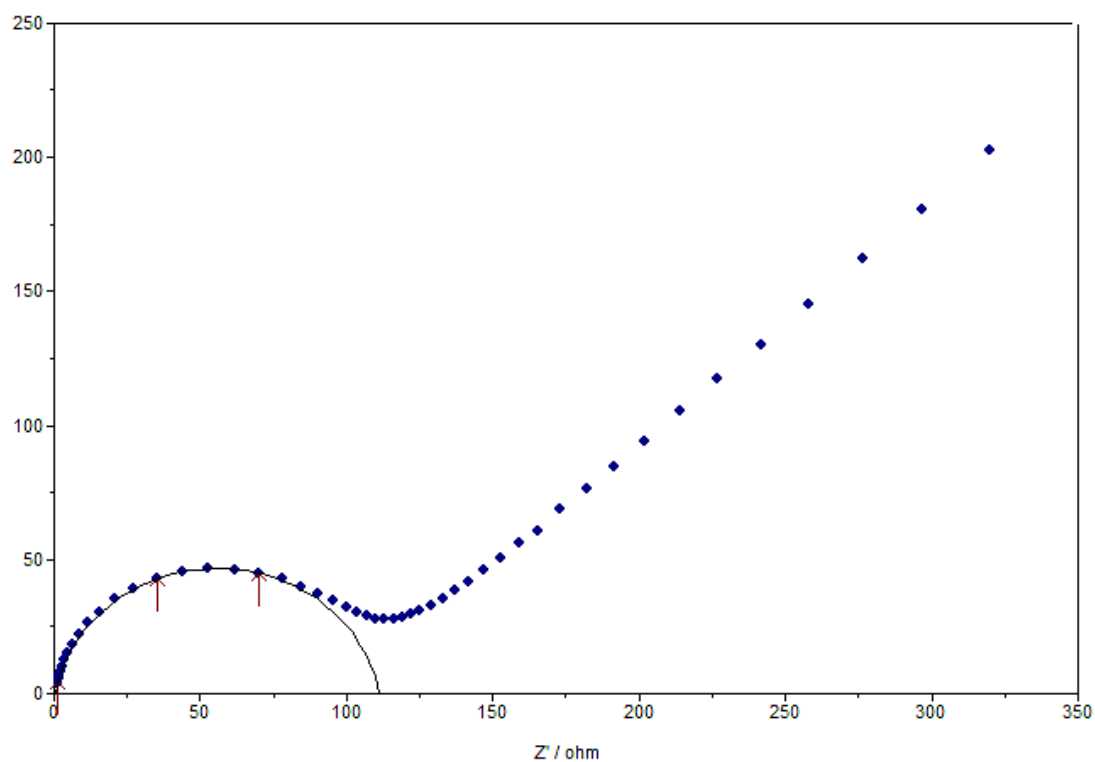
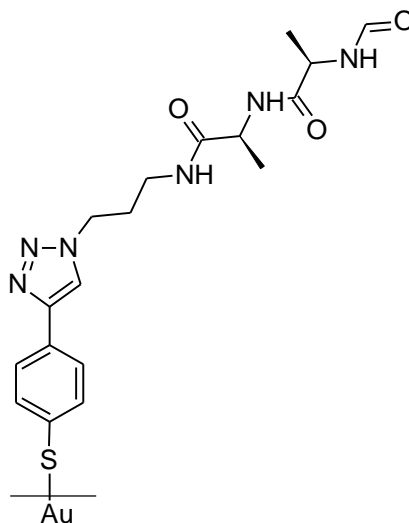


Figure 5-25 Electrochemical impedance spectra of linker A-AlaAlaDL monolayer, frequency range 10000-0.01 Hz

Contact angle measurements confirmed a change in wettability. The contact angle of neat linker A was measured to be $85 \pm 2^\circ$; the surface of linker A-AlaAlaDL was found to have more hydrophilic properties and its contact angle was to $64 \pm 3^\circ$.

5.2.2.2 LinkerA-AlaAlaLL (5B)

A schematic projection of the monolayer formed by clicking AlaAla LL functionality on linker A:



PM-IRRAS measurements confirmed the 'click' on the linker A surface, because additional peaks responsible for C-N, N-H, C=O (amide-bands I and II) were observed, as for the DL enantiomer, with a concomitant vanishing of the peak in the 3300 cm^{-1} region. The spectra of linker A-AlaAlaLL monolayer is presented in Figure 5-26 and characteristic bands are tabulated in Table 5-9.

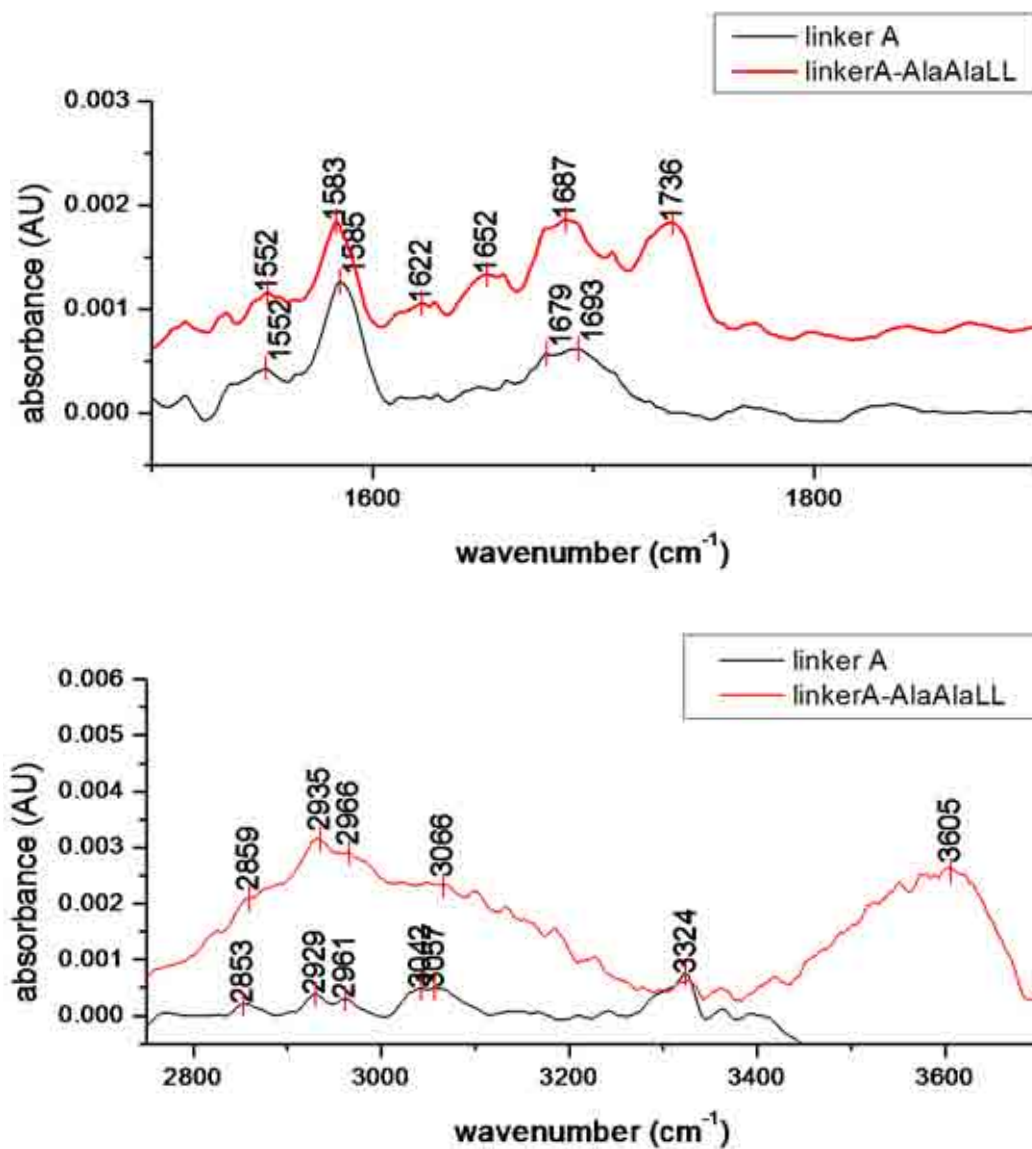


Figure 5-26 PM IRRAS spectra of linker A-AlaAlaLL (red) and linker A (black) monolayers

Characteristic vibration bands¹²

Table 5-9 Characteristic vibration bands for linker A-AlaAlaLL monolayer

Vibration type	Wavenumber/cm ⁻¹	Vibration type	Wavenumber/cm ⁻¹
$\nu_{\text{def}}(\text{N-H})$ amide (II)	1552	$\nu_{\text{s}}(\text{CH}_2)$	2857
$\nu_{\text{a bend}}(\text{N-H})$ amide (II)	1583	$\nu_{\text{a}}(\text{CH}_2)$	2929
$\nu_{\text{s}}(\text{C=O})$ amide(I)	1622	$\nu_{\text{as}}(\text{CH}_3)$	2960
$\nu_{\text{s}}(\text{C=O})\text{N}$ amide (I)	1652	$\nu_{\text{s}}(\text{C=CH})$	3066
$\nu_{\text{s}}(\text{C=O})$ amide (I)	1687	$\nu_{\text{s}}(\text{C-H})$ in acetylene group	3323
$\nu_{\text{s}}(\text{N=N-C})$	1736	$\nu_{\text{s}}(\text{N-H})$	3605

Ellipsometry measurements were performed in 2 steps to observe the monolayer building up as described for linker A-AlaAlaDL monolayers. The results are shown in Figure 5-27. The final monolayer was found to be 1.2 ± 0.2 nm thick.

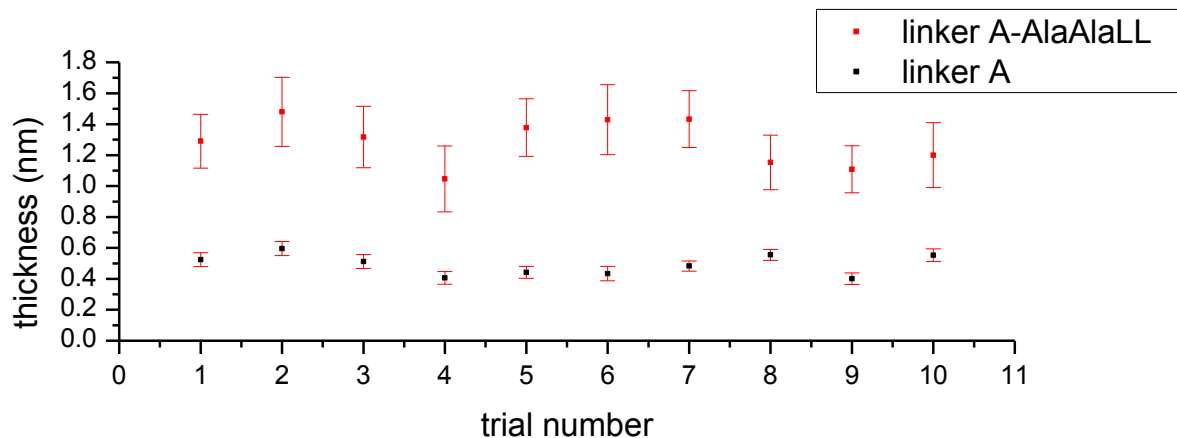


Figure 5-27 Ellipsometry measurements of linker A-AlaAlaLL monolayer

Electrochemistry measurements showed similar responses to linker A-AlaAlaDL monolayers. A cyclic voltammogram of a linker A-AlaAlaLL monolayer is presented in Figure 5-28.

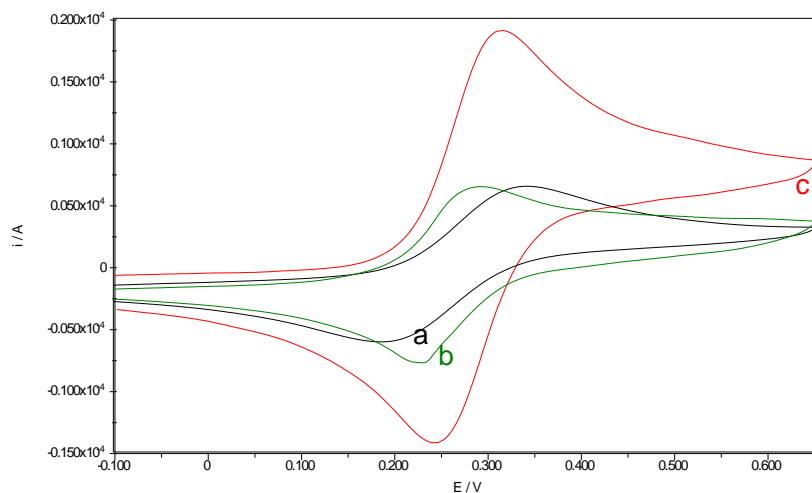


Figure 5-28 Cyclic voltammogram of (a) linker A monolayer (b) linker A-AlaAlaLL monolayer (c) bare gold electrode, scan rate 100 mV s^{-1}

EIS measurements revealed the specific capacitance to be $255 \mu\text{F cm}^{-2}$ with an R_{ct} of $0.6 \pm 0.02 \text{ k}\Omega \text{ cm}^2$, which are corresponding with the trend of values achieved for linker A-AlaAlaDL monolayers. The difference between linker A-AlaAlaDL and linker A-AlaAlaLL capacitance could be due to the fact that it is difficult to prepare two exactly the same surfaces. However the trend and the

magnitude of specific capacitance and transfer charge resistance are consistent. A typical impedance spectrum is presented in Figure 5-29.

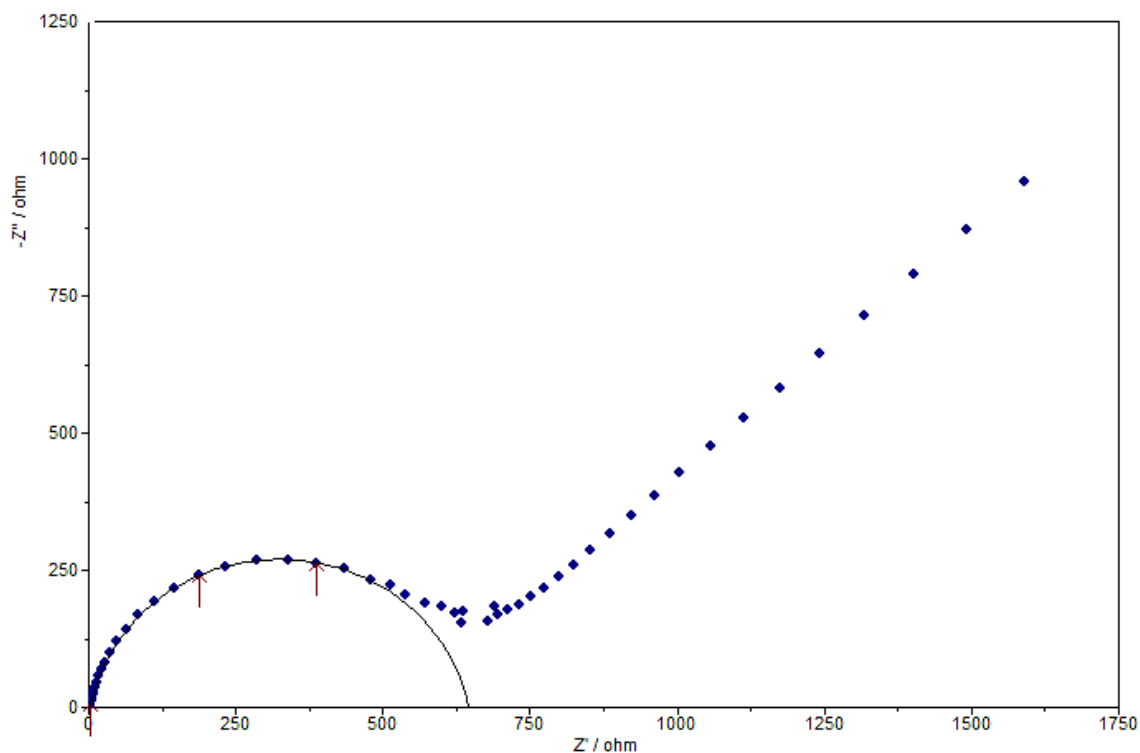
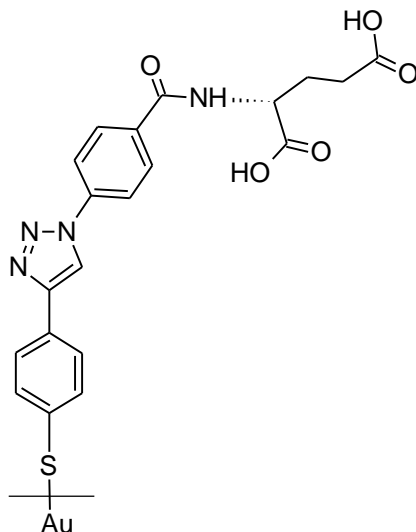


Figure 5-29 Electrochemical impedance spectroscopy of linker A-AlaAlaLL monolayer, frequency range 10000-0.01 Hz

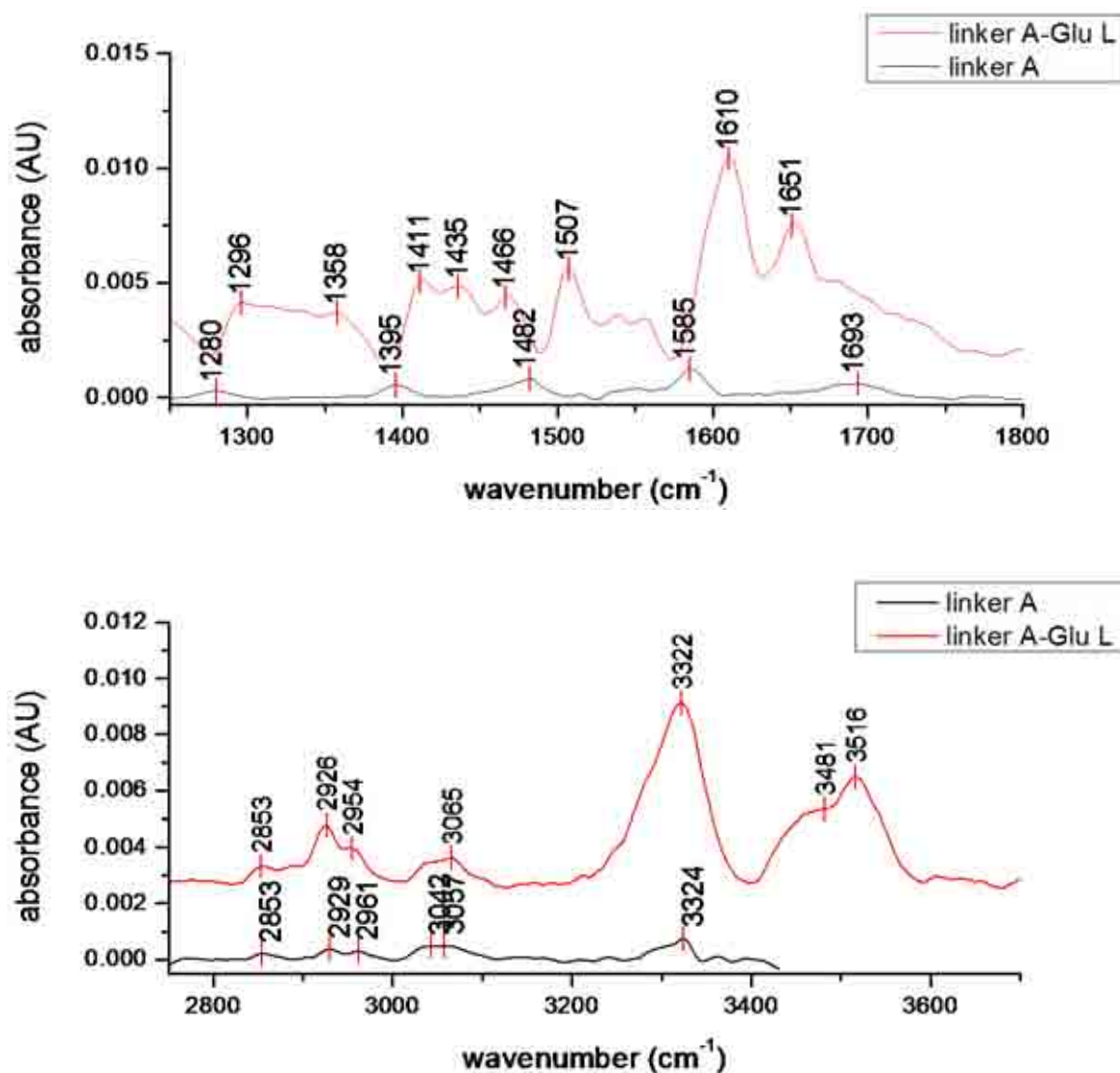
Contact angle measurements confirmed the change in wetting properties of linker A AlaAlaLL surface. The surface was found hydrophilic of a contact angle $54 \pm 3^\circ$, whilst for a neat linker A surface the contact angle equals $85 \pm 2^\circ$.

5.2.2.3 LinkerA-GluL (5C)

A schematic projection of a linker A-GluL surface is presented below:



PM- IRRAS spectra bands are presented in Figure 5-30 and tabulated in Table 5-10. The region of 1600 cm^{-1} consists of several peaks corresponding to amide bond (band I and II), benzene ring and carboxyl C=O vibration. In the region of 3300 cm^{-1} there is a sharp peak visible in the same place as for the acetylene group in linker A, however, in this case the peak corresponds to vibrations of the OH acid group. The proof for modification is then the 3500 cm^{-1} region where peaks from vibrations of symmetric and anti symmetric stretches within amide group can be observed.



5-30 PM IRRAS spectra of linker A-Glu L (red) and linker A (black) monolayers

Characteristic vibration bands¹²:

Table 5-10 Characteristic vibration bands of linker A-Glu L monolayer

Vibration type	Wavenumber/cm ⁻¹	Vibration type	Wavenumber/cm ⁻¹
$\nu_s(\text{COO}^-)$	1296	$\nu_s(\text{CH}_2)$	2853
$\nu_{\text{def}}(\text{CH}_2)$	1358	$\nu_a(\text{CH}_2)$	2926
$\nu_{\text{bend}}(\text{O-H})$	1411	$\nu_{\text{as}}(\text{CH}_3)$	2954
$\nu_{\text{bend}}(\text{CH}_2)$	1435	$\nu_s(\text{C=C})$ benzene ring	3065
$\nu_s(\text{C-C})$ benzene ring	1466	$\nu_s(\text{O-H})$ in COOH	3322
$\nu_{\text{def}}(\text{N-H})$	1507	$\nu_s(\text{N-H})$	3481
$\nu_s(\text{C=O})$	1610	$\nu_s(\text{N-H})$	3516
$\nu_{\text{def}}(\text{O-H})$	1651		

Ellipsometry measurements presented in Figure 5-31 revealed the thickness of the linker A-GluL monolayer to be $1.24 \pm 0.2 \text{ nm}$, again higher than that of linker A alone.

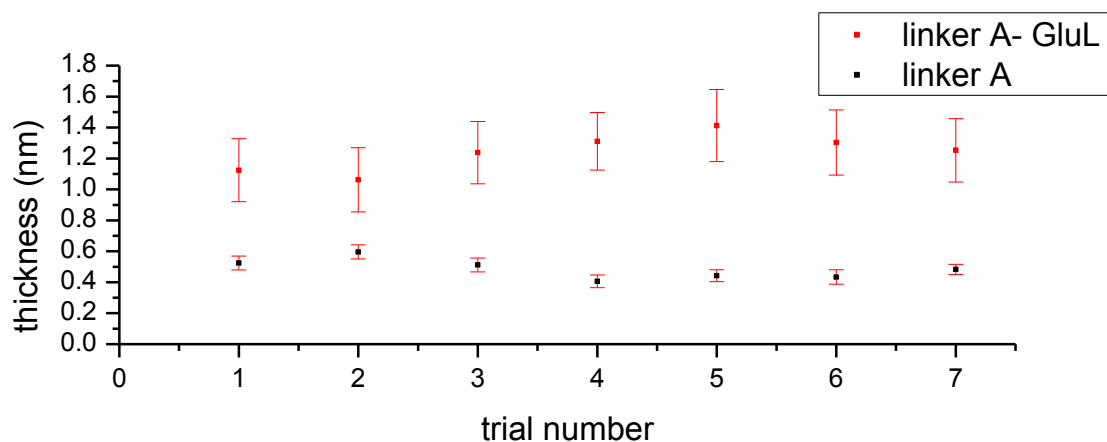


Figure 5-31 Ellipsometry measurements of linker A-GluL monolayers

Electrochemistry results are shown in Figure 5-32. These CVs show similar behaviour of linker A-GluL monolayer to the two previous surfaces with slightly less effect of peak increase of the modified surface as shown in Figure 5-32. These could be explained by the fact that the linker A-GluL monolayer has different molecular structure thus different behaviour in the electrolyte of pH greater than 7.

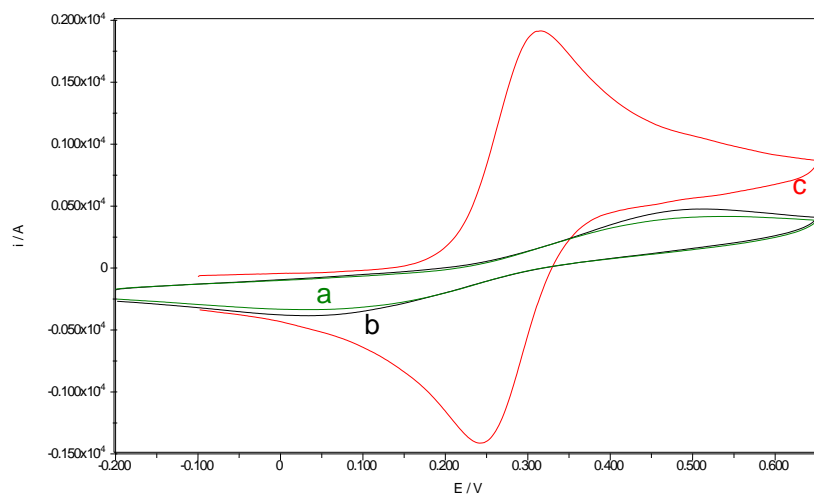


Figure 5-32 Cyclic voltammetry of (a) Linker A monolayer, (b) linker A-Glu L monolayer, (c) bare gold electrode, scan rate 100 mV s^{-1}

EIS measurements showed the specific capacitance to be $56 \pm 2 \mu\text{F cm}^{-2}$ and R_{ct} to be $0.17 \pm 0.01 \text{ k}\Omega \text{ cm}^2$, which is more than for AlaAlaDL and LL functionalities; however, the trend in the capacitance rise and charge transfer resistance drop is the same. Other measurements also showed that this type of functionality is 'more clickable' than dipeptides. A typical EIS plot is presented in Figure 5-33.

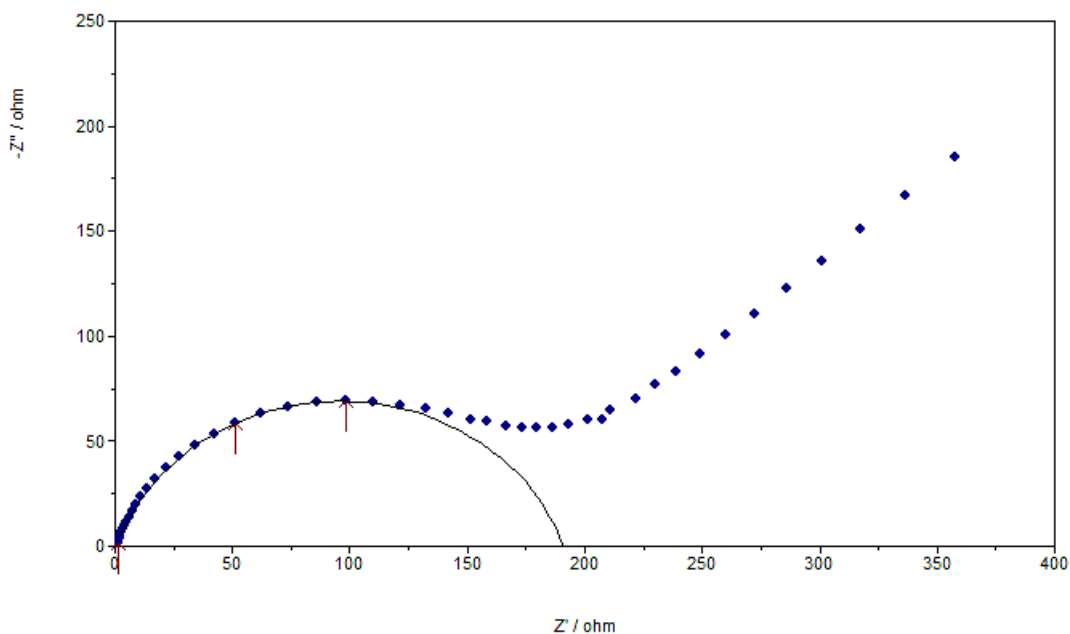
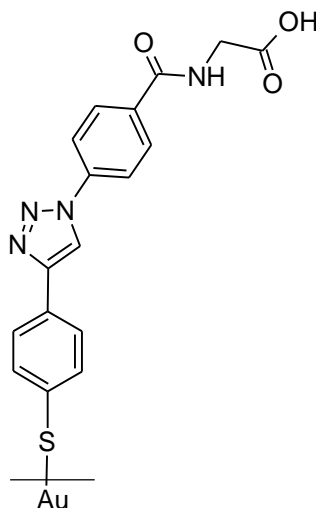


Figure 5-33 Electrochemical impedance spectra of linker A-GluL monolayer, frequency range 10000-0.1 Hz

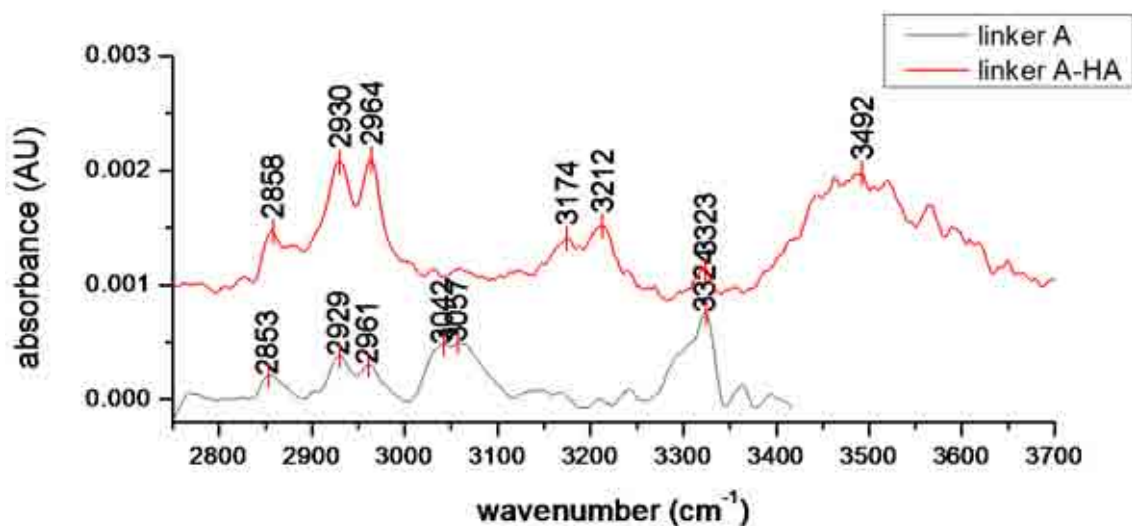
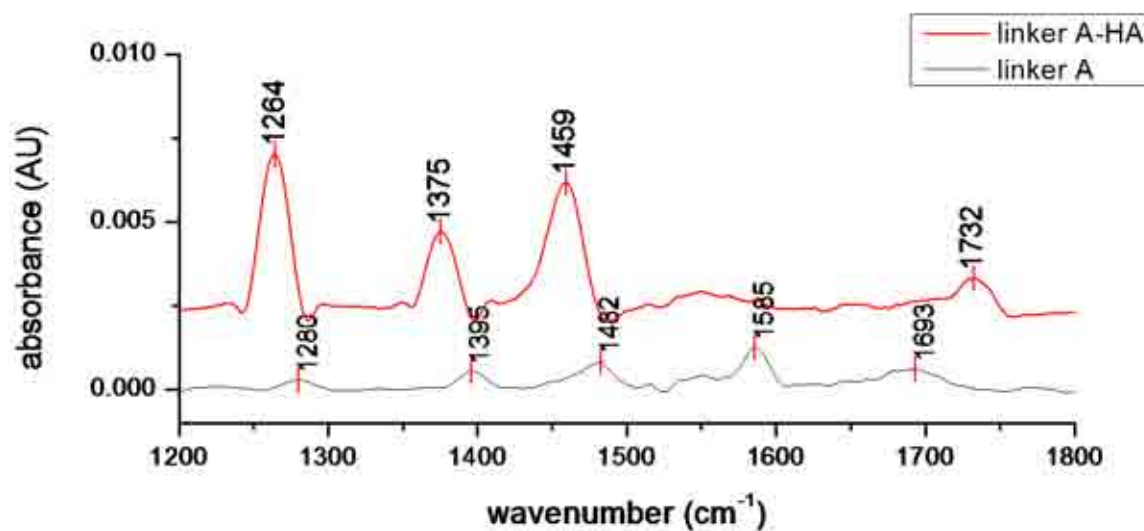
Contact angle studies gave the resulting contact angle of $31 \pm 1^\circ$, in comparison to 85° of a neat linker A.

5.2.2.4 LinkerA-HA (5D)

A schematic projection of a linker-A-HA monolayer is presented below:



PM- IRRAS spectra bands are presented in Figure 5.34 and the prominent bands are tabulated in Table 5-11. The spectrum of linker A-Ha is similar to that recorded for the linker A-GluL surface. The difference is in the intensities of peaks corresponding to acid group vibrations as linker A-HA has only one acid group. Peaks in the region of 1600 cm^{-1} and 3500 cm^{-1} corresponding to vibrations within amide groups are visible. In addition, there are peaks in the region corresponding to 3200 cm^{-1} responsible of the C-H vibrations within the benzene ring and 3320 cm^{-1} coming from OH vibrations within the acid group.



5-34 PM IRRAS spectra of linker A-HA (red) and linker A (black) monolayers

Characteristic vibration bands¹²:

Table 5-11 Characteristic vibration bands of linker A-Ha monolayer

Vibration type	Wavenumber/cm ⁻¹	Vibration type	Wavenumber/cm ⁻¹
$\nu_s(\text{C-N})$	1264	$\nu_{as}(\text{CH}_3)$	2964
$\nu_s(\text{C-N})$	1375	$\nu_s(\text{N-H})$	3174
$\nu_{def}(\text{OH})$	1459	$\nu_{stretch}(\text{O-H})$	3212
$\nu_s(\text{C=O})$	1732	$\nu_s(\text{C-H})$ in acetylene group	3332
$\nu_s(\text{CH}_2)$	2858	$\nu_s(\text{N-H})$	3492
$\nu_a(\text{CH}_2)$	2930		

Ellipsometry results, presented in Figure 5-35, showed that the linker A-Ha monolayer thickness is 1.2 ± 0.2 nm, which is slightly less than for the similar monolayer (linker A-GluL), which consisted of one more carbon in the chain. The difference could lie also in the arrangements of COOH groups.

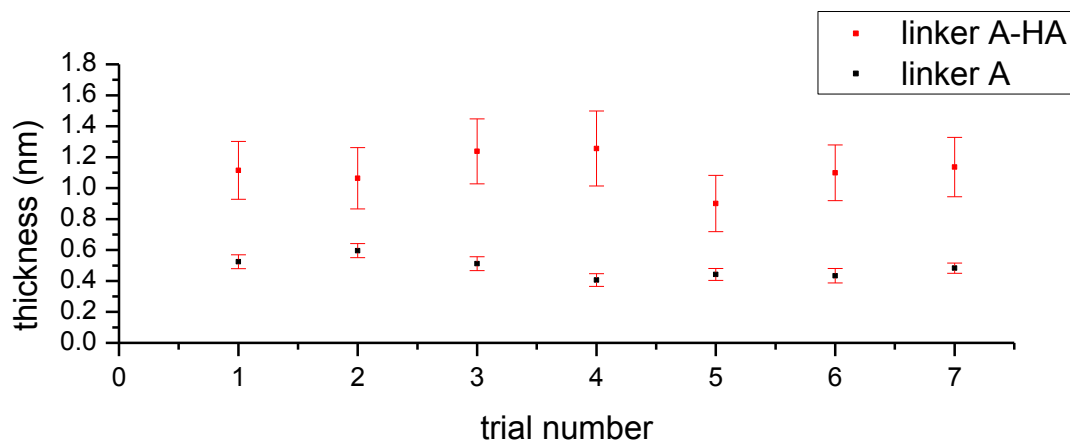


Figure 5-35 Ellipsometry measurements of linker A-GluL monolayers thickness

Electrochemistry measurements revealed the same behaviour of linker A- Ha monolayer as for linker A-GluL surfaces. A typical cyclic voltammogram is presented in Figure 5-36.

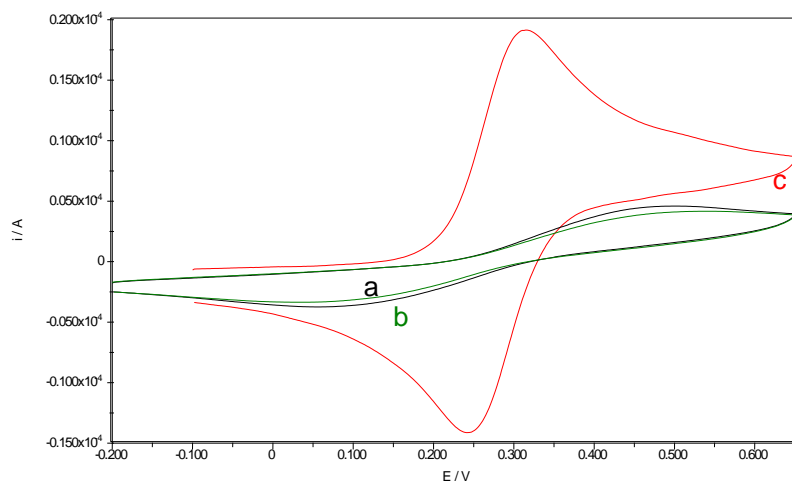


Figure 5-36 Cyclic voltammetry of (a) Linker A monolayer (b) linker A-HA monolayer (c) bare gold electrode, scan rate 100 mV s^{-1}

EIS measurements gave the results for specific capacitance of $49 \pm 1 \mu\text{F cm}^{-2}$ and R_{ct} of $0.6 \pm 0.01 \text{ k}\Omega \text{ cm}^2$, which is comparable to the results for linker A-GluL monolayer. A typical plot of impedance spectra is presented in Figure 5-37.

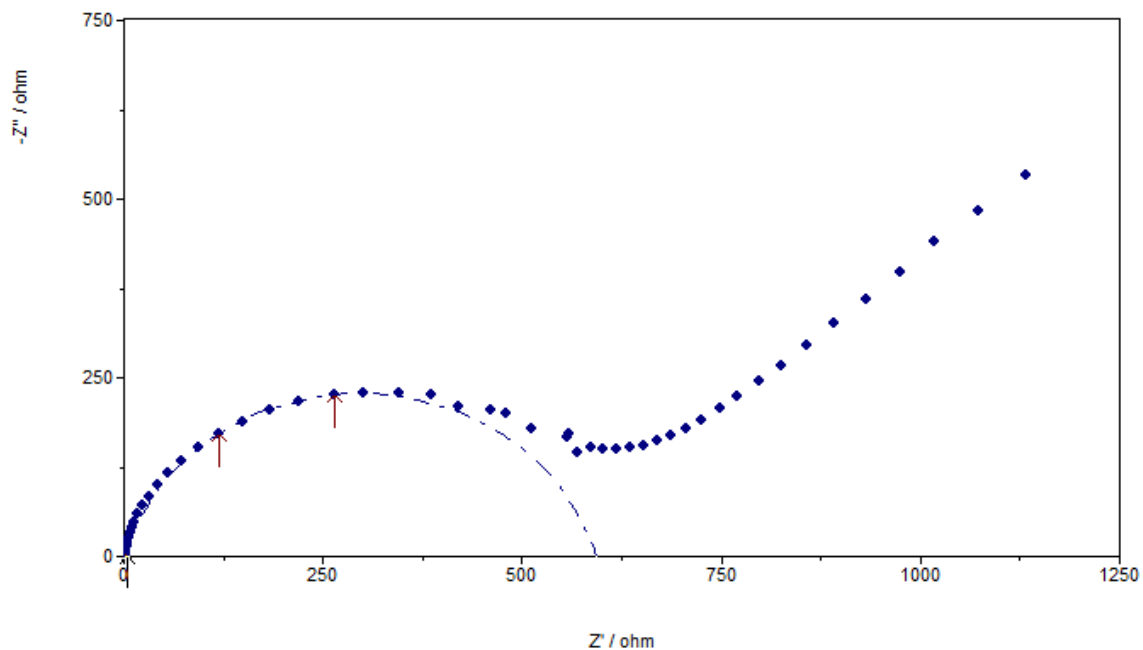
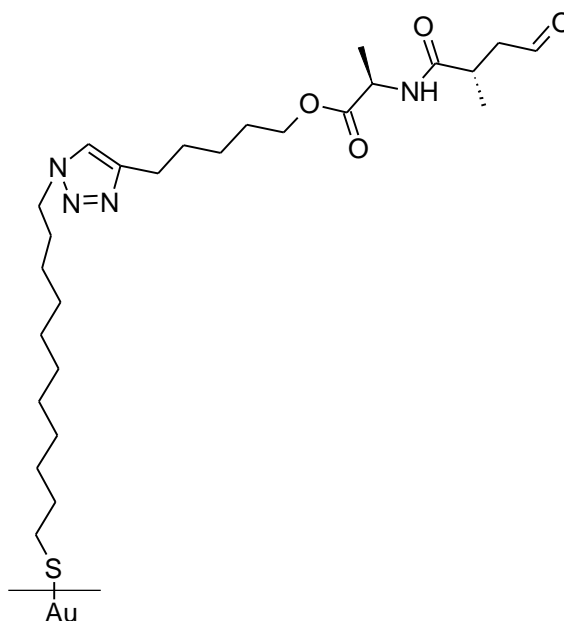


Figure 5-37 Electrochemical impedance of linker A-Ha monolayer, frequency range 10000-0.01Hz

The contact angle was found to be of $35 \pm 1^\circ$, with comparison of $85 \pm 2^\circ$ of a neat linker A surface. This indicates that the surface was successfully modified and it was more hydrophilic following the ‘click’ reaction.

5.2.2.5 LinkerB-AlaAlaDL (6A)

A schematic projection of the monolayer formed by clicking AlaAlaDL functionality on linker B is presented below:



PM-IRRAS measurements confirmed linker B modification. In the spectra presented in Figure 5-38, it could be seen that a finger print peak for linker B (2100 cm^{-1}) vanishes in the spectra of linker B-AlaAlaDL. In addition, in the region of 1100 cm^{-1} , we find peaks corresponding to the ester bonds. In the 1400 and 1600 cm^{-1} band there are broad peaks appearing, which arise from N-H, C-N and C=O vibrations. The characteristic bands are tabulated in Table 5-12.

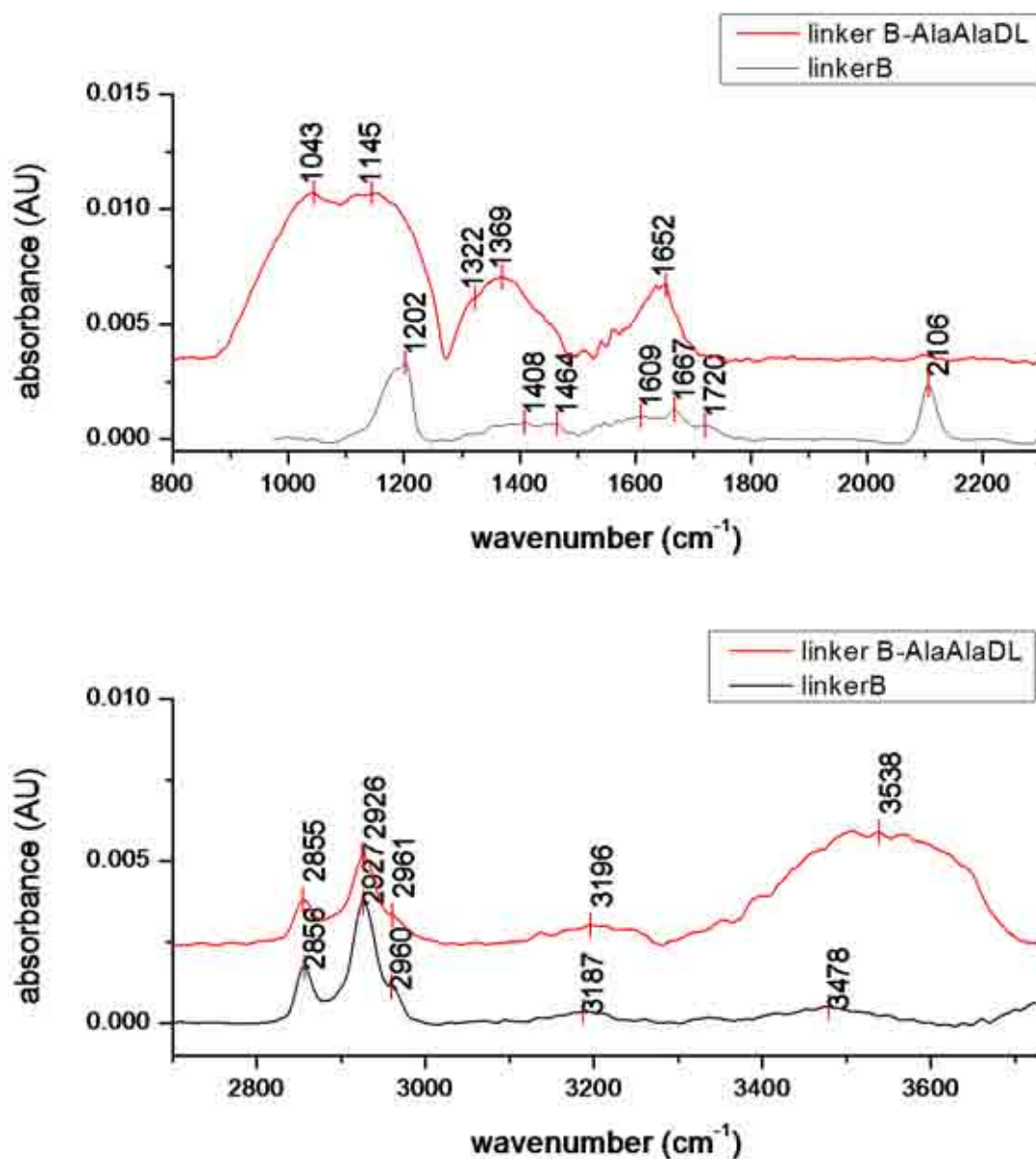


Figure 5-38 PM IRRAS spectra of linker B-AlaAlaDL monolayer (red), linkerB monolayer (black)

Characteristic vibration bands¹²:

Table 5-12 Characteristic vibration bands for linker B-AlaAlaDL monolayer

Vibration type	Wavenumber/cm ⁻¹	Vibration type	Wavenumber/cm ⁻¹
ν_s (C=O) from ester group	1043	ν_a (CH ₂)	2926
ν_s (C=O) from ester group	1145	ν_{as} (CH ₃)	2961
ν_s ((C=O)-O-C)	1369	ν_s (N-H) from amide	3196
ν_s (C=O) amide (I)	1652	ν_s (N-H) from amide	3538
ν_s (CH ₂)	2855		

Ellipsometry measurements were carried out in two steps to observe the monolayer building up. The final thickness of the monolayer was found to be 2.2 ± 0.3 nm. In Figure 5-39 the change in thickness can be seen.

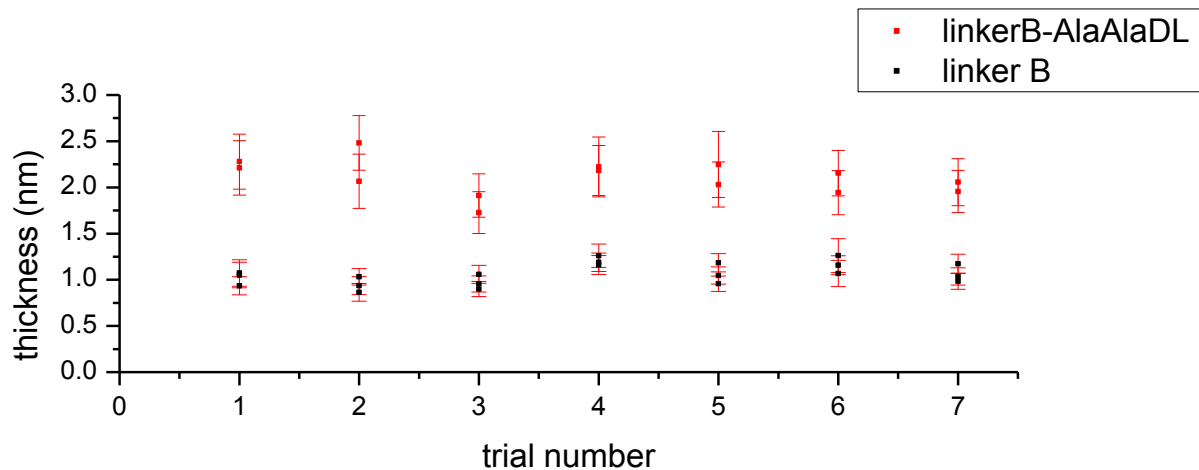


Figure 5-39 Ellipsometry measurements of linker B-AlaAlaDL monolayers

Electrochemistry measurements showed differences between linkerB-AlaAlaDL and linker B monolayer behaviour. The cyclic voltammogram presented in the Figure 5-40 shows wider and more separated peaks for modified linker.

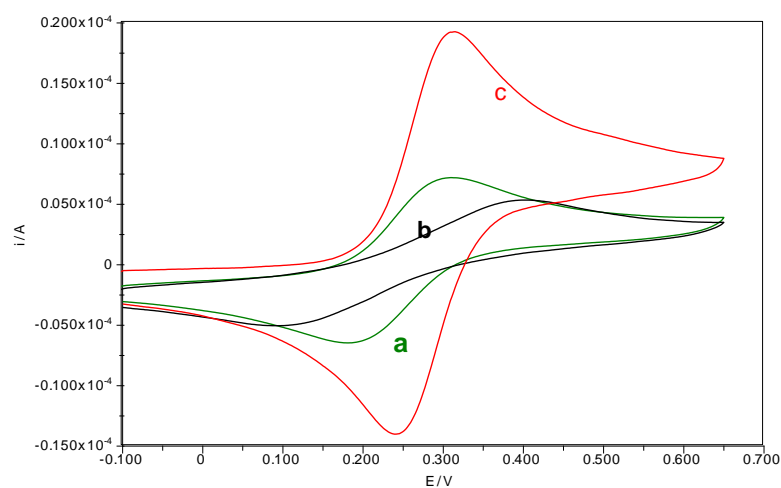


Figure 5-40 Cyclic voltammogram of (a) linker B-AlaAlaDL monolayer, (b) linker b monolayer, (c) bare gold electrode, scan rate 100 mV s^{-1}

EIS measurements, presented in Figure 5-41 revealed the value of specific capacitance to be $8.0 \pm 0.08 \mu\text{F cm}^{-2}$ and $R_{ct} 1.24 \pm 0.02 \text{ k}\Omega \text{ cm}^2$, whereas neat linker B was found to have *ca.* $1.25 \mu\text{F cm}^{-2}$.

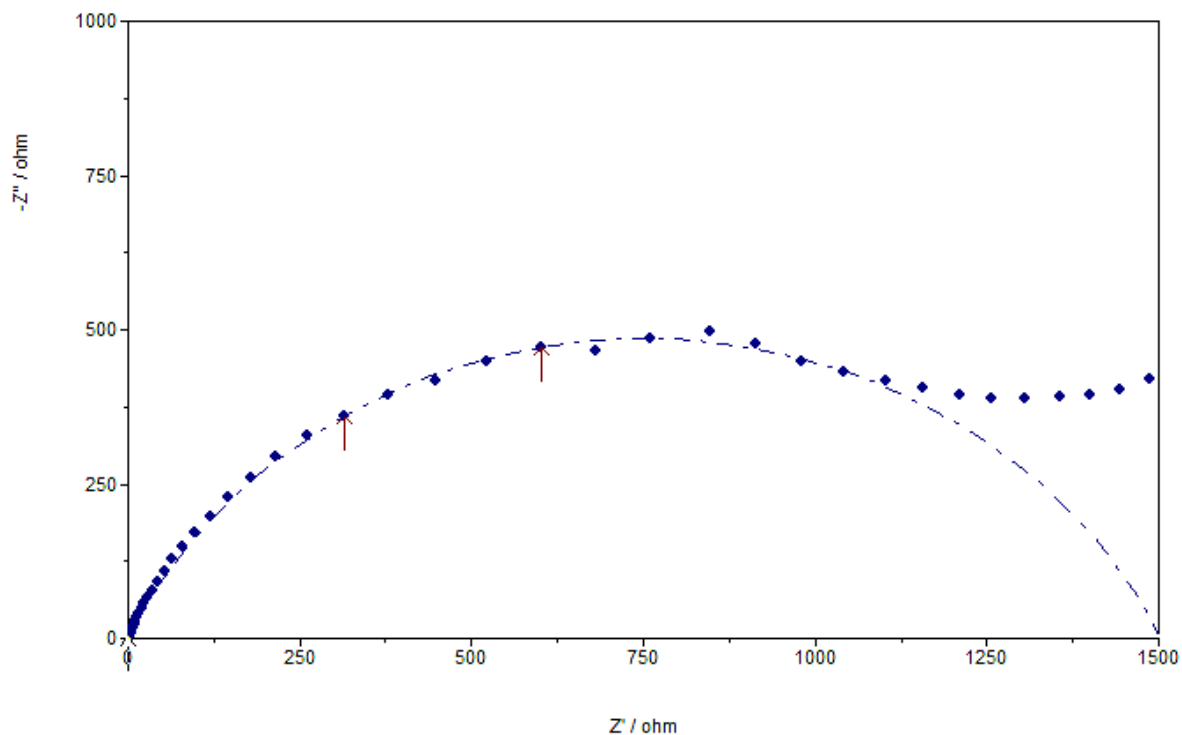
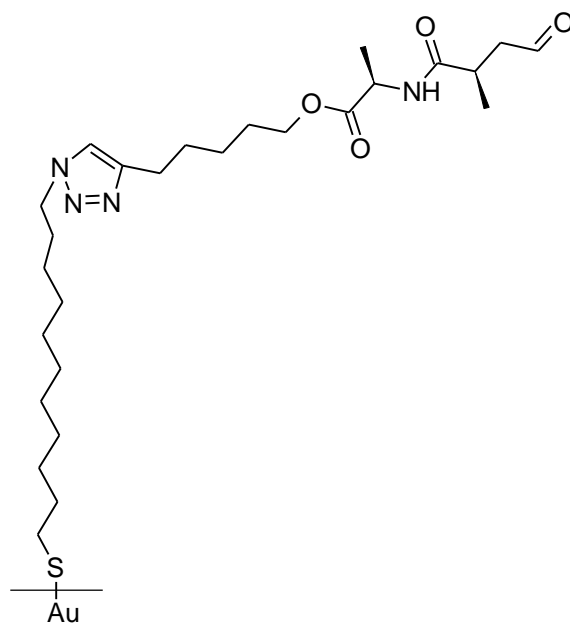


Figure 5-41 Electrochemical impedance of linker B-AlaAlaDL monolayer, frequency range 10000-0.01 Hz

Contact angle measurements confirmed the change in wetting properties. The contact angle was found to be $56 \pm 2^\circ$; compared with $78 \pm 2^\circ$ for the pure linker alone.

5.2.2.6 *LinkerB_AlalaLL (6B)*

A schematic projection of the linker B-AlaAlaLL surface is presented below,



PM-IRRAS measurements confirmed linker B modification. Peaks responsible for additional bonds were observed in the spectra shown in Figure 5-42. A C-O (ester) peak was found at 1300 cm^{-1} . Additionally a peak from N=N-N- group was found at 2100 cm^{-1} confirming the success of the click reaction. The main bands are tabulated in Table 5-13.

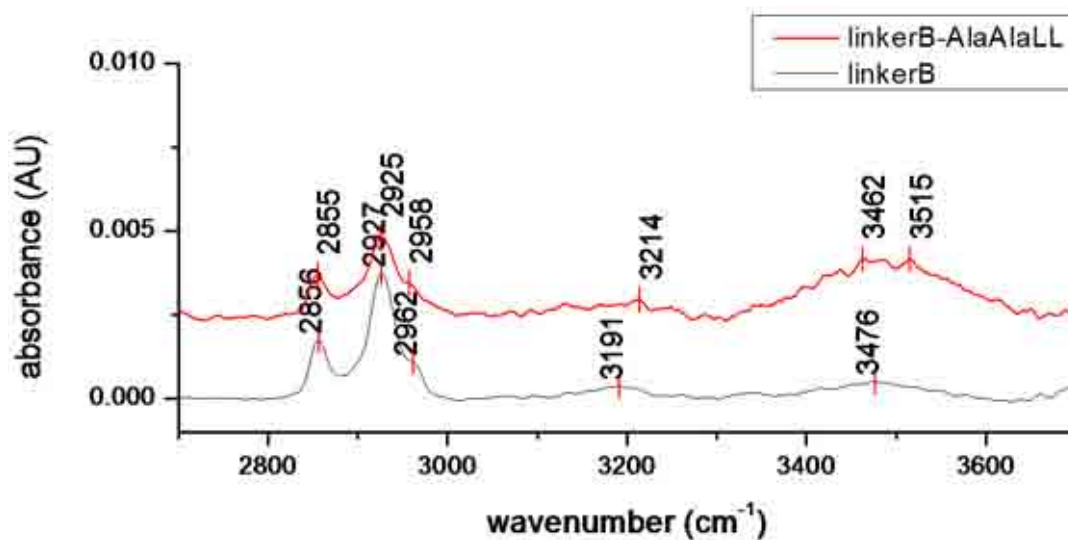


Figure 5-42 PM IRRAS spectra of linker B-AlaAlaLL (red) and linker B (black) monolayers

Characteristic vibration bands¹²:

Table 5-13 Characteristic vibration bands for linker B-AlaAla DL monolayer

Vibration type	Wavenumber/cm ⁻¹	Vibration type	Wavenumber/cm ⁻¹
ν_s (C-O) from ester group	1080	ν_s (CH ₂)	2855
ν_s (C-O) from ester group	1160	ν_a (CH ₂)	2925
ν_s (C=O)-O-C	1305	ν_{as} (CH ₃)	2958
ν_s (C=O)-O-C	1365	ν_s (N-H) from amide	3214
ν_s (C=O) amide (I)	1633	ν_s (N-H) from amide	3515

Ellipsometry measurements, presented in Figure 5-43, were carried out in two steps to observe the monolayer building up. The final thickness of the monolayer was found to be 2.4 ± 0.2 nm.

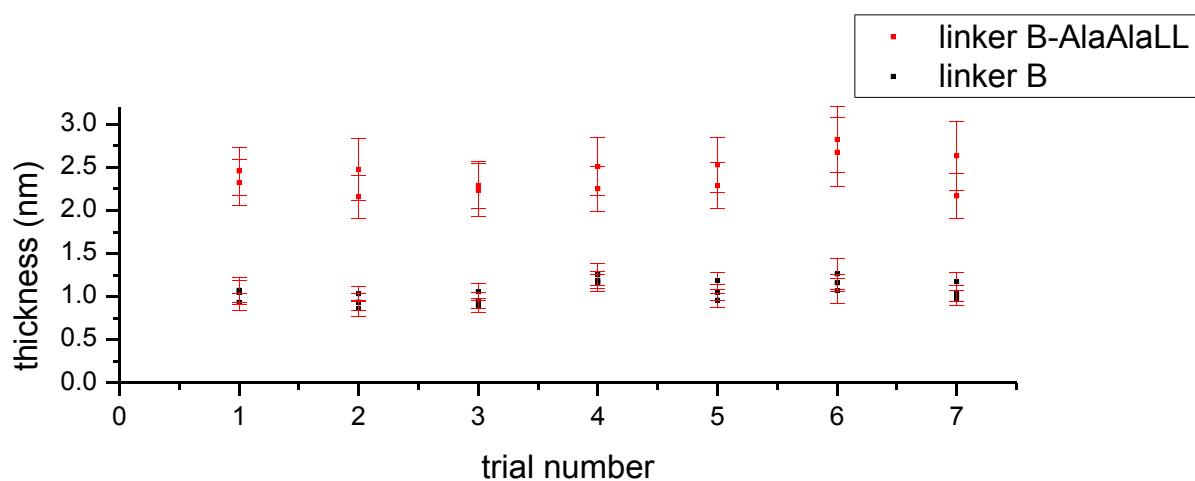


Figure 5-43 Ellipsometry measurements of Linker B-AlaAlaLL monolayer thickness

Electrochemistry measurements confirmed the same behaviour of the monolayer consisting of modified linker B-AlaAlaLL as for the AlaAlaDL enantiomer. A typical cyclic voltammogram is presented in Figure 5-44.

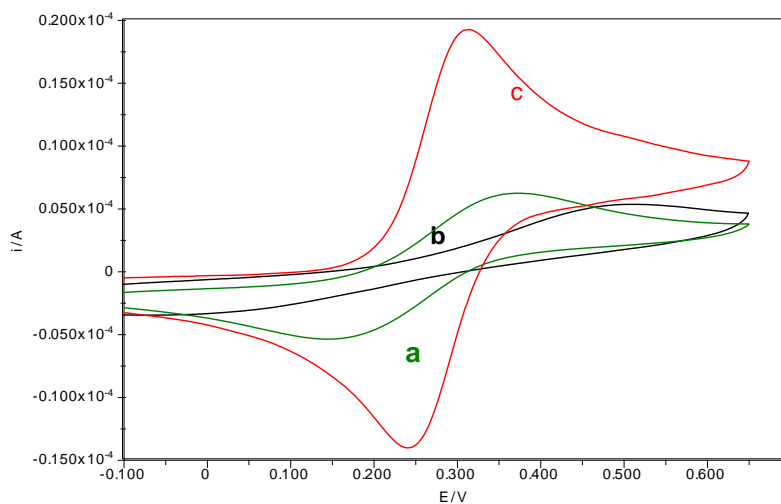


Figure 5-44 Cyclic voltammogram of (a) linker B-AlaAlaLL monolayer, (b) linker B monolayer and (c) bare electrode, scan rate 100 mV s^{-1}

EIS measurements revealed the specific capacitance to be $13.9 \pm 0.8 \mu\text{F cm}^{-2}$ and R_{ct} to be $1.5 \pm 0.03 \text{ k}\Omega \text{ cm}^2$, slightly more than for AlaAlaDL enantiomer.

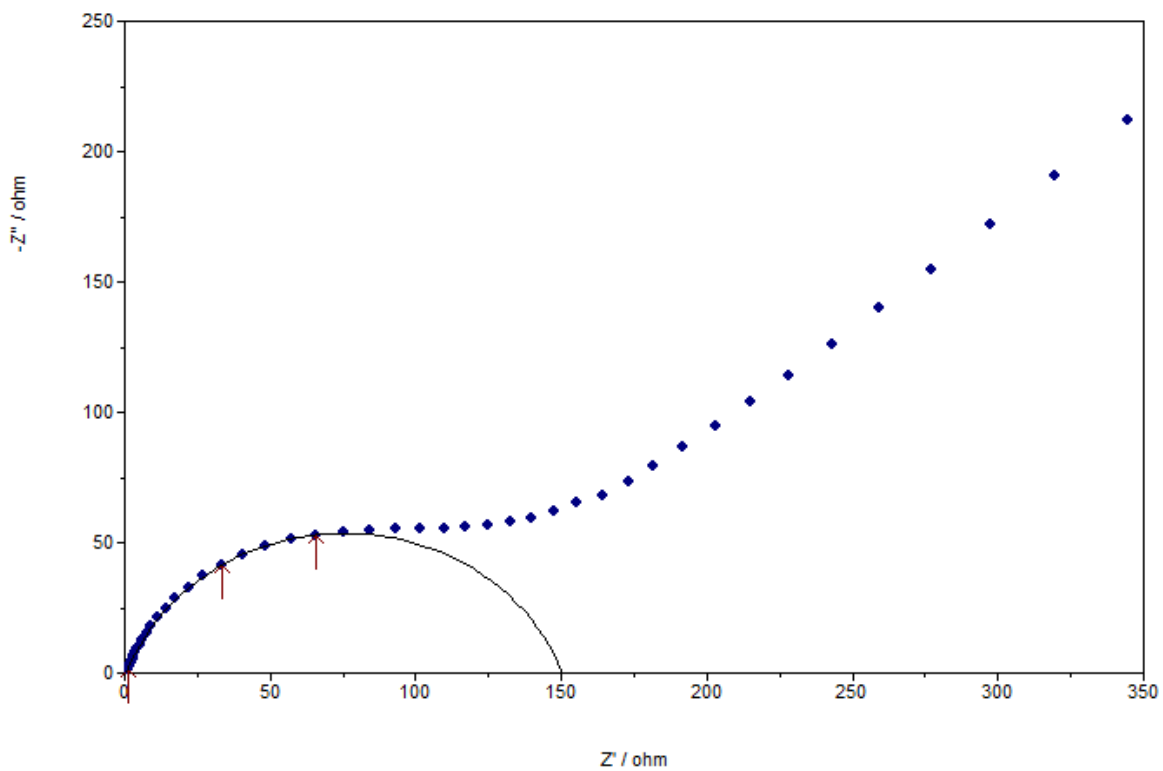
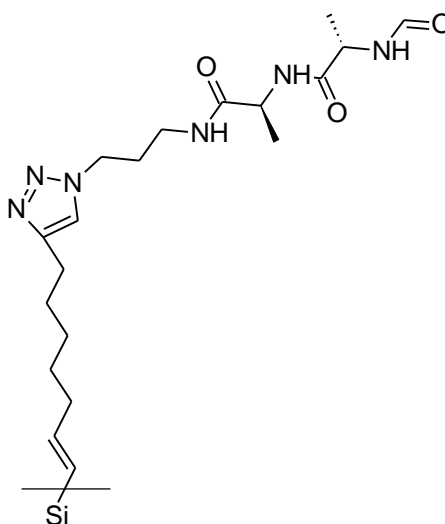


Figure 5-45 Electrochemical impedance of linker B-AlaAlaLL monolayer, frequency range 10000-0.1 Hz

Contact angle measurements confirmed the change in wetting properties. The contact angle was found to be $56 \pm 2^\circ$, whilst for pure linker monolayers its value equals to $78 \pm 2^\circ$.

5.2.2.7 LinkerC-AlaAlaDL (7A)

A schematic projection of a Linker C-AlaAlaDL monolayer adsorbed on silicon is presented below:



Because of the difficulty of using silicon samples with PM-IRRAS only ellipsometry and contact angle microscopy were used to characterise the linker C-AlaAlaLL surface.

Ellipsometry measurements were performed in two steps to observe the monolayer building up. The final thickness of the monolayer was found to be 2.9 ± 0.3 nm, as shown in Figure 5-46, whilst the neat linker C monolayer s had thickness of 1.8 ± 0.2 nm. This increase indicates the attachment of dipeptides to linker C.

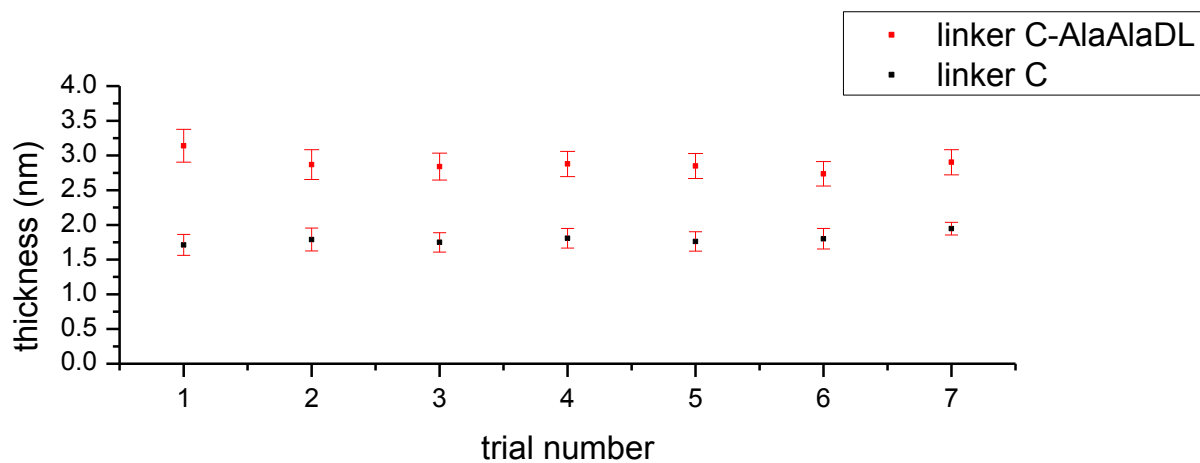
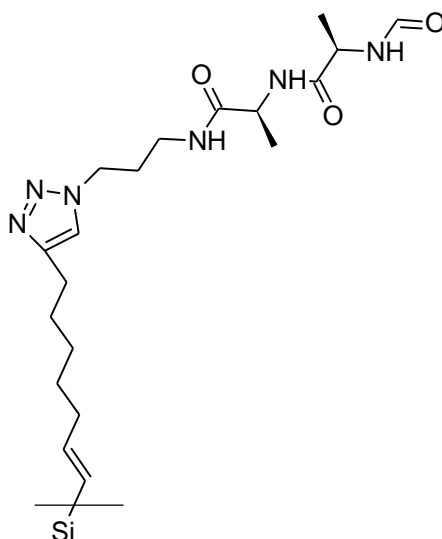


Figure 5-46 Ellipsometry measurements of linker C-AlaAlaDL monolayer thickness

Contact angle measurements demonstrated the change in wetting properties. The contact angle was found to be $34 \pm 2^\circ$; whilst for the pure linker it was $86 \pm 2^\circ$. The modified surface is more hydrophilic than linker C alone, suggesting the successful attachment of the hydrophilic peptide.

5.2.2.8 LinkerC-AlaAlaLL (7B)

A schematic projection of a Linker C-AlaAlaLL monolayer adsorbed on silicon is presented below:



Ellipsometry measurements were performed in two steps to observe the monolayer building up. The results are presented in Figure 5-47. The final thickness of the monolayer was found to be 2.75 ± 0.3 nm.

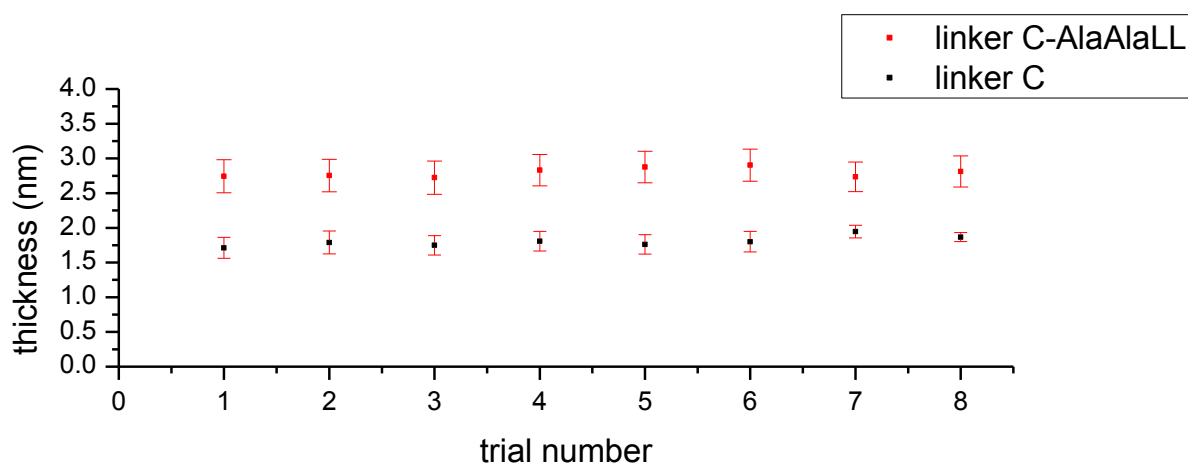


Figure 5-47 Ellipsometry measurements of linker C-AlaAlaLL monolayer on silicon

Contact angle measurements confirmed the change in wetting properties. The contact angle was found to be $34\pm 2^\circ$, whilst for the neat linker it equals to $86\pm 2^\circ$.

5.2.2.9 Parameters comparison of SAMs formed in 'click' chemistry reaction

Table 5-14 presents values of characteristic parameters of monolayers formed in two- steps functionalization.

Table 5-14 Characterisation of surfaces used and produced in 'click' chemistry reactions

Surface	Thickness (nm)	Contact angle ($^\circ$)	C ($\mu\text{F cm}^{-2}$)	R _{ct} ($\text{k}\Omega \text{cm}^2$)
Linker A	0.4-0.6	85 \pm 2	16 \pm 1	1.5 \pm 0.1
Linker A -AlaAlaDL	1.25 \pm 0.2	64 \pm 3	18 \pm 0.5	0.12
Linker A_AlaAlaLL	1.2 \pm 0.2	54 \pm 3	25 \pm 0.5	0.6
Linker A_GluL	1.24 \pm 0.2	31 \pm 1	56 \pm 2	0.17
Linker A_Ha	1.2 \pm 0.2	35 \pm 1	49 \pm 1	0.6
Linker B	1.1 \pm 0.2	78 \pm 2	1.25	18.75
Linker B-AlaAlaDL	2.2 \pm 0.3	56 \pm 2	8.0	1.24
Linker B-AlaAlaLL	2.4 \pm 0.2	56 \pm 2	13.9	1.5
Linker C	1.8 \pm 0.2	86 \pm 2	-	-
Linker C-AlaAlaDL	2.9 \pm 0.3	34 \pm 2	-	-
Linker C-AlaAlaLL	2.75 \pm 0.2	34 \pm 2	-	-

5.2.3 Discussion and conclusions

Click chemistry reactions, when performed in bulk, give almost 100% yields. When the reaction is performed on the surface it is constrained in the way that molecules can approach each other. From the characterization of monolayers prepared for the needs of this study it was found that the type of linker used for the first modification of the surface plays a significant role in its further functionalization. Contact angle microscopy studies, the most sensitive technique for probing surfaces, showed that for the short linker- linker A, following functionalization, the hydrophilic properties of the resulting surface were less than those achieved with long linkers. This could be explained by the fact that to functionalize a gold surface with linker A, deprotecting of the thiol group had to be performed, and also short thiols do not form such densely packed monolayers on gold. In the case of linker B, which consists of eleven carbon atoms the packing density is better, thus the surface after the 'click' will yield a more hydrophilic surface when the same functionality is added as there are more reactive centres in the monolayer and more dipeptides can be attached to the linker monolayer.

Stability of monolayers formed with use of linker A and linker B was investigated by electrochemistry techniques. It was found that during EIS experiments monolayers built of linker A as well as the linker A monolayer itself, decompose more readily than similar monolayers consisting of linker B. Sequential measurements of electrochemical impedance resulted in decreasing of impedance signal. It was found that for linker A monolayers this process is faster than for monolayers consisting of linker B which could be explained by the length of the linker A. Also the type of clicked functionality seems to matter as the specific capacitance for GluL and Ha functionalities was much higher than for AlaAlaDL and LL as can be seen in Table 5-14.

During electrochemistry measurements it was also found that pH of the electrolyte used for CV measurements has tremendous influence on the monolayer response to the applied voltage.

For the needs of this study only a confirmation of monolayer modification was needed thus investigation of exact influence of pH on the monolayers' behaviour was not pursued.

PM-IRRAS studies were performed for each prepared surface. During measurements it was found that surfaces modified by linker B give spectra of higher signals and the reaction is more repeatable which indicates that the length of used linker has significant influence on further functionalization by click chemistry. Also it was noticed that click chemistry reactions on surfaces should be conducted for 12-24 h with gentle nitrogen bubbling, which increases the reaction yield.

Ellipsometry measurements confirmed that thickness of the monolayers built *via* 'click' chemistry is greater than linker monolayers alone and the data are presented in Table 5-14.

For force-distance experiments we used only surfaces that possessed the most hydrophilic properties, to diminish the influence of non-reacted linker molecules on the adhesion measurements; however, this influence cannot be entirely neglected.

5.3 Reference List

1. Porter, M. D.; Bright, T. B.; Allara, D. L.; Chidsey, C. E. D. Spontaneously organized molecular assemblies. 4. Structural characterization of n-alkyl thiol monolayers on gold by optical ellipsometry, infrared spectroscopy, and electrochemistry. *Journal of the American Chemical Society* **2002**, *109* (12), 3559-3568.
2. Seneviratne, V personal communication, 2008.
3. Chidsey, C. E. D.; Loiacono, D. N. Chemical functionality in self-assembled monolayers: structural and electrochemical properties. *Langmuir* **1990**, *6* (3), 682-691.
4. Istaelachvili, J. *Intermolecular and surface forces.*; Academic Press, London: 1992.
5. Mittal, K. L. *Contact Angle, Wettability and Adhesion*; VSP, Utrecht: 2006; Vol. 4.
6. Whitesides, G. M.; Laibinis, P. E. Wet chemical approaches to the characterization of organic surfaces: self-assembled monolayers, wetting, and the physical-organic chemistry of the solid-liquid interface. *Langmuir* **1990**, *6* (1), 87-96.
7. Coates, J. Interpretation of infrared spectra, a practical approach. In *Encyclopedia of Analytical Chemistry vol 12*, Meyers, R. A., Ed.; Wiley: 2000; p 10815.
8. Finot, M. O.; McDermott, M. T. Characterization of n-alkanethiolate monolayers adsorbed to electrochemically deposited gold nanocrystals on glassy carbon electrodes. *Journal of Electroanalytical Chemistry* **2000**, *488* (2), 125-132.
9. Seneviratne, V. Friction Force Microscopy Using Self-Assembled Monolayers: Molecular Scale Roughness and Chiral Interactions-PhD thesis. 2006.
10. Himmelhaus, M.; Eisert, F.; Buck, M.; Grunze, M. Self-Assembly of n-Alkanethiol Monolayers. A Study by IR-Visible Sum Frequency Spectroscopy (SFG). *The Journal of Physical Chemistry B* **1999**, *104* (3), 576-584.
11. Imae, T.; Torii, H. In Situ Investigation of Molecular Adsorption on Au Surface by Surface-Enhanced Infrared Absorption Spectroscopy. *The Journal of Physical Chemistry B* **2000**, *104* (39), 9218-9224.
12. Socrates, G. *Infrared and Raman characteristic group frequencies: tables and charts*; 3 ed.; John Wiley and Sons Ltd.: 2001.
13. Kind, M.; Will, C. Organic surfaces exposed by self-assembled organothiol monolayers: Preparation, characterization, and application. *Progress in Surface Science* **2007**, *84* (7-8), 230-278.
14. Molinero, V.; Calvo, E. J. Electrostatic interactions at self assembled molecular films of charged thiols on gold. *Journal of Electroanalytical Chemistry* **1998**, *445* (1-2), 17-25.
15. Ulman, A. Formation and Structure of Self-Assembled Monolayers. *Chemical Reviews* **1996**, *96* (4), 1533-1554.

16. Shin, T.; Kim, K. N.; Lee, C. W.; Shin, S. K.; Kang, H. Self-Assembled Monolayer of L-Cysteine on Au(111): Hydrogen Exchange between Zwitterionic L-Cysteine and Physisorbed Water. *The Journal of Physical Chemistry B* **2003**, *107* (42), 11674-11681.
17. Ihs, A.; Liedberg, B. Chemisorption of L-cysteine and 3-mercaptopropionic acid on gold and copper surfaces: An infrared reflection-absorption study. *Journal of Colloid and Interface Science* **1991**, *144* (1), 282-292.
18. Zhang, J.; Chi, Q.; Nazmutdinov, R. R.; Zinkicheva, T. T.; Bronshtein, M. D. Submolecular Electronic Mapping of Single Cysteine Molecules by in Situ Scanning Tunneling Imaging. *Langmuir* **2009**, *25* (4), 2232-2240.
19. Linvien, D. *The Handbook of Infrared and Raman Characteristic Frequencies of Organic Molecules*; Academic Press: 1991.
20. Stuart, B. *Biological applications of infrared spectroscopy*; ACOI: Chichester, 1997.
21. Stuart, B. *Infrared spectroscopy, fundamentals and applications*; Wiley: Chichester, 1997.
22. Dakkouri, A. S.; Kolb, D. M.; Edelstein-Shima, R.; Mandler, D. Scanning Tunneling Microscopy Study of L-Cysteine on Au(111). *Langmuir* **1996**, *12* (11), 2849-2852.
23. Dodero, G.; De Michieli, L.; Cavalleri, O.; Rolandi, R.; Oliveri, L.; Dacca, A.; Parodi, R. L-cysteine chemisorption on gold: an XPS and STM study. *Colloids and Surfaces A-Physicochemical and Engineering Aspects* **2000**, *175* (1-2), 121-128.
24. Ramalechume, C.; Berchmans, S.; Yegnaraman, V.; Mandal, A. B. Electron transfer studies through mixed self-assembled monolayers of thiophenol and thioctic acid. *Journal of Electroanalytical Chemistry* **2005**, *580* (1), 122-127.
25. Uvdal, K.; Bod, P.; Liedberg, B. L-cysteine adsorbed on gold and copper: An X-ray photoelectron spectroscopy study. *Journal of Colloid and Interface Science* **1992**, *149* (1), 162-173.
26. Pearson, D. L.; Tour, J. M. Rapid Syntheses of Oligo(2,5-thiophene ethynylene)s with Thioester Termini: Potential Molecular Scale Wires with Alligator Clips. *The Journal of Organic Chemistry* **1997**, *62* (5), 1376-1387.
27. Collman, J. P.; Devaraj, N. K.; Chidsey, C. E. D. Clicking Functionality onto Electrode Surfaces. *Langmuir* **2004**, *20* (4), 1051-1053.
28. Collman, J. P.; Devaraj, N. K.; Eberspacher, T. P. A.; Chidsey, C. E. D. Mixed Azide-Terminated Monolayers: A Platform for Modifying Electrode Surfaces. *Langmuir* **2006**, *22* (6), 2457-2464.
29. Ciampi, S.; Backing, T.; Kilian, K. A.; James, M.; Harper, J. B.; Gooding, J. J. Functionalization of Acetylene-Terminated Monolayers on Si(100) Surfaces: A Click Chemistry Approach. *Langmuir* **2007**, *23* (18), 9320-9329.

6 Project 01- chiral crystallization on surfaces-studies on the origin of chirality

The main objective of this project was to investigate induction of chirality in crystals grown on chirally functionalized SAMs in the process of chiral crystallization. In this study, self assembled monolayers formed on gold deposited on mica or glass were used as a source of nucleation centres. For crystallization two types of method were used: crystallization from solution (fast cooling and evaporation of solvents) and sublimation.

6.1 Chiral crystals from achiral molecules

As described in chapter 2, there is a large number of achiral compounds that display chiral crystallization¹. In this project, representative compounds from this pool were used to investigate induction of chirality in newly formed crystals. From all available compounds we chose those which crystallize easily, have a well defined structure and for which determination of their chirality gives unambiguous results.

Sodium chlorate

As a representative of inorganic compounds NaClO_3 sodium chlorate was chosen. It forms cubic crystals with space group $P2_13$, $Z=4$, $a=6.570 \text{ \AA}^{2-5}$ and normally exhibits a morphology dominated by $\{100\}$ faces with occasionally formed $\{110\}$, $\{120\}$ and some $\{111\}$ facets, as shown in Figure 6-1.

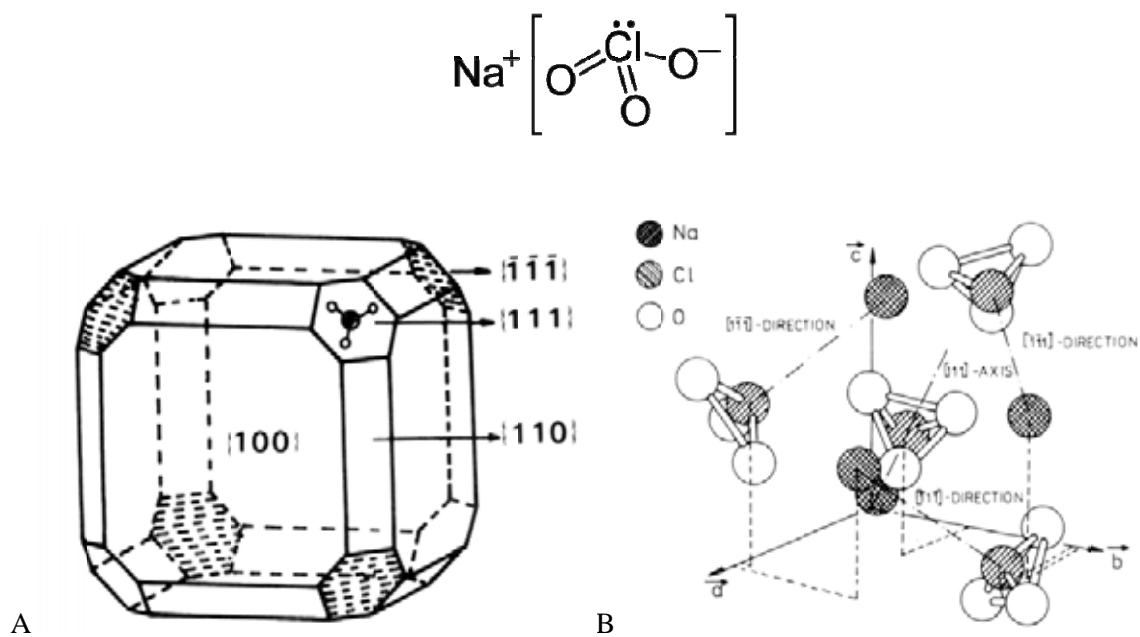


Figure 6-1 (A) The natural habit of sodium chlorate crystals and arrangement of Na^+ and (B) NaClO_3^- in the structure of the crystal⁵

Sodium chlorate crystals have been found to have two morphologies, which are enantiomers, illustrated in Figure 6-2. Its crystals are optically active, whilst its aqueous solution does not exhibit optical activity.

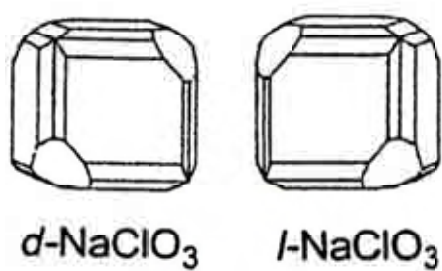


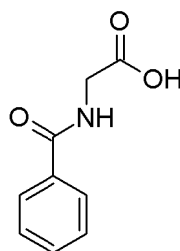
Figure 6-2 Enantiomeric forms of sodium chlorate crystals

Sodium chlorate is known to crystallize the best from aqueous solution. Slow evaporation of solvent and fast cooling give good quality crystals in satisfactory number. Air bubbling through crystallization solutions has also been reported as a method for inducing the nucleation process in sodium chlorate solution.

As a representative of organic compounds, hippuric acid and 2,4-diterbutyl-6-methylphenol (BHT) were chosen. Both hippuric acid and BHT belong to the orthorhombic system, $P2_12_12_1$ group.

Hippuric acid

Hippuric acid crystallizes forming colourless crystals belonging to the orthorhombic system, group $P2_12_12_1$, $Z=4$, $a=8.878\pm 2 \text{ \AA}$, $b=10.544\pm 6 \text{ \AA}$, $c=9.119\pm 5 \text{ \AA}$ ^{6,7}.



The molecular arrangement in a unit cell shows that the hippuric acid molecule is not extended to its maximum length. The COOH group is rotated around the N-C(8) bond forming approximately a right angle with the rest of the molecule as it is depicted in Figure 6-3. That makes one of the carboxyl oxygen atoms form hydrogen bonding with respect to the peptide oxygen atom in the molecule related to the original two fold screw axis parallel to the a axis. The molecules are further held together by a N-H \cdots O hydrogen bond to the peptide oxygen atom in the c -axis screw-related molecule. The hydrogen bonding system of hippuric acid molecule projected along a axis is shown in Figure 6-4.

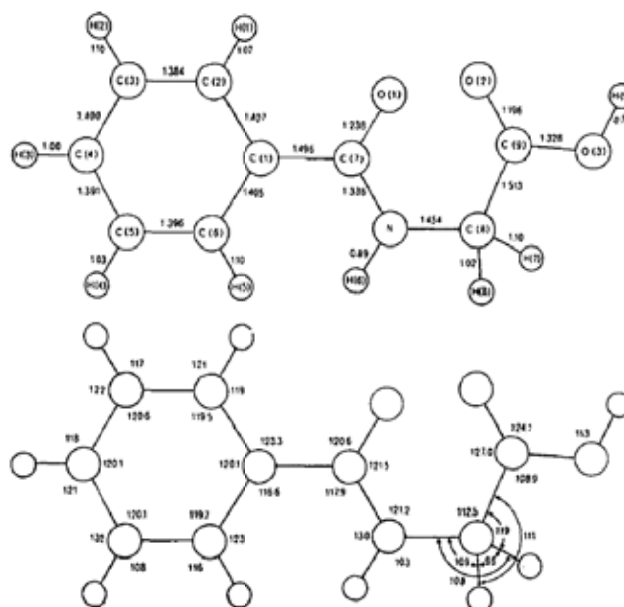


Figure 6-3 Hippuric acid molecule- bond lengths and angles⁶

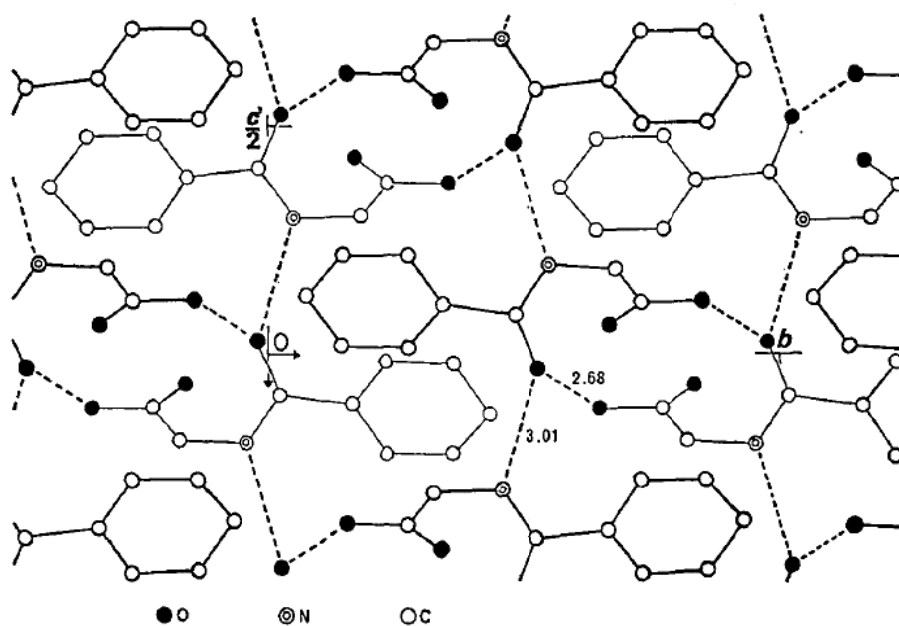


Figure 6-4 Hippuric acid crystal structure projected along a axis showing the hydrogen bonding system⁶

Hippuric acid crystal properties have recently attracted the attention of scientists from electronic and photonic fields. The non-linear optical properties of this material make it a promising candidate for NLO applications.

Hippuric acid crystallizes in two habits- trapezoidal and spike-like as shown in Figure 6-5.

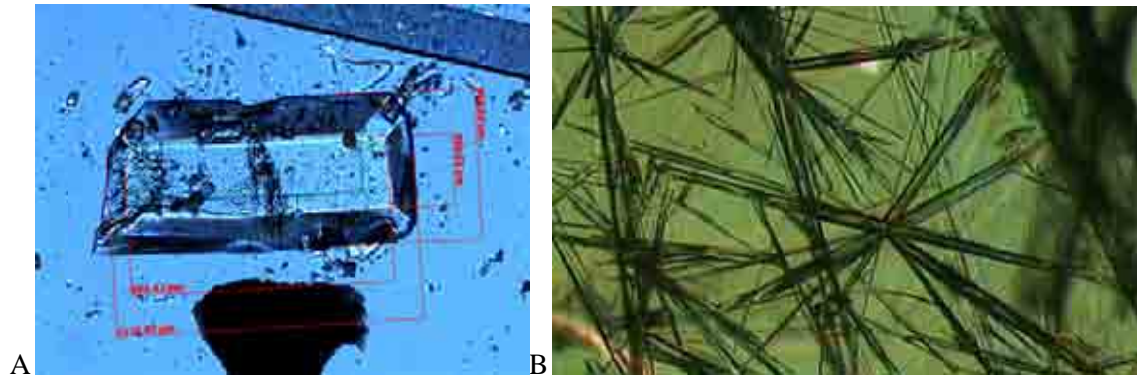


Figure 6-5 (A) Trapezoidal habit of hippuric acid crystal (magnification 50×) and (B) spike like (magnification 100×)

BHT (2,4-ditertbutyl-4-methyl-phenol)

BHT, depicted in Figure 6-6, is best known in the food industry as an anti-oxidizing agent. Its crystals belong to the orthorhombic system and chiral group $P2_12_12_1$, $Z=4$ with cell dimensions: $a=10.38\pm 0.01\text{\AA}$, $b=15.58\pm 0.01\text{\AA}$, $c=8.82\pm 0.05\text{\AA}$ ⁸. Its optical properties are, however, rarely used. BHT crystals are birefringent. Typical habits of BHT crystals are hemimorphite and rhombic pyramid, as shown in Figure 6-7.

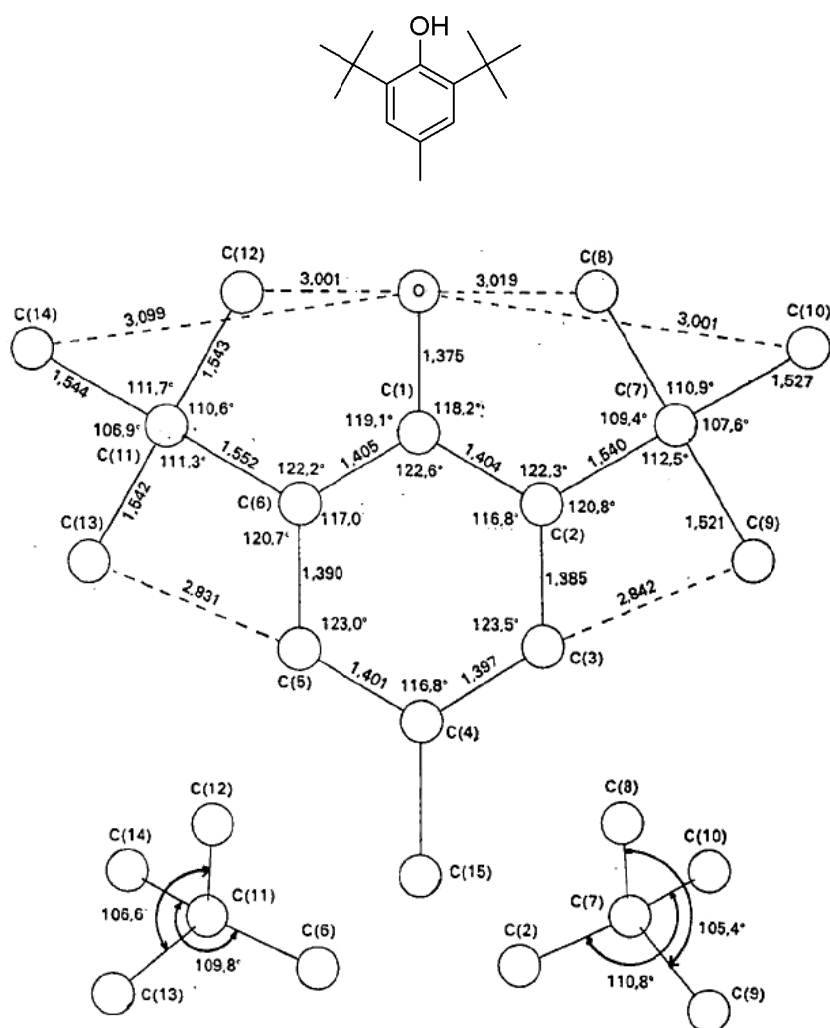


Figure 6-6 Distances and angles between atoms in the 2,6-di-tert-butyl-4-methylphenol (BHT) molecule⁸

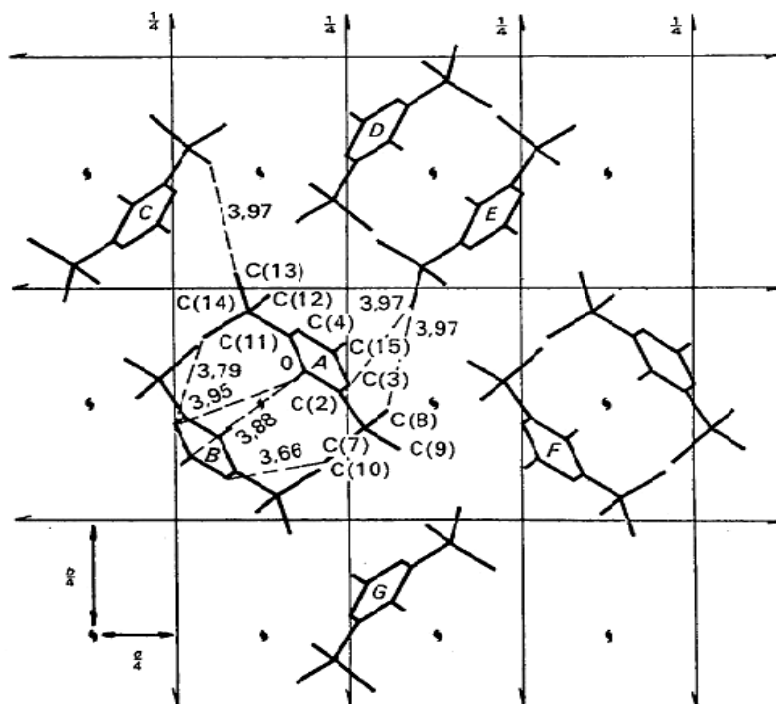


Figure 6-7 Intermolecular distances in BHT crystal and symmetry relations between molecules⁸



Figure 6-8 Typical habits of BHT crystals (magnification 100 \times), crystallization from ethanol

6.1.1 Crystallization on self assembled monolayers

A use of SAMs as nucleation substrates for crystal growth is a rapidly developing field since Aizenberg's experiments with calcium carbonate^{9,10}. So far, SAMs have been used to act as nucleating agents for crystallization of proteins¹¹, enantiomerically pure amino acids¹²⁻¹⁵, semiconductors¹⁶ iron minerals¹⁷, calcium phosphate¹⁸ and carbonate minerals¹⁹⁻²¹. The use of SAMs in crystallization is dictated by the fact they are well characterized and relatively uniform, plus their properties can be varied systematically. In regard to theory of nucleation, nucleation events must involve at least two atoms or molecules. That suggests the size of the nucleation site must be bigger than 1 nm.

Aizenberg and co-workers studied the biomineralization process on different ω -functionalized thiols¹⁹⁻²¹. Their studies revealed that calcite, vaterite and calcium carbonate can be crystallized on the mentioned SAMs and, moreover, the spacing of the headgroups and the spatial orientation determine the polymorph and nucleating face of the new crystals. It was also discovered that in the case of a COOH-terminated SAM the angle of the terminal acid group needs to match that of the carbonate in the crystal structure. The odd and even effect was used to confirm this hypothesis: different angles of COOH groups were used whilst the spacing remained constant. That had an impact on the resultant crystal form¹⁹.

Further studies on crystallization on SAMs confirmed that the crystallographic orientation of the underlying SAM as well as substrate - Au(111) is reflected in the lateral alignment of calcite crystals. Thermal annealing of SAMs and its influence on emerging crystal structure of calcite revealed that resulting crystals formed on {012} faces and linearly aligned with each other, preferring angles of 60° and 120°. This study gave basis to the hypothesis that the calcite crystals formed reflected the directions of 3-fold symmetry.

The microcontact printing technique has been also used to induce nucleation of crystals. The most spectacular use of printed SAMs has been presented by Aizenberg¹⁹. CaCO₃ was crystallized on micropatterned SAMs of HS(CH₂)₁₅COOH (15×15 μm²) separated by 100 μm, surrounded by

hexadecanethiol. Printing was conducted on different metals- Au and Ag. From this study it was determined that two factors control the number of crystals per site- the density and size of printed features and the concentration of the crystallizing solution. Once a nucleus of a critical size forms, mass transport depletes the ions in the surrounding solutions, which hinders nucleation and growth elsewhere.

Polar self-assembled monolayer templates have been also used to nucleate crystallization. 4-iodo-4'-nitrobiphenyl (INBP) has been subjected to crystallization on specially constructed polar aromatic SAMS²³. This study showed that crystals formed on nitro-terminated SAMS were growing along the $-c$ axis and iodo-terminated SAMs promoted growth along the $+c$ axis. This effect is attributed to dipole-directing nitro-iodo contacts.

Confirmation of nucleating properties of SAMs and directing growth of crystals by SAM tailoring has opened a possibility to use SAMs as a selective tool for crystallization. Studies carried out by Mastai showed a use of chiral SAMs as resolving auxiliaries in the crystallization of enantiomers from solutions. Experiments on crystallization of D and L glutamic acid^{15,24} and racemic histidine¹⁴ on chiral surfaces of L and D cysteine showed that chirally functionalized SAMs are active in chiral discrimination by crystallization. It has been discovered that crystals formed at the surfaces were of opposite chirality. Unfortunately the resulting enantiomeric excess was not very high in comparison with selectivity of chromatographic methods. Two hypotheses were given as an explanation of the enantiomeric selectivity at the surface/solution interface. The first proposes that chiral impurities control chiral discrimination during crystallization, the second proposes a stereoselective adsorption mechanism of the crystallization on chiral surfaces. Studies of Mastai and Dressler gave a basis for further investigation of chiral nucleation at surfaces and were an inspiration for this project.

6.2 Experimental details

6.2.1 Materials

6.2.1.1 Gold surfaces –substrate for SAMs preparation

All gold surfaces used for chiral crystallization were deposited on a glass substrate and prepared according to the procedure described in section 4.1 and 4.2.

Glass material used for gold deposition was borosilicate microscope glass slides (Menzel)

Gold films were of thickness of 30 and 100 nm with the adhesive layer of 3 nm of chromium. Gold substrates used were of roughness less than 15 nm to prevent nucleation being caused by surface morphology rather than functionalization. Images of typical substrates are presented in Figures 6-9 and 6-10.

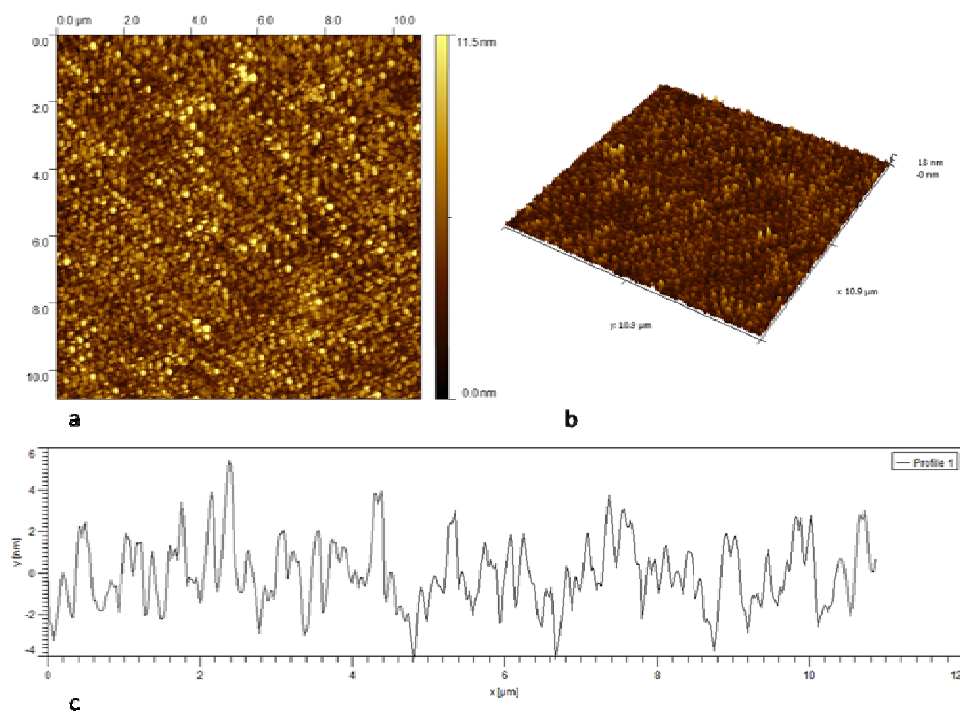


Figure 6-9 AFM image of 30 nm of gold deposited on glass (a) topography (b) 3D projection (c) profile

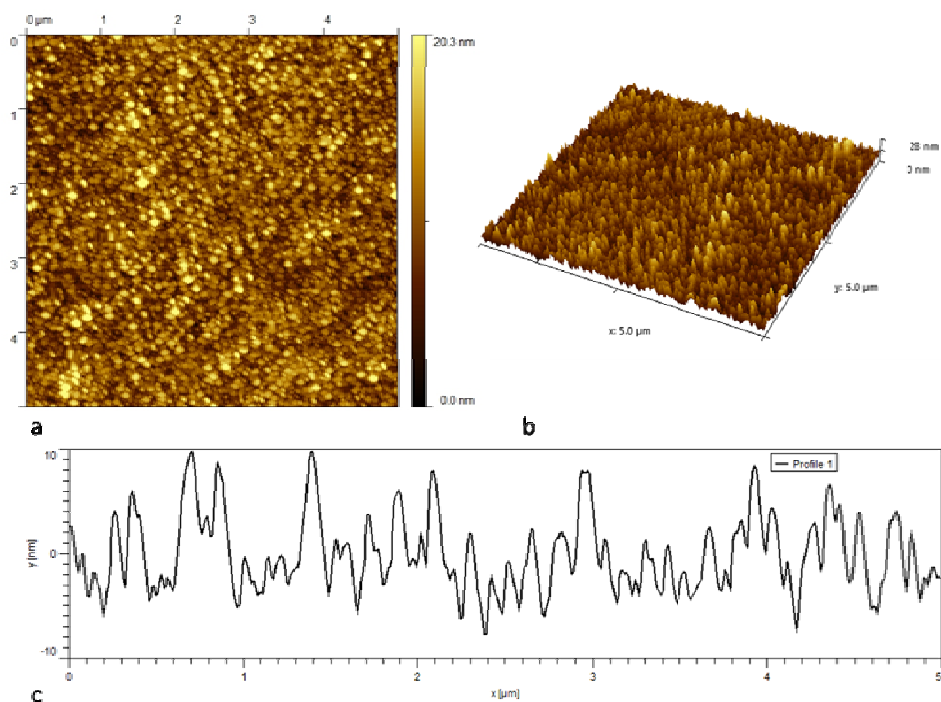


Figure 6-10 AFM image of 100nm of gold deposited on glass (a) topography (b) 3D projection (c) profile

6.2.1.2 Thiols for SAMs preparation

Self assembled monolayers used for Project 1 were prepared of:

Table 6-1 Chiral and achiral surfaces prepared for experiments

Achiral surfaces	Dodecanethiol (DDT)
	12-mercaptododecanoic acid (MDA)
Chiral surfaces	Cysteine L
	Cysteine D

DDT and MDA were used at the concentration of 1 mM as ethanol solutions. Self assembly was carried out for 24 ± 1 h.

Aqueous solutions of cysteine L and D were prepared at 1 mM concentration (water solutions). The assembly process was carried out for 24 ± 1 h.

Chemicals for crystallization experiments were bought from Aldrich. All compounds were of analytical grade.

Table 6-2 Compounds used in experiments of chiral crystallization

inorganic	Sodium chloride NaClO_3
organic	Hippuric acid (HA)
	2, 6-ditertbutyl-4-methylphenol (BHT)

6.2.2 Crystallization process –experimental details

Methods used for crystallization of target compounds are presented below.

6.2.2.1 Sodium chlorate

Sodium chlorate was crystallized by slow evaporation of solvent and fast cooling. Both methods were performed with the crystallization solution of the concentration near saturation.

For the slow evaporation method, solutions of sodium chlorate in water were used. Mixtures were made up by weighing the desired amount of sodium chlorate, transferring it into a volumetric flask and topping up with ultrapure water. Solutions were sonicated in order to dissolve all of the salt and maintained at 25°C for 40 min. The solutions were always made up fresh and used entirely during experiments (solutions were not stored).

The concentration of sodium chlorate used for experiments was of 9.80 g mL^{-1} (close to the concentration of the saturated solution 1.005 g mL^{-1} in 25°C according to the solubility chart-Appendix 2).

Slow evaporation of solvent was conducted at the temperature of 25°C, in a home-made box with controlled temperature and air flow.

Fast cooling crystallization experiments were conducted at a temperature range of 25-11°C with the cooling rate $1^{\circ}\text{C min}^{-1}$, which was found to be optimum during benchmark experiments.

Solvent evaporation crystallization

Samples subjected to the crystallization experiment were placed in glass shell vials with a flat bottom, which were cleaned beforehand according to the procedure 4.1. Samples were placed perpendicular to the bottom of the vials in order to prevent deposition of crystals formed not at the SAM/solution interface. After placing samples into vials, the crystallization solution was gently poured into vials so that a depth of solution was $1\frac{1}{2}$ times the height of the sample in the vial as illustrated in Figure 6-11. This was to allow for evaporation of the solution. It was important that the top of the sample never protruded from above the surface of the solution, to prevent the nucleation at the top of the sample edge. After that the sample was covered with a cap with orifices in order to control better the evaporation.

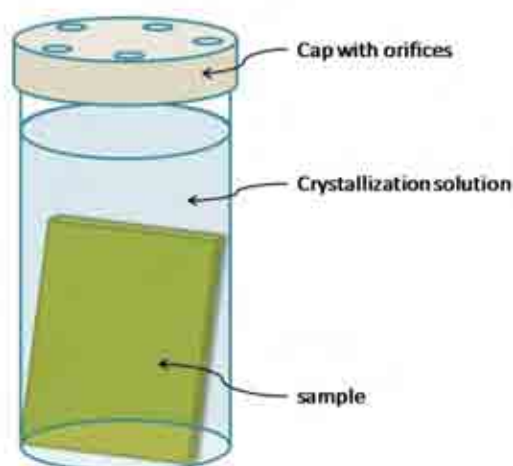


Figure 6-11 A cartoon of sample set-up

After the crystallization finished, the caps were removed and xylene was poured on top of the crystallization solution. The use of xylene had two reasons, firstly to prevent further crystallization

and secondly to ease removal of samples from the crystallization solutions. Samples were removed from crystallization solutions by very slowly dragging them through the xylene top layer, handling with tweezers. After removing, samples were placed in special a box for the xylene to be evaporated and then they were subjected to crystal analysis.

Fast cooling crystallization

Experiments using fast cooling crystallization were done using a water bath with cooling/heating rate control –Grand CamLabs UK. Samples were prepared in the same way as for the slow evaporation of solvent experiment with one exception- xylene was added on the top of the crystallization solution just before the crystallization experiment started, to prevent evaporation of solvent and to ease the removal of samples after crystallization. This set-up is illustrated in Figure 6-12.

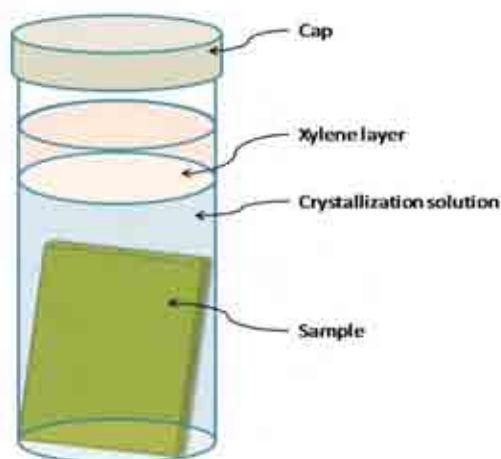


Figure 6-12 A cartoon of the sample set-up for fast cooling experiments

6.2.2.2 Hippuric acid

For hippuric acid crystallization, slow evaporation of solvent and sublimation at melting temperature was used to obtain crystals at the surface of self assembled monolayers.

Slow evaporation

Slow evaporation of solvent was performed using crystallization solutions of hippuric acid in ethanol. The concentration of solutions was 0.69 g mL^{-1} , which is close to saturation, according to the hippuric acid solubility chart. Experiments were carried out as described for sodium chlorate. No additional layer of xylene was used as hippuric acid does not crystallize rapidly. After, the crystallization samples were removed from crystallization solutions and subjected to crystal analysis.

Sublimation at melting temperature

Sublimation at melting temperature was performed with the experimental set up presented in Figure 6-13.

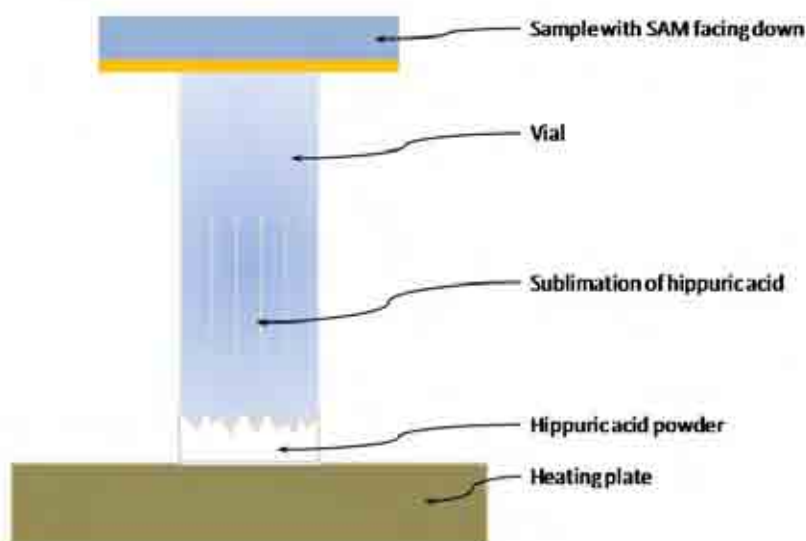


Figure 6-13 A cartoon of sample set up for crystallization by sublimation at melting temperature

Hippuric acid melts at 187°C . A heating plate was set for a temperature not higher than 180°C , below the melting temperature at which hippuric acid decomposes. At 176°C , sublimation can be observed.

1 mg of hippuric acid (analytical grade, Aldrich) was used for each crystallization. Tubes used for experiments were of 4 cm height. This allowed the vapour to cool down and crystallize. Crystallization was carried out for not longer than 3 minutes. After that time, crystals formed at gold functionalized with SAMs were visible to the bare eye.

6.2.2.3 BHT

Crystallization of BHT on self assembled monolayers was performed only by slow evaporation of solvent. Ethyl alcohol of HPLC grade was used for preparation of crystallization solutions of BHT. The concentration used for experiments was: 0.1 g mL^{-1} which is close to the saturation concentration, according to the solubility chart. Experiments were carried out following the procedure for hippuric acid.

6.2.3 Determination of chirality

Sodium chlorate

For sodium chlorate crystals, polarized light microscopy was used to determine the chirality. Sodium chlorate, belonging to the cubic system, is known to exhibit its optical properties by subtraction of certain colours from white light and moderate to maximum transmission of other colours. The hue of the colours changes as a polarizer is rotated and increases or decreases in order, depending on whether short wavelength colours or long wavelength colours are transmitted with maximum intensity by the analyser when it is rotated. When (-) crystal is subjected to analysis by polarizing light microscopy, a change of the polarizer position for 7 degrees left from crossed polarized results in a colour change. The crystal becomes reddish. The same operation in the opposite direction results in that the crystal becomes blue-ish. The intensity of the colour depends directly on the thickness of the crystal subjected to analysis. The thicker the crystal, the more intense the colour is.

For sodium chlorate crystals, changes in polarization of light going through the crystal result in change in colour as presented in Figure 6-14:

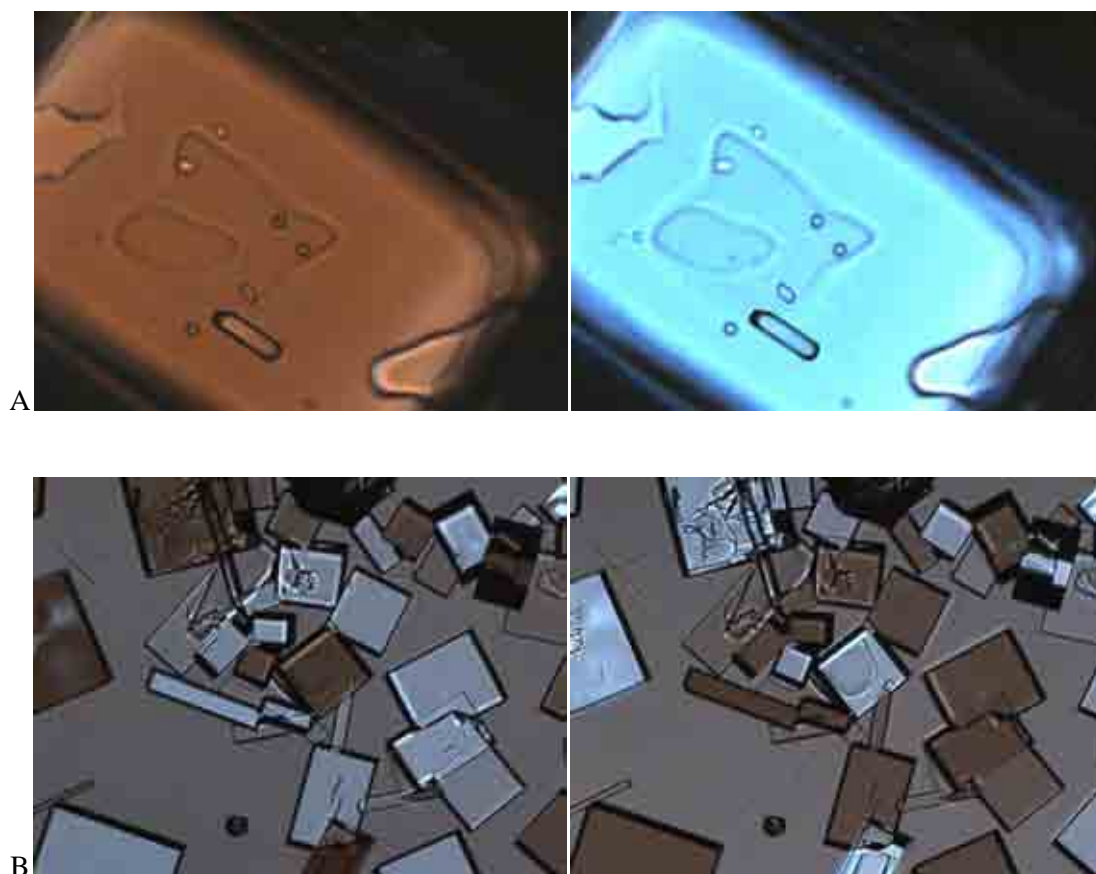


Figure 6-14 Sodium chlorate crystals in polarized light: (A) (-)-sodium chlorate crystal with polarizer positions 87 (red) and 93 (blue), (B) a group of sodium chlorate crystals in polarized light with 87 and 95 degrees of polariser

Hippuric acid

Hippuric acid crystals are made of achiral molecules; however, the crystals formed are chiral. Due to the number of refractive indices (proportional to optical axes), polarizing light microscopy cannot be used as a technique for its crystal chirality determination.

As mentioned before, birefringency of the crystal obscures the chiral effect under polarized light, as depicted in Figure 6-15.

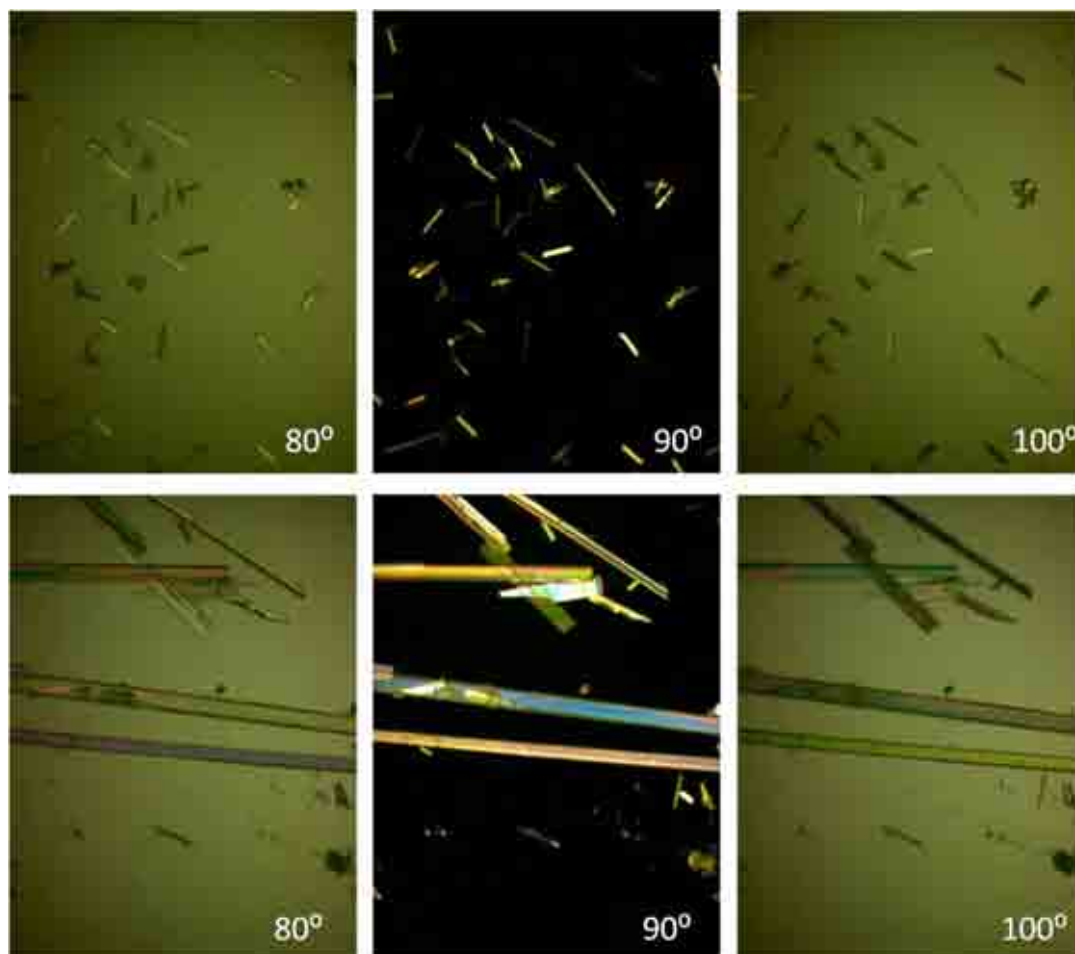


Figure 6-15 Hippuric acid crystals in polarized light, the first set (magnification 50x) shows pseudo recognition of chirality, the second (magnification 100x) shows a variety of colours which makes distinguishing between enantiomers ambiguous

For this purpose either circular dichroism spectroscopy or NSOM measurements must be used. A typical CD spectrum achieved for two enantiomeric crystals is presented in Figure 6-16:

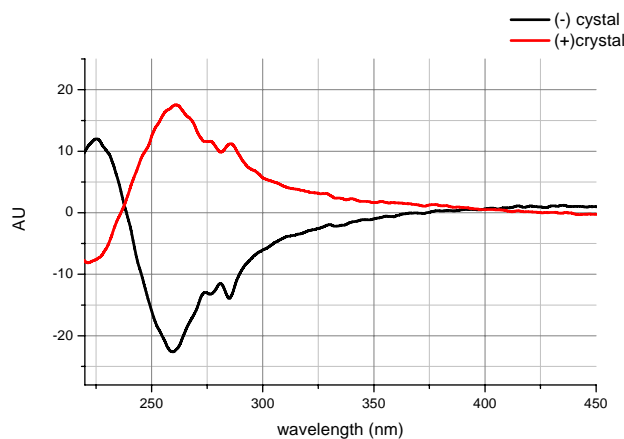


Figure 6-16 CD spectra of two enantiomeric crystals of hippuric acid.

BHT

BHT is a classic birefringent crystal which, when turned in polarized light, changes its colour every 45° rotation.



Figure 6-17 BHT crystals in polarized light. Change in light polarization causes a change in a colour; however any movement of the crystal changes the colour as well. This makes chirality measurements impossible to conduct, as was the case for hippuric acid.

Due to the classic birefringent effect, linear polarized light microscopy cannot be used as a method of chirality determination. However subjecting crystals of BHT to circular dichroism spectrometry measurements gives us a chance to distinguish between enantiomers. Typical CD spectra of two enantiomeric crystals of BHT are presented in Figure 6-18:

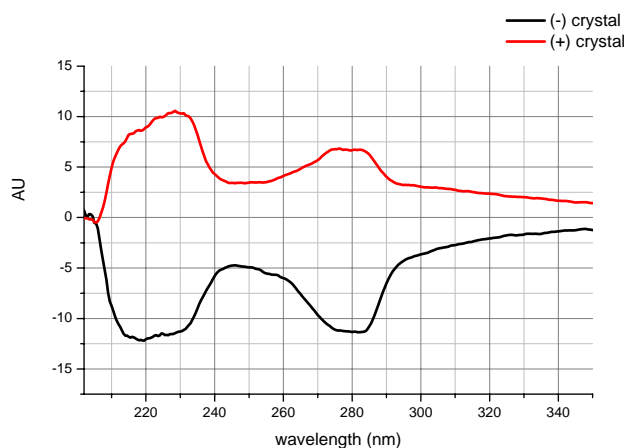


Figure 6-18 CD spectra of two enantiomeric crystals of BHT (KBr pellet technique).

6.3 Results

6.3.1 Crystallization of sodium chlorate on achiral SAMs

Objective: Investigation of nucleating properties of self assembled monolayers in sodium chlorate crystallization.

Sodium chlorate was firstly subjected to crystallization on non-modified gold surfaces and modified gold surfaces for investigation into the preference of crystallization and process optimization.

The following substrates were chosen as substrates for crystallization:

- Bare gold
- Gold modified with DDT
- Gold modified with MDA
- Gold modified with DDT by microcontact printing
- Gold modified with MDA by microcontact printing

Crystallization on bare gold substrate

Bare gold was subjected to 20 crystallization experiments for sodium chlorate. None of the gold surfaces were found to act as a source of nucleation. All of the crystals which formed were found at the bottom of crystallization vessels or the edges of the samples, where roughness was high enough to cause nucleation.

During these experiments it was found that due to the high solubility of sodium chlorate in water it is very hard to subject the obtained samples to analysis. Removing specimens from the crystallization solutions resulted in rapid crystallization of sodium chlorate from liquid remaining on the surface. A special system of removing samples from the crystallization solution has been

developed to resolve this problem. Using xylene (non-miscible with water, organic solvent) allowed removing samples from crystallization solutions with only a small residue of solution remaining.

Crystallization on gold substrates modified with DDT and MDA.

Crystallization on gold modified with DDT and MDA was conducted in order to investigate if self assembled monolayers can act as nucleating agents for sodium chlorate, and what type of modification is preferred- hydrophobic or hydrophilic.

Experiments gave positive results either in slow evaporation and fast cooling experiments for both types of methods of modification- entire surface modification with SAM and modification with a microcontact printing technique. Representative pictures of sodium chlorate crystals grown on DDT and MDA on entirely modified gold surfaces are presented in Figures 6-19 A and B:

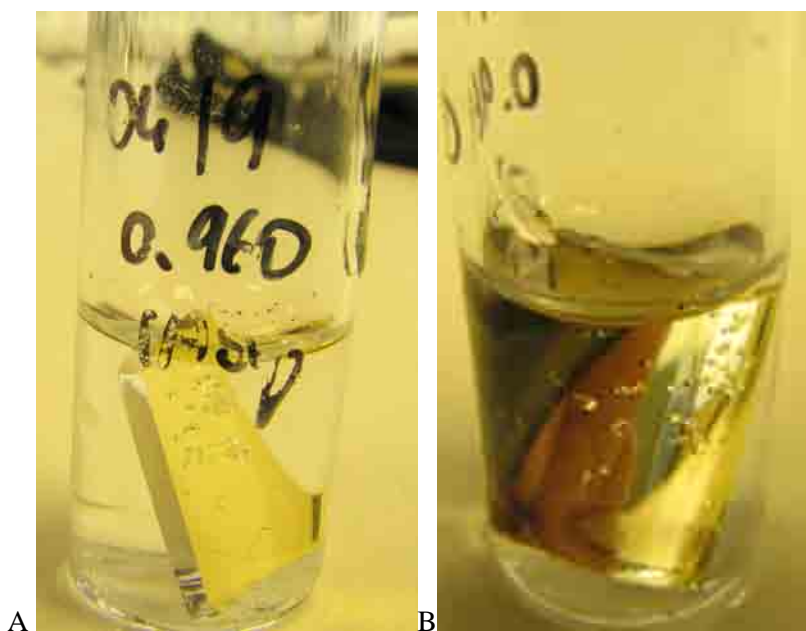


Figure 6-19 (A) sodium chlorate crystallized on DDT, (B) sodium chlorate crystallized on MDA

Experiments carried out with modified gold surfaces revealed that changes to the initial set up had to be introduced. Use of gold deposited on mica for crystallization on DDT surface resulted in the gold film stripping off the mica. For that reason surfaces formed of 100 nm of gold deposited on glass were used for further experiments. Examination of crystals formed on modified surfaces for chirality determination demonstrated that the gold film plays a significant and destructive role in probing of the

crystals' chirality. When light is reflected from the gold surface its polarity changes. That makes a use of episcopic illumination of polarized light impossible for determination of the crystals' optical properties. The problem was resolved by using 30 nm of gold deposited on glass. It was found that this film thickness does not influence distinguishing between positive and negative crystals, yet it is thick enough to allow SAM formation.

Crystallization on gold modified with DDT and MDA by microcontact printing

To confirm that nucleation is occurring because of the presence of modification, crystallization on printed SAMs was conducted. Microcontact printing was done using a master with feature dimensions: 20×20, 20×40 and 20×60 μm . An image of the master is given in Figure 6-20.



Figure 6-20 Optical microscope image (episcopic illumination) of the master used for microcontact printing of the thiols

Images of crystals grown on SAM-modified Au are presented in Figure 6-21.

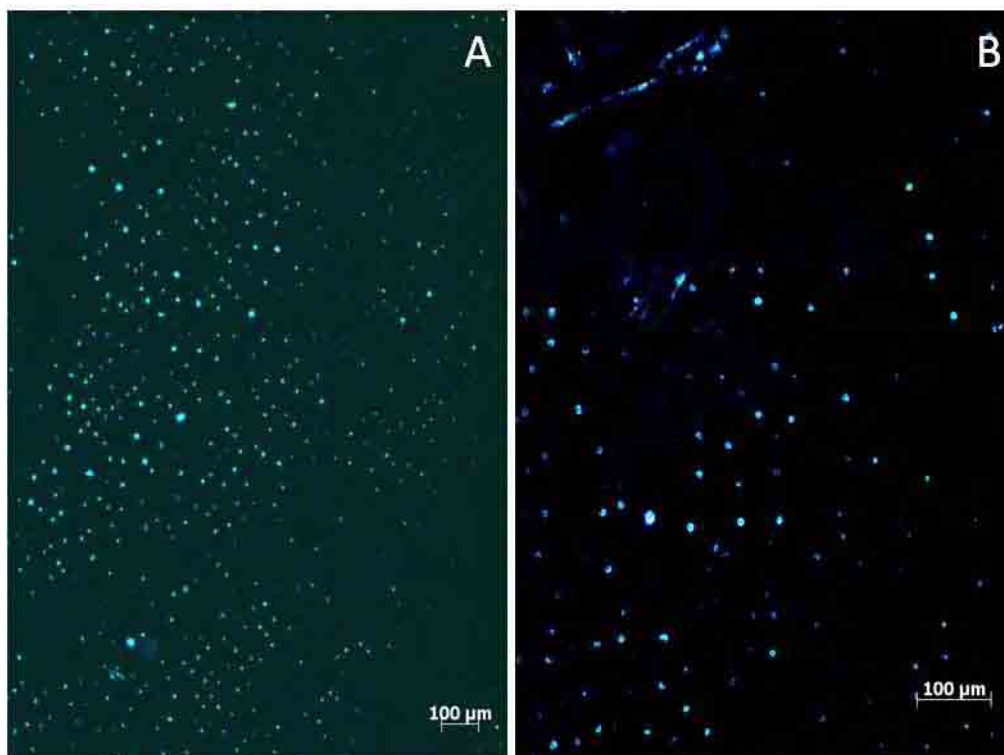


Figure 6-21 Sodium chlorate crystals grown on DDT monolayer printed on 30 nm gold film, optical microscope images (diascopic illumination, polarized light): (A) magnification 50×, (B) magnification 100×

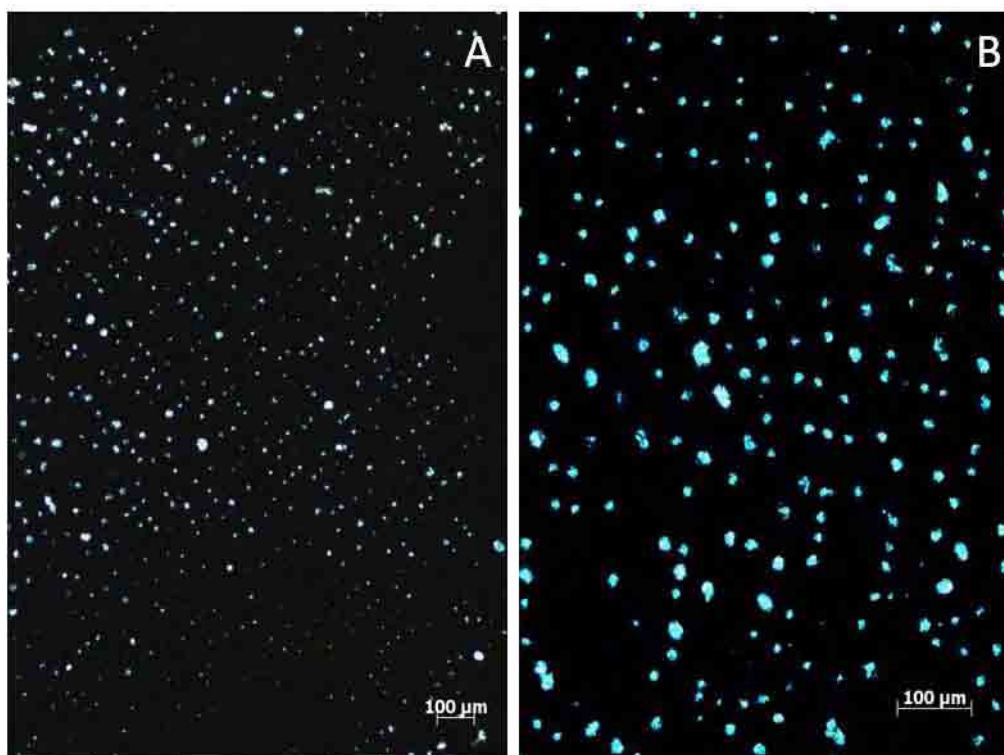


Figure 6-22 Sodium chlorate crystals grown on MDA monolayer printed on 30 nm gold film, optical microscope images (diascopic illumination, polarized light): (A) magnification 50×, (B) magnification 100×

Close examination of crystallization experiments conducted on achiral SAMs of DDT and MDA confirmed that crystallization occurs at the interface of SAM/crystallization solution and use of microcontact printing showed that sodium chlorate prefers the MDA surface as a nucleation site compared with DDT. Crystals had formed in larger numbers and formed a better shape on MDA printing.

Determination of chirality and statistics of sodium chlorate crystals grown on achiral monolayers:

Crystallization of sodium chlorate on gold surfaces modified with DDT

Table 6-3 Results from crystallization of sodium chlorate on DDT surface

Trial number	Surface modification	Number of crystals subjected to chirality analysis	Number of (+) crystals	Number of (-) crystals	Number of crystals with no chirality	Resolution %
1	DDT	20	5	9	6	30
2		20	10	8	2	10
3		28	13	9	6	21.4
4		18	5	7	4	22.2
5		16	4	7	5	31.3
6		20	1	10	3	15
7		11	4	4	3	27.3
8		30	11	13	6	20
9		19	10	5	4	21.1
10		20	7	8	5	25
Total		202	78	80	44	21.8

The resolution was calculated using the formula:

$$R = \frac{\text{number of crystals with no chirality effect}}{\text{total number of crystals}} \times 100\%$$

Graphical presentation of the results from Table 6-3 is shown in Figure 6-23. Consideration of individual experiments leads to the conclusion that there are more experiments with excessive number of (-) crystals than (+) crystals; however, the total number of (+) crystals is comparable with the total number of (-) crystals. This difference could be explained by the fact that the surfaces used for crystallization were not always of the same quality due to the gold surface roughness, SAM layer imperfection, *etc.* Yet, consideration of the total number of crystals gives better insight into chiral induction. The overall number of (+) and (-) crystals shows no preference in chirality induction.

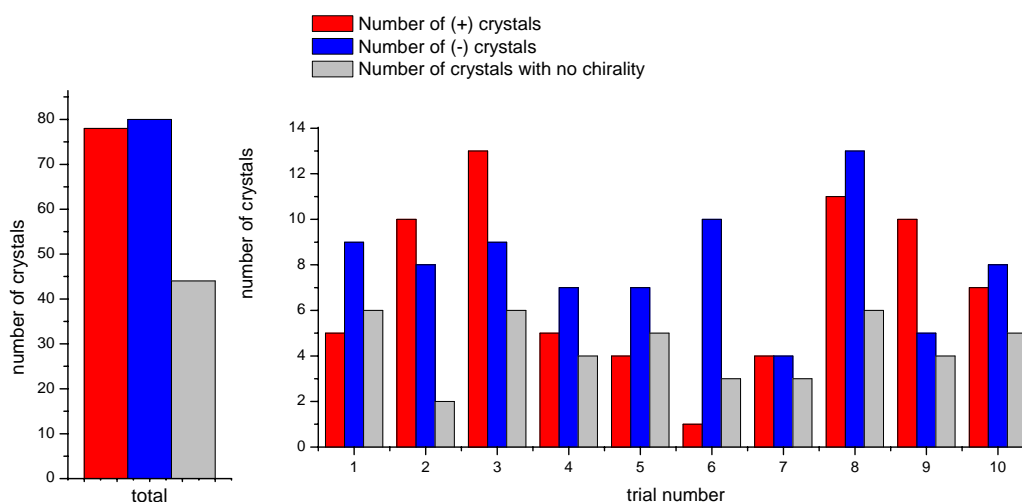


Figure 6-23 Presentation of total amount of crystal and their chirality from all and individual experiments carried out on DDT surface

Moreover, in each experiment, there was a certain number of crystals showing no chiral properties. These crystals were either too small to observe the colour change or had no chiral properties related to the way they were formed. The last column in Table 6-3 presents the percentage, which is the resolution of the method applied for determination of chirality. The resolution is calculated in regard to the number of crystals that exhibit no chirality effect. The total number of 21.8% shows that the method gives some uncertainty, however can be used for determination of chirality.

Crystallization of sodium chlorate on gold surfaces modified with MDA

Results achieved for crystallization of sodium chlorate on MDA monolayer are similar to the results for crystallization on DDT. Individual experiments (data presented in Table 6-4 and Figure 6-24) show that there are more experiments resulting with small excess of (-) crystals;

however, the total amount of (+) and (-) forms from all experiments is almost in balance. The method resolution achieved from experiments on MDA is comparable to the number achieved for DDT monolayer.

Table 6-4 Presentation of total amount of crystal and their chirality from all and individual experiments carried out on MDA surface

Trial number	Surface modification	Number of crystals subjected to chirality analysis	Number of + crystals	number of - crystals	Number of crystals with no chirality	Resolution %
1	MDA	15	5	7	3	20
2		19	6	7	6	31.6
3		14	6	5	3	21.4
4		28	10	14	4	14.3
5		20	9	5	6	30
6		14	5	6	3	21.4
7		14	6	6	2	14.3
8		22	8	9	5	22.7
9		13	6	4	3	23.1
10		12	6	2	4	33.3
Total		171	67	65	39	22.8

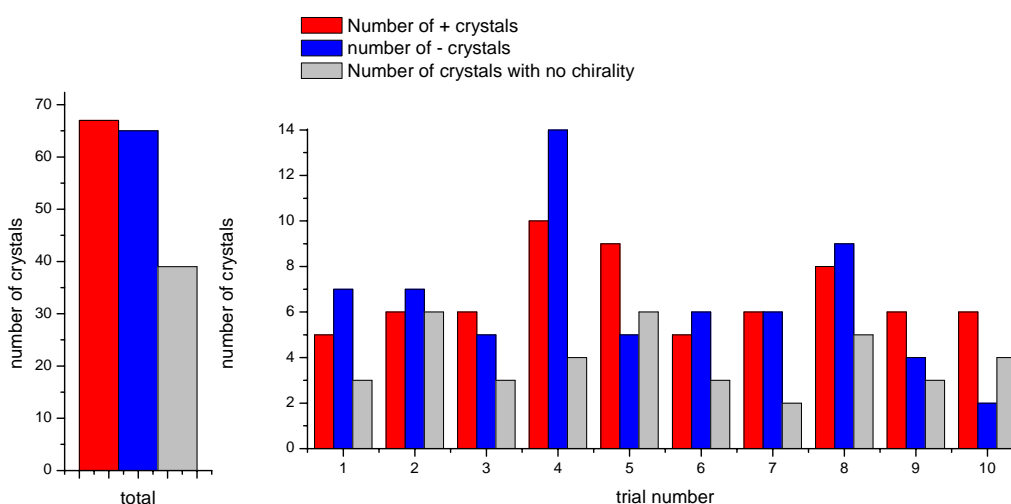


Figure 6-24 Presentation of total amount of crystal and their chirality from all and individual experiments carried out on MDA surfaces.

In the case of DDT, the total amount of crystals subjected to analysis was equal to 202, but only 158 crystals exhibited chiral properties.

The enantiomeric excess *e.e.* was calculated out using the formulae:

$$e.e.(+) = \frac{(\text{number of (+)crystals} - \text{number of (-)crystals})}{(\text{number of (+)crystals} + \text{number of (-)crystals})} \cdot 100\%$$

$$e.e.(-) = \frac{(\text{number of (-)crystals} - \text{number of (+)crystals})}{(\text{number of (+)crystals} + \text{number of (-)crystals})} \cdot 100\%$$

Equation 6-1

The enantiomeric excess of the (-) form of sodium chlorate was calculated to be 1.26%; in the case of MDA the enantiomeric excess for the (+) form of sodium chlorate was equal to 1.51%. Both results are less than 10% and indicate that sodium chlorate crystallizes with no preferences for chiral form, which was expected as neither DDT nor MDA has chiral properties.

6.3.2 Crystallization of hippuric acid on achiral SAMs

Objective: Investigation of nucleating properties of self assembled monolayers in hippuric acid crystallization.

Crystallization of hippuric acid on DDT and MDA printed on gold

Crystallization of hippuric acid on MDA and DDT surfaces led to the growth of spike-like crystals in both cases; however, with use of the microcontact technique it was discovered that hippuric acid prefers the MDA surface. In all crystallization experiments many more crystals of HA were formed on the SAM with acidic groups. Typical pictures of hippuric acid grown on DDT and MDA micro contact printed surfaces are presented in Figure 6-25. The red square represents the area with DDT surface; the green square represents the area with MDA surface.

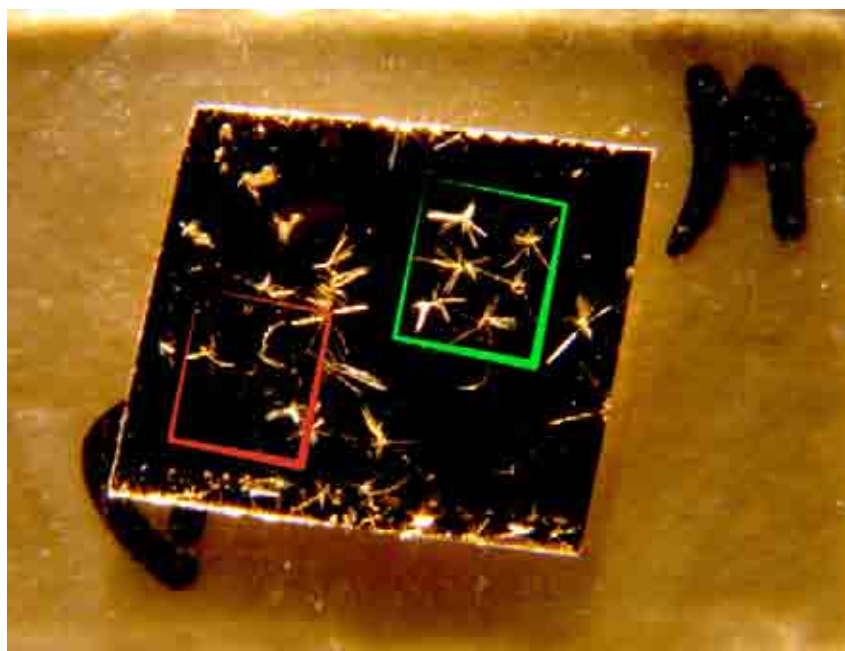


Figure 6-25 Hippuric acid grown on MDA (green square) and DDT (red square) printed SAM.

As it shown in the figure, more crystals have formed on the surface area modified with MDA. The surface modified with DDT nucleated much fewer crystals. The area in between the red and green squares is a no-modified gold surface. Due to impurities and surface unevenness some crystals have formed on that area as well, but they were not subjected to chirality determination.

Determination of chirality and statistics of HA crystals grown on achiral monolayers.

Chirality measurements of hippuric acid crystals were carried out with CD. Crystals with a positive CD effect at the wavelength 260 nm were noted as (+) and with a negative effect, as (-). The results are presented in Table 6-5 and Figure 6-26 for DDT, and in Table 6-6 and Figure 6-27 for MDA surfaces.

Table 6-5 Results from crystallization of hippuric acid on DDT surfaces

Trial number	surface	Total number of crystals subjected to chirality analysis	(+) crystals	(-) crystals	Number of crystals with no cd effect	Resolution %
1	DDT	46	15	18	8	17.4
2		33	11	18	4	12.1
3		32	14	15	3	9.4
Total		111	40	51	15	13.5

$$ee(-)=12.1\%$$

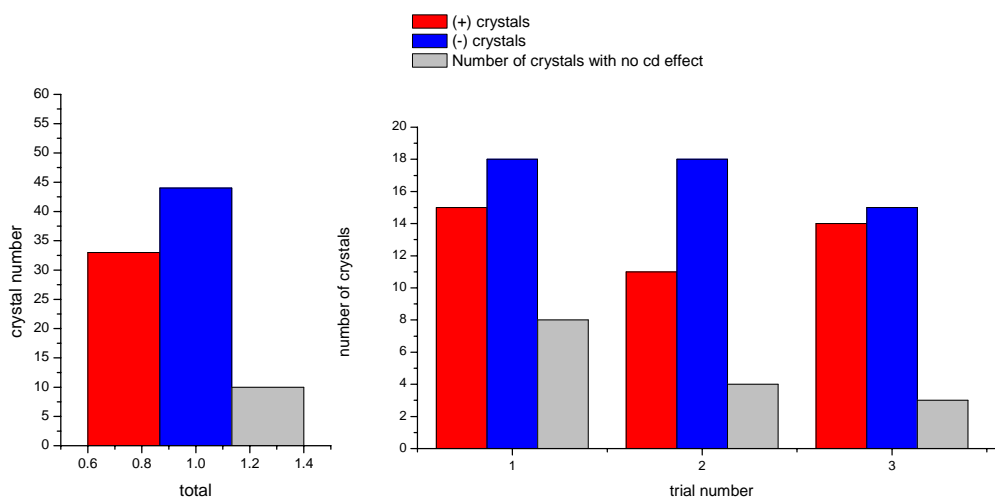


Figure 6-26 Presentation of total amount of HA crystals and their chirality -in total and from individual trials

Table 6-6 Results from crystallization of hippuric acid on MDA surface

Trial number	surface	Total number of crystals subjected to chirality analysis	(+) crystals	(-) crystals	Number of crystals with no cd effect	Resolution %
1	MDA	40	15	19	6	15
2		33	13	18	2	6
3		15	5	7	2	13.3
Total		88	33	44	10	11.4

$$ee(-)=12.9\%$$

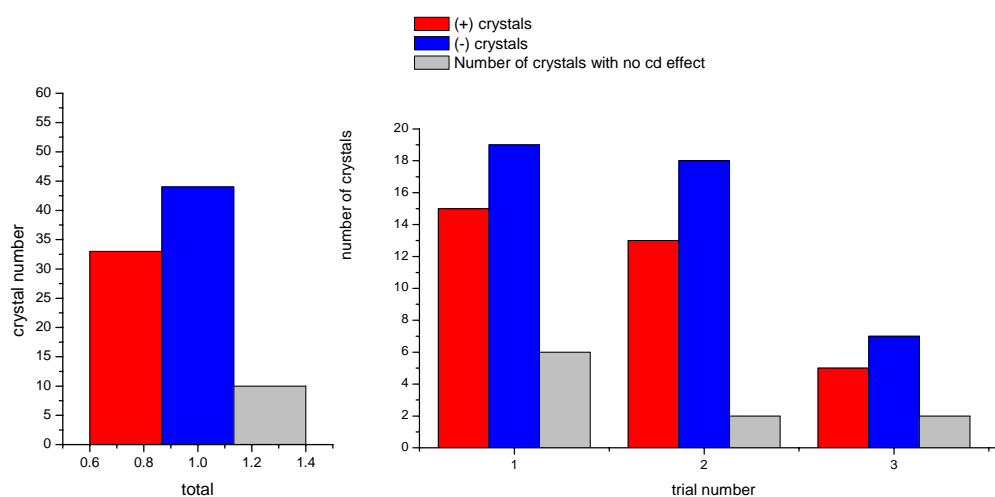


Figure 6-27 Presentation of total amount of HA crystals and their chirality -in total and from individual trials

The statistics revealed slight preference in crystal handedness. The overall distribution of L and D crystals, in both cases, showed that formation of (-) crystals is in favour. The enantiomeric excess of the (-) form for the DDT surface was calculated to be 12.08%; for the MDA surface it was 12.9%. Neither DDT nor MDA are chiral monolayers; the slight preference in crystallization could come from chemical compatibility of hippuric acid and studied monolayers.

6.3.3 Crystallization of sodium chlorate on chiral SAMs of cysteine L and cysteine D

Objective: investigation of inductive properties of chiral SAMs in chiral crystallization of sodium chlorate.

Crystallization of sodium chlorate on cysL and cysD films resulted with crystal growth on both surface types. Crystallization was carried out until the crystals were large enough to examine them with polarized light microscopy (the larger crystal, the better chirality recognition, due to the colour intensity).

However, the crystallization on cysteine L and D always gave smaller crystals in comparison with crystallization on MDA or DDT for the same crystallization conditions. Only in a few cases were sodium chlorate crystals large enough to subject them to polarizing light examination. Figure 6-28 shows typical crystals grown on an L-cysteine surface.

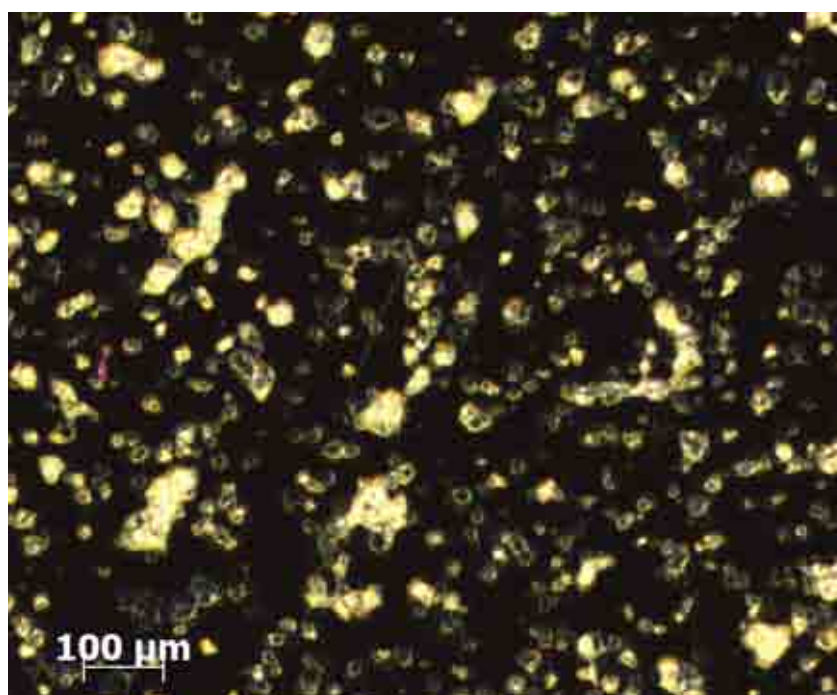


Figure 6-28 Sodium chlorate crystals grown on gold (100 nm) modified with cysteine L. Magnification 50 \times - the residue visible between crystals is caused by xylene.

Due to the very small size of the formed crystals (20 μm or less) as well as problems with their chirality determination caused by gold (gold polarizes light back) the technique of NSOM with

polarized light was used to measure the chiral properties of crystals. NSOM measurements were conducted on a specially built system combining NSOM with polarized light. All measurements were performed by the group of Yitzhak Mastai- Bar Illan University, Israel. NSOM reflections for NaClO_3 crystals grown on cysteine monolayers are presented in Figure 6-29.

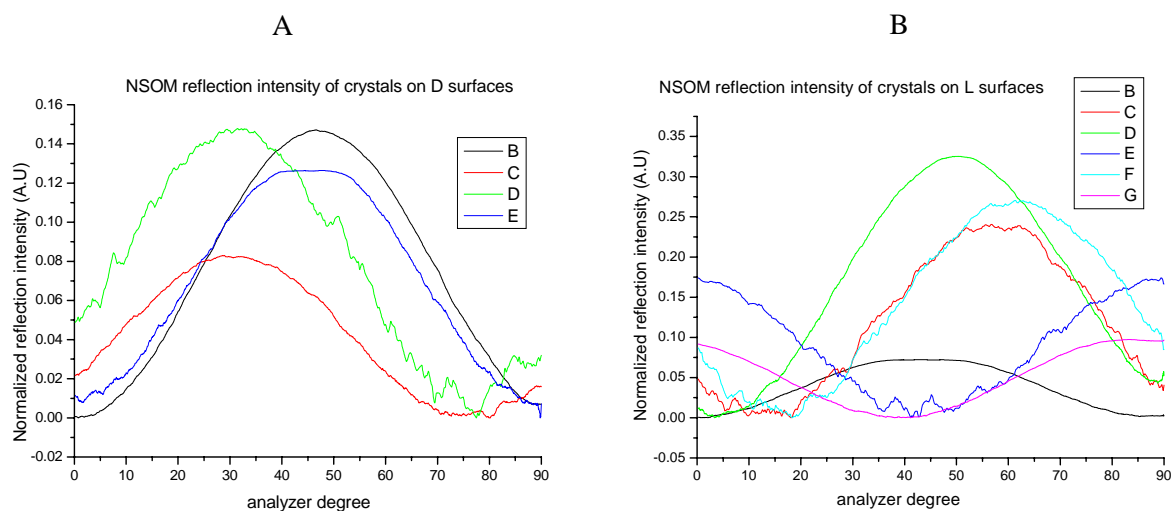


Figure 6-29 NSOM reflection intensity for sodium chlorate crystals formed on (A) cysteine L (B) cysteine D

On the D cysteine surface, all of the measured crystals exhibit the same behaviour- max reflection in the range of 30-55 degree.

On the L cysteine surface only 50% of the measured crystals exhibit maximum reflection in the range 30-55 degrees.

Unfortunately, due to the lack of time only one set of samples was measured. From this measurement, however, it could be assumed that chiral modification of the surface can act as an inducer of chirality in sodium chlorate crystals. Ordinary polarized light technique (polarized light microscopy) gave less ambiguous results due to the small size of formed crystals. Despite all changes made in sample preparation, in many cases, it was not possible to distinguish between the colours of crystals.

6.3.4 Crystallization of hippuric acid on chiral surfaces- cysteine L and D

Two different methods of chirality determination were employed to investigate preferences in chirality of formed crystals: circular dichroism and NSOM with polarized light.

In the first, crystals were grown until they were large enough to harvest and were examined with use of circular dichroism spectrometry (Nujol mull method).

During crystallization it was found that the amount of crystals successfully formed on a single sample was less than four. Three specimens were usually used in a single crystallization trial. Results from those measurements are presented in Table 6-7 and Figure 6-30.

Table 6-7 Crystallization results from crystallization of hippuric acid on L and D cysteine

Total number of trials	surface	Total number of crystals	Number of crystals with (+) cd effect	Number of crystals with (-) cd effect	Numbers of crystals with no cd effect	Resolution %
5	cysL	32	11	18	3	9.4
		% of total	34.4	56.3	9.3	
						ee(-)=24.1%
5	cysD	27	13	9	5	18.5
		% of total	48.2	33.3	18.5	
						ee(+)=18.1%

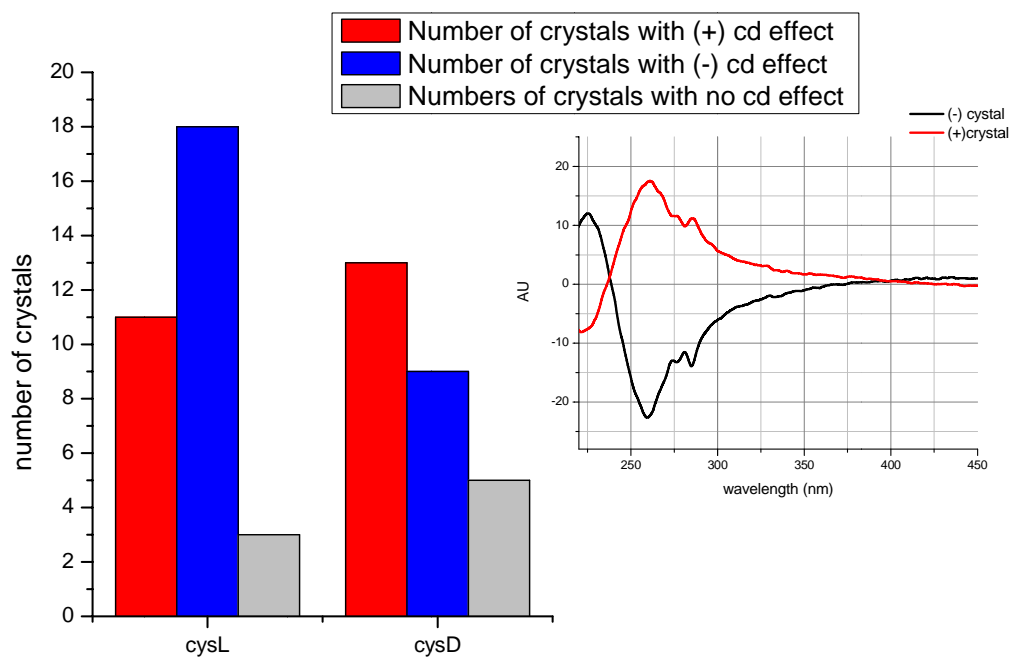


Figure 6-30 Comparison of amount of crystals of hippuric acid formed on cysteine L and cysteine D from all experiments and CD spectroscopy of hippuric acid enantiomeric crystals

In the second, which employs polarized light to NSOM, only one sample was measured. The results are presented in Figure 6-31.

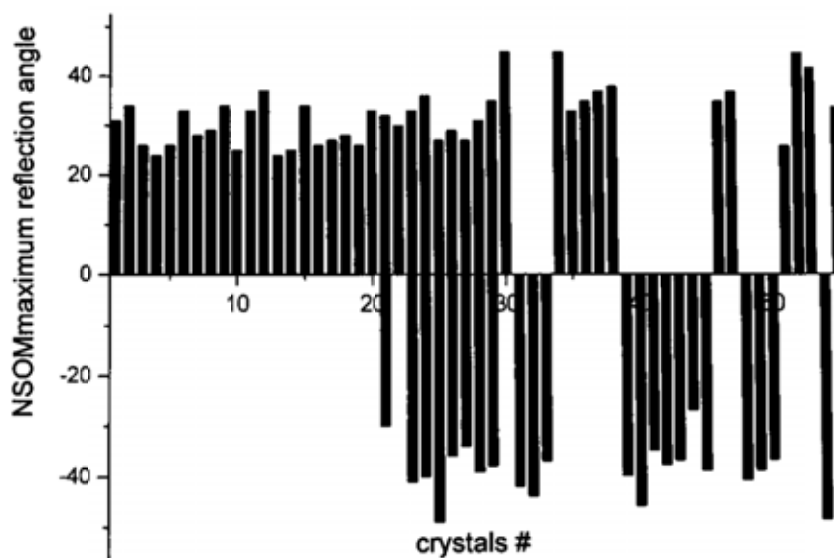


Figure 6-31 NSOM reflection angle for hippuric acid crystals grown on cysteine D

For 63 measured crystals, 22 had a negative reflection angle. The enantiomeric excess calculated for this sample is $ee(+)=30.2\%$.

6.3.5 Crystallization of BHT on chiral SAMs- cysteine L and D

To investigate preferences in chirality of crystals formed in crystallization of BHT on cysteine L and D surfaces circular dichroism was used. The results are presented in Table 6-8 and Figure 6-32.

Table 6-8 Crystallization results from crystallization of hippuric acid on L and D cysteine

Total number of trials	surface	Number of crystals	Number of crystals with + cd effect	Number of crystals with – cd effect	Numbers of crystals with no cd effect	Resolution %
5	cysL	29	11	15	3	10.3
		% of total	37.9	51.7	10.3	
						$ee(-)=14.6\%$
5	cysD	26	14	10	2	7.4
		% of total	53.8	38.5	7.7	
						$ee(+)=13.6\%$

It was found that on cysteine L surfaces BHT crystallizes with (-) form preference and on cysteine D with (+) form preference. The enantiomeric excess is however low ~14%. This low value could arise from the method applied to perform chirality determination. So far NSOM measurements gave the best results in chirality determination with no crystals lost. The circular dichroism method applies only to the crystals of a certain size, thus many of the grown crystals specimens could not be tested for chirality determination. This probably affects the most the low value of the achieved enantiomeric excess.

Graphical representation of the data gathered in Table 6-8 is presented in Figure 6-32.

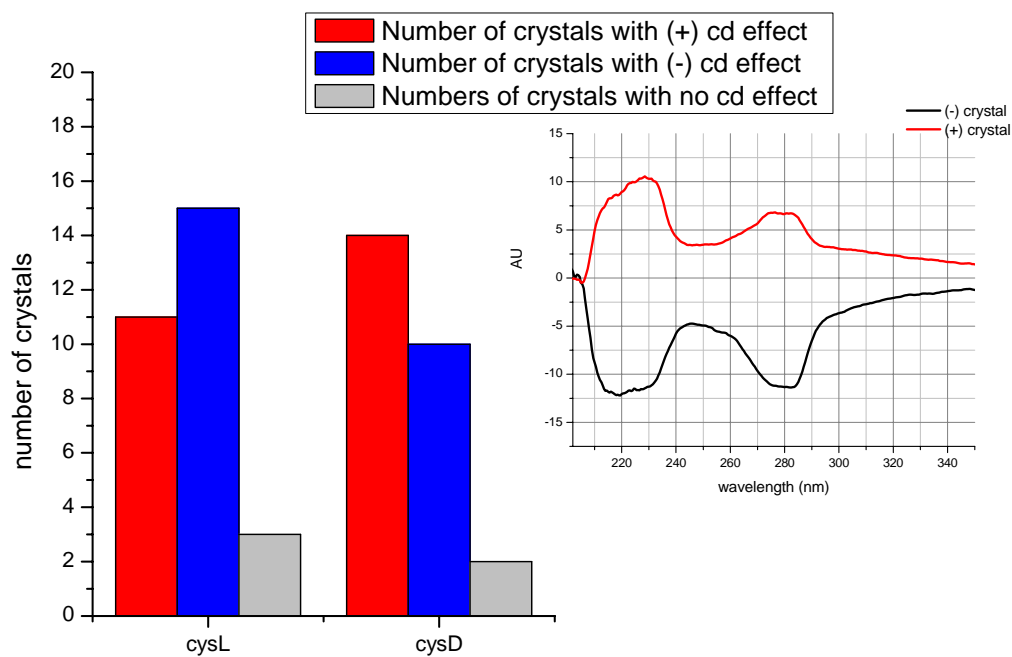


Figure 6-32 Comparison of amount of BHT crystals formed on cysteine L and cysteine D from all experiments and CD spectroscopy of BHT enantiomeric crystals

Unfortunately the measurements of BHT crystals grown on D and L cysteine with NSOM were not performed due to the lack of time. However it is believed that this type of measurement could shine more light into chirality induction in crystals caused by chiral monolayers.

6.4 Discussion and conclusions

In the presented project representative inorganic and organic compounds were tested for chiral crystallization on modified gold surfaces. Initial experiments revealed that sodium chlorate- an inorganic compound- tends to crystallize on SAMs equipped with acidic groups with more preference. Sodium chlorate is known to possess high oxidation properties, which might partially explain this preference. SAMs with acidic groups are not particularly susceptible to react with NaClO_3 at room temperature. In the case of DDT- a SAM with only a hydrocarbon chain- no gaseous phase formed on the sample surface was found during experiments; however, formation of smaller crystals in smaller amounts could be evidence for partial SAM decomposition. Positive results of NaClO_3 crystallization on acidic surfaces showed the possibility of using cysteines as a chiral modification for gold.

Chirality determination of NaClO_3 crystals grown on achiral SAMs confirmed that there is no preference in emerging crystals. The enantiomeric excess in DDT and MDA cases was 1.26 and 1.51%, respectively, indicating these types of surfaces do not induce chirality. Experiments conducted on the same type of surfaces with use of hippuric acid as a molecule to crystallize showed slight chiral preference in the emerged crystals- the (-) form of hippuric acid appeared more frequently. This result could be explained by greater chemical compatibility of hippuric acid and DDT and MDA monolayers as it was proved by Matsura¹ that chemical compatibility influences chiral crystallization. Experiments of chiral crystallization of sodium chlorate conducted on surfaces modified with L and D cysteine showed preference in chirality of emerged crystals. Since the amount of crystals of NaClO_3 grown on cysteines was larger than in the case of achiral SAMs, plus their sizes were a lot smaller, the examination with polarized light was not feasible. For the polarized light method, a crystal of certain thickness is needed to determine unambiguously its colour change. Despite the fact preliminary results with the use of this technique were positive, NSOM measurements were conducted to test crystals' chirality with better sensitivity. Measurements carried out with external help of Y. Mastai from Bar Ilan University showed a little chiral preference in the formed crystals. Unfortunately, due to the lack of time only one set of samples of NaClO_3 was examined with NSOM, from which we could not calculate the enantiomeric excess. We believe that more NSOM measurements of NaClO_3 crystals

grown on cysteines would shine more light on the subject of chiral induction in sodium chlorate chiral crystallization.

In the organic part of the project hippuric acid (HA) and 2,6-di-*tert*-butyl-4methylphenol (BHT) were subjected to crystallization on surfaces modified with cysteines. Both compounds were chosen with regard to their structural similarity to the cysteine molecule. As it was proved before, compounds tend to crystallize more easily on SAMs possessing the most similar atom distances to the crystallized compound²³. During experiments it was found that hippuric acid crystallizes more easily and with larger amount on surfaces of cysteines than BHT, although both compounds were successfully grown on cysteine surfaces. For chirality determination CD spectroscopy was used. Due to the method limitations only crystals of a certain size could be tested. The fragility of the HA crystals caused the loss of many samples during crystal harvesting. Final CD measurements revealed a little preference in chirality. On cysteine L, the enantiomeric excess of (-) hippuric acid was found to be 24.1%; on cysteine D, the enantiomeric excess of (+) form was 18.1%. NSOM measurements confirmed preference for cysteine D which had an enantiomeric excess for (+) form of 30.2%.

For BHT crystallization on cysteines similar results were found with one exception: BHT tends to crystallize less spontaneously on cysteine surfaces.

The little enantiomeric excess we encountered could be explained by several factors. First, the techniques we used for chirality determination are not sensitive enough to test all formed crystals. Second, it might be the case that the films of cysteines we produced for chiral crystallization experiments are not oriented well enough to nucleate crystallization in the same way. As it has shown recently, pH has a significant impact on the cysteine arrangement on the gold surface^{25,26}. Also it should be taken in account that other aspects of crystallization dominate over induction of chirality, namely a polarity effect. The experiments were conducted in polar, protic solvents (water, ethanol). Those two factors made us conclude that more crystallization experiments (taking into account cysteine film formation in different pH, kinetics, solvent dependence and polar interactions) should be carried out to confirm fully induction of chirality by chiral SAMs in non-chiral compounds. We

believe that only this type of experiment can fully resolve a problem of chiral induction. Chemical and geometrical compatibility of the SAM/crystal interface can be taken as a third factor. The chemical compatibility of the studied interfaces is decreasing in the order: hippuric acid/cysteines > BHT/cysteines > sodium chlorate/cysteines. This order has its reflection in the ease of crystal growth. The poorest yield of crystals grown on cysteines was encountered for sodium chlorate, which is not fully chemically compatible. We believe that for this compound a more suitable chiral modification of gold should be engineered to achieve satisfactory results.

6.5 Reference List

1. Matsuura, T.; Koshima, H. Introduction to chiral crystallization of achiral organic compounds spontaneous generation of chirality. *Journal of Photochemistry and Photobiology C-Photochemistry Reviews* **2005**, *6* (1), 7-24.
2. Burke-Laing, M. E.; Trueblood, K. N. Sodium chlorate: precise dimensions for the ClO₃⁻ ion. *Acta Crystallographica Section B* **1977**, *33* (8), 2698-2699.
3. Glazer, A. M.; Stadnicka, K. On the origin of optical activity in crystal structures. *Journal of Applied Crystallography* **1986**, *19* (2), 108-122.
4. Ramachandran, G. N.; Chandrasekaran, K. S. The absolute configuration of sodium chlorate. *Acta Crystallographica* **1957**, *10* (10), 671-675.
5. Ristic, R.; Sherwood, J. N.; Wojciechowski, K. Morphology and growth kinetics of large sodium chlorate crystals grown in the presence and absence of sodium dithionate impurity. *The Journal of Physical Chemistry* **1993**, *97* (41), 10774-10782.
6. Ringertz, H. The molecular and crystal structure of hippuric acid. *Acta Crystallographica Section B* **1971**, *27* (2), 285-291.
7. Ramachandran, E.; Raji, P.; Ramachandran, K.; Natarajan, S. Photoacoustic study of the thermal and optical properties of hippuric acid. *Crystal Research and Technology* **2006**, *41* (5), 481-486.
8. Maze-Baudet, M. Structure cristalline de trois phenols encombrés: le diméthyl-2,3 phenol, le méthyl-2 bromo-3 phenol et le ditertiobutyl-2,6 méthyl-4 phenol. *Acta Crystallographica Section B* **1973**, *29* (3), 602-614.
9. Han, T. Y. J.; Aizenberg, J. Calcium carbonate storage in amorphous form and its template-induced crystallization. *Chemistry of Materials* **2008**, *20* (3), 1064-1068.
10. Aizenberg, J. Self-assembled monolayers as templates for inorganic crystallization: A bio-inspired approach. *Engineering of Crystalline Materials Properties* **2008**, 17-32.

11. Pham, T.; Lai, D.; Ji, D.; Tuntiwechapikul, W.; Friedman, J. M.; Randall Lee, T. Well-ordered self-assembled monolayer surfaces can be used to enhance the growth of protein crystals. *Colloids and Surfaces B: Biointerfaces* **2004**, *34* (3), 191-196.
12. Nakanishi, T.; Banno, N.; Matsunaga, M.; Asahi, T.; Osaka, T. Crystallization of leucine on a self-assembled monolayer with covalently attached enantiomeric leucine molecules. *Colloids and Surfaces A: Physicochemical and Engineering Aspects* **2006**, *284-285*, 270-275.
13. Lee, A. Y.; Ulman, A.; Myerson, A. S. Crystallization of Amino Acids on Self-Assembled Monolayers of Rigid Thiols on Gold. *Langmuir* **2002**, *18* (15), 5886-5898.
14. Dressler, D. H.; Mastai, Y. Enantioselective crystallization of histidine on chiral self-assembled films of cysteine. *Journal of Colloid and Interface Science* **2007**, *310* (2), 653-660.
15. Dressler, D. H.; Hod, I.; Mastai, Y. Stabilization of [alpha]-l-glutamic acid on chiral thin films-- A theoretical and experimental study. *Journal of Crystal Growth* **2008**, *310* (7-9), 1718-1724.
16. Jiang, P.; Liu, Z. F.; Cai, S. M. Growing Monodispersed PbS Nanoparticles on Self-Assembled Monolayers of 11-Mercaptoundecanoic Acid on Au(111) Substrate. *Langmuir* **2002**, *18* (11), 4495-4499.
17. Nagtegaal, M.; Stroeve, P.; Tremel, W. Growth of FeO(OH) crystals on self-assembled monolayers on gold. *Thin Solid Films* **1998**, *327*, 571-575.
18. Tarasevich, B. J.; Chusuei, C. C.; Allara, D. L. Nucleation and growth of calcium phosphate from physiological solutions onto self-assembled templates by a solution-formed nucleus mechanism. *Journal of Physical Chemistry B* **2003**, *107* (38), 10367-10377.
19. Aizenberg, J. Patterned crystallization of calcite in vivo and in vitro. *Journal of Crystal Growth* **2000**, *211* (1-4), 143-148.
20. Aizenberg, J. Crystallization in patterns: A bio-inspired approach. *Advanced Materials* **2004**, *16* (15), 1295-1302.
21. Aizenberg, J. New Nanofabrication Strategies: Inspired by Biomineralization. *Mrs Bulletin* **2010**, *35* (4), 323-330.
22. Han, Y. J.; Aizenberg, J. Shape, size and morphology control of inorganic crystals with self-assembled monolayers. *Biological and Bioinspired Materials and Devices* **2004**, *823*, 115-119.
23. Hiremath, R.; Varney, S. W.; Swift, J. A. Oriented Crystal Growth of 4-Iodo-4-nitrobiphenyl on Polar Self-Assembled Monolayer Templates: A Case for Chemical Epitaxy. *Chemistry of Materials* **2004**, *16* (24), 4948-4954.
24. Dressler, D. H.; Mastai, Y. Chiral crystallization of glutamic acid on self assembled films of cysteine. *Chirality* **2007**, *19* (5), 358-365.
25. Nazmutdinov, R. R.; Manyurov, I. R.; Zinkicheva, T. T.; Jang, J.; Ulstrup, J. Cysteine adsorption on the Au(111) surface and the electron transfer in configuration of a scanning tunneling microscope: A quantum-chemical approach. *Russian Journal of Electrochemistry* **2007**, *43* (3), 328-341.

26. Zhang, J. D.; Chi, Q. J.; Nazmutdinov, R. R.; Zinkicheva, T. T.; Bronshtein, M. D. Submolecular Electronic Mapping of Single Cysteine Molecules by in Situ Scanning Tunneling Imaging. *Langmuir* **2009**, 25 (4), 2232-2240.

7 Project 02-AFM study of chiral recognition on surfaces

The main objective of this study is to investigate chiral discrimination between chirally modified AFM tips and surfaces using 'click chemistry' reactions.

7.1 Force distance spectroscopy as a tool for chiral recognition

The first studies on chiral surfaces were carried out in the early 1980s by Weis and McConnell¹, who discovered that monolayers of chiral amphiphilics in water form a number of phases. Monolayers were prepared with the Langmuir Blodgett technique and transferred onto mica surfaces for study by AFM. Soon after, another group observed a separation of chiral phases in a monolayer of racemic amphiphilics (tetracyclic alcohol)². They found that at a low pressure molecules were randomly oriented on the surface but, under increasing compression, racemates were formed with growing domains. The domains were composed of single enantiomers. This discovery was an inspiration for determining the absolute chirality of molecules on the surfaces.

The first studies on the determination of absolute chirality of molecules on surfaces were carried out with use of STM. It was shown that the technique is efficient not only for chirality determination but also to study chiral symmetry breaking. Raval^{3,4} discovered that doping racemates with certain amounts of 'sergeant' molecules resulted in the formation of large domains of single enantiomers.

Studies by Berndt⁵ revealed that chiral domains could be moved with an STM tip with no damage to the assembly. That suggested that very strong intermolecular interactions existed between the molecules forming the domains.

The idea of probing surface chirality by employing chemical force microscopy was inspired by chromatographic separation of mixed enantiomers.

7.1.1 Chemical Force Microscopy

Chemical Force Microscopy (CFM) is a derivative of Atomic Force Microscopy in which an AFM tip is functionalized with molecules. The interactions between such a modified tip and a sample give an insight into the forces acting at the interface. CFM was used for the first time by McKendry⁶. Studies on forces between a surface functionalized with enantiomers of mandelic acid and the tip modified with Pirkle resin (3,5-dinitrobenzoyl phenylglycine)- terminated thiol revealed that CFM could be successfully used for chiral recognition. *S-S* and *R-R* interactions were found to be considerably smaller than *S-R* and *R-S*, as it is presented in Figure 7-1:

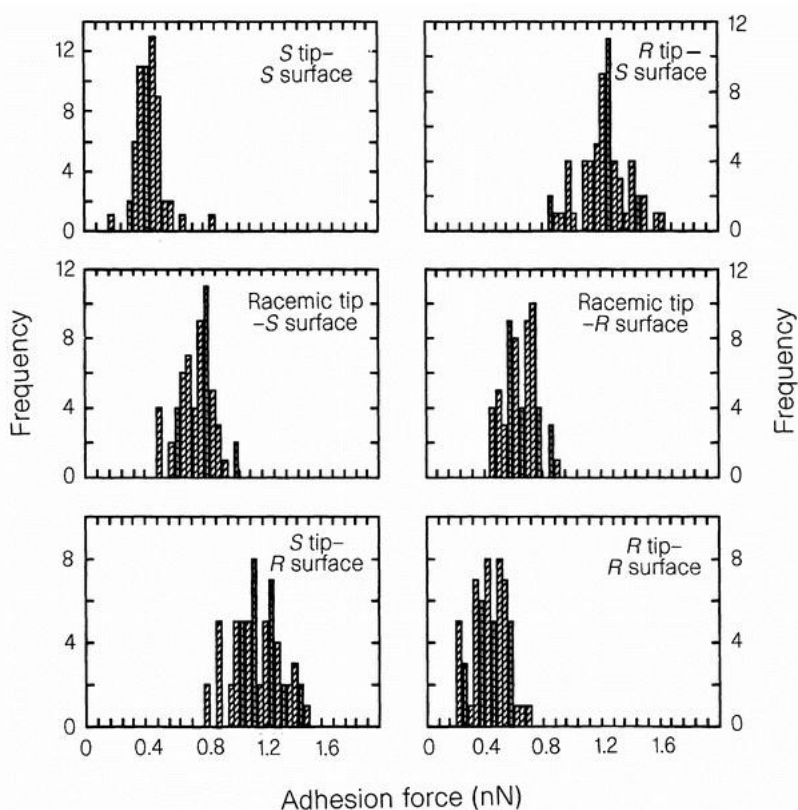


Figure 7-1 A set of histograms of the adhesion forces recorded for gold coated tip functionalized with 3,5 dinitrobenzoyl phenylglycine and gold surface functionalized with R, S and racemic mandelic acid in ethanol⁶

The authors made the assumption that packing of the enantiomers was the same and that the resulting surfaces had the same mechanical properties. Additionally, the solvation of the surfaces was thought to be the same. With this assumption the differences in the adhesion forces were proposed to arise due to the chemistry between the tip and the surface. Complementary studies of frictional maps were carried out on the same sets and revealed a contrast between stripes made of *R* and *S* enantiomers when imaged by the tip functionalized only with one enantiomer. The existence of this contrast confirmed that the friction difference is caused by real chemical interactions and not by the packing difference.

Another attempt to discriminate between chiral interactions was made by Mahapatro⁷, who worked with self assembled monolayers functionalised with phenylalanine and serine. In this study an SPM probe was also modified with Pirkle resin. This research revealed that a large, bulky head group enhances the chiral discrimination whilst small groups such as -CH₃, reduce it. Hydroxyl groups were found to have small chiral discrimination in comparison with phenyl groups. Pirkle resin was also used to discriminate between hydrophobic enantiomers of benzylmethylamine and naphthyl ethylamine; however, low adhesion forces were observed when hydrophobic molecules were used. The conclusion from considering the electrostatic component in basic chiral molecules was that chiral amines were protonated under experimental conditions and they were more likely not to undergo discrimination by Pirkle resin. In this study it was also observed that the hydrogen bonding plays a significant role in chiral discrimination. The adhesion forces observed for amines were smaller than for mandelic acid. From this it was concluded that the presence of an acidic group in the chiral moiety enhances the chiral discrimination by Pirkle resin.

Nita conducted studies of *S* and *R*-N-(1-phenyl)-N'-[(3-truetoxy)propyl urea] attached to oxidised silicon⁸. In contrast to the Pickle resin studies, the tip and the surface were modified with the same enantiomers of N-(1-phenyl)-N'-[(3-truetoxy)propyl urea]. The adhesion forces were carried out in various solvents, which revealed that hydratation of the surface obscures chirality discrimination, highlighting the importance of solvent influence on chiral discrimination. When a less polar solvent (methanol) was used the discrimination was successfully observed. This study resulted with an

observation of higher forces for homo-chiral surfaces than for hetero-chiral. Experiments carried out in hexane and CS₂ were not successful in terms of chiral discrimination.

Another pair of chiral compounds was used by Otsuka⁹. 3,5-dinitrobenzoyl phenylglycine, a chiral stationary phase (CPS) was used to distinguish the enantiomers of a 2,2,2-trifluoro-1-(9-anthryl)ethanol derivative. CPS was attached to the surface of silicon and 2,2,2-trifluoro-1-(9-anthryl)ethanol to the AFM tip. Adhesion forces were measured in isopropanol. A broad distribution of forces in histograms was observed for hetero-chiral pairs. Recorded forces were larger than 10 nN. There was no good separation observed in the histograms. Use of mandelic acid did not have a significant influence on the separation in the force histograms either.

A simpler approach to chiral discrimination was recently presented by Seneviratne¹⁰, who employed Mosher's acid derivatives (α -methoxy- α -trifluoromethylphenylacetic acid), a popular derivatising agent for amines and alcohols, to chiral recognition studies. An AFM tip and gold surface were functionalized with enantiomers of Mosher acid derivatives. The studies were carried out in ethanol, water, isopropanol, dodecane and chiral solvents: *S* and *R* 2-butanol. The best chiral discrimination was observed for ethanol and isopropanol, emphasizing an influence of the solvent nature on the chiral discrimination. Experiments conducted with chiral solvents showed that the adhesion forces increase in order of *SSS*>*SSR*>*SRS*>*SRR* of tip-solvent-surface combination. The experiments showed also that introduction of solvent of opposite chirality enhances the adhesion forces but diminishes chiral discrimination.

So far the CFM studies have used direct tip and surface modification in which a purpose synthesis was carried out for each experiment. The difficulty in derivatisation of chiral molecules with thiols has limited the number of studies. Use of click chemistry reactions for surface modification could make the formation of chiral surfaces easier. In this study we investigate the influence of this way of surface modification on chiral recognition.

7.2 Experimental details

7.2.1 Click chemistry as a tool for chiral SAMs formation

The CuAAC reaction, commonly called ‘click chemistry’, was performed in order to achieve chirally functionalized SAMs. Three different compounds were used as linkers for further reacting with molecules bearing the desired functional group.

Compounds used for modification of linker A are presented in Table 7-1 and the corresponding expected surface functionalizations are given in Table 7-2.

Table 7-1 Compounds used for functionalization of linker A monolayer

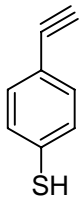
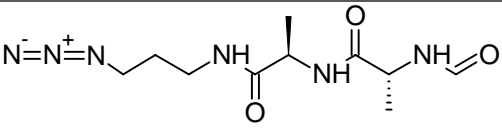
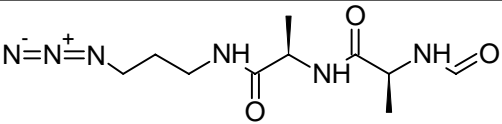
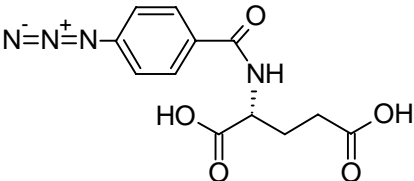
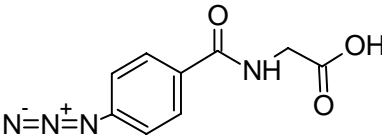
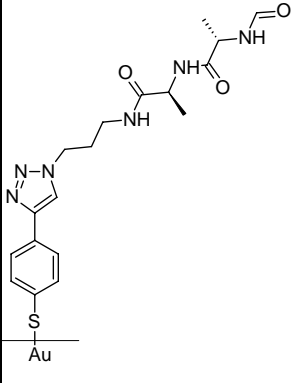
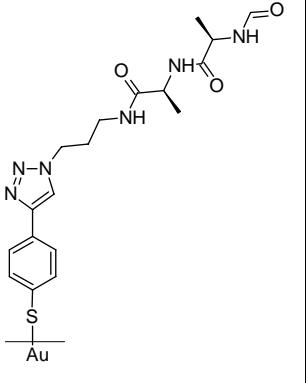
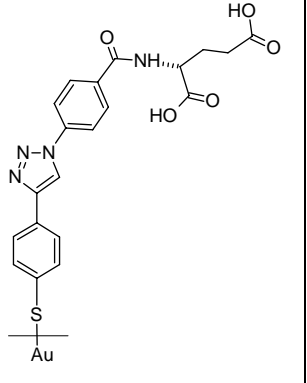
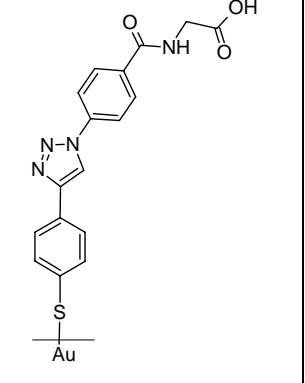
Surface	Linker	Functional group
Au	Linker A  4-ethynylbenzenethiol	 (I) N-formyl-D-alanyl-L-alanine azidopropyl amide
		 (II) N-formyl-L-alanyl-L-alanine azidopropyl amide
		 (III) (2R)-2-[[4-azidophenyl]carbonyl]amino} pentanedioic acid
		 (IV) 4-azido-benzyloaminoacetic acid

Table 7-2 Schematic projection of surfaces achieved by modification of linker A monolayers with compounds 1-4

Surface AI - linkerA-AlaAlaDL	Surface AII - linkerA-AlaAlaLL	Surface AIII - linker A-GluL	Surface AIV - linker A-HA
			

Compounds used for modification of linker B are presented in Table 7.3 and the corresponding expected surface functionalizations are given in Table 7-4.

Table 7-3 Compounds used for modification of linker B monolayer

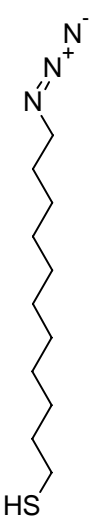
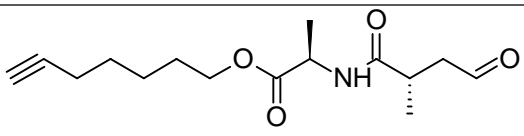
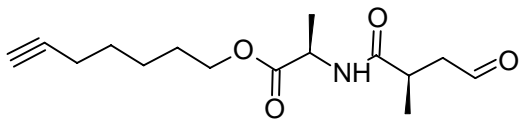
Surface	Linker	Functional group
Au		 (V) N-formyl-D-alanyl-L-alanine-6-heptyn-1-ol ester
		 (VI) N-formyl-L-alanyl-L-alanine-6-heptyn-1-ol ester

Table 7-4 Schematic projection of surfaces achieved by modification of linker B monolayers with compounds V and VI

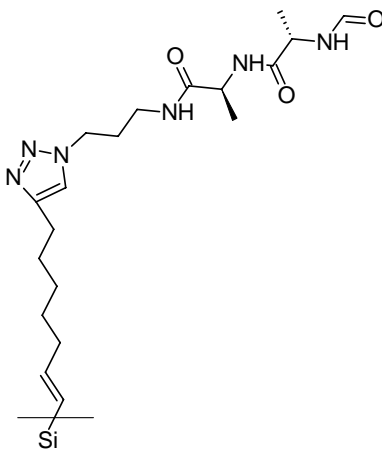
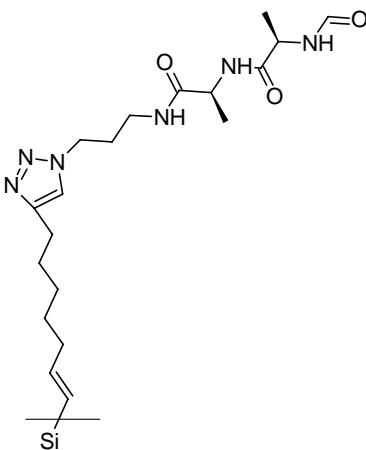
Surface BV - linkerB-AlaAlaDL	Surface BVI - linkerB-AlaAlaLL

Compounds used for modification of linker C are presented in Table 7.5 and the corresponding expected surface functionalizations are given in Table 7-6.

Table 7-5 Compounds used for modification of linker C monolayer

Surface	Linker	Functional group
Si	Linker C 	 (I)N-formyl-D-alanyl-L-alanine azidopropyl amide
	1,8-nonadiyne 	 (II)N-formyl-L-alanyl-L-alanine azidopropyl amide

Table 7-6 Schematic projection of surfaces achieved by modification of linker C monolayers with compounds I and II

Surface CI - linkerB-AlaAlaDL	Surface CII - linkerB-AlaAlaLL
	

All compounds used for functionalization of linkers were synthesized in the collaboration group of Professor Alan Rowan; Radabout University Nijmegen, Netherlands.

All surfaces produced with the Cu-AAC reaction were subjected to characterization. Their properties are described in detail in Chapter 5.

7.2.2 Cantilever modification

In the study of the adhesion forces two types of AMF cantilevers were used: DNP-S Veeco probes and CSC38 Micromash probes. Since both of these probes have bare silicon nitride tips, a thin gold film deposition had to be performed beforehand.

7.2.2.1 Gold deposition on AFM cantilevers

Deposition of gold on AFM tips was performed according to the procedure 4.2. The cantilevers were mounted on a specially designed plate and put into the UVO cleaner (Jelight Company) for 20 min beforehand in order to remove adsorbed impurities. After placing the plate with cantilevers into the depositing chamber the process was conducted with no change from that described in section 4.2.

7.2.2.2 Click chemistry on AFM cantilevers

AFM cantilevers coated with 10 nm of gold were subjected to modification with linkers as described in section 6.2.1.1. Modification was performed in the same solutions as for gold surfaces to ensure that both substrates were modified in the same way.

Click chemistry reaction was performed in small, glass petridishes. Stirring the reacting solution was achieved by placing the petridishes on a shaker. Since it is extremely hard to investigate modification of the tips, the functionalization reaction conditions were kept as close as possible to the one described for surface specimens. The tip surface coverage might be however not the same for all cantilevers due to the different curvature of each tip. This should be kept in mind because it might have an influence on the recorded adhesion forces.

7.2.3 AFM experiment set-up

All AFM experiments were performed with a 5500 Pico Plus Agilent AFM. Studies of adhesion forces required conducting experiments in liquid medium. A specially designed holder for samples, presented in Figure 7.2, was used that allows switching between samples without disassembling the whole set up.

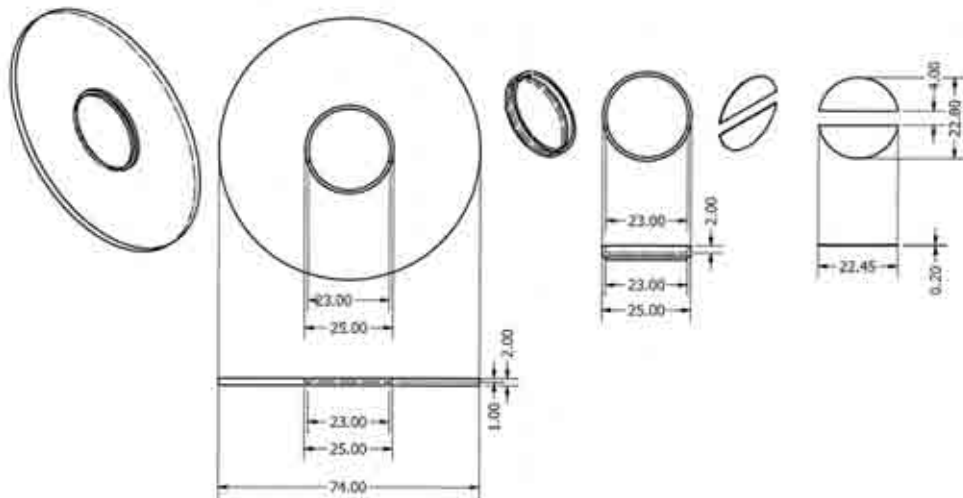


Figure 7-2 Schematic of an AFM sample holder-liquid cell

The liquid cell was designed to have a volume of *ca.* 1 cm^3 . The inner cell was made of non magnetic stainless steel whilst the outer ring and the cover for specimens were made of magnetic material. Additionally, underneath the sample holder, there were 6 strong magnets to keep the specimens cover in place.

The force distance experiments were performed with the use of the set up presented in Figure 7-3.

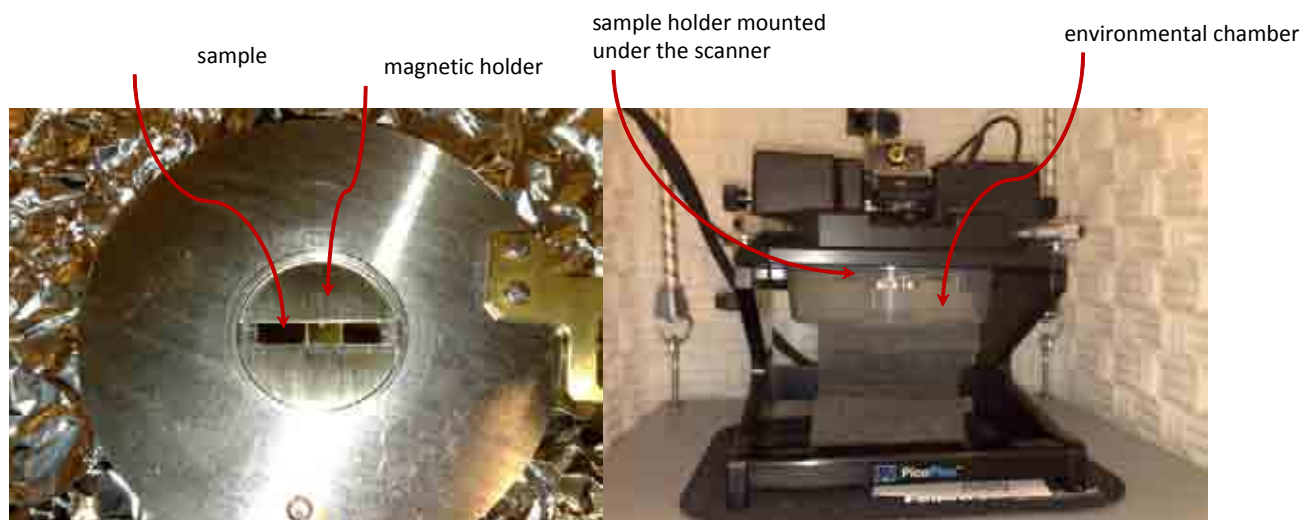


Figure 7-3 Sample holder with specimens mounted and AFM experimental set-up

A batch of samples, two samples of the surface to be tested and a reference, was placed in the liquid cell, clamped with a sample cover. After that the liquid cell was rinsed with HPLC grade ethanol 3 times before filling with 1 mL of ethanol of the same grade. The sample holder was then mounted in the AFM instrument, covered with an environmental chamber to prevent evaporation and thermostatted at 21°C for 40 min before running force-distance experiments. After the system reached equilibrium the tip was approached to the sample and force-distance measurements were performed. All force-distance curves were recorded with the servo-feedback switched off. The velocity of the tip was the same for all F-D experiments. The loading force was set to be no more than 2 nN as at that force covalent bonds are not able to break. For each tip-sample pair a set of 200 curves was gathered. Each surface was probed in 3 different places. After performing force-distance experiments the used cantilevers were subjected to spring constant determination.

A ThermalK module was used to perform measurements of spring constant values. Each cantilever was tested three times and the achieved value was averaged.

For force-distance curve analysis, both nominal and measured values were used. The reason for such data treatment lays in data presentation found in previous publications. In this study we

wanted to show how important it is to determine spring constant values and how much it can influence final data.

The data gathered during experiments were subjected to the statistical analysis- histograms were built with use of a set consisting of 200 force-distance cycles.

For determination of adhesion forces two programs were used: KSpec19¹¹ and a program written in *IGOR PRO* (Appendix I).

7.3 Chiral recognition studies of self assembly monolayers formed in 'click chemistry' reaction

Up to date all studies carried out on chiral recognition were conducted in the way that tips and surfaces were modified directly in one step reactions. Recent development in 'click chemistry' as well as studies on protein- protein interactions were the inspiration for this project. Additionally, the functionalities chosen for this study consist of not one, but two, chiral centres. Our aim was to investigate if and how the second chiral centre influences chiral recognition. For that we carried out studies involving tips modified in the same way as the surface and tips modified with cysteine, which possess similar in structure, one chiral centre.

As the use of click chemistry reaction in chiral recognition studies makes the system under investigation complex, preliminary studies of adhesion between unmodified linker surfaces were necessary.

7.3.1 Determination of adhesion forces for unmodified systems

Preliminary studies on unmodified systems were carried out in order to investigate adhesion forces acting between linkers. Those forces are of interest because they could not be neglected in studying fully modified systems. As mentioned in section 6.4.2, the modification of linkers varies, depending on the linker. Despite the fact that studies on fully modified systems were performed on the surfaces which gave satisfactory PM-IRRAS spectra and small contact angle, local surface inhomogeneity cannot be neglected.

7.3.1.1 Linker A interactions

Tip: Au || surface: linker A

In studies of adhesion forces between gold tip and linker A surface, performed in ethanol, the adhesion force was found to be 0.097 ± 0.059 nN. A typical histogram is presented in Figure 7-4:

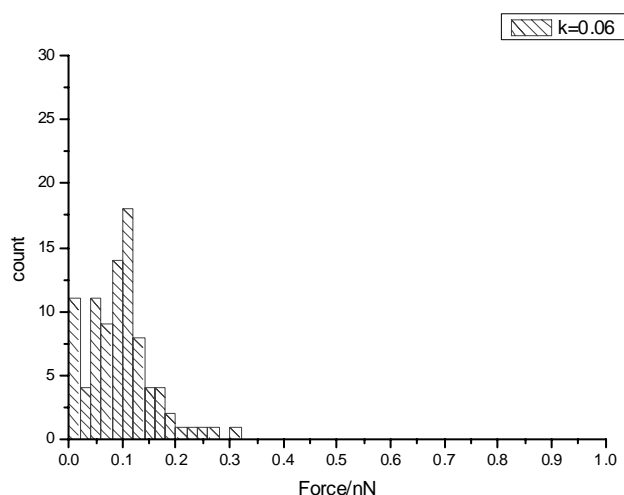


Figure 7-4 Histogram of adhesion forces between gold tip and linker A surface calculated with nominal spring constant.

Tip: Linker A || surface: Linker A

In all experiments carried out by performing approach and retract cycles between tip and surface modified with linker A, no adhesion forces were observed. If the adhesion exists it is so small that is obscured by the thermal noise of the cantilever. The adhesion force was then assumed to be close to zero.

A typical curve for linker A-linker A interaction is presented in Figure 7-5.

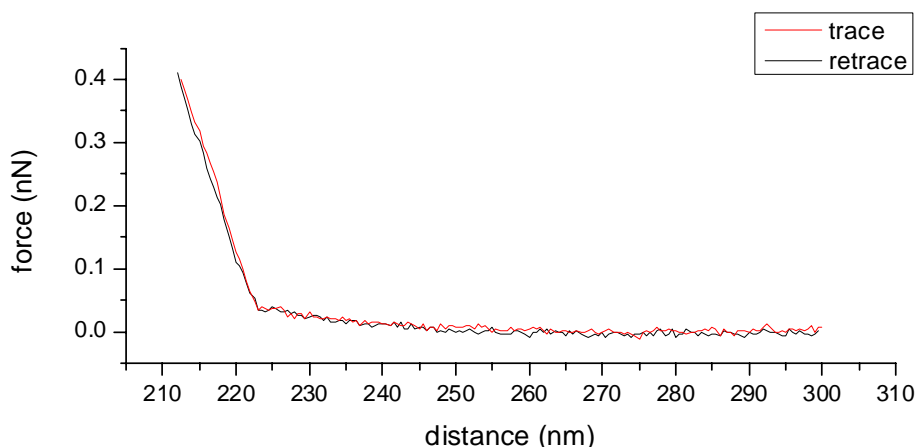


Figure 7-5 A typical force- distance curve for linker A - linker A interaction

7.3.1.2 LinkerB interactions

Tip: linker B || surface: linker B

From the studies of linker B-linker B interactions it was found that two adhesion forces are acting at the interface. The functional group of linker B is the azide group $-N=N^+=N^-$, where the charge is delocalized. That could have an influence on two bands of forces appearing whilst probing the interface.

During measurements it was also found that values obtained using the nominal spring constant were significantly different from values of 'true' force. This is due to the fact that each cantilever used for adhesion force studies was coated with gold beforehand. Coating of cantilevers has an impact on their physical properties and thus spring constant. For this reason each cantilever was tested with the thermal K module to investigate its spring constant value and two histograms of adhesion forces are presented- first (red) for the measured spring constant, and the second (grey) for the nominal spring constant. Spring constant measurements were performed after the force-distance studies. In only a few cases the chip was lost during thermal noise measurement and, in these cases, the adhesion forces were calculated only for nominal spring constant. The difference between the forces obtained using the different spring constants is illustrated in Figure 7-6.

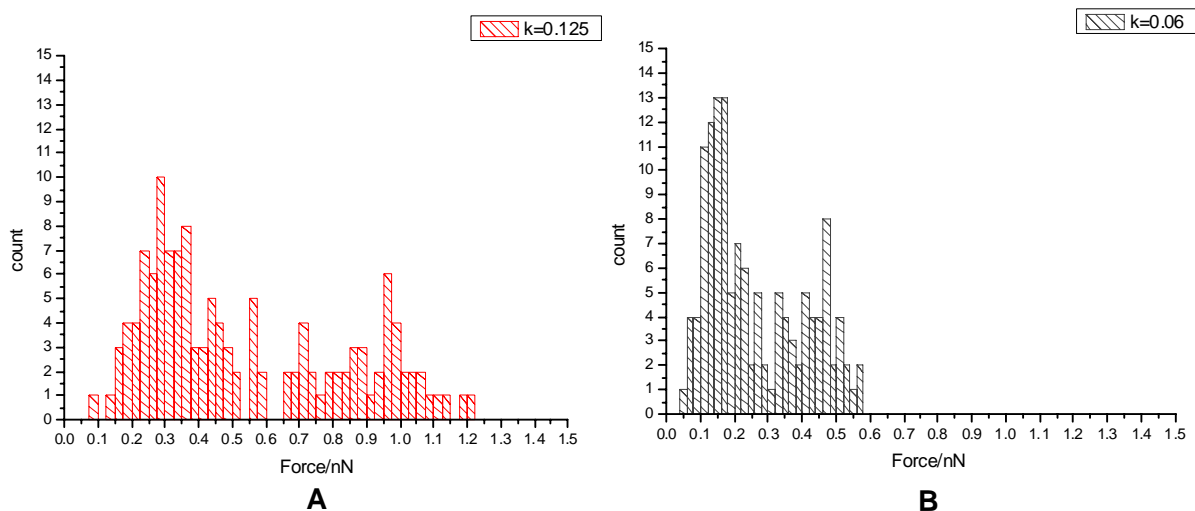


Figure 7-6 Adhesion forces for linker B- linker B interaction (A) calculated with measured spring constant (B) calculated with nominal spring constant

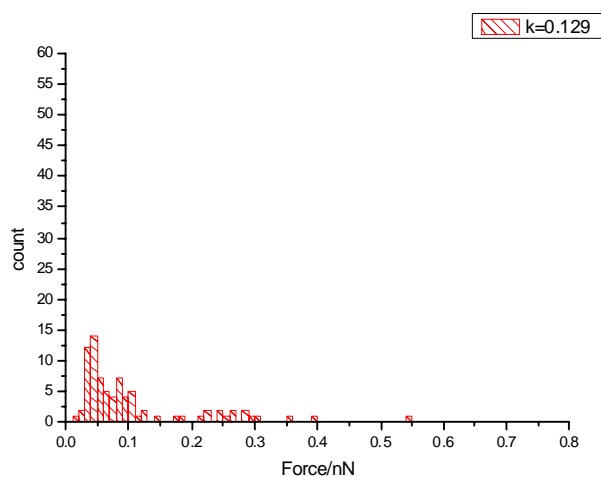
Values of adhesion forces are the values of the highest frequency density and their error was calculated as a standard deviation for a considered force band.

The adhesion forces are illustrated in Table 7-7:

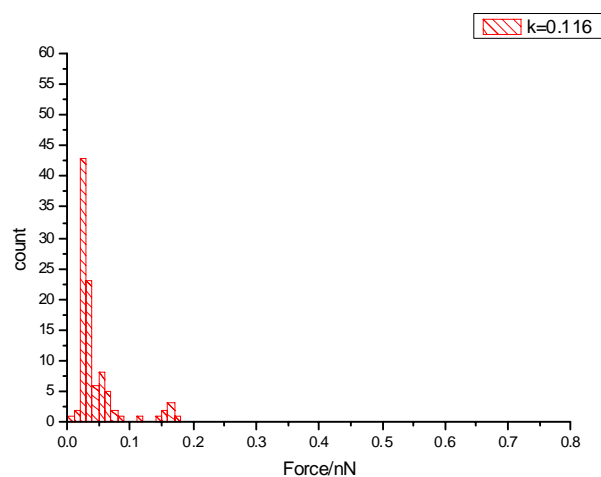
Table 7-7 Adhesion forces of linker B -linker B interaction

Spring constant (N m^{-1})	Adhesion1 (nN)	Adhesion2 (nN)
$k=0.125$	0.354 ± 0.133	0.924 ± 0.132
$k=0.06$	0.162 ± 0.055	0.433 ± 0.069

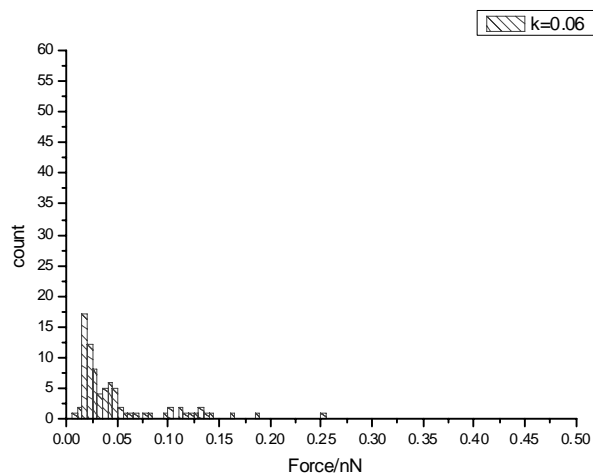
Linker B was also probed with cysteine D and cysteine L-modified tips. In both cases comparable adhesion forces were recorded for measurements performed in ethanol, as presented in Figure 7.7 and detailed in Table 7-8.

Tip: cysteine D || surface: linker B

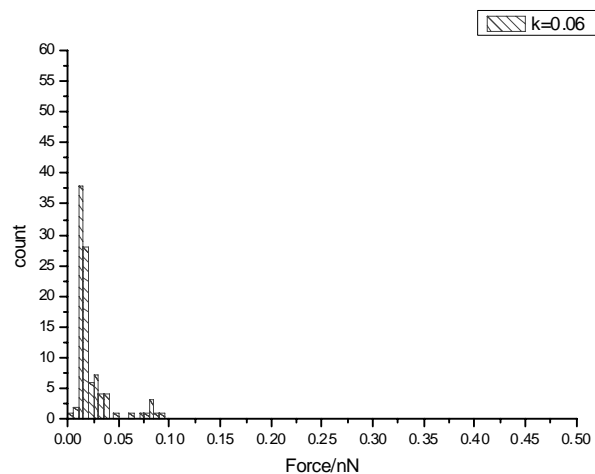
IA

Tip: cysteine L || surface linker B

IIA



IB



IIB

Figure 7-7 Adhesion forces between tips modified with cysteine D and linker B surface (IA-measured spring constant, IB- nominal spring constant) and cysteine L and linker B surface (IIA-measured spring constant, IIB nominal spring constant)

Table 7-8 Adhesion forces between tips modified with D and L cysteine and surface modified with linker B

Tip:cysteine D surface:linker B		Tip:cysteine L surface:linker B	
Spring constant (N m^{-1})	Adhesion force (nN)	Spring constant (N m^{-1})	Adhesion force (nN)
0.129	0.063 ± 0.028	0.116	0.035 ± 0.01
0.06	0.034 ± 0.021	0.06	0.018 ± 0.007

7.3.1.3 Cysteine interactions

Preliminary studies on cysteine enantiomers were also carried out to differentiate between forces acting at the interface of unmodified tip-modified surface and the interface with both-tip and surface modified. These results are presented in Figure 7-8 and the adhesion forces are detailed in Table 7-9.

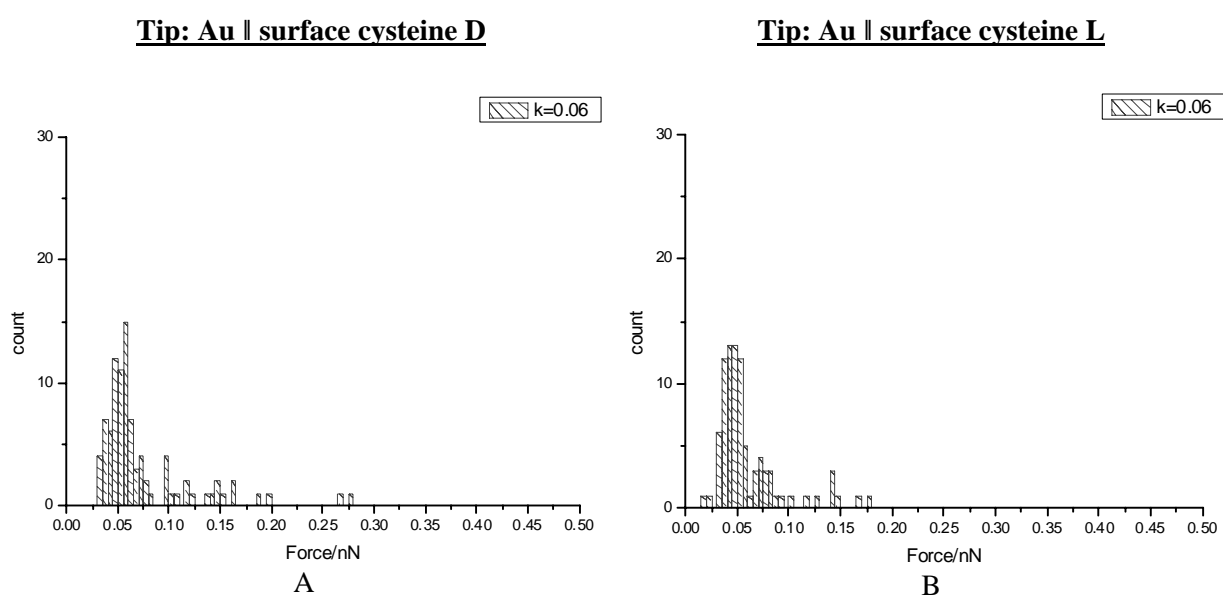


Figure 7-8 Histogram of adhesion forces between (A) Au tip and cysteine D surface and (B) Au tip and cysteine L surface, both calculated with nominal spring constant

Table 7-9 Adhesion forces between unmodified gold tip and surface modified with D and L cysteine

Tip: Au surface cysteine D		Tip: Au surface cysteine L	
Spring constant (N m^{-1})	Adhesion force (nN)	Spring constant (N m^{-1})	Adhesion force (nN)
0.06	0.056 ± 0.033	0.06	0.056 ± 0.031

7.3.2 Determination of forces for fully modified systems

Herein we define a fully modified system as a surface which poses the desired functionality as a result of the Cu-AAC reaction. In this project two groups of such surfaces were studied: first, formed in one step, cysteines on gold; and the second, formed in two steps, *via* click chemistry. The second group compounds are equipped with two, one and no chiral centres.

7.3.2.1 Cysteine interactions

The system of cysteines was chosen for preliminary studies on chiral recognition on surfaces. A molecule of cysteine possesses only one chiral centre. Although the functional groups at the centre are small (-NH₂, -COOH), the presence of acidic and amine groups makes the molecule of interest in chiral recognition. It was shown before that -COOH group enhances ability for chiral recognition⁷. Also the presence of amine groups and acidic groups enhances the chance for hydrogen bond forming, which was also found to have positive influence on chiral discrimination. Cysteine interactions were studied in two types of liquid media: (i) protic solvent, ethanol and (ii) a buffer of pH close to the cysteine isoelectric point, a sodium acetate buffer of pH 5.2. The buffer of pH 5.2 was chosen to see how a charge change enhances chiral discrimination⁸.

The histograms and measured adhesion forces for the four tip-surface combinations are presented first for ethanol: Figure 7-9 and 7-10 and Tables 7-10 and 7-11 and second for buffer of pH 5.2: Figures 7-11 and 7-12 and Tables 7-12 and 7-13.

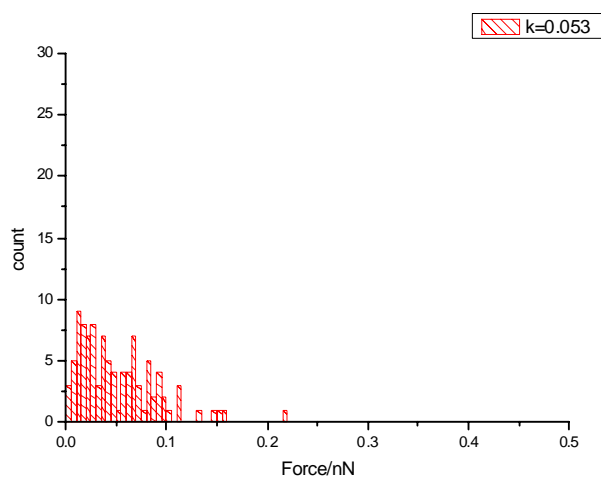
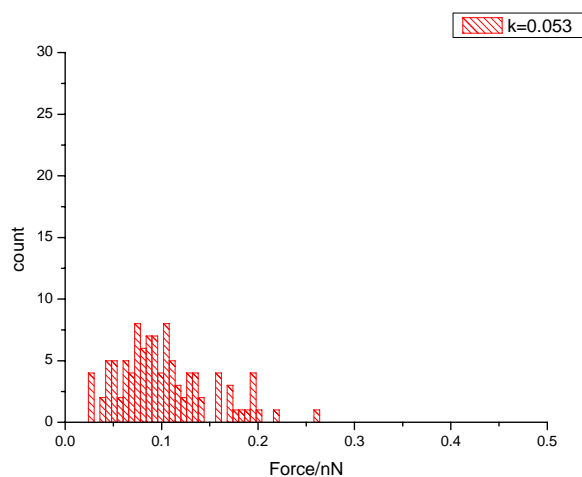
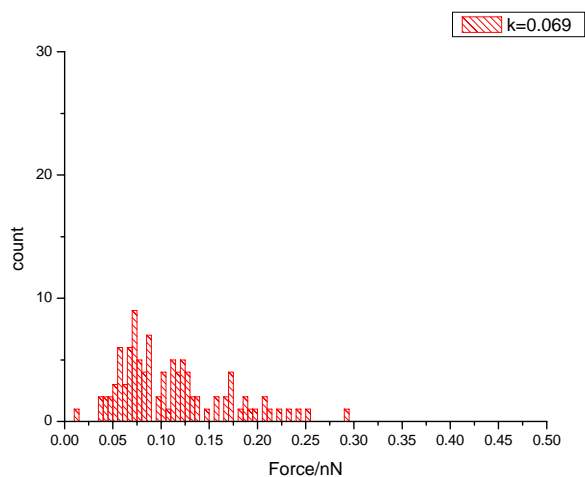
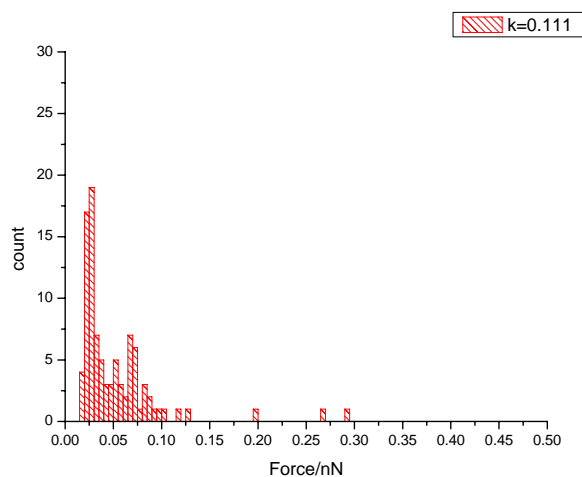
Tip: cysteine D || surface: cysteine D**Tip: cysteine D || surface: cysteine L****Tip: cysteine L || surface: cysteine D****Tip: cysteine L || surface: cysteine L**

Figure 7-9 Histograms of cysteine enantiomers adhesion forces recorded in ethanol, calculated with use of measured spring constant

Table 7-10 Adhesion forces for the combinations of tip- surface modified with D and L cysteine obtained by use of calculated spring constant

Tip: cysteine D surface: cysteine D		Tip: cysteine D surface: cysteine L	
Spring constant (Nm^{-1})	Adhesion force (nN)	Spring constant (Nm^{-1})	Adhesion force (nN)
0.053	0.051 ± 0.039	0.053	0.105 ± 0.056
Tip: cysteine L surface: cysteine D		Tip: cysteine L surface: cysteine L	
Spring constant (Nm^{-1})	Adhesion force (nN)	Spring constant (Nm^{-1})	Adhesion force (nN)
0.069	0.109 ± 0.054	0.111	0.051 ± 0.044

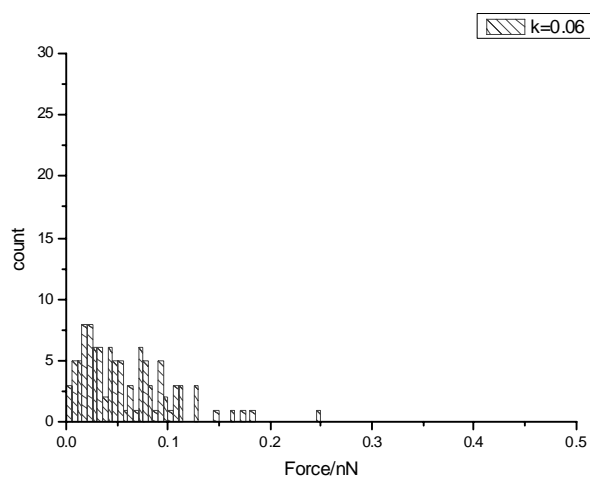
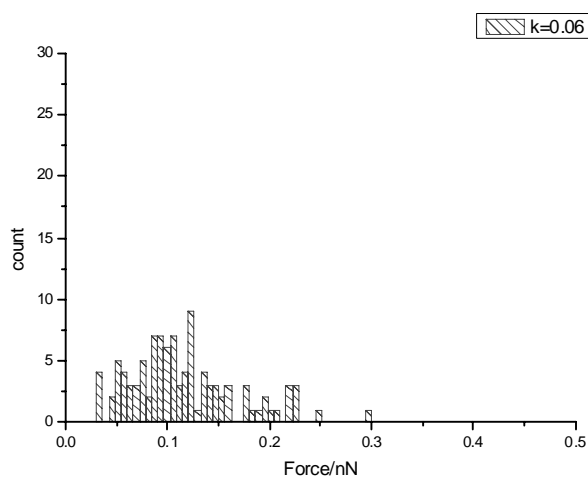
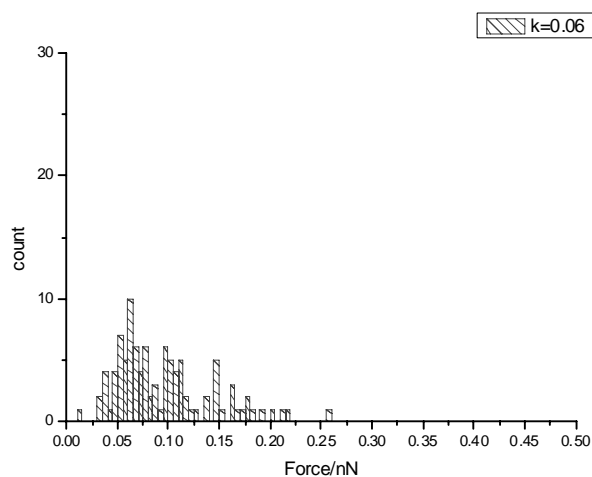
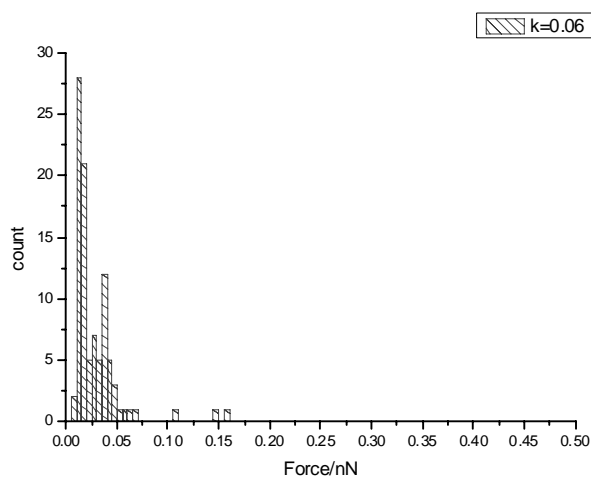
Tip: cysteine D || surface: cysteine D**Tip: cysteine D || surface: cysteine L****Tip: cysteine L || surface: cysteine D****Tip: cysteine L || surface: cysteine L**

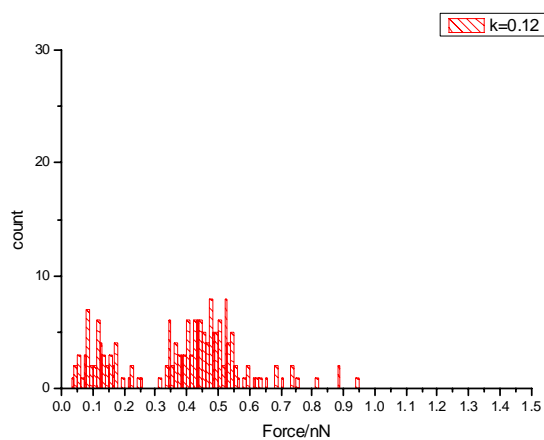
Figure 7-10 Histograms of cysteine enantiomers adhesion forces recorded in ethanol, calculated with use of nominal spring constant

Table 7-11 Adhesion forces for the combinations of tip- surface modified with D and L cysteine obtained by use of nominal spring constant

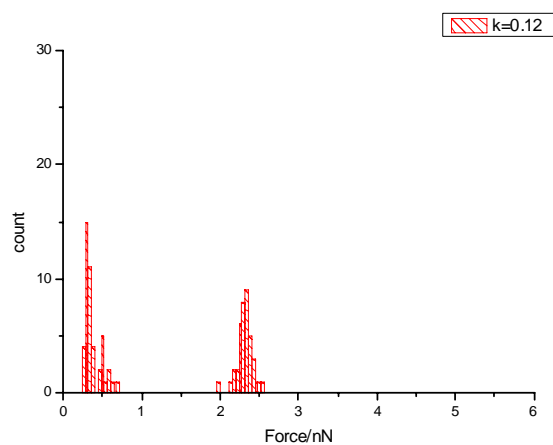
Tip: cysteine D surface: cysteine D		Tip: cysteine D surface: cysteine L	
Spring constant (N m^{-1})	Adhesion force (nN)	Spring constant (N m^{-1})	Adhesion force (nN)
0.06	0.057 ± 0.044	0.06	0.119 ± 0.063
Tip: cysteine L surface: cysteine D		Tip: cysteine L surface: cysteine L	
Spring constant (N m^{-1})	Adhesion force (nN)	Spring constant (N m^{-1})	Adhesion force (nN)
0.06	0.095 ± 0.047	0.06	0.038 ± 0.022

Cysteines in buffer solution pH 5.2

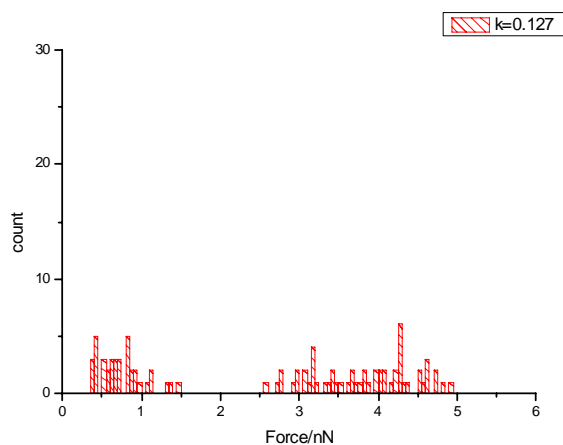
Tip: cysteine D || surface: cysteine D



Tip: cysteine D || surface: cysteine L



Tip: cysteine L || surface: cysteine D



Tip: cysteine L || surface: cysteine L

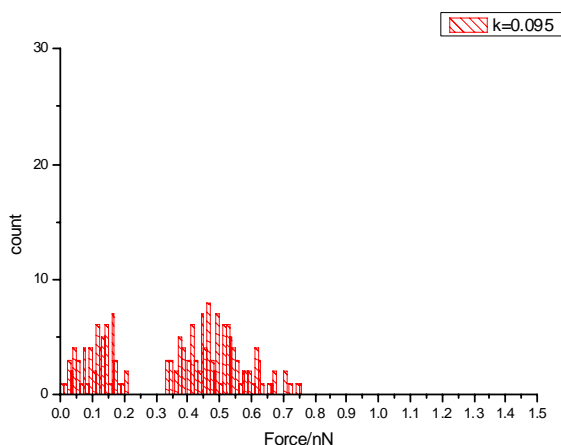


Figure 7-11 Histograms of cysteine enantiomers adhesion forces recorded in buffer pH 5.2, calculated with use of measured spring constant

Table 7-12 Adhesion forces for the combinations of tip- surface modified with D and L cysteine obtained by use of calculated spring constant in buffer of pH 5.2

Tip: cysteine D surface: cysteine D			Tip: cysteine D surface: cysteine L		
Spring constant (N m ⁻¹)	Adhesion force (nN)		Spring constant (N m ⁻¹)	Adhesion force (nN)	
	1	2		1	2
0.12	0.124±0.053	0.488±0.057	0.12	0.374±0.058	2.314±0.108
Tip: cysteine L surface: cysteine D			Tip: cysteine L surface: cysteine L		
Spring constant (N m ⁻¹)	Adhesion force (nN)		Spring constant (N m ⁻¹)	Adhesion force (nN)	
	1	2		1	2
0.12	0.746±0.289	3.931±0.668	0.095	0.112±0.052	0.498±0.096

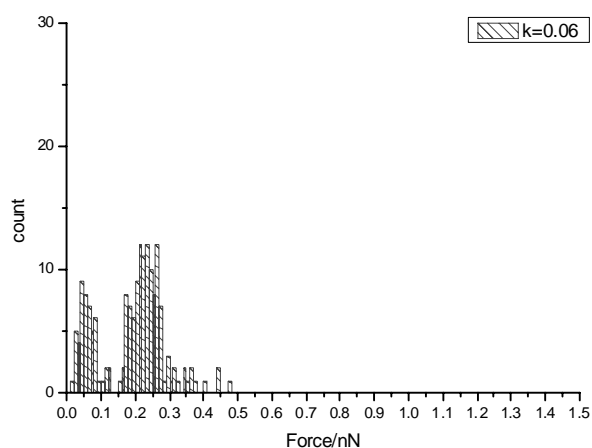
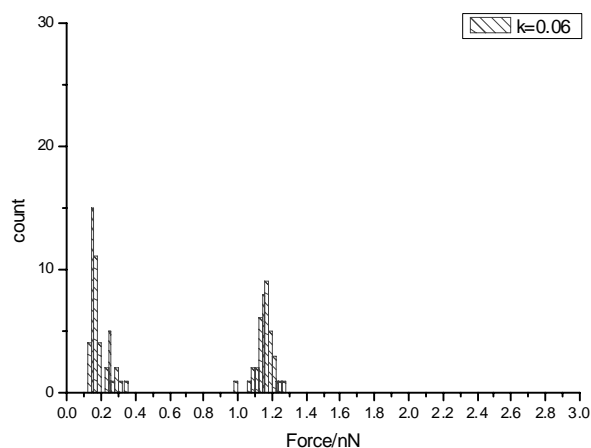
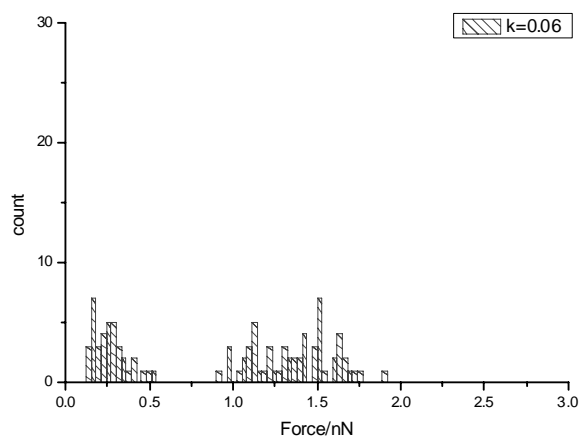
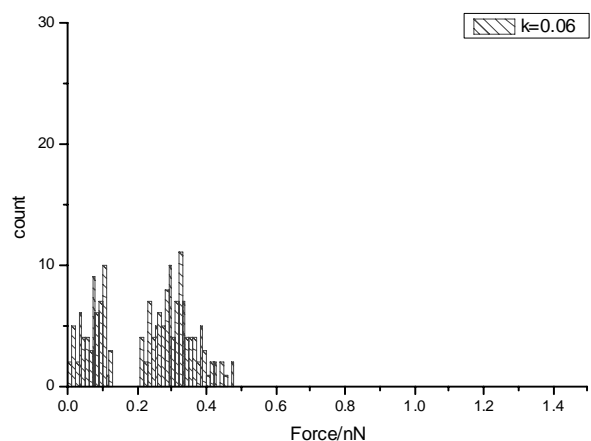
Tip: cysteine D || surface: cysteine D**Tip: cysteine D || surface: cysteine L****Tip: cysteine L || surface: cysteine D****Tip: cysteine L || surface: cysteine L**

Figure 7-12 Histograms of cysteine enantiomers adhesion forces recorded in buffer pH 5.2, calculated with use of nominal spring constant

Table 7-13 Adhesion forces for the combinations of tip- surface modified with D and L cysteine obtained by use of nominal spring constant in buffer of pH 5.2

Tip: cysteine D surface: cysteine D			Tip: cysteine D surface: cysteine L		
Spring constant (N m ⁻¹)	Adhesion force (nN)		Spring constant (N m ⁻¹)	Adhesion force (nN)	
	1	2		1	2
0.06	0.062±0.026	0.244±0.058	0.06	1.87±0.054	1.157±0.051
Tip: cysteine L surface: cysteine D			Tip: cysteine L surface: cysteine L		
Spring constant (N m ⁻¹)	Adhesion force (nN)		Spring constant (N m ⁻¹)	Adhesion force (nN)	
	1	2		1	2
0.06	0.263±0.102	1.362±0.236	0.06	0.07±0.033	0.314±0.061

From the experiments with surfaces modified with cysteines, chiral discrimination was observed. For *R-S* and *S-R* interactions the recorded forces in ethanol were shifted to higher force values and spread wider, whilst for homochiral interactions there were narrower bands of forces recorded. This could be explained by the fact that molecules interact in the way that all functional groups come together close enough to interact at the same time. Despite the fact, that they possess –COOH groups, which enhances the ability of a molecule for chiral discrimination, cysteine is not charge-free and this causes additional forces to emerge during the interaction. Larger forces acting at the *S-R*, *R-S* combinations could be also explained by the possible hydrogen bonding influence, shown schematically in Figure 7-13.

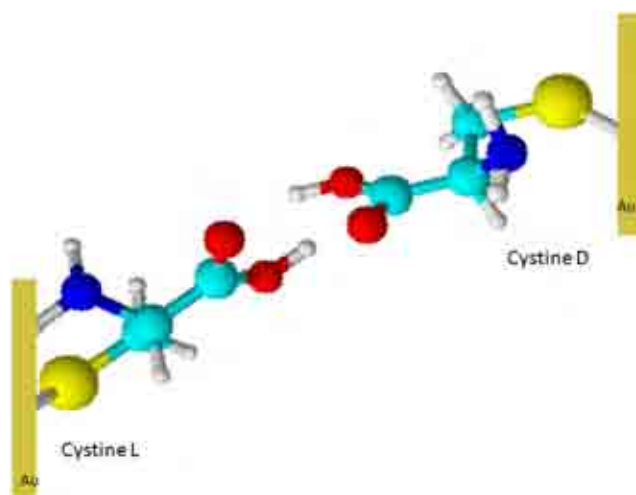


Figure 7-13 D and L cysteine possible interaction

The above result was also observed for the same system tested in a buffer solution of pH 5.2 with one difference- two bands of forces were encountered for a single measurement. For homochiral interactions they are close together whilst for heterochiral they are further apart. Measurements conducted in buffer solutions showed that the charge of functional groups plays a significant role in the recognition of chirality and this for cannot be neglected for amphiphilic molecules. For more

complex studies of this system, measurements at different pH should be conducted. In this project we focused mainly on using ethanol due to the lack of time for measurements in different solvents.

7.3.2.2 Interactions of linker A chiral derivatives

As a first system to study chiral discrimination and influence of the second chiral centre, a chiral derivative of linker A was chosen. The chiral derivatives consist of two alanine groups. In our case we were using dipeptides of conformations DL and LL. The reason for that is that the other enantiomers (LD and DD) were not successfully synthesised yet. The preliminary molecular mechanics (MM2) studies of the molecule with gold bonded covalently to the sulphur showed that it has the minimum energy when it is coiled and intermolecular hydrogen bonds are formed. This led us to assume that the inner chiral centre could be revealed and influence chiral discrimination.

In this experiment tips modified with DL and LL derivative were tested against surfaces modified the same way. The surfaces are illustrated in Figure 7-14.

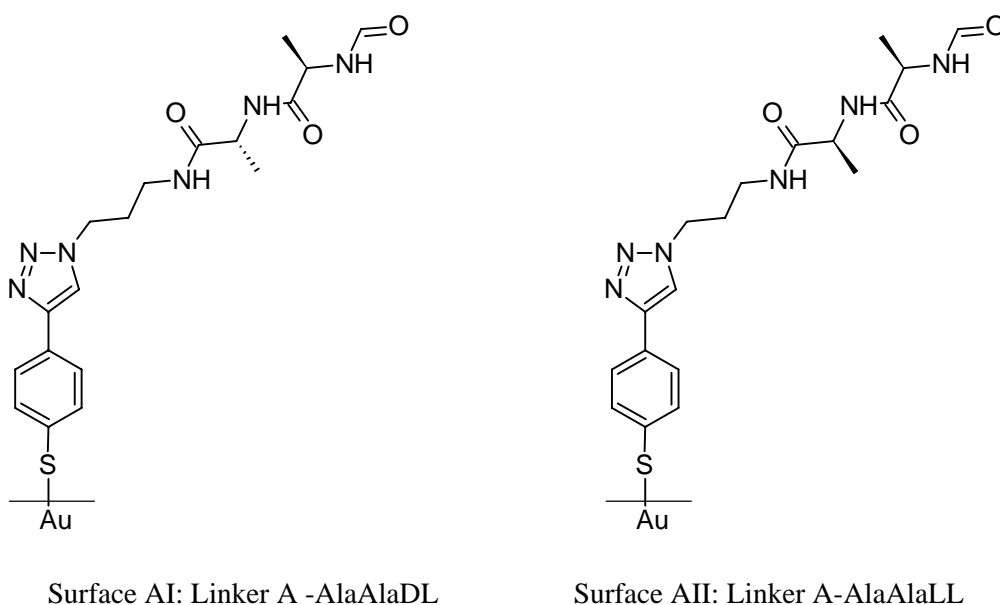


Figure 7-14 Enantiomers of linker A chiral derivatives

The results are presented in Figures 7-15 and 7-16 and the adhesion forces are in Table 7-14 and 7-15.

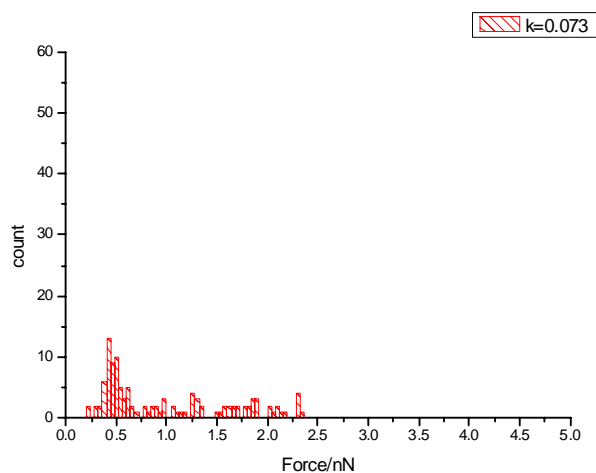
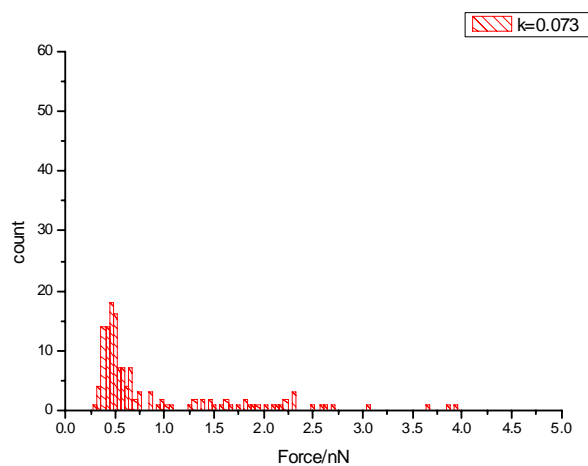
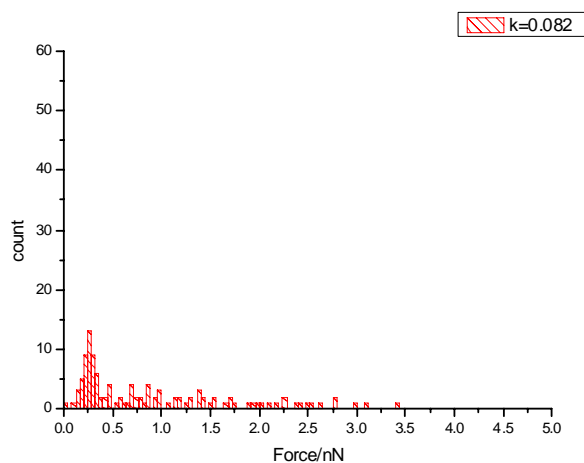
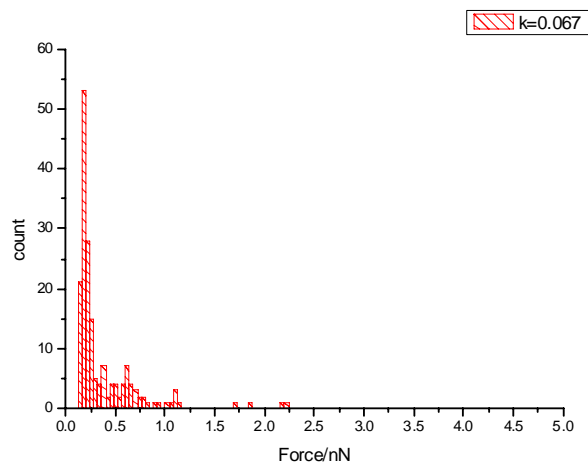
Tip: L.A-AlaAlaDL || surface: L.A-AlaAlaDL**Tip: L.A-AlaAlaDL || surface: L.A-AlaAlaLL****Tip: L.A-AlaAlaLL || surface: L.A-AlaAlaDL****Tip: L.A-AlaAlaLL || surface: L.A-AlaAlaLL**

Figure 7-15 Adhesion force histograms of linker A chiral derivatives calculated with use of measured spring constant

Table 7-14 Adhesion forces of linker A chiral derivatives calculated with measured spring constant

Tip: L.A-AlaAlaDL surface: LA-AlaAlaDL		Tip: L.A-AlaAlaDL surface: L.A-AlaAlaLL	
Spring constant (N m^{-1})	Adhesion force (nN)	Spring constant (N m^{-1})	Adhesion force (nN)
0.073	0.474 ± 0.107	0.073	0.542 ± 0.188
Tip: L.A-AlaAlaLL surface: L.A-AlaAlaDL		Tip: L.A-AlaAlaLL surface: L.A-AlaAlaLL	
Spring constant (N m^{-1})	Adhesion force (nN)	Spring constant (N m^{-1})	Adhesion force (nN)
0.082	0.303 ± 0.136	0.067	0.223 ± 0.077

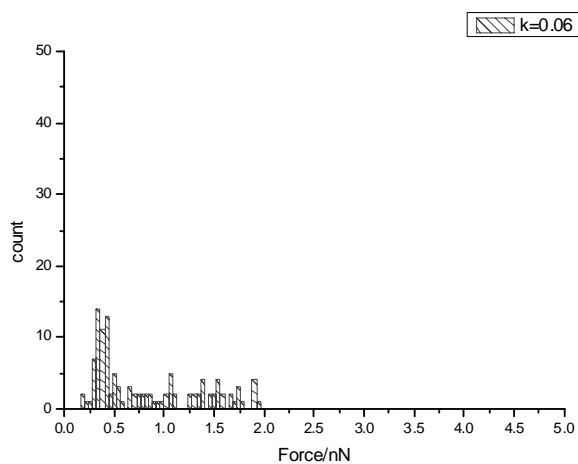
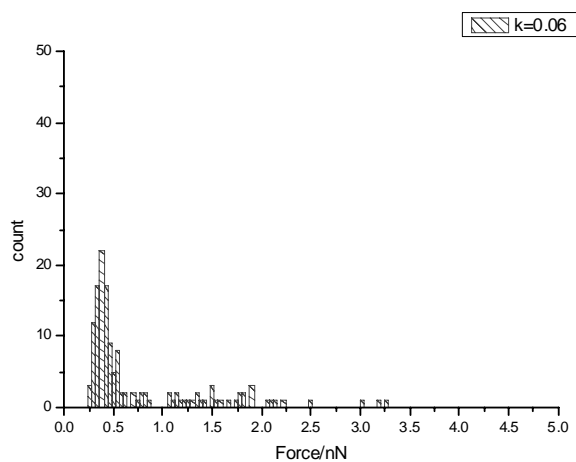
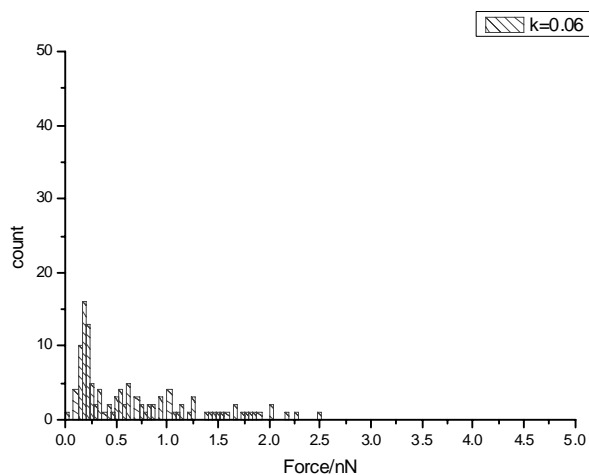
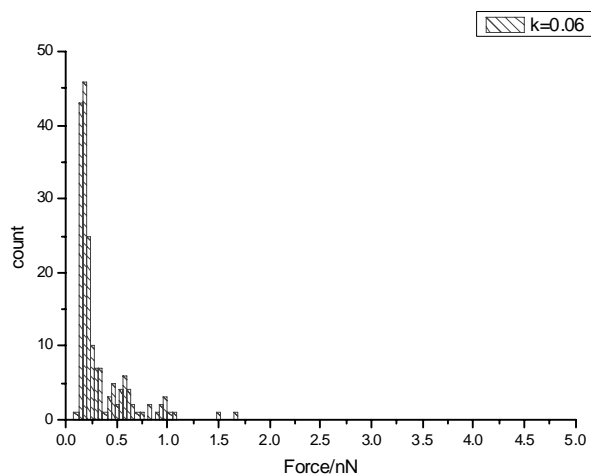
Tip: L.A-AlaAlaDL || surface: L.A-AlaAlaDL**Tip: L.A-AlaAlaDL || surface: L.A-AlaAlaLL****Tip: L.A-AlaAlaLL || surface: L.A-AlaAlaDL****Tip: L.A-AlaAlaLL || surface: L.A-AlaAlaLL**

Figure 7-16 Adhesion force histograms of linker A chiral derivatives calculated with use of nominal spring constant

Table 7-15 Adhesion forces of linker A chiral derivatives calculated with use of nominal spring constant.

Tip: L.A-AlaAlaDL surface: L.A-AlaAlaDL		Tip: L.A-AlaAlaDL surface: L.A-AlaAlaLL	
Spring constant N m^{-1}	Adhesion force nN	Spring constant N m^{-1}	Adhesion force nN
0.06	0.389 ± 0.088	0.06	0.445 ± 0.154
Tip: L.A-AlaAlaLL surface: L.A-AlaAlaDL		Tip: L.A-AlaAlaLL surface: L.A-AlaAlaLL	
Spring constant N m^{-1}	Adhesion force nN	Spring constant N m^{-1}	Adhesion force nN
0.06	0.222 ± 0.100	0.06	0.194 ± 0.058

Studies of linker A chiral derivatives interactions showed that the smallest forces were recorded for the homochiral type of contact, which is consistent with previous results achieved by Mahapatro and Seneviratne^{7,10}. DL-DL interaction (notation: tip- surface) forces are however comparable with DL-LL, which indicates that the molecules are not 'touching' each other by the groups at the terminal chiral centre but by the inner one. Hydrogen bonding and charge of the groups can have significant influence on recorded forces. For combination of LL-DL probing pair, smaller forces in comparison to DL-LL interactions were recorded. It could be explained by the fact that modification on the tip might be less dense and for that the molecule could be of less coiled conformation. To understand this result in a better way, additional studies of probing linker A chiral derivatives possessing only one chiral centre were conducted.

Chiral and achiral derivatives interaction with LA-AlaAlaDL and LL surface

In this case the tip was modified to possess one and no chiral centre, but keeping similar functional groups to linker A AlaAlaLL and DL derivatives. The modifications of the tip are illustrated in Figure 7-17.

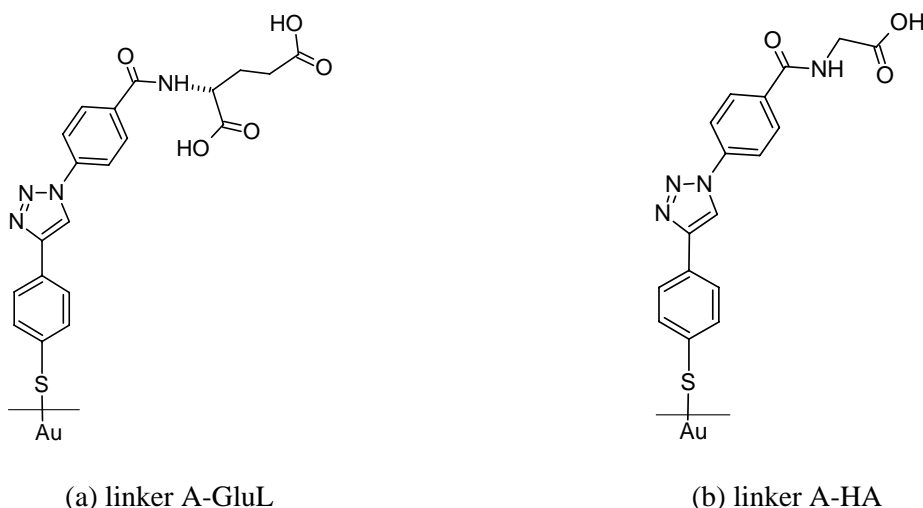


Figure 7-17 Tip modifications for experiments of probing linker A chiral derivatives of two chiral centres with (a) linker A derivatives possessing one chiral centre and (b) with no chiral centres

The results are presented in Figures 7-18 and 7-19 and Tables 7-16 and 7-17.

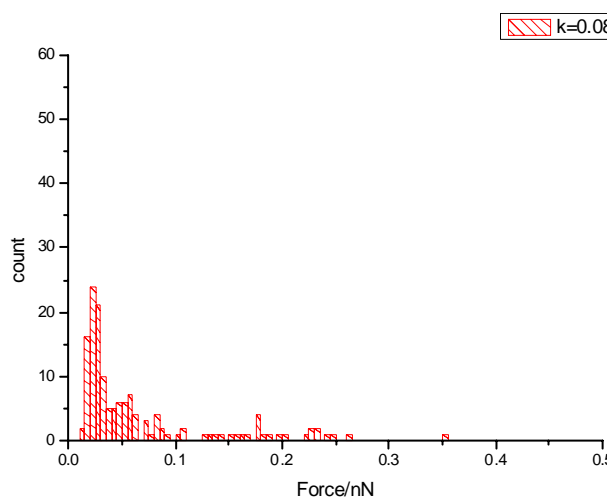
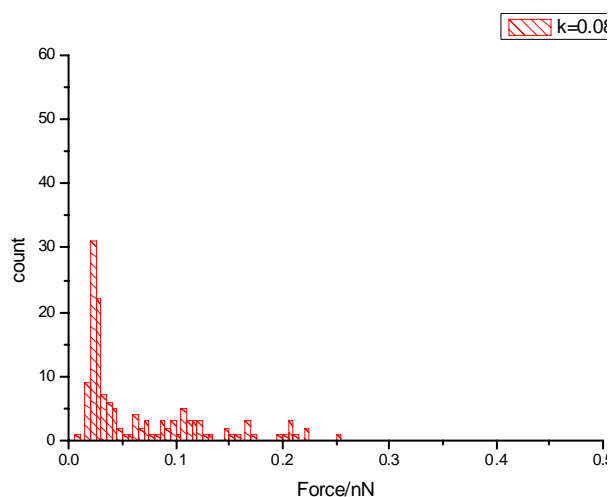
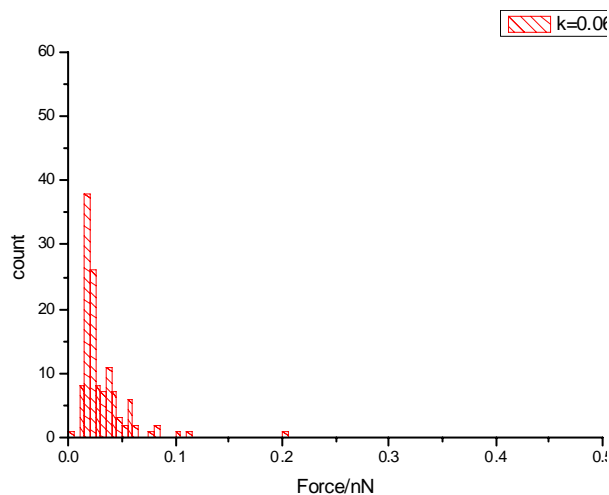
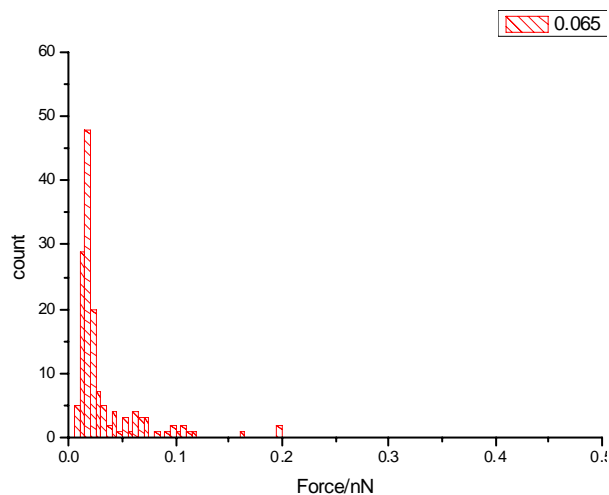
Tip: L.A-GluL || surface: L.A-AlaAlaDL**Tip: L.A-GluL || surface: L.A-AlaAlaLL****Tip: L.A-Ha || surface: L.A-AlaAlaDL****Tip: L.A-Ha || surface: L.A-AlaAlaLL**

Figure 7-18 Adhesion force histograms of linker A chiral derivatives with two chiral centres probed with linker A chiral derivative of one chiral centre and no chiral centre, calculated with use of measured spring constant

Table 7-16 Adhesion forces between tips modified with linker-A GluL and linker A-HA and surface modified with linker A chiral derivatives possessing two chiral centres

Tip: L.A-GluL surface: L.A-AlaAlaDL			Tip: L.A-GluL surface: L.A-AlaAlaLL		
Spring constant (N m ⁻¹)	Adhesion force (nN)		Spring constant (N m ⁻¹)	Adhesion force (nN)	
0.084	0.038±0.022	0.196±0.051	0.084	0.027±0.008	0.0124±0.0051
Tip: L.A-Ha surface: L.A-AlaAlaDL			Tip: L.A-Ha surface: L.A-AlaAlaLL		
Spring constant (N m ⁻¹)	Adhesion force (nN)		Spring constant (N m ⁻¹)	Adhesion force (nN)	
0.065	0.030±0.013		0.065	0.028±0.007	

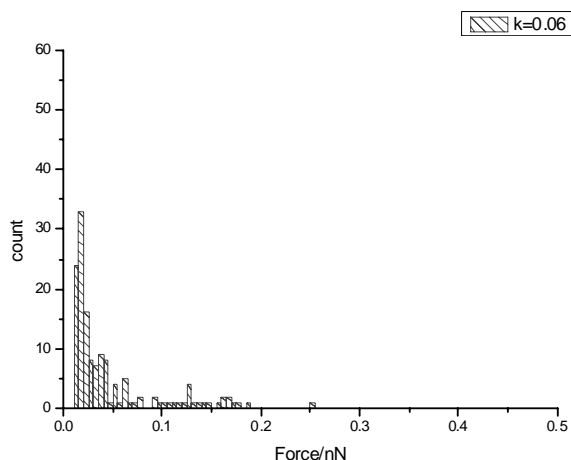
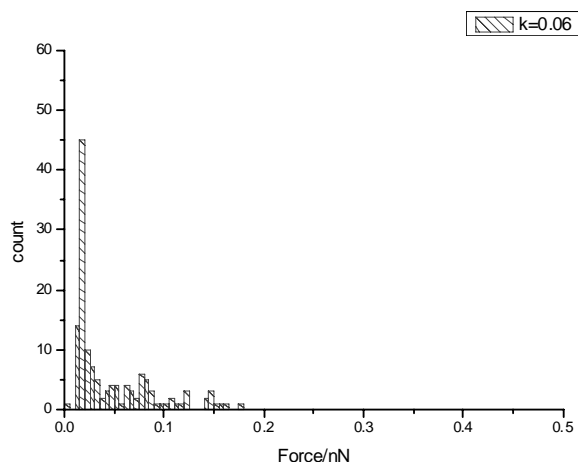
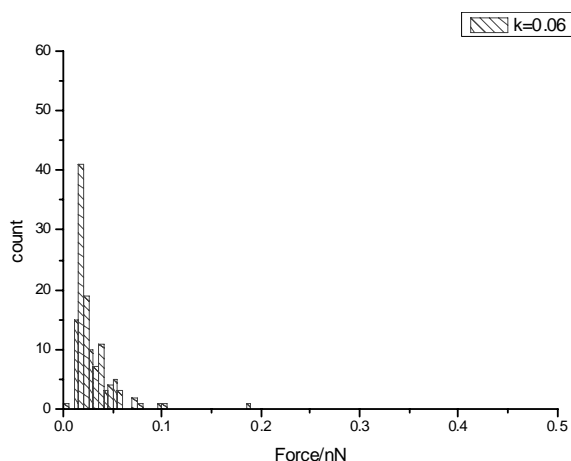
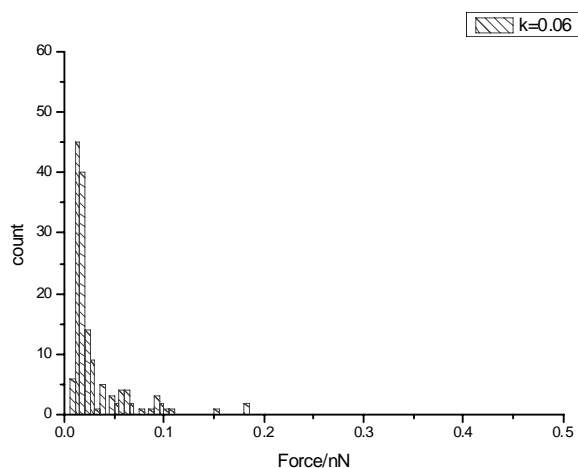
Tip: L.A-GluL || surface: L.A-AlaAlaDL**Tip: L.A-GluL || surface: L.A-AlaAlaLL****Tip: L.A-Ha || surface: L.A-AlaAlaDL****Tip: L.A-Ha || surface: L.A-AlaAlaLL**

Figure 7-19 Adhesion force histograms of linker A chiral derivatives with two chiral centres probed with linker A chiral derivative of one chiral centre and no chiral centre, calculated with use of nominal spring constant

Table 7-17 Adhesion forces between tips modified with linker-A GluL and linker A-HA and surface modified with linker A chiral derivatives possessing two chiral centres

Tip: L.A-GluL surface: L.A-AlaAlaDL			Tip: L.A-GluL surface: L.A-AlaAlaLL		
Spring constant (N m^{-1})	Adhesion force (nN)		Spring constant (N m^{-1})	Adhesion force (nN)	
0.06	0.027 ± 0.016	0.14 ± 0.036	0.06	0.019 ± 0.06	0.089 ± 0.036
Tip: L.A-Ha surface: L.A-AlaAlaDL			Tip: L.A-Ha surface: L.A-AlaAlaLL		
Spring constant (N m^{-1})	Adhesion force (nN)		Spring constant (N m^{-1})	Adhesion force (nN)	
0.06	0.028 ± 0.012		0.06	0.025 ± 0.006	

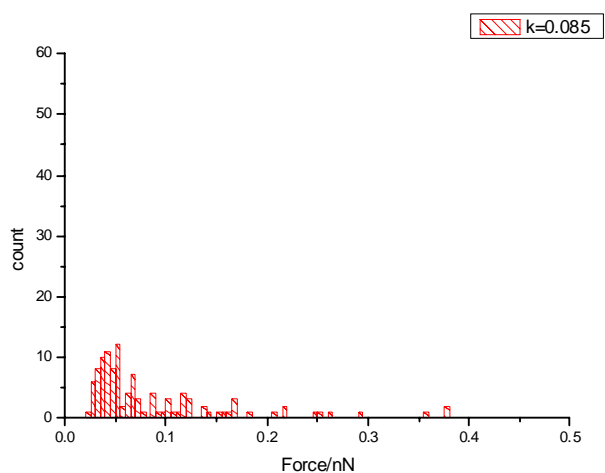
Experiments conducted with a probing molecule equipped with only one chiral centre confirmed that the molecules at the surface are of a conformation which reveals the inner chiral centre. Bigger forces were encountered for the linker A-GluL and linker A AlaAlaDL combination than for the linker A-GluL and linker A- AlaAlaLL.

Use of achiral molecules at the end of the tip showed no significant difference either between forces encountered for probing surfaces of DL and LL enantiomer, or for the histogram shape. This confirmed that use of GluL derivatives possessing only one chiral centre can be used for chiral recognition, although to understand the system in a better way studies in media of different pH values should be conducted.

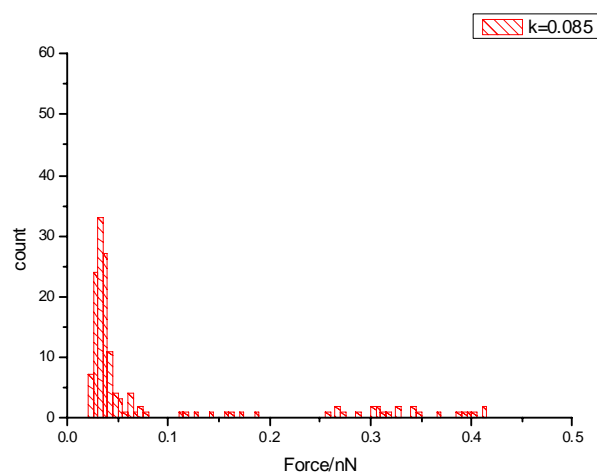
7.3.2.3 Interactions of cysteines and linker A chiral derivatives

Figures 7-20 and 7-21 present results obtained for probing surfaces modified with linker A chiral derivatives with tips modified with D and L cysteine. These experiments were conducted to investigate if cysteine enantiomers can be used for probing chirality and how the results compare with experiments conducted in section 7.3.2.2.

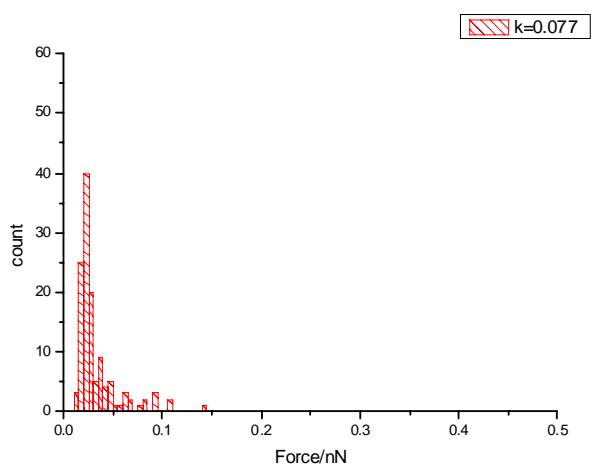
Tip: cysteine D || surface: L.A-AlaAlaDL



Tip: cysteine D || surface: L.A-AlaAlaLL



Tip: cysteine L || surface: L.A-AlaAlaDL



Tip: cysteine L || surface: L.A-AlaAlaLL

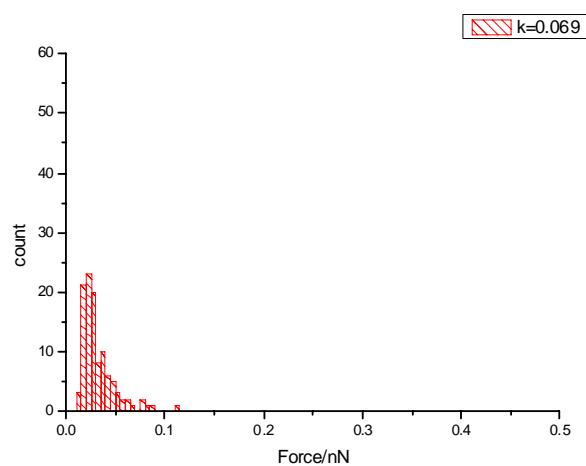


Figure 7-20 Adhesion force histograms of D and L cysteine and linker A chiral derivatives interactions, calculated with use of measured spring constant

Table 7-18 Adhesion forces of interactions between tip modified with D and L cysteine and surface modified with linker A chiral derivatives calculated with use of measured spring constant

Tip: cysteine D surface: L.A-AlaAlaDL		Tip: cysteine D surface: L.A-AlaAlaLL	
Spring constant (N m^{-1})	Adhesion force (nN)	Spring constant (N m^{-1})	Adhesion force (nN)
0.085	0.068 ± 0.03	0.085N/m	0.043 ± 0.03
Tip: cysteine L surface: L.A-AlaAlaDL		Tip: cysteine L surface: L.A-AlaAlaLL	
Spring constant (N m^{-1})	Adhesion force (nN)	Spring constant (N m^{-1})	Adhesion force (nN)
0.077	0.031 ± 0.017	0.069	0.034 ± 0.017

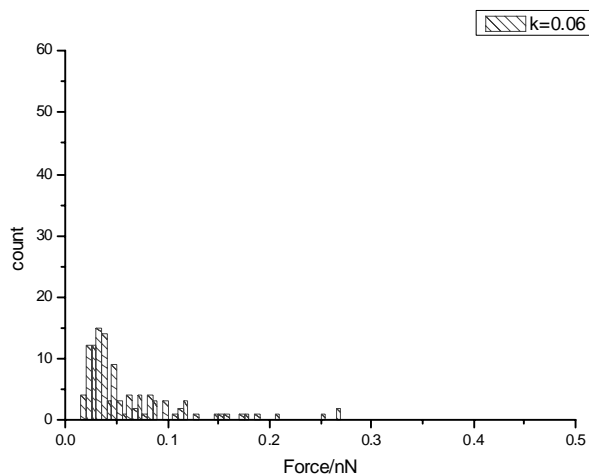
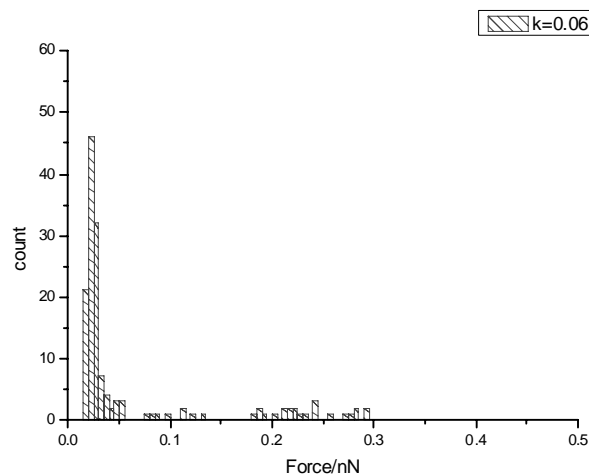
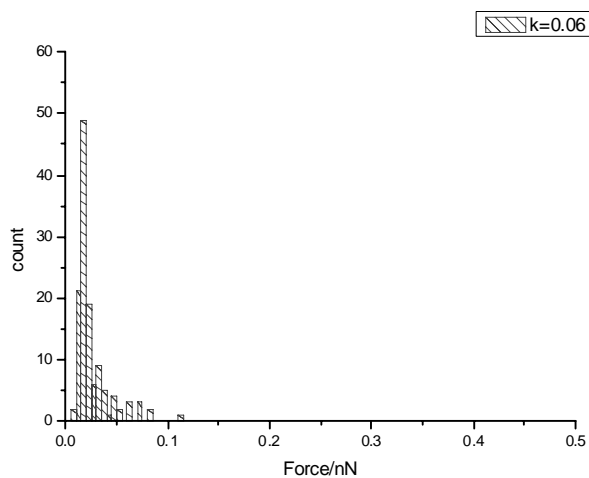
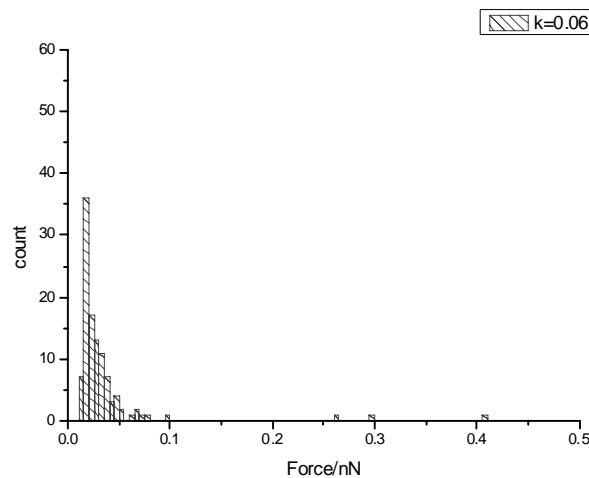
Tip: cysteine D || surface: L.A-AlaAlaDL**Tip: cysteine D || surface: L.A-AlaAlaLL****Tip: cysteine L || surface: L.A-AlaAlaDL****Tip: cysteine L || surface: L.A-AlaAlaLL**

Figure 7-21 Adhesion force histograms of D and L cysteine and linker A chiral derivatives interactions, calculated with use of nominal spring constant

Table 7-19 Adhesion forces of interactions between tip modified with D and L cysteine and surface modified with linker A chiral derivatives calculated with use of measured spring constant

Tip: cysteine D surface: L.A-AlaAlaDL		Tip: cysteine D surface: L.A-AlaAlaLL	
Spring constant (N m ⁻¹)	Adhesion force (nN)	Spring constant (N m ⁻¹)	Adhesion force (nN)
0.06	0.048±0.028	0.06	0.031±0.021
Tip: cysteine L surface: L.A-AlaAlaDL		Tip: cysteine L surface: L.A-AlaAlaLL	
Spring constant (N m ⁻¹)	Adhesion force (nN)	Spring constant (N m ⁻¹)	Adhesion force (nN)
0.06	0.024±0.013	0.06	0.032±0.017

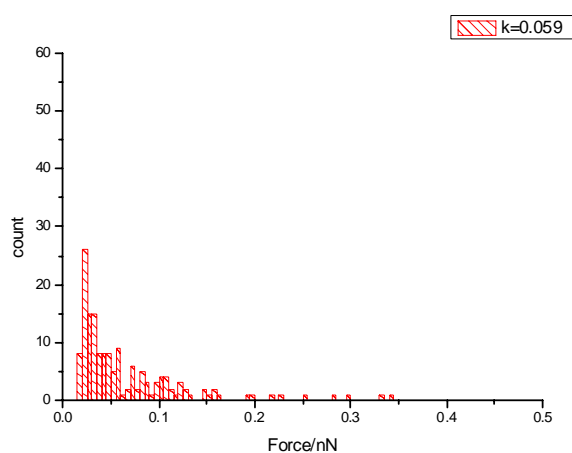
The results obtained for interactions of cysteines with linkerA, chiral derivatives show two things. First, the surface quality has tremendous influence on achieved histograms. Second, cysteines can be used for chiral discrimination; however, in the case of dipeptides there is a need of media change for a solvent of pH close to the cysteine isoelectric point. The force bands are not significantly shifted or spread. The existence of additional forces coming from the charge of functional groups might obscure the recognition.

The trend in the histograms confirms the influence of the second (the innermost) chiral centre. The adhesion forces dispersion is as follows: D-DL > D-LL > L-LL ≥ L-DL. Forces recorded for L-LL and L-DL pairs are close in values, however L-LL interactions are slightly higher. The same trend was also observed for linker B and C chiral derivatives presented later in this chapter. This indicates that the groups of the second (more inner) chiral centre interact with the probing molecules. This interaction could come from the charge of these functional groups; therefore additional studies with use of media of different pH are needed to understand the systems more deeply.

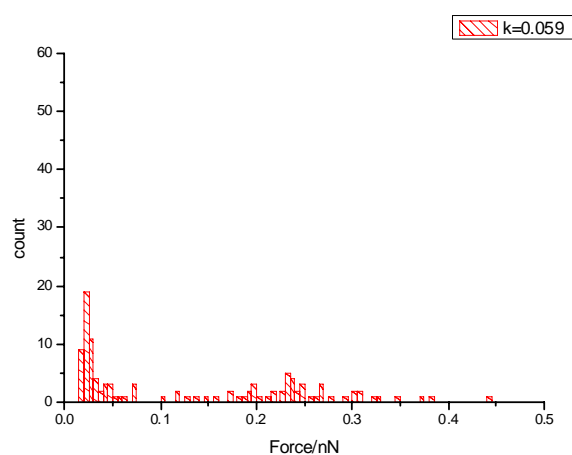
7.3.2.4 Interactions of cysteines with linker A chiral and achiral derivatives

Results of probing gold surfaces modified with linker A derivatives possessing only one and no chiral centres with tips modified with D and L cysteine are presented in Figures 7-22 and 7-23. The adhesion forces of these interactions are given in Tables 7-20 and 7-21. These experiments were conducted in order to see how the shape of histograms and adhesion force changes if there is no chiral centre and only one chiral centre present at the surface.

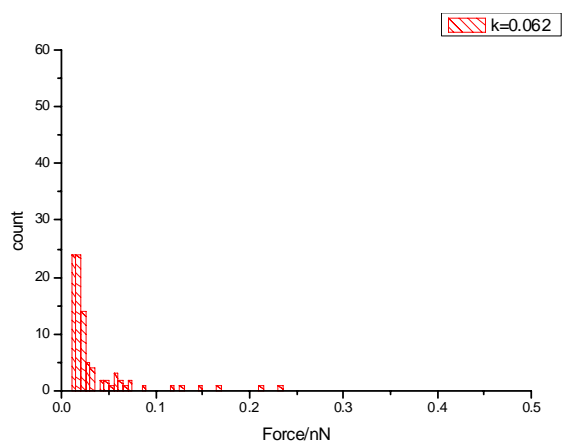
Tip: cysteine D || surface: L.A-GluL



Tip: cysteine D || surface: L.A-Ha



Tip: cysteine L || surface: L.A-GluL



Tip: cysteine L || surface: L.A-Ha

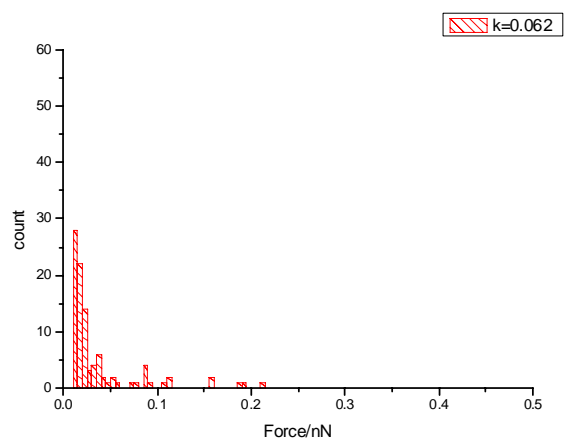


Figure 7-22 Adhesion force histograms of D and L cysteine and linker A chiral and achiral derivatives interactions, calculated with use of measured spring constant

Table 7-20 Adhesion force of D and L cysteine modified tip and linker A chiral and achiral derivatives interactions, calculated with use of measured spring constant

Tip: cysteine D surface: L.A-GluL		Tip: cysteine D surface: L.A-Ha	
Spring constant (N m^{-1})	Adhesion force (nN)	Spring constant (N m^{-1})	Adhesion force (nN)
0.059	0.04 ± 0.021	0.059	0.031 ± 0.015 0.237 ± 0.069
Tip: cysteine L surface: L.A-GluL		Tip: cysteine L surface: L.A-Ha	
Spring constant (N m^{-1})	Adhesion force (nN)	Spring constant (N m^{-1})	Adhesion force (nN)
0.062	0.023 ± 0.014	0.062	0.026 ± 0.01

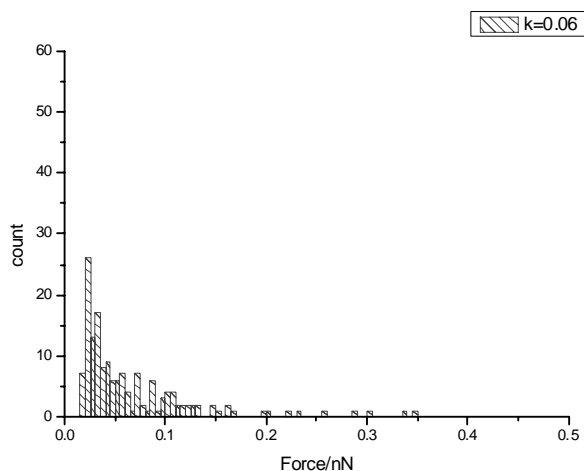
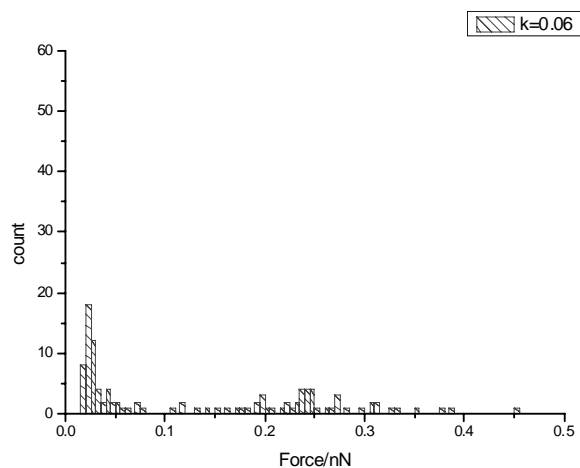
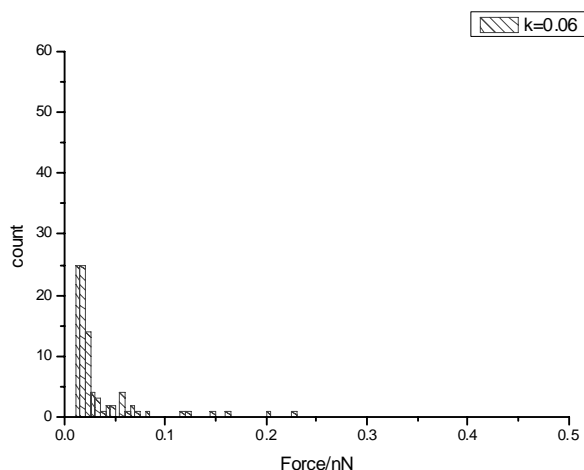
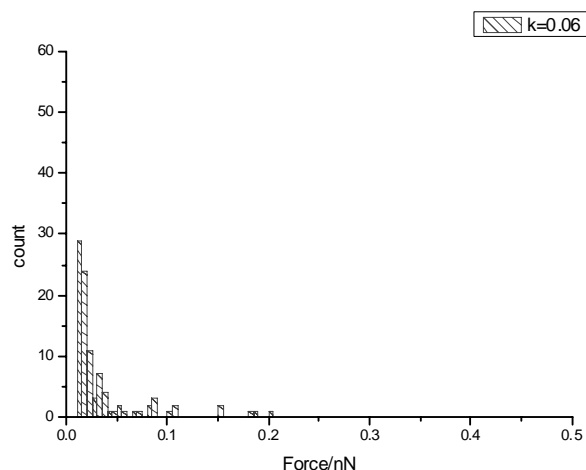
Tip: cysteine D || surface: L.A-GluL**Tip: cysteine D || surface: L.A-Ha****Tip: cysteine L || surface: L.A-GluL****Tip: cysteine L || surface: L.A-Ha**

Figure 7-23 Adhesion force histograms of D and L cysteine and linker A chiral and achiral derivatives interactions, calculated with use of nominal spring constant

Table 7-21 Adhesion force of D and L cysteine modified tip and linker A chiral and achiral derivatives interactions, calculated with use of nominal spring constant

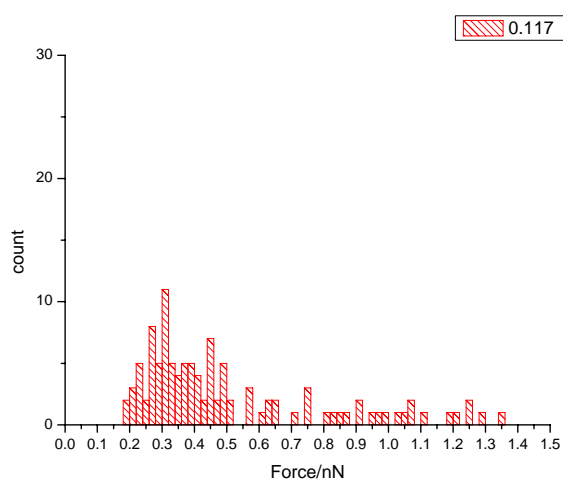
Tip: cysteine D surface: L.A-GluL		Tip: cysteine D surface: L.A-Ha		
Spring constant (N m ⁻¹)	Adhesion force (nN)	Spring constant (N m ⁻¹)	Adhesion force (nN)	
0.06	0.04±0.021	0.06	0.031±0.015	0.241±0.07
Tip: cysteine L surface: L.A-GluL		Tip: cysteine L surface: L.A-Ha		
Spring constant (N m ⁻¹)	Adhesion force (nN)	Spring constant (N m ⁻¹)	Adhesion force (nN)	
0.06	0.024±0.015	0.06	0.026±0.011	

Adhesion forces recorded for cysteine interactions with linker A-Glu L and linker A-Ha, showed that cysteines could be used for chiral recognition. Cysteine D- linker A-GluL pairs gave higher adhesion forces than cysteine L-linker A-GluL, as was expected as the homochiral interaction were already found to be smaller than heterochiral^{6,7}. Cysteine interactions with linker A-Ha showed, however, that there are additional forces acting at the interface. Two bands of forces recorded for cysteine D-linker A-Ha could indicate two things; neither an influence of inner hydrogen bonding in the surface molecule could not be neglected nor the charge of the functional groups. Studies in the aprotic solvents and solvents of the pH close to Ha derivative isoelectric point could shine more light on the influence of these factors on the intermolecular forces.

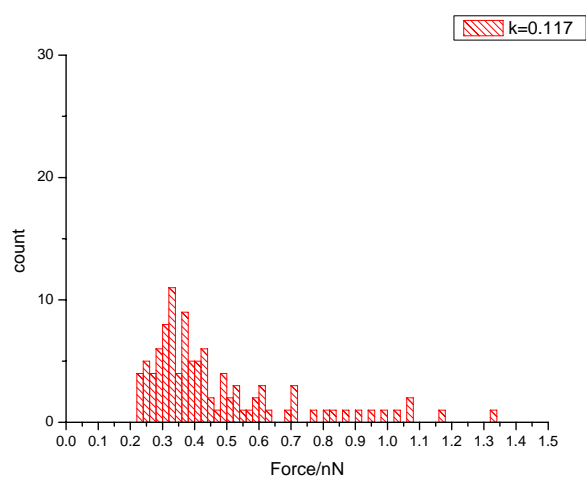
7.3.2.5 Interactions of cysteines with linker B chiral derivatives

Results of probing surfaces modified with linker B chiral derivatives with tips functionalized with D and L cysteine are presented in Figures 7-24 and 7-25. The characteristic adhesion forces are presented in Tables 7-22 and 7-23.

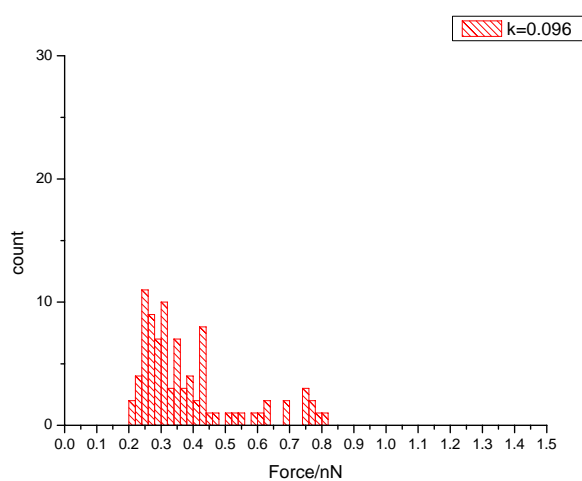
Tip: cysteine D || surface: L.B-AlaAlaDL



Tip: cysteine D || surface: L.B-AlaAlaLL



Tip: cysteine L || surface: L.B-AlaAlaDL



Tip: cysteine L || surface: L.B-AlaAlaLL

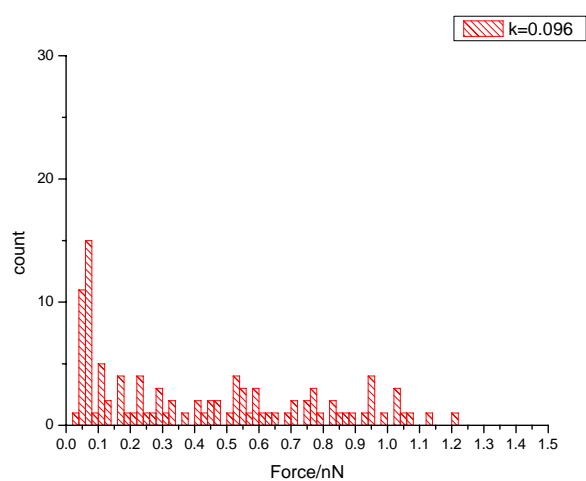


Figure 7-24 Adhesion force histograms of D and L cysteine and linker B chiral derivatives interactions, calculated with use of measured spring constant

Table 7-22 Adhesion force of D and L cysteine and linker B chiral derivatives interactions, calculated with use of measured spring constant

Tip: cysteine D surface: L.B-AlaAlaDL		Tip: cysteine D surface: L.B-AlaAlaLL	
Spring constant (N m^{-1})	Adhesion force (nN)	Spring constant (N m^{-1})	Adhesion force (nN)
0.117	0.508 ± 0.293	0.117	0.396 ± 0.124
Tip: cysteine L surface: L.B-AlaAlaDL		Tip: cysteine L surface: L.B-AlaAlaLL	
Spring constant (N m^{-1})	Adhesion force (nN)	Spring constant (N m^{-1})	Adhesion force (nN)
0.096	0.340 ± 0.100	0.096	0.243 ± 0.198

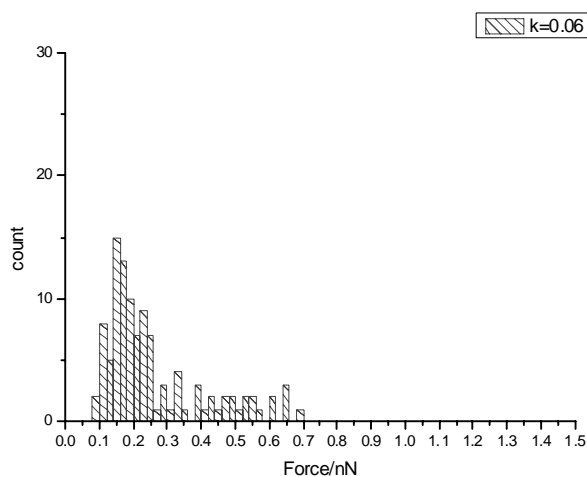
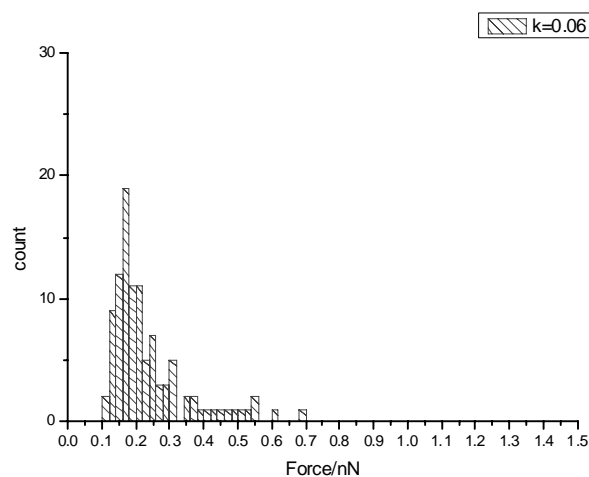
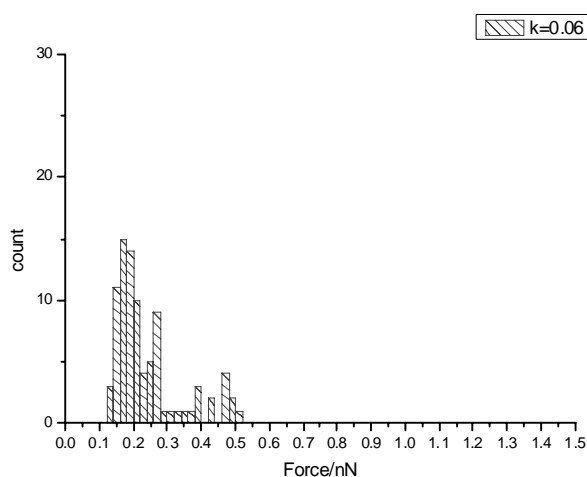
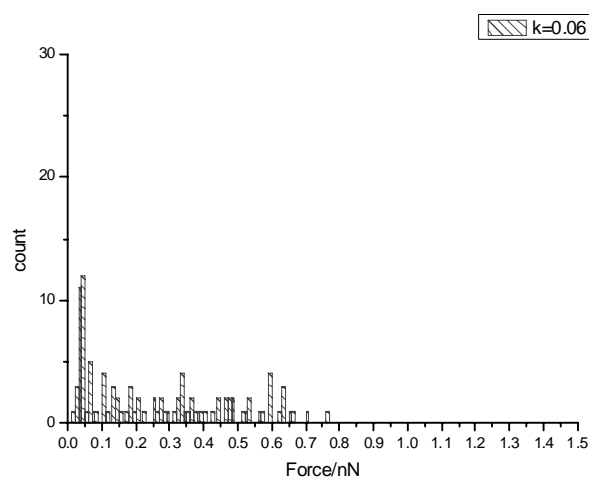
Tip: cysteine D || surface: L.B-AlaAlaDL**Tip: cysteine D || surface: L.B-AlaAlaLL****Tip: cysteine L || surface: L.B-AlaAlaDL****Tip: cysteine L || surface: L.B-AlaAlaLL**

Figure 7-25 Adhesion force histograms of D and L cysteine and linker B chiral derivatives interactions, calculated with use of nominal spring constant

Table 7-23 Adhesion force of D and L cysteine and linker B chiral derivatives interactions, calculated with use of nominal spring constant

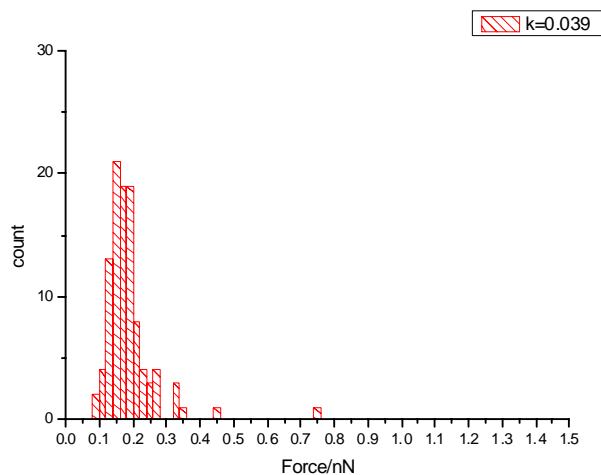
Tip: cysteine D surface: L.B-AlaAlaDL		Tip: cysteine D surface: L.B-AlaAlaLL	
Spring constant (N m ⁻¹)	Adhesion force (nN)	Spring constant (N m ⁻¹)	Adhesion force (nN)
0.06	0.260±0.150	0.06	0.203±0.064
Tip: cysteine L surface: L.B-AlaAlaDL		Tip: cysteine L surface: L.B-AlaAlaLL	
Spring constant (N m ⁻¹)	Adhesion force (nN)	Spring constant (N m ⁻¹)	Adhesion force (nN)
0.06	0.213±0.063	0.06	0.152±0.123

The obtained results repeat in some way the trend recorded for cysteines and linker A chiral derivatives. In the case of linker B the cysteine L-L.B-AlaLL interactions consist of two force bands- one (narrow)-of small adhesion force values and the second (broad) of higher values, larger in frequency than that recorded for cysteine L-L.B.-AlaDL interactions. This shows that the influence of the second chiral centre could come from the surface quality- the more reacted surfaces give less possibility for different functional groups to interact with probing molecules.

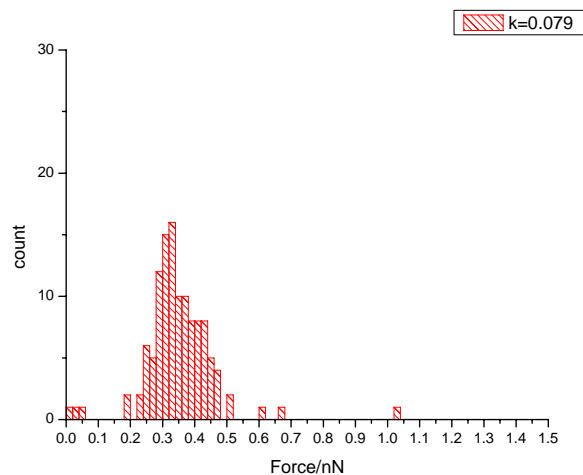
7.3.2.6 Interactions of cysteines with linker C derivatives

Interactions of cysteines with linker C chiral derivatives are illustrated in Figures 7-26 and 7-27. The characteristic adhesion forces are presented in Tables 7.24 and 7.25:

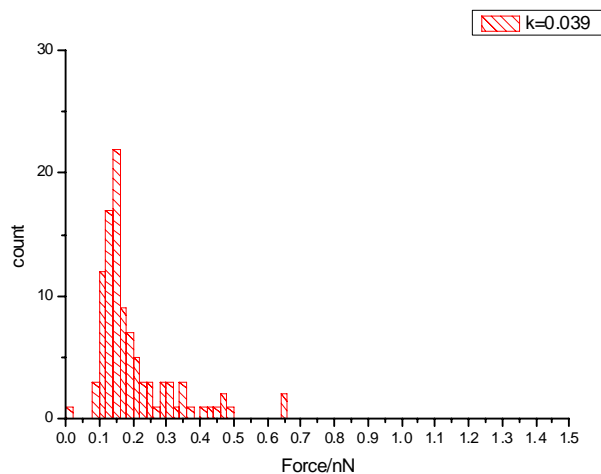
Tip: cysteineD || surface L.C-AlaDL



Tip: cysteineD || surface L.C -AlaLL



Tip: cysteineL || surface L.C -AlaAlaDL



Tip: cysteineL || surface L.C -AlaAlaLL

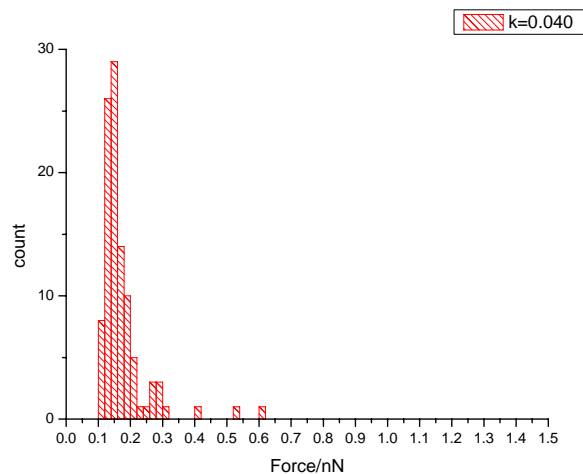


Figure 7-26 Adhesion force histograms of D and L cysteine and linker C chiral derivatives interactions, calculated with use of measured spring constant

Table 7-24 Adhesion force of D and L cysteine and linker C chiral derivatives interactions, calculated with use of measured spring constant

Tip: cysteine D surface: L.C-AlaAlaDL		Tip: cysteine D surface: L.C-AlaAlaLL	
Spring constant (N m^{-1})	Adhesion force (nN)	Spring constant (N m^{-1})	Adhesion force (nN)
0.039	0.167 ± 0.033	0.079	0.339 ± 0.082
Tip: cysteine L surface: L.C-AlaAlaDL		Tip: cysteine L surface: L.C-AlaAlaLL	
Spring constant (N m^{-1})	Adhesion force (nN)	Spring constant (N m^{-1})	Adhesion force (nN)
0.039	0.158 ± 0.031	0.040	0.162 ± 0.043

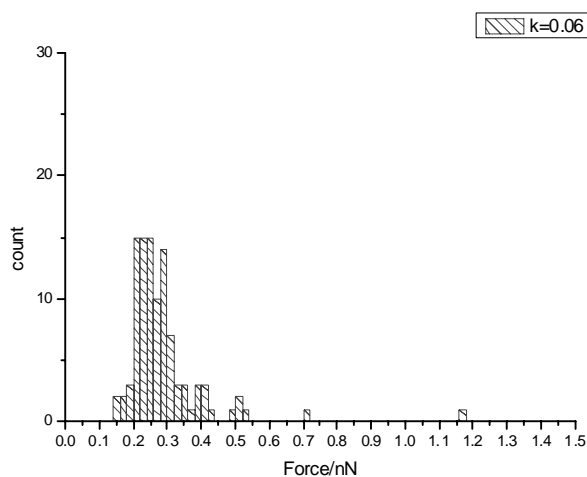
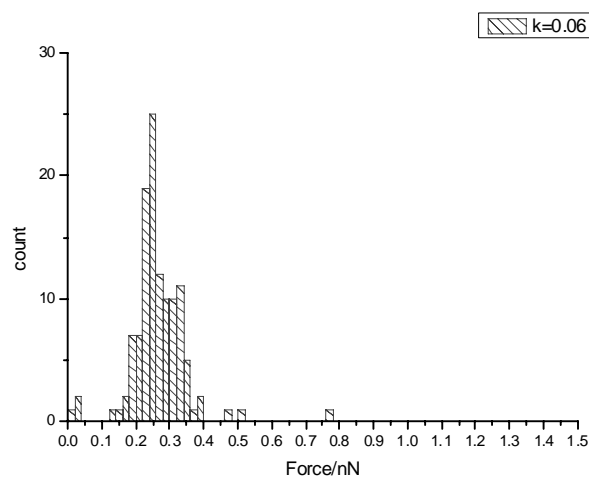
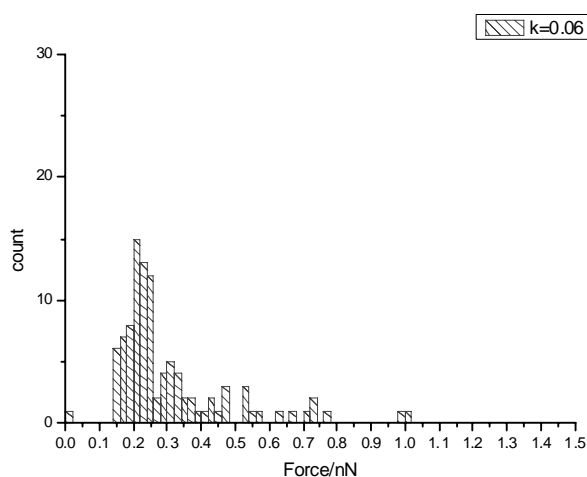
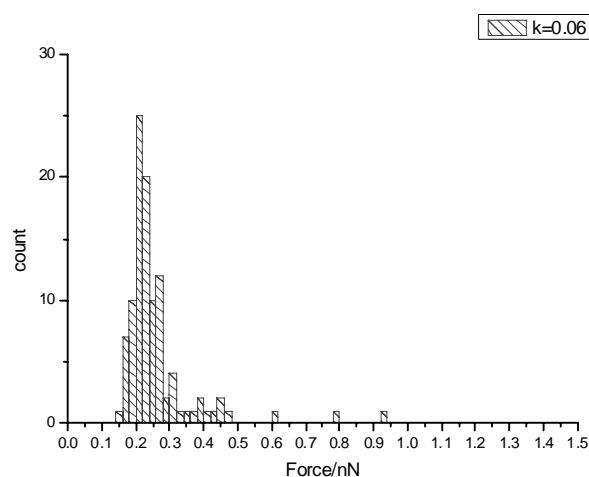
Tip: cysteine D || surface: L.C-AlaAlaDL**Tip: cysteine D || surface: L.C-AlaAlaLL****Tip: cysteine L || surface: L.C-AlaAlaDL****Tip: cysteine L || surface: L.C-AlaAlaLL**

Figure 7-27 Adhesion force histograms of D and L cysteine and linker C chiral derivatives interactions, calculated with use of nominal spring constant

Table 7-25 Adhesion force of D and L cysteine and linker C chiral derivatives interactions, calculated with use of nominal spring constant

Tip: cysteine D surface: L.C-AlaAlaDL		Tip: cysteine D surface: L.C-AlaAlaLL	
Spring constant (N m ⁻¹)	Adhesion force (nN)	Spring constant (N m ⁻¹)	Adhesion force (nN)
0.06	0.258±0.051	0.06	0.257±0.062
Tip: cysteine L surface: L.C-AlaAlaDL		Tip: cysteine L surface: L.C-AlaAlaLL	
Spring constant (N m ⁻¹)	Adhesion force (nN)	Spring constant (N m ⁻¹)	Adhesion force (nN)
0.06	0.244±0.048	0.040	0.162±0.043

The trend in adhesion forces recorded for cysteines- linker C chiral derivatives interactions is consistent with the trend observed for cysteines-linker A chiral derivatives. Both of the linkers used for producing chiral surfaces are equipped with terminal acetylene groups. Surface characterization showed that the linkers with terminal acetylene groups react with functionalities in better yield thus give better surface coverage. That gives the molecules less ability to change conformation. In this case, the second chiral centre might be slightly revealed and its functional groups might interact with probing molecules.

7.3.2.7 Interactions of linker B chiral derivatives

Linker B chiral derivatives is the second system studied in this project. The MM2 (molecular mechanics) studies on the chiral derivatives of linker B showed that as for the linker A the molecule tends to coil, which could reveal a second chiral centre. However in the case of linker B chiral derivatives the coiling trend is slightly less than in similar modification of linker A. The hetero atom ring next to the benzene ring induces a coiling trend in linker A. Moreover, the length of linker B causes the monolayer to be more stable and dense, which has an impact on the final linker B modification. The use of such systems was dictated by the fact that the characteristics of the linker B chiral derivatives showed better stability and higher yield of the linker B modification. Modification of gold surfaces with linker B chiral derivatives is presented in Figure 7-28.

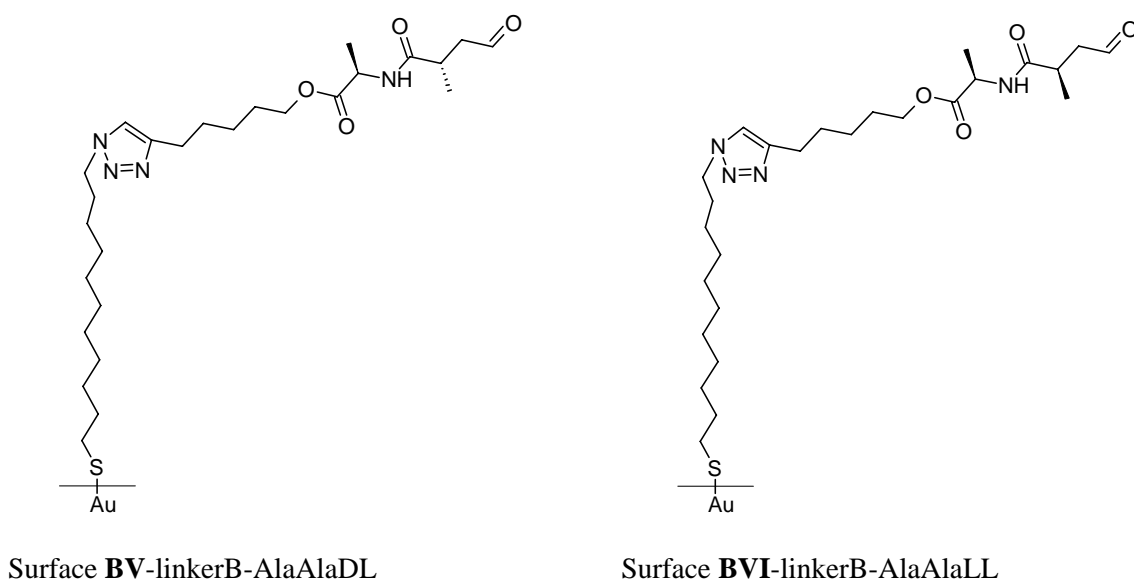


Figure 7-28 Enantiomers of linker B chiral derivatives

Interactions between tip and surface modified with chiral derivatives of linker B are presented in Figure 7.29 and 7-30, the characteristic adhesion forces are given in Tables 7-26 and 7-27.

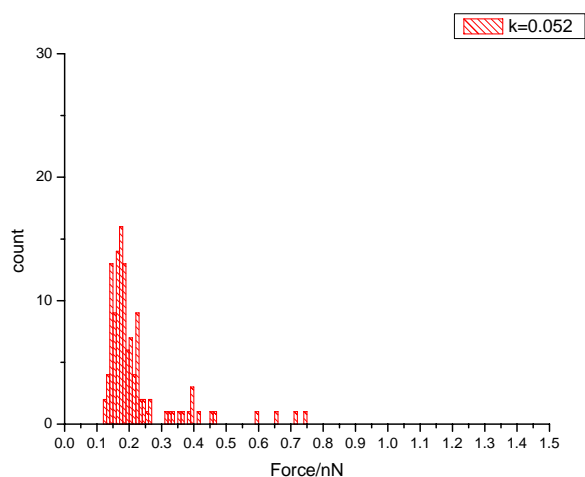
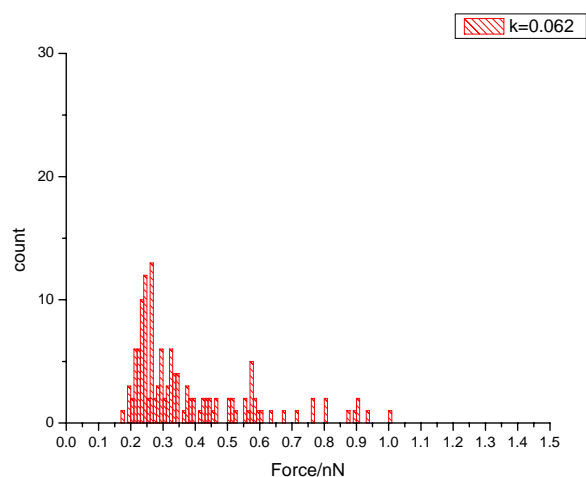
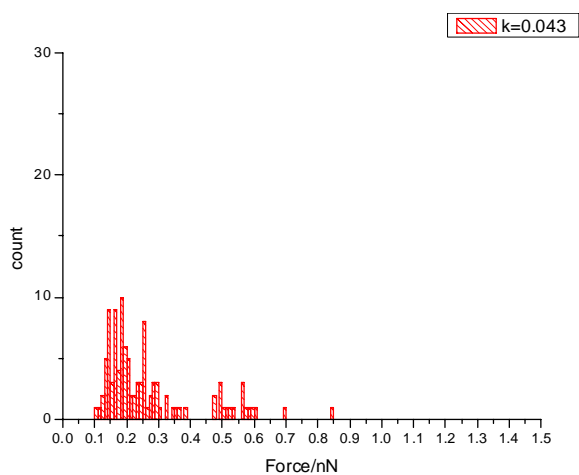
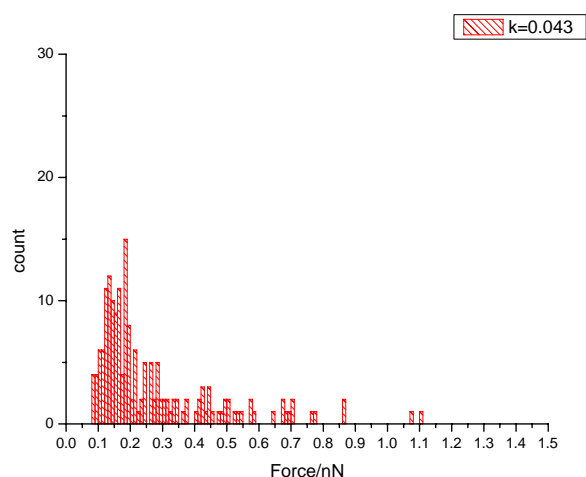
Tip: L.B-AlaAlaDL || surface: L.B -AlaAlaDL**Tip: L.B -AlaAlaDL || surface: L.B -AlaAlaLL****Tip: L.B -AlaAlaLL || surface: L.B -AlaAlaDL****Tip: L.B -AlaAlaLL || surface: L.B -AlaAlaLL**

Figure 7-29 Adhesion force histograms of linker B chiral derivatives calculated with use of measured spring constant

Table 7-26 Adhesion forces of linker B chiral derivatives calculated with use of measured spring constant

Tip: L.B-AlaAlaDL surface: L.B -AlaAlaDL		Tip: L.B -AlaAlaDL surface: L.B -AlaAlaLL	
Spring constant (Nm^{-1})	Adhesion force (nN)	Spring constant (Nm^{-1})	Adhesion force (nN)
0.052	0.179 ± 0.029	0.062	0.273 ± 0.052
Tip: L.B -AlaAlaLL surface: L.B -AlaAlaDL		Tip: L.B -AlaAlaLL surface: L.B -AlaAlaLL	
Spring constant (Nm^{-1})	Adhesion force (nN)	Spring constant (Nm^{-1})	Adhesion force (nN)
0.043	0.167 ± 0.027	0.043	0.158 ± 0.04

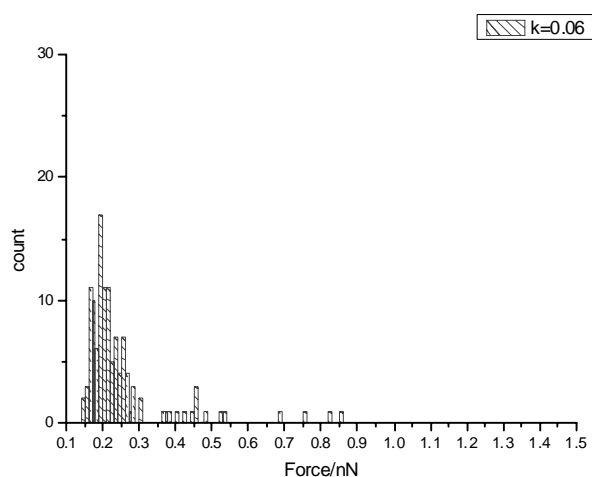
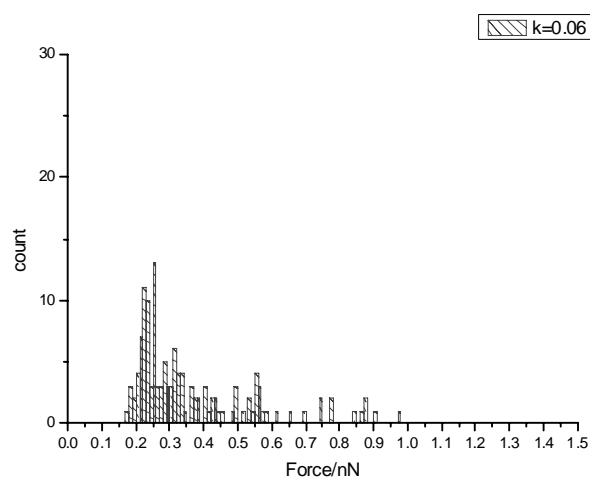
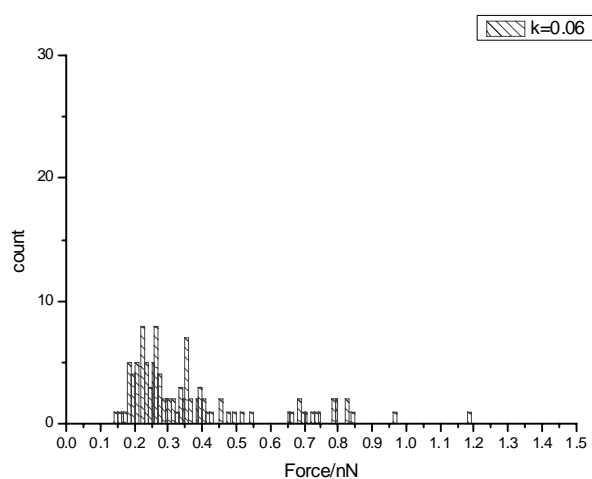
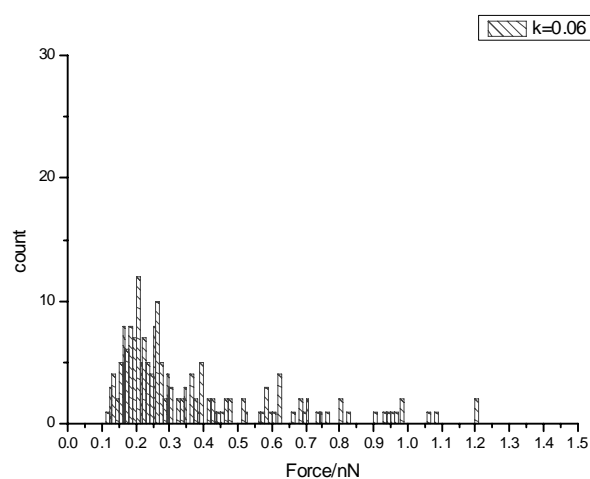
Tip: L.B-AlaAlaDL || surface: L.B -AlaAlaDL**Tip: L.B -AlaAlaDL || surface: L.B -AlaAlaLL****Tip: L.B -AlaAlaLL || surface: L.B -AlaAlaDL****Tip: L.B -AlaAlaLL || surface: L.B -AlaAlaLL**

Figure 7-30 Adhesion force histograms of linker B chiral derivatives calculated with use of nominal spring constant

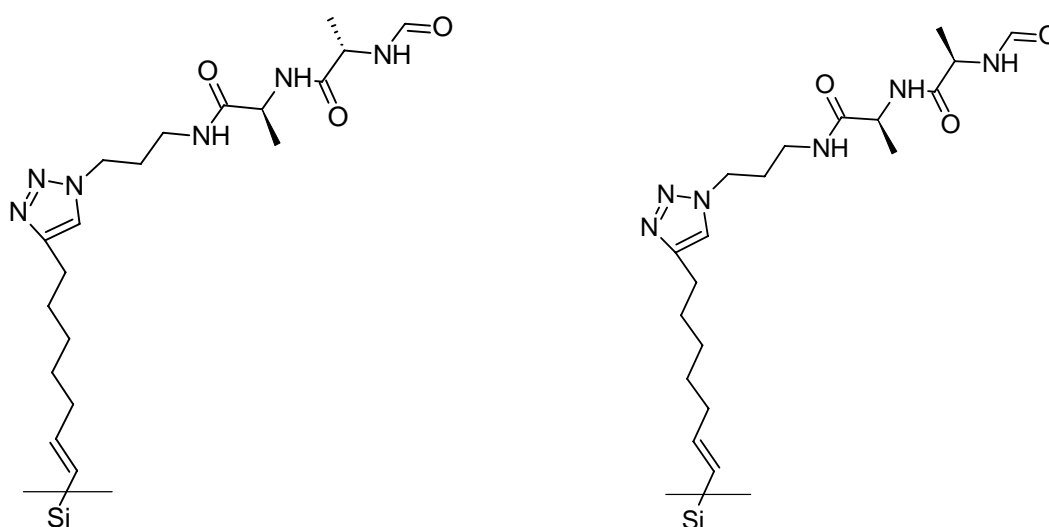
Table 7-27 Adhesion forces of linker B chiral derivatives calculated with use of nominal spring constant

Tip: L.B-AlaAlaDL surface: L.B -AlaAlaDL		Tip: L.B -AlaAlaDL surface: L.B -AlaAlaLL	
Spring constant (N m ⁻¹)	Adhesion force (nN)	Spring constant (N m ⁻¹)	Adhesion force (nN)
0.06	0.207±0.034	0.06 N	0.265±0.051
Tip: L.B -AlaAlaLL surface: L.B -AlaAlaDL		Tip: L.B -AlaAlaLL surface: L.B -AlaAlaLL	
Spring constant (N m ⁻¹)	Adhesion force (nN)	Spring constant (N m ⁻¹)	Adhesion force (nN)
0.06	0.233±0.038	0.06 N	0.221±0.055

In linker B chiral derivatives interaction studies it was found that higher adhesion forces are present when hetero chiral molecules are 'touching' each other. The results are similar to linker A chiral derivatives' interactions. The adhesion force is descending in the order: DL-LL > DL-DL > LL-DL > LL-LL. The most interesting is the middle part, namely interactions DL-DL and LL-DL. Yet again the encountered forces showed that there is an additional factor acting here, which is assumed to consist of molecule coiling, hydrogen bond forming and charge influence. From the previous studies it is known that the interactions of homochiral molecules produce smaller forces than interactions of heterochiral molecules. Here, the addition of the second chiral centre (meaning the inner one) influences the total net adhesive force. Great probability of inner hydrogen bonding makes DL-LL interaction forces greater than those of LL-DL. When the tip consisting of DL chiral derivative touches LL derivatives the force is greater than for the opposite combination. Molecules on the tip are more 'free' and not as compactly packed as molecules on the large flat surface thus they have greater possibility to coil and form inner hydrogen bonding. This leads to the conclusion that the DL derivative has more tendencies for coiling. This might explain the trend observed in the adhesion force order.

7.3.2.8 Interactions of linker B chiral derivatives with linker C chiral derivatives

The reason for studying such systems was very simple: there is not an easy way to functionalize silicon nitride tips with nonadiyne. Hence linker B chiral derivatives were used for probing linker C chiral derivative surfaces. Silicon surfaces modified with linker C chiral derivatives are presented schematically in Figure 7-31.



Surface **CI**- linkerB-AlaAlaDL

Surface **CII**- linkerB-AlaAlaLL

Figure 7-31 Enantiomers of linker C chiral derivatives

Results of probing linker C chiral derivatives with tips modified with linker B chiral derivatives are presented in Figures 7.32 and 7.33. The characteristic adhesion forces are given in Tables 7-28 and 7-29.

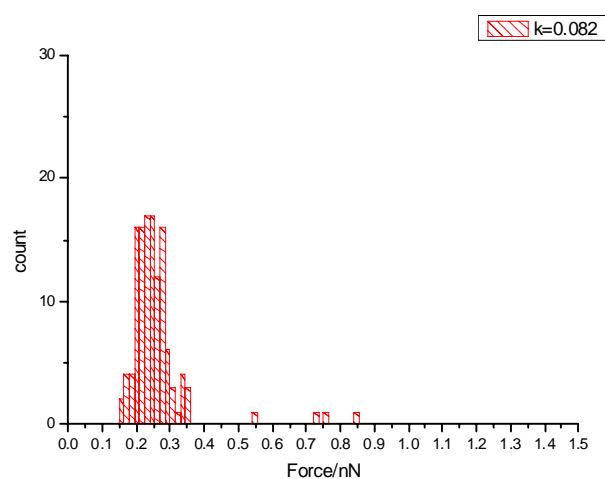
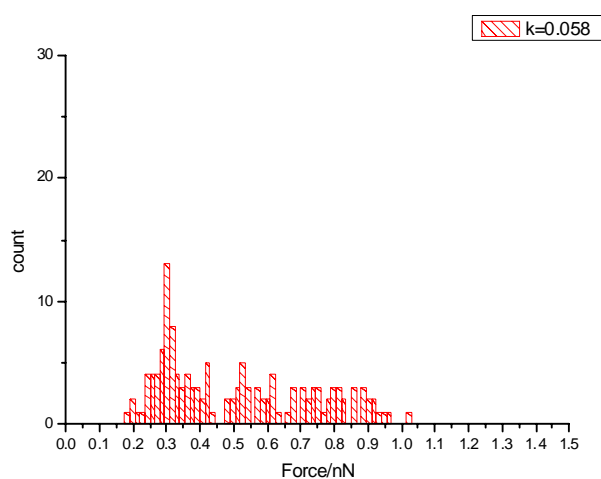
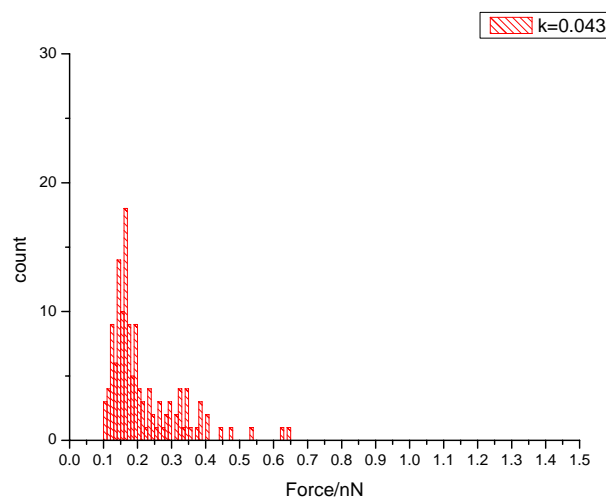
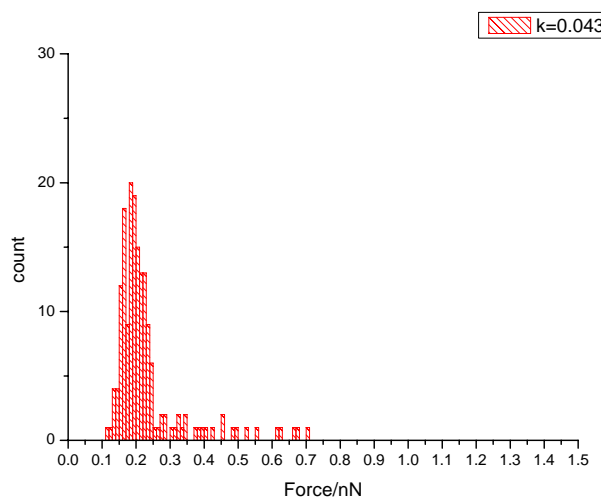
Tip: L.B -AlaAlaDL || surface: L.C-AlaAlaDL**Tip: L.B -AlaAlaDL || surface: L.C -AlaAlaLL****Tip: L.B -AlaAlaLL || surface: L.C -AlaAlaDL****Tip: L.B -AlaAlaLL || surface: L.C -AlaAlaLL**

Figure 7-32 Adhesion force histograms of linker B and C chiral derivatives interactions, calculated with use of measured spring constant

Table 7-28 Adhesion force of linker B and C chiral derivatives interactions, calculated with use of measured spring constant

Tip: L.B-AlaAlaDL surface: L.C-AlaAlaDL		Tip: LB-AlaAlaDL surface: L.C-AlaAlaLL	
Spring constant (N m^{-1})	Adhesion force (nN)	Spring constant (N m^{-1})	Adhesion force (nN)
0.058	0.318 ± 0.061	0.82	0.26 ± 0.095
Tip: L.B-AlaAlaLL surface: L.C-AlaAlaDL		Tip: L.B-AlaAlaLL surface: L.C-AlaAlaLL	
Spring constant (N m^{-1})	Adhesion force (nN)	Spring constant (N m^{-1})	Adhesion force (nN)
0.043	0.194 ± 0.032	0.043	0.165 ± 0.033

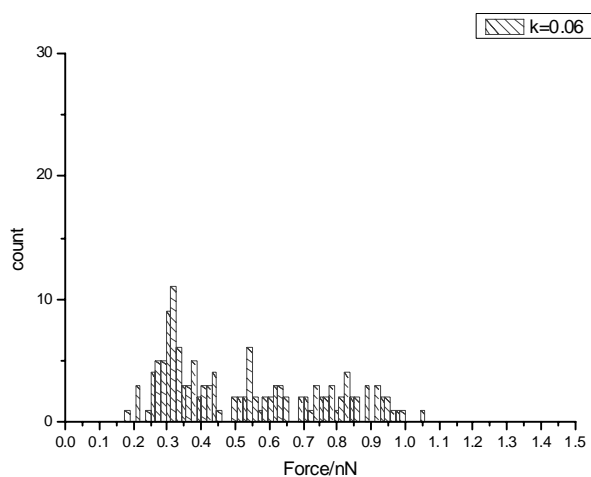
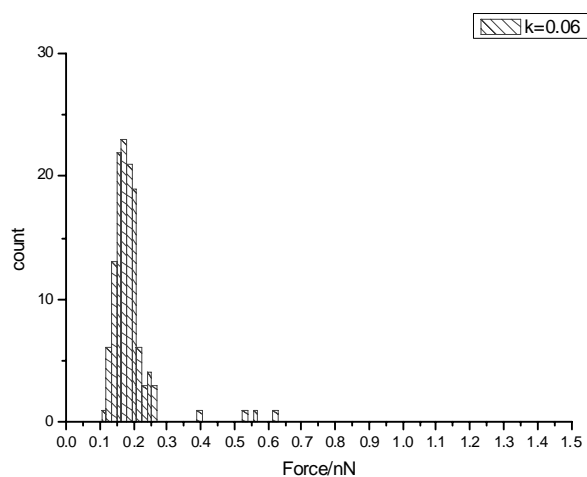
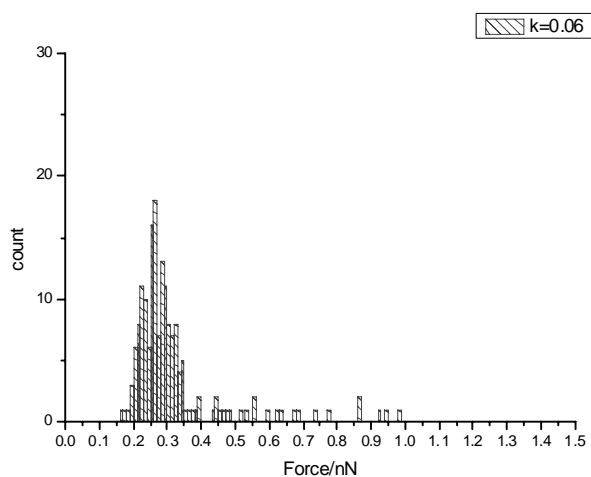
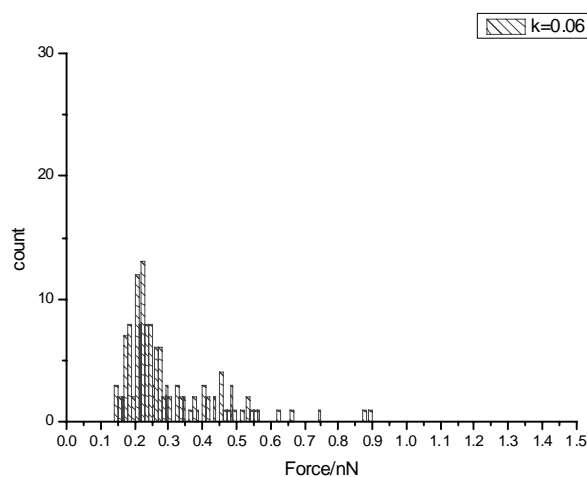
linkerB-AlaAlaDL on linkerC-AlaAlaDL**linkerB-AlaAlaDL on linkerC-AlaAlaLL****linkerB-AlaAlaLL on linkerC-AlaAlaDL****linkerB-AlaAlaLL on linkerC-AlaAlaLL**

Figure 7-33 Adhesion force histograms of linker B and C chiral derivatives interactions, calculated with use of nominal spring constant

Table 7-29 Adhesion force of linker B and C chiral derivatives interactions, calculated with use of nominal spring constant

Tip: LB-AlaAlaDL surface: L.C-AlaAlaDL		Tip: L.B-AlaAlaDL surface: L.C-AlaAlaLL	
Spring constant (N m^{-1})	Adhesion force (nN)	Spring constant (N m^{-1})	Adhesion force (nN)
0.06	0.329 ± 0.063	0.06	0.19 ± 0.07
Tip: L.B-AlaAlaLL surface: L.C-AlaAlaDL		Tip: B-AlaAlaLL surface: L.C-AlaAlaLL	
Spring constant (N m^{-1})	Adhesion force (nN)	Spring constant (N m^{-1})	Adhesion force (nN)
0.06	0.271 ± 0.045	0.06	0.230 ± 0.047

The studies of this system showed a little difference to the two previous combinations. Interaction of DL-DL pairs had the highest adhesion forces. The other results are consistent with the data achieved for linker A and linker B chiral derivative interactions. In this case, a surface of silicon modified with nonadiyne was used as a base for click chemistry. This surface is not prepared in the standard 'self assembly' way but by harsh treatment of a silicon surface with diyne with preliminary HF etching. That makes it more ordered and sensitive for further treatment. Contact angle measurements of final linker C surface functionalization showed the biggest change in wetting properties. That indicates this kind of linker (length plus functional group) is the best for click chemistry. In this case the coiling trend was also found to be less than for linker A, which has significant influence on the achieved results.

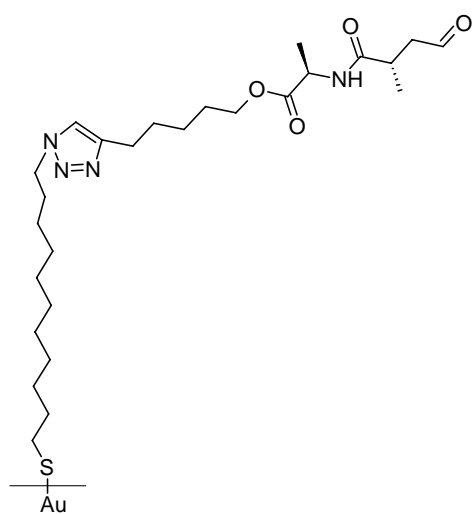
Studies of linker A, B and C chiral derivative interactions showed not only that chiral recognition is observed but also revealed that there is a possibility to see if the molecules have different spatial alignment.

7.3.2.9 Interactions of linker B chiral derivatives with linker A derivatives

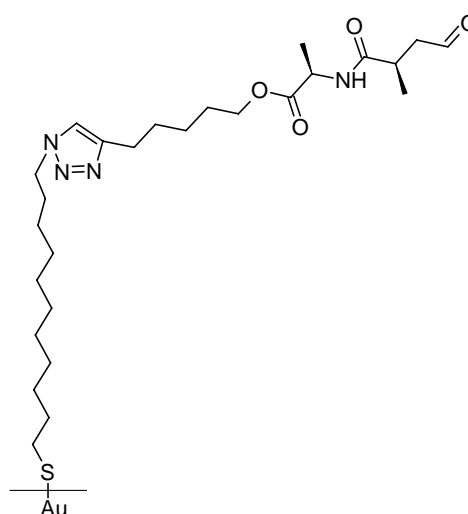
7.3.2.9.1 Interactions of Linker B chiral derivatives with linker A chiral derivatives possessing two chiral centres

Previous results of probing surfaces of linker C chiral derivatives showed a need for conducting studies on linker B chiral derivatives probing linker A chiral derivatives. As a first combination for tests molecules presented in Figure 7-34 were used.

Tip modification:

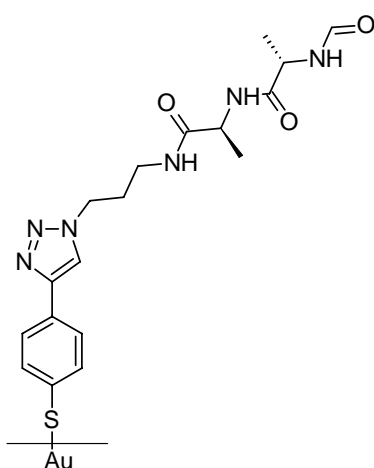


(a) linkerB-AlaAlaDL

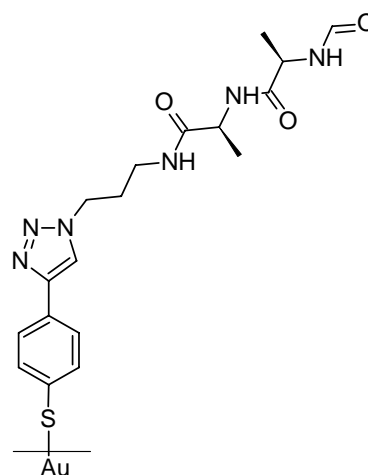


(b) linkerB-AlaAlaLL

Surface modification:



(c) linkerA-AlaAlaDL

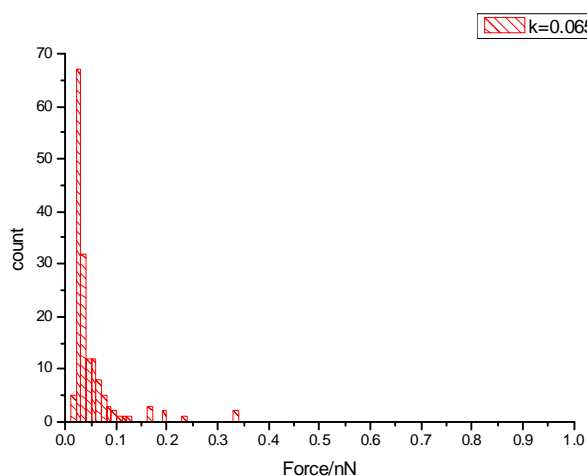


(d) linkerA-AlaAlaLL

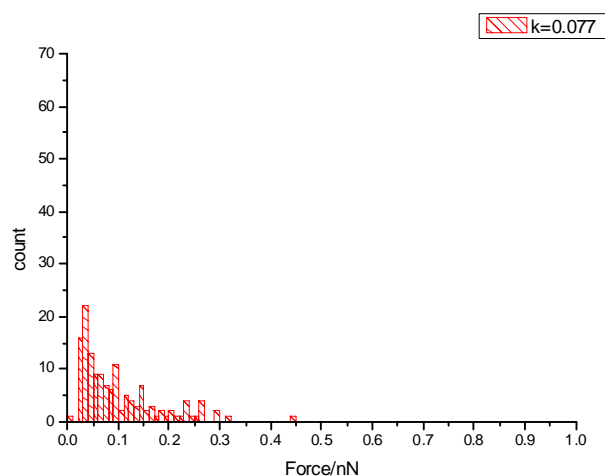
Figure 7-34 (a) and (b) tip modification with linker B chiral derivatives, (c) and (d) surface modification with linker A chiral derivatives

The results of force- distance experiments are presented in the figures 7.35 and 7.36.

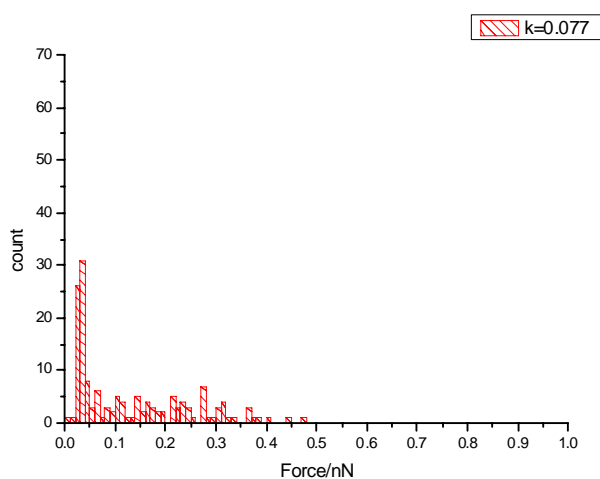
Tip: LB-AlaAlaDL || surface: L.A -AlaAlaDL



Tip: LB-AlaAlaDL || surface: L.A -AlaAlaLL



Tip: LB-AlaAlaLL || surface: L.A -AlaAlaDL



Tip: LB-AlaAlaLL || surface: L.A -AlaAlaLL

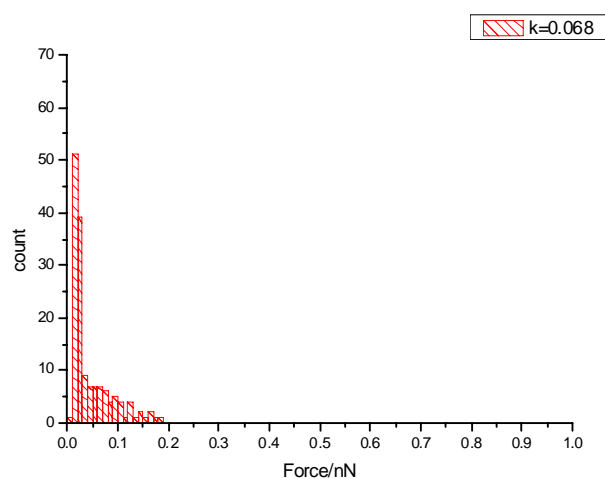


Figure 7-35 Adhesion force histograms of linker B and A chiral derivatives interactions, calculated with use of measured spring constant

Table 7-30 Adhesion forces of linker B and A chiral derivatives interactions, calculated with use of measured spring constant

Tip: LB-AlaAlaDL surface: L.A-AlaAlaDL		Tip: L.B-AlaAlaDL surface: L.A-AlaAlaLL	
Spring constant (N m^{-1})	Adhesion force (nN)	Spring constant (N m^{-1})	Adhesion force (nN)
0.065	0.037 ± 0.017	0.077	0.051 ± 0.021
Tip: L.B-AlaAlaLL surface: L.A-AlaAlaDL		Tip: >B-AlaAlaLL surface: L.A-AlaAlaLL	
Spring constant (N m^{-1})	Adhesion force (nN)	Spring constant (N m^{-1})	Adhesion force (nN)
0.077	0.047 ± 0.027	0.068	0.030 ± 0.019

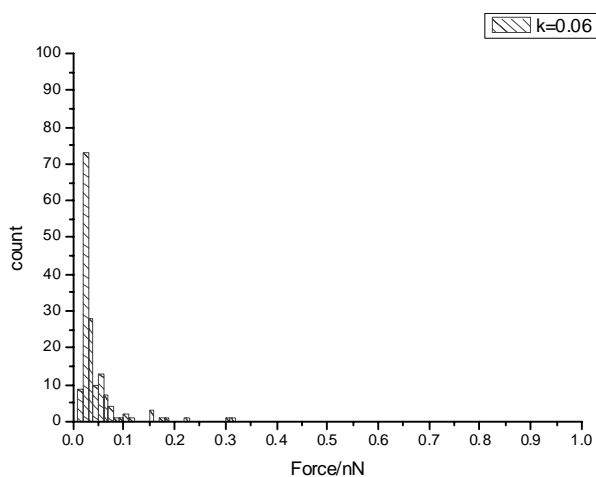
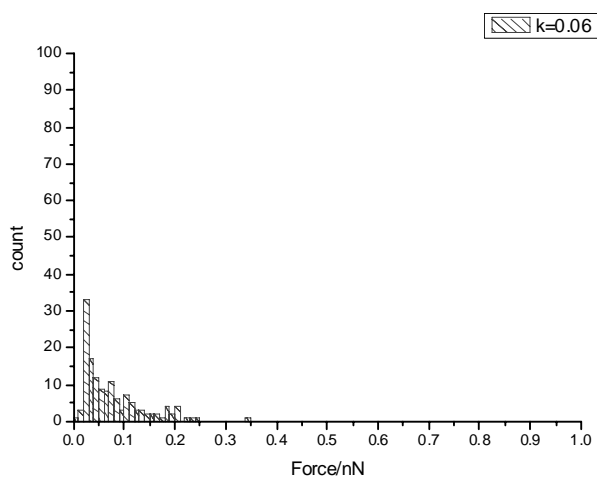
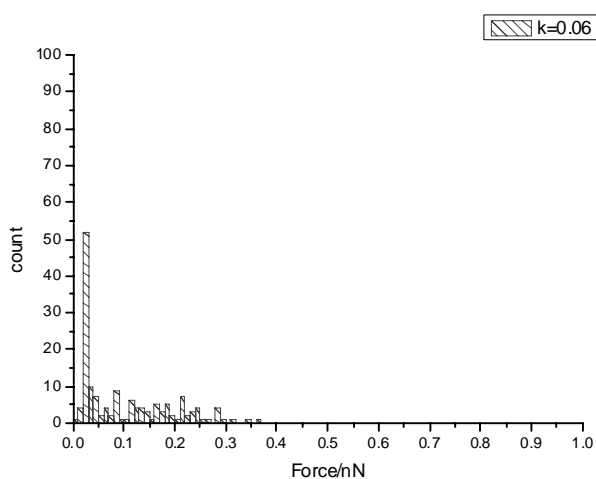
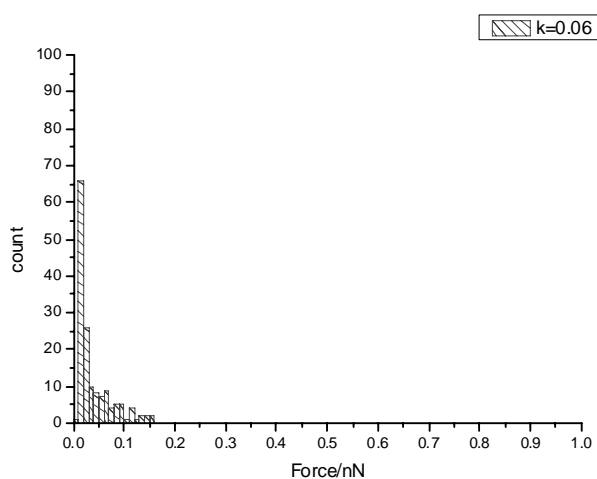
Tip: LB-AlaAlaDL || surface: L.A -AlaAlaDL**Tip: LB-AlaAlaDL || surface: L.A -AlaAlaLL****Tip: LB-AlaAlaLL || surface: L.A -AlaAlaDL****Tip: LB-AlaAlaLL || surface: L.A -AlaAlaLL**

Figure 7-36 Adhesion force histograms of linker B and A chiral derivatives interactions, calculated with use of nominal spring constant

Table 7-31 Adhesion forces of linker B and A chiral derivatives interactions, calculated with use of nominal spring constant

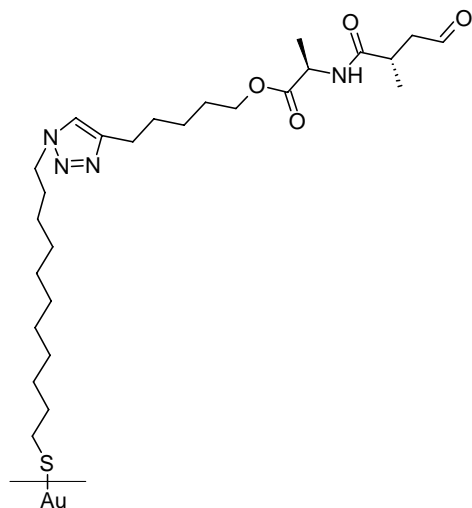
Tip: LB-AlaAlaDL surface: L.A-AlaAlaDL		Tip: L.B-AlaAlaDL surface: L.A-AlaAlaLL	
Spring constant (N m^{-1})	Adhesion force (nN)	Spring constant (N m^{-1})	Adhesion force (nN)
0.06	0.034 ± 0.015	0.06	0.039 ± 0.016
Tip: L.B-AlaAlaLL surface: L.A-AlaAlaDL		Tip: >B-AlaAlaLL surface: L.A-AlaAlaLL	
Spring constant (N m^{-1})	Adhesion force (nN)	Spring constant (N m^{-1})	Adhesion force (nN)
0.06	0.036 ± 0.021	0.06	0.0271 ± 0.017

The results presented in this section show the same trend recorded for experiment sets of linker B and linker C chiral derivatives. Yet again the adhesion forces encountered for linker B-AlaAlaDL molecules touching linker A-AlaAlaLL surface were greater than for linker B-AlaAlaLL derivatives touching linker A-AlaAlaLL surfaces. The difference between these experiments and experiments recorded for linker B and C chiral derivatives is that the forces recorded for probing surfaces made of linker A chiral derivatives are much less. These arise from the poor surface coverage as it were shown in section 7.3.2.2. The tip curvature and the quality of its modification play a significant role in this type of experiments; however it cannot yet be fully controlled.

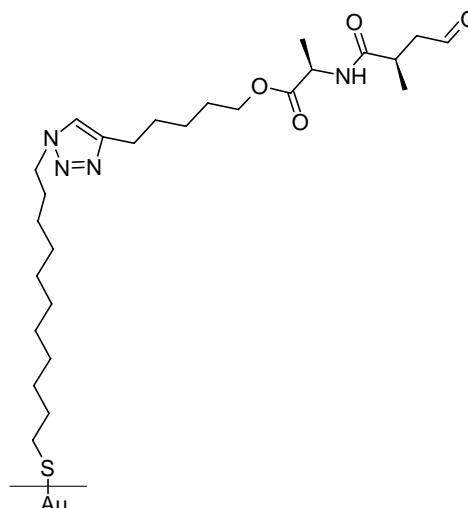
The trend in force order $DL-LL > DL-DL > LL-DL > LL-LL$ could be clearly seen in the histograms which makes us believe that the small magnitude of forces recorded come only from the quality of tip and surface modification.

7.3.2.9.2 Linker B-AlaAlaDL and LL interactions with Linker A chiral and achiral derivatives possessing one chiral centre

In this set of experiments tips were modified with linker B chiral derivatives and the probed surface modified with linker A chiral derivative possessing one chiral centre and no chiral centre. Tip and surface modifications are presented in Figure 7-37.

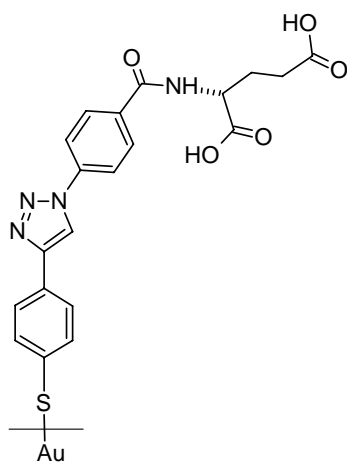


(a) linkerB-AlaAlaDL

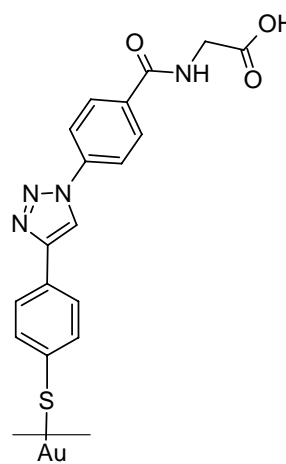


(b) linkerB-AlaAlaLL

Surface modification

(c) Surface **AIII**- linker A-GluL

One chiral centre

(d) Surface **AIV**- linker A-HA

Achiral

Figure 7-37 (a),(b) Tip modifications-linker B chiral derivatives, (c) surface modified with linker A chiral derivative possessing one chiral centre, (d) surface modified with linker A derivative with no chiral centre.

Results of probing surfaces functionalised with one and no chiral centres with tips equipped with linkerB chiral derivatives are presented in Figures 7-38 and 7-39. The characteristic adhesion forces are given in Tables 7-32 and 7-33.

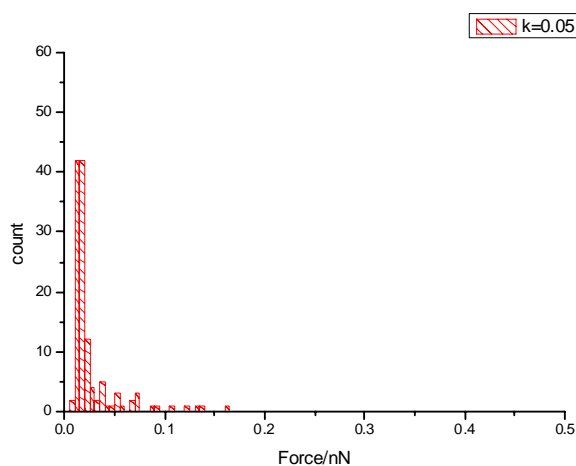
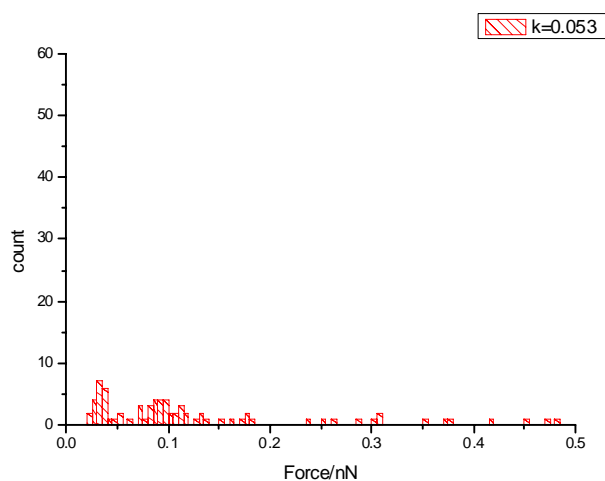
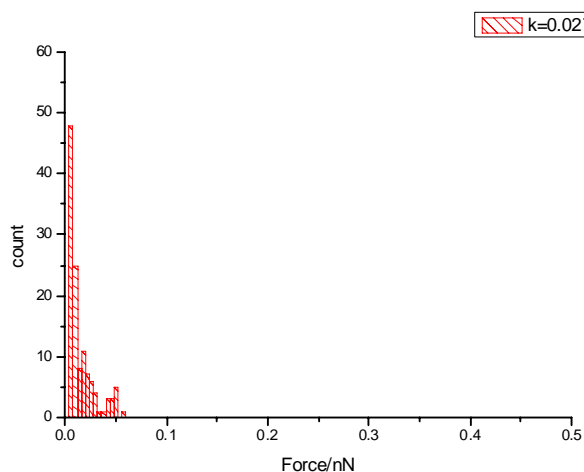
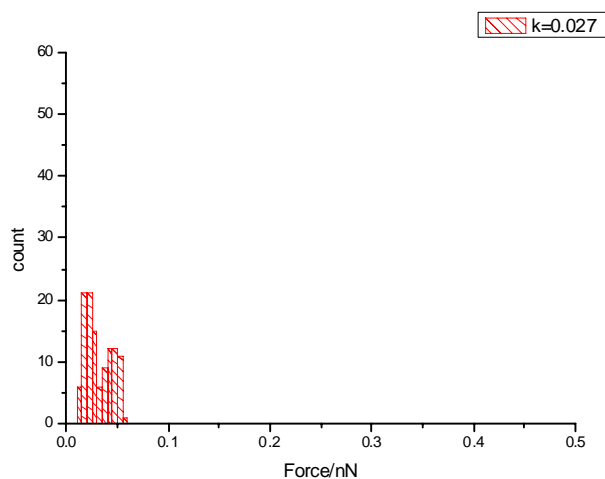
Tip: L.B-AlaAlaDL || surface: L.A-GluL**Tip: L.B-AlaAlaDL || surface: L.A-Ha****Tip: L.B-AlaAlaLL || surface: L.A-GluL****Tip: L.B-AlaAlaLL || surface: L.A-Ha**

Figure 7-38 Adhesion force histograms of linker B chiral derivatives with two chiral centres and A chiral and achiral derivatives interactions, calculated with use of measured spring constant

Table 7-32 Adhesion force of linker B chiral derivatives with two chiral centres and A chiral and achiral derivatives interactions, calculated with use of measured spring constant

Tip: L.B-AlaAlaDL surface: L.A-GluL		Tip: L.B-AlaAlaDL surface: L.A-Ha		
Spring constant (Nm ⁻¹)	Adhesion force (nN)	Spring constant (Nm ⁻¹)	Adhesion force (nN)	
0.053	0.021±0.01	0.053	0.036±0.009	0.109±0.032
Tip: L.B-AlaAlaLL surface: L.A-GluL		Tip: L.B-AlaAlaLL surface: L.A-Ha		
Spring constant (Nm ⁻¹)	Adhesion force (nN)	Spring constant (Nm ⁻¹)	Adhesion force (nN)	
0.027	0.019±0.004	0.027	0.02±0.008	0.048±0.0012

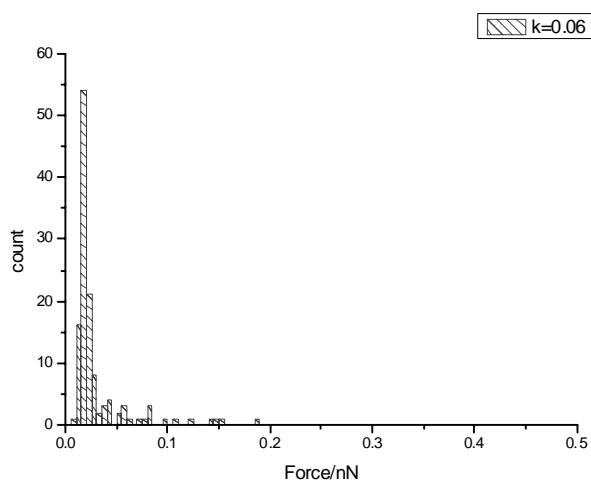
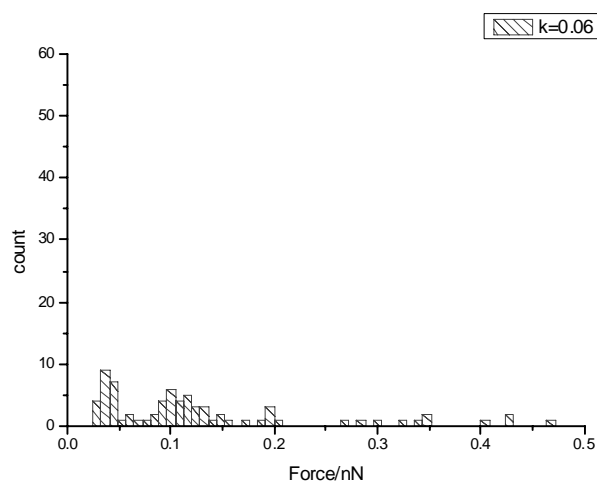
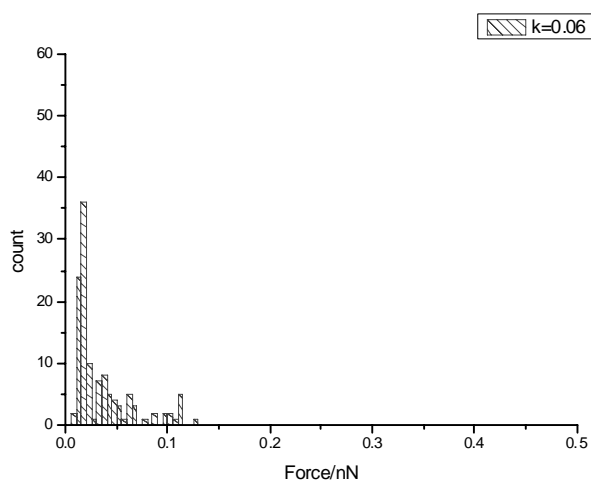
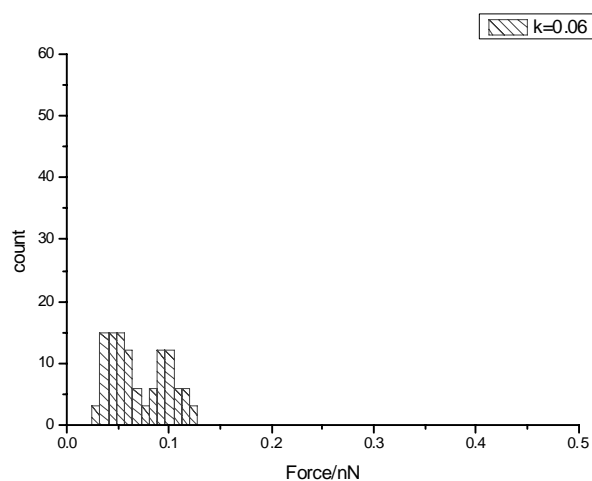
Tip: L.B-AlaAlaDL || surface: L.A-GluL**Tip: L.B-AlaAlaDL || surface: L.A-Ha****Tip: L.B-AlaAlaLL || surface: L.A-GluL****Tip: L.B-AlaAlaLL || surface: L.A-Ha**

Figure 7-39 Adhesion force histograms of linker B chiral derivatives with two chiral centres and A chiral and achiral derivatives interactions, calculated with use of nominal spring constant

Table 7-33 Adhesion force of linker B chiral derivatives with two chiral centres and A chiral and achiral derivatives interactions, calculated with use of nominal spring constant

Tip: L.B-AlaAlaDL surface: L.A-GluL		Tip: L.B-AlaAlaDL surface: L.A-Ha			
Spring constant (Nm ⁻¹)	Adhesion force (nN)	Spring constant (Nm ⁻¹)	Adhesion force (nN)		
0.06	0.021±0.01	0.06	0.04±0.009	0.123±0.036	
Tip: L.B-AlaAlaLL surface: L.A-GluL		Tip: L.B-AlaAlaLL surface: L.A-Ha			
Spring constant (Nm ⁻¹)	Adhesion force (nN)		Spring constant (Nm ⁻¹)	Adhesion force (nN)	
0.06	0.041±0.08	0.149±0.055	0.06	0.05±0.011	0.1±0.02

These results indicate unambiguously that the final structure of prepared surfaces plays a great role in the interaction testing. Preliminary MM2 studies showed that GluL and Ha derivatives are less coiled than dipeptide derivatives. When a tip equipped with linker B chiral derivatives with two chiral centres 'touches' a L.A-GluL surface there is only one band of adhesion force present. When the same kind of tip touches a L.A-Ha surface two force bands can be found in histograms. It could be explained by the fact that L.A-GluL has two acidic groups in the terminal part of the molecule, so the chance to hit them is bigger than in case of L.A-Ha which possesses only one COOH group. In the case of GluL, the two COOH groups are further apart, although they might interact and form intermolecular hydrogen bonds. Thus might result in less ability of the GluL end to interact with the tip modification. In the case of Ha the probability of inter- hydrogen bonding is less, thus forces encountered for L.B chiral derivatives and L.A-Ha are bigger and with two bands. Those two bands are corresponding to functional group interactions. The tests showed that there is no significant difference in histograms between pairs: L.B-AlaAlaDL –L.A-Ha and L.B-AlaAlaLL-L.A.Ha (data calculated with use of nominal spring constant), indicating that the force depends on functional group interactions. The calculated data using the measured spring constants show that for L.B-AlaLL and L.A-Ha pairs the forces are lower. In this case, the need for presenting two sets of histograms is explained. Determination of the spring constant of a cantilever *via* thermal K measurement requires additional measurements. During cantilever mount and also during F-D experiments it is likely to break the cantilever or corrupt it in a way that may give a false spring constant value. In these circumstances, comparison of data calculated with nominal k value may be more relevant.

7.4 Discussion and conclusion

From the experiments carried out on cysteine systems in ethanol and in a buffer of pH close to the cysteine isoelectric point, it was concluded that this molecule can be used in chiral discrimination. The effect of recognition was found to be enhanced in the medium of pH 5.2.

When cysteines were used for discrimination of chirality of dipeptides in ethanol, slight chiral discrimination was found with an indication of influence of the second chiral centre. The main explanation of this fact could be that between cysteines and the dipeptides used the possibility of hydrogen bonding formation is less than for the system of cysteine-cysteine. Additionally, the charge of single functional groups can influence the measurements along with a coiled structure of dipeptides that can hide or reveal functional groups. It has its expression especially in the results of cysteine D-L.X.AlaAlaLL and cysteine L-L.X.AlaAlaDL (where X stands for linker A,B and C). The experiments show that for all linkers the tendency is: cysteine D- AlaAlaLL > cysteine L- AlaAlaDL >> cysteine L-AlaAlaLL. That might be explained by the coiling tendency of molecules and charge influence plus specific 'second chiral centre influence'. As expected, cysteine L-L.X.AlaAlaLL interactions are the smallest as the molecules feel homochirality. Cysteine D interactions with AlaAlaDL are slightly different for linker C. They are almost of the same values of forces as for cysteine L-AlaAlaLL whilst for other linkers cysteine D- AlaAlaDL interactions are much higher than for cysteine L-AlaAlaLL. That might be explained by the fact that linker C is assembled on Si surfaces in a different way, thus the click chemistry undergone with higher yield. That prevents excessive coiling of molecules and it is expressed by different force dispersion.

Studies of cysteine interactions with linker A chiral derivatives with only one chiral centre (GluL) gave expected results of higher adhesion forces for D-L interactions than for L-L probing pairs. Unfortunately the D enantiomer of glutamic acid was not successfully synthesised and therefore we could not conduct experiments over the full enantiomeric range.

Experiments conducted with cysteines and linker A achiral derivatives possessing the same functional groups showed that the main force band for cysteine D-Ha interactions is slightly higher than for the cysteine L-Ha pair. However, in the case of cysteine D-Ha it was found that an additional band of forces (values ~ 0.2 nN) appeared. For cysteine L-Ha such forces appear to a much lesser extent. This shows that the charge influence and hydrogen bonding cannot be neglected when studying chiral recognition by cysteines. It was shown that conducting measurements in buffer of pH close to the isoelectric point can enhance the recognition effect by diminishing the influence of the functional group charge.

When the same kind of surface was probed by tips functionalised by molecules possessing two chiral centres similar results to cysteines were found. Two bands of forces were encountered for L.B-AlaAlaDL and LL probing linker A-Ha surfaces. Linker B chiral derivative interactions with linker A-GluL gave expected results of higher forces for DL-L interactions. When comparing L.B-AlaAlaDL interactions with GluL and Ha surfaces one can see a distinct difference in the histogram shape: one, sharp band for the GluL surface and two spread bands for the Ha surface. Studies conducted on the system of tips modified with linker A-GluL and Ha probing surface A chiral derivatives did not show this tendency in such a clear way. This could be explained by different surface quality of the tips and/or probed surface.

Additional studies in use of different pH media should be conducted to fully understand what forces go along with chiral interactions. Studies of chiral recognition for systems fully modified with enantiomers possessing two chiral centres confirm these conclusions.

For linker A chiral derivatives possessing two chiral centres the forces are of order: ***DL-LL > DL-DL > LL-DL >> LL-LL*** with forces 0.542-0.22 nN. The same order was found for linker B chiral derivatives interactions and linker B chiral derivatives probing surfaces of linker A chiral derivatives. However the forces encountered for the last two are smaller. For linker B chiral modifications they were of range 0.273-0.167 nN, whilst for linker B chiral modifications probing linker A chiral derivatives the forces were found to be an order less than for linker A chiral derivative-

linker A chiral derivative. These differences in values and agreement in the trend could be explained by tip curvature. For the experiments we used tips of the same type; however their shape and tip radius are not the same. Moreover, to functionalise them with thiols, prior deposition of 10 nm of gold was required. That could change the tips curvature dramatically and make some of them more flat than others. These differences between tips are reflected in their spring constants values. It was found that for tips coming from different deposition batches different spring constant values were recorded.

Studies of linker B chiral derivatives probing surface of linker C chiral derivatives revealed the order of forces to be: *DL-DL* > *DL-LL* > *LL-DL* >> *LL-LL*. The same situation was found in studies of cysteines probing surfaces of linker C chiral derivatives, confirming that the quality of the surface has tremendous influence on the measurements.

It was also observed that in every case there was a number of additional force bands recorded. Because of the fact that studies for partially modified systems were not done due to the lack of time it is hard to assign these forces to single interactions. However they are thought to come from the interactions between modified linker and bare linker as the forces of interactions between molecules functionalized with single functional groups are known to be greater than 0.3 nN^{12,13}.

Click chemistry reaction used for this study was found extremely hard to maintain on the same level of quality. Only the best surfaces were used for force-distance studies. From all of the histograms we learnt that additional studies of partially modified systems are needed to fully understand the nature of the recorded forces.

7.5 Reference List

1. Weis, R. M.; McConnell, H. M. Two-Dimensional Chiral Crystals of Phospholipid. *Nature* **1984**, *310* (5972), 47-49.
2. Eckhardt, C. J.; Peachey, N. M.; Swanson, D. R.; Takacs, J. M.; Khan, M. A.; Gong, X.; Kim, J. H.; Wang, J.; Uphaus, R. A. Separation of Chiral Phases in Monolayer Crystals of Racemic Amphiphiles. *Nature* **1993**, *362* (6421), 614-616.
3. Humblot, V.; Raval, R. Chiral metal surfaces from the adsorption of chiral and achiral molecules. *Applied Surface Science* **2005**, *241* (1-2), 150-156.
4. Raval, R. Chiral expressions at metal surfaces. *Current Opinion in Solid State & Materials Science* **2003**, *7* (1), 67-74.
5. Bohringer, M.; Morgenstern, K.; Schneider, W. D.; Berndt, R. Separation of a racemic mixture of two-dimensional molecular clusters by scanning tunneling microscopy. *Angewandte Chemie-International Edition* **1999**, *38* (6), 821-823.
6. McKendry, R.; Theoclitou, M. E.; Rayment, T.; Abell, C. Chiral discrimination by chemical force microscopy. *Nature* **1998**, *391* (6667), 566-568.
7. Mahapatro, M.; Gibson, C.; Abell, C.; Rayment, T. Chiral discrimination of basic and hydrophobic molecules by chemical force spectroscopy. *Ultramicroscopy* **2010**, *97* (1-4), 297-301.
8. Nita, S.; Horton, J. H.; Cann, N. M. Solvation of the N-(1-Phenylethyl)-N-[3-(triethoxysilyl)propyl]-urea Chiral Stationary Phase in Mixed Alcohol/Water Solvents. *The Journal of Physical Chemistry B* **2006**, *110* (19), 9511-9519.
9. Otsuka, H.; Arima, T.; Koga, T.; Takahara, A. Rational model for chiral recognition in a silica-based chiral column: chiral recognition of N-(3,5-dinitrobenzoyl)phenylglycine-terminated alkylsilane monolayer by 2,2,2-trifluoro-1-(9-anthryl)ethanol derivatives by chemical force microscopy. *Journal of Physical Organic Chemistry* **2005**, *18* (9), 957-961.
10. Seneviratne, V. Friction Force Microscopy Using Self-Assembled Monolayers: Molecular Scale Roughness and Chiral Interactions-PhD thesis. 2006.
11. Baumgartner, W.; Hinterdorfer, P.; Schindler, H. Data analysis of interaction forces measured with the atomic force microscope. *Ultramicroscopy* **2000**, *82* (1-4), 85-95.
12. Burnham, N. A.; Dominguez, D. D.; Mowery, R. L.; Colton, R. J. Probing the surface forces of monolayer films with an atomic-force microscope. *Phys. Rev. Lett.* **1990**, *64* (16), 1931.
13. Frisbie, C. D.; Rozsnyai, L. F.; Noy, A.; Wrighton, M. S.; Lieber, C. M. Functional Group Imaging by Chemical Force Microscopy. *Science* **1994**, *265* (5181), 2071-2074.

8 Final conclusions

Two main objectives of the presented study were:

- To investigate if chirally tailed SAMs can influence chirality in crystals formed of achiral compounds, which undergo chiral crystallization
- To study chiral recognition on surfaces consisting of molecules possessing two chiral centres in the terminal part of the SAM.

The first objective was partially fulfilled as we discovered out that to determine chirality of crystals formed on chiral SAMs more sophisticated methods need to be used. NSOM measurements showed that this technique can give more insight on inducing direction in chiral crystallization. In our case only a few NSOM measurements could be conducted, but the results were in favour of enantioselectivity.

In the study it was also found that the surface preparation could have an influence on the crystal formation. Cysteine assembly on gold surfaces should be conducted at a different pH to achieve the most densely packed surface.

Final crystallization results gave a perspective for further studies in the subject of inducing chirality in crystals in chiral crystallization processes.

At some stage of Project 01 the idea to use surfaces prepared by click chemistry arose. Further investigation (subsequent studies in Project 02) into the preparation of such surfaces and their final quality led us to decide not to use these surfaces for crystallization. For studies of inducing chirality over chiral crystallization, surfaces made in a one-step preparation should be used; two-step preparation process increase the number of imperfections and any surface defect can start a nucleation process.

The second objective was fully realised in terms of studies in ethanol. As shown in section 7.4, the inner chiral centre can be detected by chiral recognition. It was also found that for dipeptides the influence of additional factors, such as hydrogen bonding and the charge of functional groups cannot be neglected. Additional studies of cysteine interactions showed that they could be diminished by conducting experiments in the medium of pH close to the tested molecules' isoelectric point. To diminish the influence of hydrogen bonding formation, studies in aprotic solvent should be conducted.

From the studies of systems fully modified in AAC reactions it was also found that the surface structure depends on the linker type, thus different force dispersion was observed. Tests carried out with use of tips modified with chiral and achiral groups confirmed that conformation at the chiral centre causes the specific recognition.

The overall conclusion from Project02 is that the studies gave only a partial answer as to the influence of the additional forces acting at the tip- surface interface as we could not conduct experiments with use of AlaAlaLD and DD enantiomers. However, the achieved results give a perspective for further investigation in this subject.

Click chemistry reactions at surfaces are worth mentioning here. It was found that the final structure of the surface is influenced by the linker used in a tremendous way. Force- distance experiments showed that additional studies of surfaces made with the Cu-AAC reaction should be conducted to fully understand the 'coiling' tendency of the molecules. STM studies of the molecules formed in two- steps preparation might be more supportive when comparing MM2 simulations of these molecules anchored to the surface.

Results achieved in this study gave a good basis for future work either in chiral crystallization and chiral recognition. It is believed that conducting chiral crystallization of hippuric acid and BHT on more chemically compatible SAM will give positive results when determination of chirality is performed using NSOM technique. Chiral recognition studies showed that pH of the liquid used for F-D spectroscopy plays a significant role in observing the recognition effect. Future work should be

carried out towards determination pH influence on the recognition effect. The fact that only AlaAlaDL and AlaAlaLL enantiomers were successfully synthesised was found as an obstacle to conduct full set of chiral interaction measurements. Works towards discovering the way of synthesis of AlaAlaDD and AlaAlaLD enantiomers would give a possibility to fully complete Project 02.

Appendix 1

Igor Pro procedure code for force-distance data analysis:

```

...
#pragma rtGlobals=1          // Use modern global access method.

Macro AFMpanel()

dowindow AFMpanel0

if(V_flag)

killwindow AFMpanel0

endif

newdatafolder/o/s root:AFMloader

make/o/n=1 datalistwave, springconst, meanforce, OLS, springconstenter, bin, numbins

make/o/t/n=1 datalist

numbins=15

bin=.5

        PauseUpdate; Silent 1          // building window...

        NewPanel/K=1/N=AFMpanel /W=(108,98,614,560) as "AFM Panel"

        ShowTools/A

        ListBox fileloadlist, win=AFMpanel0, pos={16,41},size={170,156}, mode=4,
listwave=root:AFMloader:datalist, selwave=root:AFMloader:datalistwave

        Button setpath, win=AFMpanel0, pos={16,12},size={92,22},title="Set Path to Data",
Proc=AFMbutton

        Button Loaddat, win=AFMpanel0, pos={18,213},size={76,23},title="Loaddata",
Proc=AFMbutton

        setvariable springconstenter, win=AFMpanel0, pos={18,240}, size={200,20},
title="Given Spring Constant", value=root:AFMloader:springconstenter

        setvariable springconst, win=AFMpanel0, pos={18,260}, disable=2, size={200,20},
title="Spring Constant", value=root:AFMloader:springconst

        setvariable Force, win=AFMpanel0, pos={18,280}, size={200,20}, disable=2,
title="Mean Force", value=root:AFMloader:meanforce

```

```
setvariable OLS, win=AFMpanel0, pos={18,310}, size={200,20}, disable=2,
title="OLS", value=root:AFMloader:OLS
```

```
setvariable binparameter, win=AFMpanel0, pos={200,5}, size={250,20}, title="Bin
width (relative to the avg. dev.)", value=root:AFMloader:bin,limits={.1,10,.1}
```

```
setvariable numbins, win=AFMpanel0, pos={200,35}, size={200,20}, title="Number of
Bins", value=root:AFMloader:numbins,limits={3,100,1}
```

```
Button nextplot, win=AFMpanel0, pos={18,340}, size={150,25},title="Next set of
data", Proc=AFMbutton
```

```
Button deletedata, win=AFMpanel0, pos={180,340}, size={150,25},title="This data is
shit", Proc=AFMbutton
```

```
Button reanalyze, win=AFMpanel0, pos={360,340}, size={150,25},title="reanalyze
previous", Proc=AFMbutton
```

```
button refreshcheck,win=AFMpanel0, pos={200,80},size={150,25},title="refresh peak
(cursor C)",proc=AFMbutton
```

```
EndMacro
```

```
function AFMbutton(ctrlname):buttoncontrol
```

```
string ctrlname
```

```
if(cmpstr(ctrlname,"setpath")==0)
```

```
setpathproc()
```

```
elseif(cmpstr(ctrlname,"Loaddat")==0)
```

```
loaddatapro()
```

```
elseif(cmpstr(ctrlname,"nextplot")==0)
```

```
calolsproc()
```

```
elseif(cmpstr(ctrlname,"deletedata")==0)
```

```
nodata()
```

```
elseif(cmpstr(ctrlname,"reanalyze")==0)
```

```
alltraceplot()
```

```
elseif(cmpstr(ctrlname,"refreshcheck")==0)
```

```
SVAR newfolder=root:AFMloader:newfolder
NVAR backgroundleft=$( "root:rawAFMdata:"+newfolder+": "+"backgroundleft")
wave retrace=root:AFMloader:retrace

textbox/W=checkdata/C/A=lt/N=peak "peak at "+num2str(retrace[pcsr(C,"checkdata")][1])
endif
end

static function setpathproc()
newpath/Q/O/M="Where is yo Data dude?" AFMdir
setdatafolder root:AFMloader
string files
files=indexedfile(AFMdir,-1,"????")
variable n
n=itemsinlist(files, ";")
make/o/n=(n) datalistwave, curvelistwave
make/o/t/n=(n) datalist
variable i
for(i=0; i<n; i+=1)
datalist[i]=stringfromlist(i, files)
endfor
end

static function loaddataprocc()
variable i
variable j
setdatafolder root:AFMloader
string newfolder1
```

```
prompt newfolder1, "Name of New Folder"
doprompt "Enter Folder Name", newfolder1
string/g newfolder,folders
folders=""
newfolder=newfolder1
newdatafolder/o/s $("root:AFMloader:"+newfolder)
string/g currentfolder
wave/t datalist=root:AFMloader:datalist
wave datalistwave=root:AFMloader:datalistwave
wave curvelistwave=root:AFMloader:curvelistwave

wave springconst=root:AFMloader:springconst
wave meanforce=root:AFMloader:meanforce
wave OLS=root:AFMloader:OLS
wave bin=root:AFMloader:bin
wave numbins=root:AFMloader:numbins

wave springconstenter=root:AFMloader:springconstenter
for(i=0;i<1000;i+=1)
wave olddat=$("testdat"+num2str(i))
if(waveexists(olddat))
killwaves olddat
else
break
endif
endfor
variable/g m
variable u,n
```

```

newdatafolder/o/s root:rawAFMdata

m=-1

curvelistwave=0

for(i=0;i<(dimsize(datalist,0));i+=1)

curvelistwave[i]=0

    if(datalistwave[i]==1)

        folders+=datalist[i]+";"

                m+=1

                newdatafolder/o/s $("root:AFMloader:"+newfolder)

                make/d/o/n=(m+1) OLSwave, springwave

                    currentfolder=datalist[i]

                    newdatafolder/o/s $("root:rawAFMdata:"+newfolder)

                    getfilefolderinfo/Q/P=AFMdir datalist[i]

                        newdatafolder/o/s $("root:rawAFMdata:"+newfolder+"."+datalist[i]+".")

                        if(V_logEOF>2000)

                            loadwave/Q/N=testdat/J/M/K=1/V={"\t","$",0,0}/L={0,51,0,0,0}/P=AFMdir
datalist[i]

                            else

                                doalert 1,"file "+datalist[i]+" don't have a lot of data. Do you want to try and
load it anyway?"

                                    if(V_flag==1)

                                        loadwave/Q/N=testdat/J/M/K=1/V={"\t","$",0,0}/L={0,51,0,0,0}/P=AFMdir
datalist[i]

                                        else

                                            make/o/d/n=3 testdat0

```

```
endif
endif
wave testdata=$("root:rawAFMdata:"+newfolder+": "+datalist[j]+": "+testdat0")

testdata[][2]*=springconstenter
//make a wave with all data

    wave testdat0
    dowindow checkdata
    if(V_flag)
        killwindow checkdata
    endif
    setdatafolder root:AFMloader
    make/o/d/n=(dimsize(testdata,0)/2,2) trace, retrace,yvalues
    make/o/d/n=(dimsize(testdata,0)/2,1) yvalues
    for(j=1;j<dimsize(testdata,0);j+=1)
        if(testdata[j-1][1]<testdata[j][1])
            trace[][0]=testdata[p][1]
            trace[][1]=testdata[p][2]
            retrace[][0]=testdata[x+j][1]
            retrace[][1]=testdata[x+j][2]
        break
    endif
endfor

setdatafolder $("root:rawAFMdata:"+newfolder)
variable/g peak,backgroundleft,backgroundright, forcloc
```

```

display/k=1/N=checkdata trace[][1] vs trace[][0]
appendtograph/W=checkdata retrace[][1] vs retrace[][0]
modifygraph
rgb(retrace)=(0,0,64000),mode(trace)=2,mode(retrace)=2
ModifyGraph mode=4,marker=19,mrkThick=5
legend
yvalues=retrace[p][1]
findpeak/Q/N yvalues
cursor/W=checkdata A trace (dimsize(trace,0)-1)
cursor/W=checkdata B trace ((dimsize(trace,0)-1)-.8*(V_PeakLoc))
yvalues=retrace[p][1]
findpeak/Q/N yvalues
if(V_flag==0)
    peak=V_PeakVal

    forceloc=V_peakLoc
    cursor/W=checkdata C retrace (round(V_PeakLoc))
    make/o/d/n=(dimsize(retrace,0)-round(V_PeakLoc)-12)
retracebackgroundslope
    n=-1
    for(u=(round(V_PeakLoc)+2);u<(dimsize(retrace,0)-
round(V_PeakLoc)-10);u+=1)
        n+=1
        curvefit      line,      retrace[u,dimsize(retrace,0)-
1][1]/x=retrace[u,dimsize(retrace,0)-1][0]/D
        retracebackgroundslope[n]=K1
    endfor

```



```

retracebackgroundslope      findpeak/Q/N/R=(1,.8*dimsize(retracebackgroundslope,0))

//display/k=1/N=retracebackground retracebackgroundslope
backgroundleft=forceloc+2+V_Peakloc-1
cursor/W=checkdata D retrace (backgroundleft)
cursor/W=checkdata E retrace (dimsize(retrace,0))

else
    doalert 1,"no peak was found in the data. Do you want to
    abort? if you know the data is not so good, click no, then the shit data button."
    if(V_flag==1)
        abort
    endif
    cursor/W=checkdata C retrace (100)
    cursor/W=checkdata D retrace (120)
    cursor/W=checkdata E retrace (dimsize(retrace,0))
endif

//now to subtract the bacground of the retrace

textbox/W=checkdata/A=lt/N=peak "peak at "+num2str(V_PeakVal)
textbox/W=checkdata/A=MT/N=file "file name "+datalist[i]
showinfo

doupdate
pauseforuser checkdata, AFMpanel0

wave
force1=$("root:rawAFMdata:"+newfolder+"."+currentfolder+":Force1")
if(force1[0]<1e50)//check if data is bad. if so force1 will be nan
    curvelistwave[i]=1
else

```

```
        curvelistwave[i]=0
    endif

    douupdate
endif
endfor
alltraceplot()

end

//Plot all of the curves on one graph
static function alltraceplot()
SVAR newfolder=root:AFMloader:newfolder
setdatafolder $("root:rawAFMdata:"+newfolder)
make/o/n=(1) Forcewave, forcehist
variable i
variable m
m=-1
wave/t datalist=root:AFMloader:datalist
wave curvelistwave=root:AFMloader:curvelistwave
for(i=0;i<(dimsize(datalist,0));i+=1)
    if(curvelistwave[i]==1)
        m+=1
        setdatafolder $("root:rawAFMdata:"+newfolder+"."+datalist[i]+".")
        wave voltagetrace,voltageretrace, Force1, testdat0
        wave numbins=root:AFMloader:numbins
```

```
wave bin=root:AFMloader:bin
make/o/d/n=(dimsize(voltagetrace,0)) normtrace, normretrace
normtrace=-1*voltagetrace[p][1]
//normtrace=voltagetrace[p][1]/wavemin(normtrace)
normretrace=-1*voltageretrace[p][1]
//normretrace=voltageretrace[p][1]/wavemin(normretrace)
dowindow alltrace
if(V_flag)
appendtograph/W=alltrace normtrace vs voltagetrace[][0]
appendtograph/W=alltrace normretrace vs voltageretrace[][0]
modifygraph rgb($"normtrace#+num2str(m))=(64000-m*1000,m*5000,0)
modifygraph rgb($"normretrace#+num2str(m))=(64000-m*1000,m*5000,0)
else
display/k=1/N=alltrace normtrace vs voltagetrace[][0]
appendtograph/W=alltrace normretrace vs voltageretrace[][0]

endif

redimension/n=(m+1) Forcewave, forcehist
Forcewave[m]=Force1

endif

endfor
//legend

wavestats Forcewave
histogram/B={.95*V_min,V_adev*bin,numbins} Forcewave, forcehist//
```

```
dowindow forceplot
    if(V_flag)
        killwindow forceplot
    endif

display/k=1/N=forceplot forcehist
modifygraph/W=forceplot mode(forcehist)=5
label left, "Frequency"
label bottom, "Force (nN)"
textbox/N=text0/W=forceplot "Mean is "+num2str(mean(Forcewave))

end

static function calolsproc()

setdatafolder root:AFMloader
SVAR newfolder=root:AFMloader:newfolder
wave trace=$("root:AFMloader:"+trace")
SVAR currentfolder=$("root:AFMloader:"+newfolder+":currentfolder")
wave testdata=$("root:rawAFMdata:"+newfolder+": "+currentfolder+": "+testdat0")
wave trace=root:AFMloader:trace
wave retrace=root:AFMloader:retrace
setdatafolder $("root:AFMloader:"+newfolder)
variable/g left
variable/g right
wave curvelistwave=root:AFMloader:curvelistwave
```

```
NVAR peak=$( "root:rawAFMdata:"+newfolder+": "+"peak" )
```

```
peak=retrace[pcsr(C,"checkdata")][1]
```

```
left=pcsr(A,"checkdata")
```

```
right=pcsr(B,"checkdata")
```

```
curvefit line,  
trace[pcsr(A,"checkdata"),pcsr(B,"checkdata")][1]/x=trace[pcsr(A,"checkdata"),pcsr(B,"check  
data")][0]/D
```

```
wave OLS=root:AFMloader:OLS
```

```
OLS=abs(1/K1)
```

```
string test
```

```
SVAR currentfolder=$( "root:AFMloader:"+newfolder+":currentfolder" )
```

```
setdatafolder $( "root:rawAFMdata:"+newfolder+": "+"currentfolder+"")
```

```
make/o/d/n=1 OLS1, Force1, Spring1
```

```
OLS1=abs(1/K1)
```

```
make/d/o/n=(dimsize(trace,0),2) voltagetrace,voltageretrace
```

```
voltagetrace[][1]=trace[p][1]*OLS1
```

```
voltageretrace[][1]=retrace[p][1]*OLS1
```

```
voltagetrace[][0]=trace[p][0]
```

```
voltageretrace[][0]=retrace[p][0]
```

```
duplicate/o/r=(pcsr(d,"checkdata"),pcsr(e,"checkdata"))(1,1) retrace,background
```

```
variable meanbk=mean(background)
```

```
peak=retrace[pcsr(C,"checkdata")][1]
```

```
Force1=abs((peak-mean(background))*OLS1)
```

```
Spring1=1
```

```
dowindow checkdata
```

```
if(V_flag)
killwindow checkdata
endif
end

static function nodata()
//just reset counter "m" and kill window
SVAR newfolder=$("root:AFMloader:newfolder")

SVAR currentfolder=$("root:AFMloader:"+newfolder+":currentfolder")
setdatafolder $("root:rawAFMdata:"+newfolder+": "+currentfolder+"")
make/o/d/n=1 OLS1, Force1, Spring1
SVAR newfolder=root:AFMloader:newfolder
NVAR m=$("root:AFMloader:"+newfolder+":m")
wave Forcewave=$("root:AFMloader:"+newfolder+":Forcewave")
m=dimsize(Forcewave,0)-1
OLS1=nan
Force1=nan
Spring1=nan
dowindow checkdata
if(V_flag)
killwindow checkdata
endif
end
```

Appendix 2

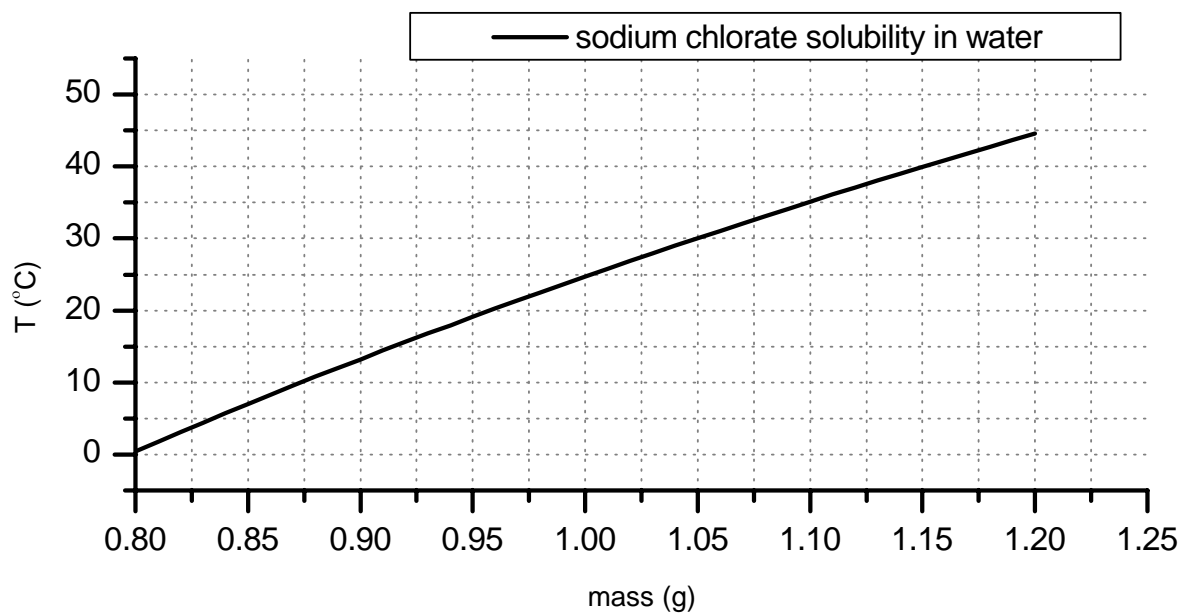


Figure I Sodium chlorate solubility in water, *The Agrochemicals Handbook*. 1983. The Royal Society of Chemistry, The University, Nottingham, England.